2015

BrachyView: a novel imaging system using timepix for intraoperative dynamic dose planing for low dose rate prostrate Brachytherapy treatment

Kevin Jia-Jin Loo
University of Wollongong

BrachyView: A Novel Imaging System Using Timepix for Intraoperative Dynamic Dose Planning for Low Dose Rate Prostate Brachytherapy Treatment

A thesis submitted in fulfilment of the
requirements for the award of the degree

Doctor of Philosophy

from

UNIVERSITY OF WOLLONGONG

by

Kevin Jia-Jin Loo
Bachelor of Medical Radiation Physics (Honours Class I)
University of Wollongong, 2010

CENTRE FOR MEDICAL RADIATION PHYSICS
2015

Abstract

Prostate cancer is one of the most commonly diagnosed cancers in the western world, accounting for nearly 30% of all male malignancies. Radiation treatment of such cancer has high success rates, and depends primarily on the physician's ability to deliver a conformal therapeutic dose to the tumour. This involves a process of treatment planning, brachytherapy implantation, and post-implant dosimetric verification.

The conformity of the achieved dose distribution to the treatment plan strongly correlates with the accuracy of seed implantation in a prostate brachytherapy treatment procedure. Incorrect seed placement leads to both short and long term complications, including urethral and rectal toxicity. The author presents BrachyView, a novel concept of a fast intraoperative treatment planning system, to provide real-time seed placement information based on in-body gamma camera data. BrachyView combines the high spatial resolution of a pixellated silicon detector (Medipix2) with the volumetric information acquired by a transrectal ultrasound (TRUS). The two systems will be embedded in the same probe so as to provide anatomically correct seed positions for intraoperative planning and postimplant dosimetry in real time during implantation. Dosimetric calculations are based on the TG-43 method using the real position of the seeds.

The purpose of this thesis is to demonstrate the feasibility of BrachyView using the Medipix pixel detector and a pinhole collimator to reconstruct the real-time 3D position of low dose-rate brachytherapy seeds in a phantom. The design and geometry of the system was optimised by means of Monte Carlo methods, verifying the truncated

cone design of the pinhole and thickness of lead collimator.

BrachyView incorporates Medipix detectors coupled to a multipinhole collimator. Three-dimensionally triangulated seed positions from multiple planar images are used to determine the seed placement in a PMMA prostate phantom in real time. MATLAB codes were used to test the reconstruction method and to optimise the device geometry. The results presented in this thesis show a 3D position reconstruction accuracy of the seed in the range of 0.5-3 mm for a 10-60 mm seed-to-detector distance range (Z direction), respectively. The BrachyView system also demonstrates a spatial resolution of 0.25 mm in the XY plane for sources at 10 mm distance from the Medipix2 detector plane, comparable to the theoretical value calculated for an equivalent gamma camera arrangement. The author successfully demonstrated the capability of BrachyView for real-time imaging (using a 3s data acquisition time) of different brachytherapy seed configurations (with an activity of 0.05 U) in a PMMA prostate phantom.

Following this, additional experimental studies involving 20 active I-125 seeds verified the applicability of BrachyView as a real-time intraoperative imaging system for prostate LDR brachytherapy. Seed positions were co-registered with a clinical CT scan, showing accuracy within 1-3mm of expected positions. Finally, the multimodality imaging capabilities of the BrachyView system were evaluated in both CT and X-ray transmission imaging, making use of a microfocus X-ray tube and tissue-equivalent prostate phantoms.

The newly developed miniature gamma camera component of BrachyView, with its high spatial resolution and real time capability, allows accurate 3D localisation of implanted sources in a prostate phantom. Combination of the gamma camera with the transrectal ultrasound in a single probe will complete the BrachyView system. This thesis addresses issues of ionising radiation detection in cancer therapy, leading to seed position determination and object imaging.

Statement of Originality

This is to certify that the work described in this thesis is entirely my own, except where due reference is made in the text.

No work in this thesis has been submitted for a degree to any other university or institution.

Signed

Kevin Jia-Jin Loo
July, 2015

Acknowledgments

I would like to thank:

Prof. Anatoly Rosenfeld, Dr Marco Petasecca, Dr Michael Lerch, Dr Mitra Safavi-Naeini, Mrs Karen Ford, and the rest of the staff and students at CMRP, UOW who made this work possible. Prof. Stanislav Pospisil, Dr Jan Jakubek, Ivan Caicedo, Benedikt Bergmann and the rest of the ARDENT team for a memorable three years in Europe. My family for supporting me and teaching me the value of education. My friends all around the world for reminding me to work hard so I can play harder. And Chicko's for their schnitzel burgers.

Contents

List of Figures

List of Tables

List of Abbreviations

ADT	Androgen Deprivation Therapy
CMOS	Complementary Metal-Oxide-Semiconductor
CMRP	Centre for Medical Radiation Physics
CTU	Czech Technical University
DICOM	Digital Imaging and Communications in Medicine
EBRT	External Beam Radiation Therapy
GUI	Graphic User Interface
HDR	High Dose Rate
IEAP	Institute of Experimental and Applied Physics
IO	Intraoperative
LDR	Low Dose Rate
MSKCC	Memorial Sloan-Kettering Cancer Center
OARs	Organs at Risk
OSEM	Ordered Subset Expectation Maximisation
PPB	Permanent Prostate Brachytherapy
PSA	Prostate-Specific Antigen
RP	Radical Prostatectomy
SCD	Source collimator distance
TRUS	Transrectal Ultrasound

Chapter 1

Introduction

Prostate cancer is the highest occurring cancer in Australian males. With early detection however, treatment has a high success rate by either surgical techniques or radiation therapy. Recently, the use of permanent radioactive implants has grown to become a popular choice for men facing prostate cancer. This technique is known as brachytherapy.

Permanent prostate brachytherapy (PPB) consists of the permanent implantation of low energy radioactive sources directly into the patient's prostate. This technique is typically guided by transrectal ultrasound imaging in conjunction with X-ray fluoroscopy and post-implant CT scans. However, the nature of these imaging techniques do not allow for adjustments during implant in cases of poor dosimetry or tumour and gland coverage. The location of these brachytherapy seeds is the largest contributor to dosimetric error, and therefore clinical treatment outcome.

In the brachytherapy community, there has been recent discussion concerning the use of real-time intraoperative treatment planning techniques based on real-time imaging. Some investigations have been undertaken to implement real-time imaging systems for brachytherapy implant guidance. To date, no system exists that is robust and cost-effective for widespread use.

By utilising the novel semiconductor detector Medipix (and later generation Timepix)

coupled with a unique pinhole camera system, BrachyView is proposed by CMRP as an in-body imaging device capable of providing real-time seed localisation. This would allow a real-time optimisation of the implant, thereby ensuring maximal dose coverage of the tumour and treatment outcome.

The application of Timepix also opens up the possibility of other imaging modalities such as CT and soft tissue diagnostic imaging, suggesting the use of BrachyView as an ultra-functional, multi-modality imaging device for the effective management of the brachytherapy procedure.

1.1 Objectives, Overview and Summary of Contributions of this Thesis

The objectives of this thesis are as follows:

- Develop a novel imaging and dose planning system for low dose rate prostate brachytherapy implant treatments;
- Use high-resolution Timepix detectors for imaging of implanted I-125 brachytherapy implants;
- Test a pinhole system coupled with aforementioned Timepix detectors in accuractely localising sources within three-dimensions;
- Propose an intraoperative dynamic dosimetric system to optimise patient outcomes by avoiding critical structures surrounding the prostate anatomy;
- Test the applicability of Timepix for use in tomographic measurements for post-implant dosimetric checks;
- Present BrachyView as a unique, ultra-functional imaging probe, with capability for multiple modalities in imaging.

The Thesis is divided into the following chapters:

- Chapter 1 presents an introduction to the main topics covered in the Thesis;
- Chapter 2 presents a comprehensive review of relevant literature, outlining the history and modern practices of prostate brachytherapy;
- Chapter 3 presents a detailed description of the proposed novel detector assembly for use in BrachyView;
- Chapter 4 presents the analytical and simulation models used to optimise the pinhole collimator characteristics used in experimental work;
- Chapter 5 presents a detailed description of the pinhole used in experimental phantom studies for proof of concept studies in BrachyView. Using this pinhole system, LDR seed localisation was performed. This work resulted in the following publications and presentations:

  K.J. Loo, M. Petasecca, Z. Han, D.L. Cutajar, M. Weaver, M. Lerch, P.E. Metcalfe, S. Meikle, S. Pospisil, J. Jakubek, J.A. Bucci, M. Zaider, A.B. Rosenfeld, BrachyView: In-prostate real time seed position imaging for prostate brachytherapy using Medipix camera, *20th Annual Australasian Brachytherapy Group Meeting*, 2011

  K.J. Loo, M. Safavi, M. Lerch, Z. Han, J. Jakubek, S. Pospisil, S. Meikle, M. Zaider, J. Bucci, A.B. Rosenfeld, BrachyView: A novel in-body imaging system for prostate brachytherapy, *Nuclear Science Symposium and Medical Imaging Conference (NSS/MIC) 2011 IEEE*, pp. 279-281, 2011

  M. Petasecca, K.J. Loo, Z. Han, P.E. Metcalfe, S. Meikle, S. Pospisil, J. Jakubek, J.A. Bucci, M. Zaider, M.L. Lerch, Y. Qi, A.B. Rosenfeld, BrachyView: proof-of-principle of a novel in-body gamma camera for low dose-rate prostate brachytherapy, *Medical Physics*, vol. 40, no. 4, 2013

- Chapter 6 presents experimental and analytic work performed to evaluate the application of Timepix detectors in CT reconstruction of implanted LDR seeds. This work resulted in the following publications and presentations:

K.J. Loo, M. Petasecca, M. Safavi-Naeini, Z. Han, BrachyView: Tomographic reconstruction using Timepix detectors in post-implant dosimetry checks for permanent prostate brachytherapy implants, *Nuclear Science Symposium and Medical Imaging Conference (NSS/MIC) 2013 IEEE*, pp. 1-3, 2013

- Chapter 7 presents experimental work performed with Timepix for evaluation of soft tissue diagnostic imaging using a medical tissue-equivalent prostate gel phantom. This work resulted in the following publications and presentations:

  K.J. Loo, J. Jakubek, J. Zemlicka, M. Petasecca, M. Safavi-Naeini, J. Bucci, M. Zaider, A.B. Rosenfeld, Feasibility study into the application of Timepix detectors for soft tissue thickness imaging in prostate brachytherapy treatment, *Radiation Measurements*, vol. 71, pp. 329-332, 2014

1.2 Presentations and Invited Talks

This work has been presented at the following conferences and meetings:

- 2010
  - Australian Rotary Health PhD Scholars Dinner, Parramatta City, Australia, June 7: invited talk.
- 2011
  - Australian Rotary Health District Conference, Bathurst, Australia, March 18: invited talk.
  - 20th Annual Australasian Brachytherapy Group Meeting, Perth, Australia, April 28-30: oral presentation.
  - Australian Rotary Health PhD scholars Dinner, Parramatta City, Australia, May 9: invited talk.
  - Rotary Club of Berrima District Lunch, Berrima, Australia, July 6: invited talk.

  - IEEE Nuclear Science Symposium and Medical Imaging Conference, Valencia, Spain, October 23-29: poster presentation.

- 2012

  - 21st Annual Australasian Brachytherapy Group Meeting, Canberra, Australia, March 1-3: oral presentation.
  - Australian Rotary Health District Conference, Wollongong, Australia, March 18: invited talk.
  - World Congress on Medical Physics and Biomedical Engineering, Beijing, China, May 26-31: oral presentation (by Prof. Anatoly Rosenfeld).
  - 1st Annual ARDENT Workshop, Vienna, Austria, November 20-23: oral presentation.

- 2013

  - HSC Physics class, Illawarra Christian School, Cordeaux Campus, Wollongong, Australia, April 9: oral presentation.
  - Australian Rotary Club meeting, Parramatta, Australia, April 15: oral presentation.
  - ARDENT Meeting, Geneva, Switzerland, June 13: oral presentation.
  - HSC Physics class, Kirawee High School, Sydney, Australia, September 2: oral presentation.
  - 17th Annual Conference on Solid State Dosimetry, Recife, Brazil, September 22-27: poster and oral presentation.
  - IEEE Nuclear Science Symposium and Medical Imaging Conference, Seoul, South Korea, October 27-November 2: two oral presentations.
  - 2nd Annual ARDENT Workshop and Mid-Term Review, Milan, Italy, October 14-18: oral presentation.
  - National Radiation Protection Institute (SURO), Prague, Czech Republic, November 20: invited talk.

  - Marie Curie Actions: Horizon 20/20, Florence, Italy, November 26-27: invited talk.

- 2014

  - 3rd Annual ARDENT Workshop, Burgthann, Germany, September 30: oral presentation.

- 2015

  - IBA Dosimetry, Memphis, USA, February 11: oral presentation.
  - 4th Annual ARDENT Workshop, Prague, Czech Republic, June 22: oral presentation.
  - 4th Annual ARDENT Workshop Outreach Program, Prague, Czech Republic, June 24: oral presentation.

1.3 Funding Support and Awards

This work was supported by the Australian National Health and Medical Research Council (NHMRC) under Development Grant 1000557 entitled ”A new multifunctional probe for in-body radiation imaging and dosimetry during brachytherapy treatment of prostate cancer”, which is a collaboration between the University of Wollongongs Centre for Medical Radiation Physics (lead investigator Prof Anatoly Rosenfeld), the Czech Technical University’s Institute of Experimental and Applied Physics (Dr Jan Jakubek), St George Cancer Care Centre (Dr Joseph Bucci), the University of Sydney’s Brain & Mind Research Institute (Dr Steven Meikle), and Memorial Sloan-Kettering Cancer Center (Prof Marco Zaider).

This research was also supported by the Australian Rotary Health Foundation for a research topic involving prostate cancer. Between 2010 and 2012, this scholarship was awarded by the Rotary Club of Parramatta City (Rotary District 9680).

In 2011, the work conducted as outlined in Chapter 5 was awarded the IEEE Nuclear Physics and Plasma Science (NPSS) Phelps Educational Grant. This award was for ”exceptional promise as a graduate student in any of the fields of the NPSS, exceptionally good work in those fields”. In 2012, this work was awarded the best presentation in the university-wide speaking contest 3 Minute Thesis and was taken to the Trans-Tasman finals held at the University of Queensland.

In 2013, this research received continued support through the ARDENT (Advanced Radiation Dosimetry European Network Training) program. The ARDENT Marie Curie Initial Training Network (ITN) is an international collaboration across 8 international institutes, and funded by CERN (Geneva, Switzerland). This is a 3 year research contract (commenced February 2013) part of which this Thesis is a deliverable.

Chapter 2

Literature Review

This Chapter presents a comprehensive review of literature related to prostate cancer and brachytherapy treatments. Section 2.1 highlights the incidence rates of prostate cancer in Australia, detailing the rising problem to men's health that cancer poses. Section 2.1.2 explains the treatment options available for men who opt for radiation therapy, including details on isotope use. Section 2.2 presents the history of prostate brachytherapy, in particular the advent of ultrasound-guided imaging proposed by Holm et al. Section 2.2.3 explains the use of ultrasound imaging in modern brachytherapy procedures and Section 2.3 details the different approaches brachytherapy practitioners use for treatment planning, including the debate of the traditional pre-planned technique versus intraoperative planning. Section 2.4 explains the importance of dosimetric analysis and the correlation with treatment outcome for prostate cancer patients. Section 2.5 presents the various methods used and tested for real-time seed localisation. Section 2.6 introduces the Timepix detector as a viable option for application in real-time imaging of the PPB implant. Section 2.7 details the use of pinholes in a novel 'gamma camera' mode in conjunction with the Timepix detectors as the basis of the BrachyView system. Finally, Section 2.8 presents a summary of the main concepts covered in this Chapter and their implications for the experimental work carried out in this Thesis.

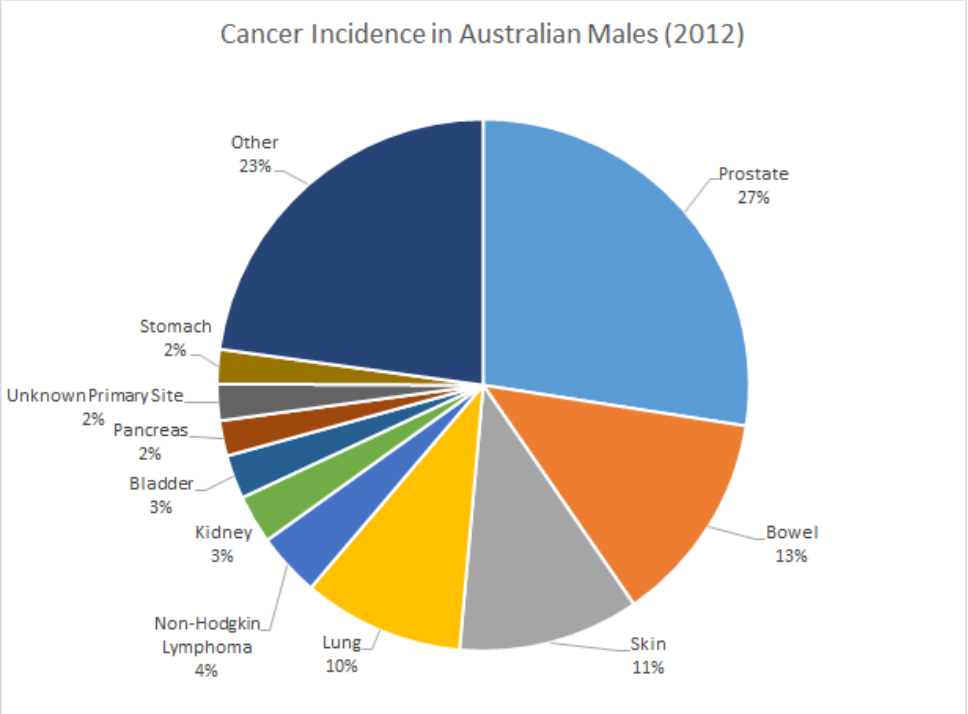

Figure 2.1 Cancers in males according to National Cancer Statistics Clearing House, AIHW.

2.1 Prostate Cancer in Australia

Prostate cancer is widely regarded internationally as one of the most prevalent problems in today's radiation oncology community. In 2012, it is estimated that 120,710 new cases were diagnosed with more than half (56%) of all cancers diagnosed in Australian males. The most commonly diagnosed cancers in males was prostate cancer accounting for 27% of all male cancers diagnosed, and is in fact the most common cancer in overall statistics. The next most common cancer, bowel cancer with 8,760 new diagnoses, had less than half the prostate statistic. The next three most common cancers were skin melanoma (7,440), lung cancer (6,620) and non-Hodgkin lymphoma (2,620) (19).

In 2012, it is estimated that 1 in 3 males were diagnosed with cancer by the age of 75, increasing to 1 in 2 by age 85. The risk is highest for prostate cancer, estimated at 1 in 8 before the age of 75, and 1 in 6 by age 85. The overall trend for prostate

Cancer site	2006	2007	2008	2009	2010
Colorectal	7,448	7,644	7,827	8,015	8,209
Skin melanoma	6,143	6,383	6,625	6,875	7,135
Prostate	16,011	16,923	17,835	18,784	19,775

Table 2.1
Annual rates of incidence for Australian men based on Australian Institute of Health and Welfare statistics. (19)

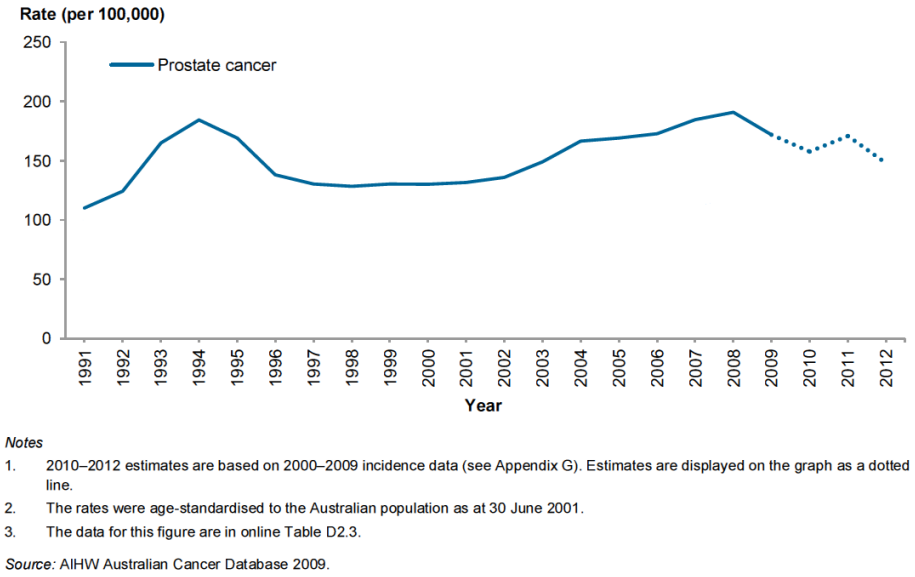

Notes

1. 2010–2012 estimates are based on 2000–2009 incidence data (see Appendix G). Estimates are displayed on the graph as a dotted line.
2. The rates were age-standardised to the Australian population as at 30 June 2001.
3. The data for this figure are in online Table D2.3.

Source: AIHW Australian Cancer Database 2009.

Figure 2.2 Trends in incidence of prostate cancer in males, Australia, 1991 to 2009, with estimates to 2012

cancer has been a gradual increase with some fluctuations in more recent years.

The peaks in prostate cancer rates are thought to be caused by changes in cancer screening and detection rather than an elevated risk of disease. PSA (prostate-specific antigen) testing first became available in 1987 and was first listed in the Medicare Benefits Schedule in 1989, accounting for the peak in the earl 1990s. The second recent rise in incidence numbers is a result of other changes in diagnostic procedures such as lowering the investigation threshold. Nonetheless, the incidence rate of prostate cancer is consistently high and the risk is ever-growing for Australian men.

LEADING CAUSES OF DEATH(a), **Australia - Selected years - 2002, 2006, 2011**(b)

Cause of death and ICD code	2002 no.	Rank	2006 no.	Rank	2011 no.	Rank
Ischaemic heart diseases (I20-I25)	26 063	1	23 132	1	21 513	1
Cerebrovascular diseases (I60-I69)	12 533	2	11 479	2	11 251	2
Dementia and Alzheimer disease (F01, F03, G30)	4 364	6	6 550	4	9 864	3
Trachea, bronchus and lung cancer (C33-C34)	7 303	3	7 353	3	8 114	4
Chronic lower respiratory diseases (J40-J47)	6 256	4	5 463	5	6 570	5
Diabetes (E10-E14)	3 329	9	3 669	8	4 209	6
Colon, sigmoid, rectum and anus cancer (C18-C21)	4 649	5	3 857	6	4 087	7
Blood and lymph cancer (including leukaemia) (C81-C96)	3 791	7	3 700	7	3 978	8
Heart failure (I50-I51)	3 367	8	2 902	11	3 488	9
Diseases of the urinary system (N00-N39)	2 887	11	3 197	9	3 386	10
Prostate cancer (C61)	2 852	12	2 951	10	3 294	11
Breast cancer (C50)	2 716	13	2 643	13	2 937	12
Influenza and pneumonia (J09-J18)	3 084	10	2 711	12	2 492	13
Pancreatic cancer (C25)	1 834	15	2 077	15	2 416	14
Intentional self-harm (X60-X84)(c)	2 320	14	2 118	14	2 272	15
Skin cancers (C43-C44)	1 462	17	1 648	17	2 087	16
Accidental falls (W00-W19)	629	38	1 288	20	1 845	17
Hypertensive diseases (I10-I15)	1 353	20	1 500	18	1 802	18
Cardiac arrhythmias (I47-I49)	1 226	21	1 280	21	1 612	19
Cirrhosis and other diseases of liver (K70-K77)	1 354	19	1 416	19	1 589	20

Figure 2.3 Causes listed are the leading causes of death for all deaths registered in 2011, based on WHO recommended tabulation of leading causes.

While being the most common cancer in Australian men, prostate cancer is the second most common cause of cancer-related deaths as discussed in Section 2.1.1.

2.1.1 Prostate Cancer Mortality in Australia

According to the Australian Bureau of Statistics (21) prostate cancer consistently ranks in the top 20 leading causes of death in Australia based on data evalation methods presented in the Bulletin of the World Health Organisation (22).

From a total of 22,421 deaths from cancer in males in 2010, the most common was lung cancer (4,934), followed by prostate cancer (3,3235) and bowel cancer (2,205).

From a total of 22,017 deaths from cancer in males in 2005, the most common was lung cancer (4,711 deaths), followed by prostate cancer (2,949). Colorectal cancer (2,322), unknown primary site (1,829) and pancreatic cancer (964) comprise the others. These accounted for 58% of all deaths from cancer in males.

Statistics released for 2008 by the ABS are such that of a total of 42,418 registered cancer-related deaths in Australia occurred. In 2008, prostate cancer was the cause of 3,031 registered deaths, which accounts for 4.1% of all male deaths. The median age at death for prostate cancer was 81.0 years. This is close to the median age for all male deaths (77.9 years). Potential life lost from deaths due to prostate cancer was 9,178 years.

2.1.2 Treatment Options

The treatment options for prostate cancer include radical prostatectomy (RP), external beam radiation therapy (EBRT), hormonal therapy (androgen deprivation therapy, or ADT), watchful waiting, and temporary and permanent brachytherapy (permanent prostate brachytherapy, or PPB). The relative efficacy of each method is a matter of some contention but since the 1980s, permanent brachytherapy has moved to the forefront.

Brachytherapy involves the insertion of radioactive sources directly into the affected organ, rather than delivering through EBRT. These sources are usually smaller than 5 mm in length and when deployed in an array their net effect is to deliver a therapeutic cloud of radiation to the affected organ. Some common areas where brachytherapy is used include the eye, breast, some skin and brain, and the prostate.

From a clinical standpoint, brachytherapy is a simple outpatient procedure that avoids the need for hospitalisation and allows rapid recovery and return to normal activity. It has also produced excellent 10-year patient outcomes as reported by Nag et al (23). As opposed to EBRT, which can take up to 6 weeks to complete, brachytherapy patients can return home after one or two days of treatment.

Brachytherapy utilises radioactive sources like iodine-125 (I-125) or palladium-103 (Pd-103), which allow dose escalation within the prostate with a rapid dose fall-off (steep dose gradient) in surrounding healthy tissues.

There are two options in prostate brachytherapy. These are either low dose rate

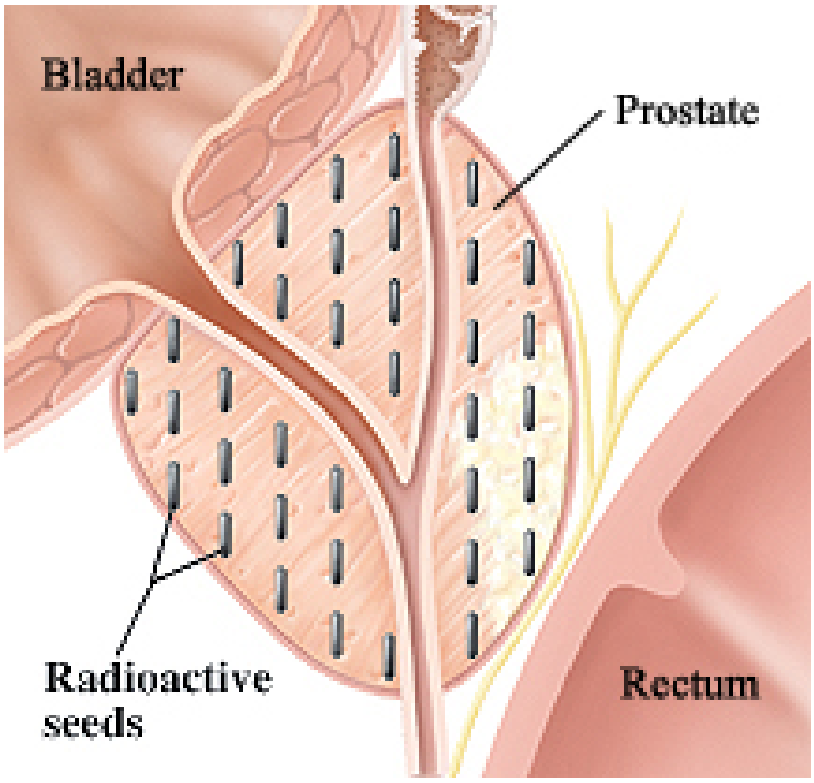

Figure 2.4 Brachytherapy sources implanted in prostate. Image courtesy of Mount Nittany Health.

Principle Radionuclide	I-125	
Radionuclide purity	I-125	$> 99.9\%$
	I-126	$< 0.005\%$
Half-life	59.43 days	
Energy level	X-ray	27.4 keV
	X-ray	31.4 keV
	Gamma	35.5 keV
	Fluorescent X-rays from Ag rod	22.1, 25.2 keV

Table 2.2 Physical properties of the I-125 seeds as presented by Oncura.

(LDR) or high dose rate (HDR). In this thesis, we will discuss the development of a novel imaging technique for PPB LDR, which relies mainly on the use of the I-125 radioisotope.

2.1.2.1 I-125 as Radioactive Source

I-125 sources are the most common source used in LDR brachytherapy. I-125 has a half-life of 59.4 days and a relatively low peak energy of 28.3 keV, consisting of a series of peaks ranging from 22.1-35.5 keV. The low energy is important for its steep dose gradient and ease of shielding. I-125 is also easily produced in medium flux nuclear reactors. Because of these favourable characteristics, I-125 seed sources are considered to be one of the best isotopes for use in prostate brachytherapy and is the premier choice for centres in Australia and the United States. It is also used in eye and breast brachytherapy procedures. There is a wide range of seed designs available but one of the most common choices is the 6711 model: Nycomed-Amersham 6711 (OncoSeed), as shown in Figure 2.7.

The seeds themselves consist of I-125 deposited on the surface of a silver core and encased within a titanium cylinder. They are 4.5 mm in total length and have an active length of 3 mm. The specific physical properties of the seed are outlined in Table 2.2. I-125 decays by electron capture with the emission of characteristic photons and electrons. The electrons are absorbed in the titanium wall.

Seeds with total apparent activity from 0.191 to 1.01 mCi (usually 0.4 mCi) are

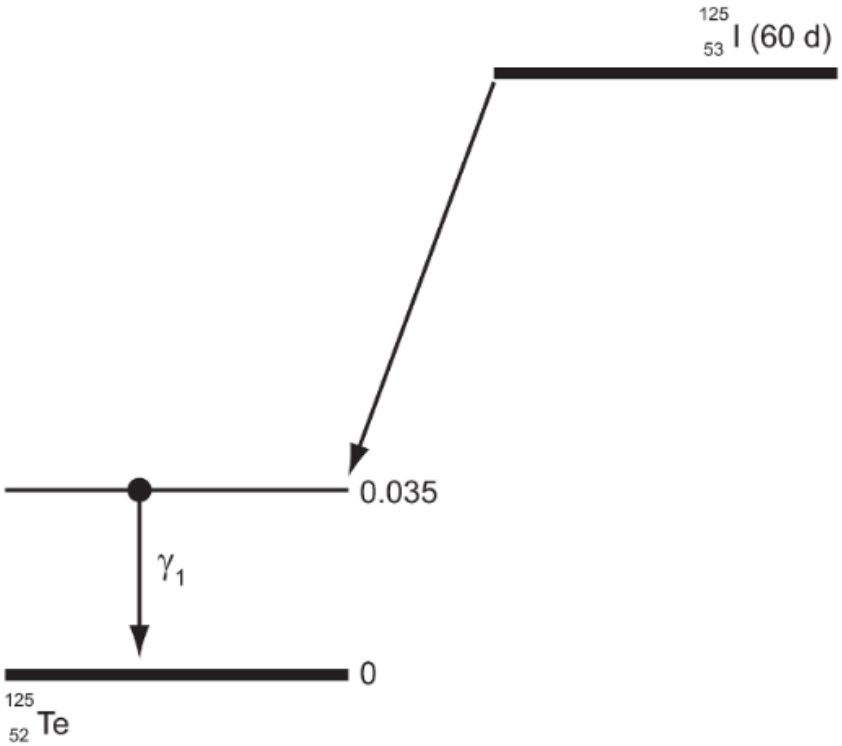

Figure 2.5 Decay scheme of I-125 showing electron capture and a maximum photon energy emission of 35 keV.

Number	Radiation (i)	Frequency of Emission (n_i)	Mean Energy (MeV) ($\bar{E}_i$)
1	γ1	0.068	0.035
2	K conversion electron	0.746	0.004
3	L conversion electron	0.107	0.031
4	M conversion electron	0.080	0.035
5	X-ray—K(α)	1.176	0.027
6	X-ray—K(β)	0.240	0.031
7	X-ray—L	0.215	0.004
8	KLL Auger electron	0.137	0.023
9	KLX Auger electron	0.058	0.026
10	KXY Auger electron	0.01	0.030
11	LMM Auger electron	1.49	0.003
12	MXY Auger electron	3.59	0.001

Figure 2.6 Radiations emitted in the Decay of I-125.

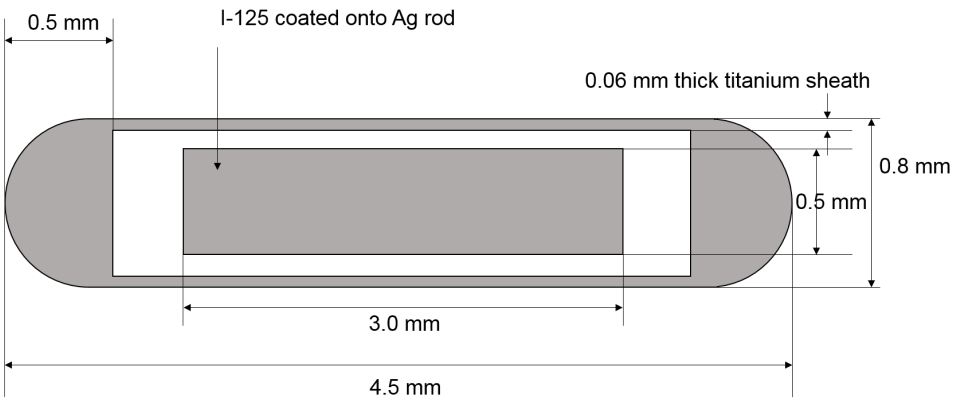

Figure 2.7 Model 6711 I-125 seed schematic by Oncoseed (1)

.

used for permanent interstitial implantation of selected localised tumours with low to moderate radiosensitivity. These are used either as primary treatment (such as in prostate cancer) or for treatment of residual disease after excision of the primary tumour. Anywhere between 80-120 seeds are typically implanted directly into the gland according to preplanning volume studies and dosimetric requirements for effective dose distribution. Apart from prostate cancer, tumours of the head, neck, lung, pancreas and the eye are also commonly treated by brachytherapy techniques.

One of the main dosimetric issues to consider in brachytherapy implants is source localisation.

Ir-192 is another commonly used source in brachytherapy procedures, but with separate application in HDR procedures.

2.1.2.2 Ir-192 as Radioactive Source

HDR treatment utilises a high-activity source such as Ir-192 to irradiate the prostate gland and tumour in a technique known as afterloading. Ir-192 differs greatly from the I-125 source introduced in Section 2.1.2.1 with a mean photon energy of 0.38 MeV and half-life of 73.8 days by beta decay. Furthermore, rather than being inserted surgically, the implant is only temporary with high-dose exposure is also achieved.

HDR techniques are typically used as booster treatments in conjunction with EBRT (also known as combined modality, as opposed to monotherapy).

Once the catheters have been implanted into the prostate and through the applicator template, the patient is moved to a specially shielded room for HDR treatment. Following CT-based treatment planning, in which the catheter positions are verified, several high dose fractions ranging from 4-6 Gy each are administered over 1-3 days. In the case of HDR monotherapy, a typical recommended dose is around 40 Gy delivered in fractions. The American Brachytherapy Society suggests 10.5 Gy$\times$3, 8.5-9.5 Gy$\times$4, or 6.0-7.5 Gy$\times$6 fractions.

The radiation is delivered by an afterloader apparatus. The source is positioned with specific dwell times and source locations according to the treatment plan. Source dwell positions are selected by suitable and accurate mechanical extension of the length of the thin transport cable, to which the source is attached. The Ir-192 source is moved into successive needles by inserting and withdrawing the cable (see Figure 2.8).

Only a single source is used as it is moved through each catheter by the afterloader. HDR treatment is usually followed by EBRT to the prostate and periprostatic tissues to a dose of approximately 50 Gy using conventional techniques (24).

HDR therapy is only suitable for cases where the tumour is well localised and relatively small. While the source is different to that in LDR treatment, the dosimetric goal remains the same such that the technique is based on ultrasound imaging and online calculations of dose distribution- live planning that consists of updating needle position based on dose parameters. Ideally, a homogeneous radiation field should exist around the catheters inserted into the prostate volume and conform to the target volume, and if possible, a cold spot (low dose area) around the urethra.

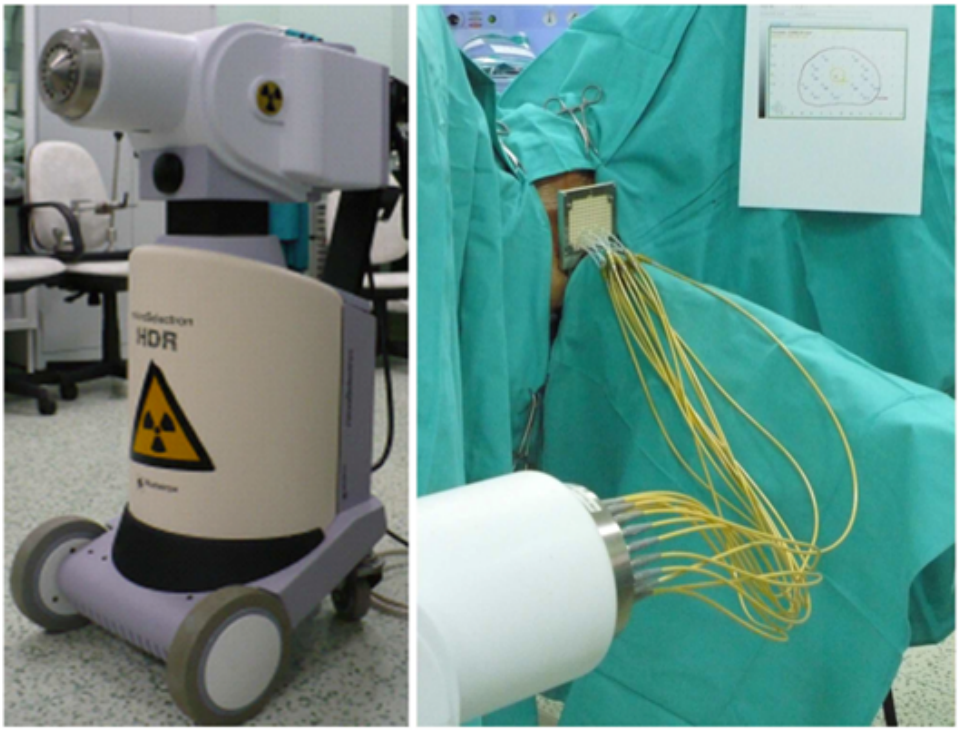

Figure 2.8 (left) MicroSelectron HDR afterloading unit. (Right) Catheters shown connecting the channel sockets in the 18-channel treatment head of the MicroSelectron unit with the needles inserted in the patient (2).

2.2 Brachytherapy for Prostate Cancer

The basic underlying principle across the literature and all research in brachytherapy is to deliver more radiation dose to the tumour and less to the surrounding normal tissues in an ongoing effort to improve the therapeutic ratio for prostate cancer treatment (25). Zerbib et al. (20) state that ”the optimal treatment strategy for a patient with prostate cancer should provide long-term disease control with minimal treatment-related morbidity and maximal preservation of quality of life”. Choice of treatment strategies change with time as evident in the two decades since the 1980s, where there has been a significant decrease in watchful waiting (active surveillance) and RP procedures, whilst accompanied by a marked increase in brachytherapy and primary androgen deprivation therapy.

In watchful waiting, patients with low-risk tumour characteristics are actively monitored without sacrificing risk of cure or unnecessary disease progression. Radiotherapy options are either external beam radiotherapy (EBRT) or brachytherapy.

There is substantial evidence as quoted by Zerbib et al that greater radiation doses are critical to achieve optimal tumour control for patients with clinically localised diseases.

EBRT is an effective, non-invasive form of radiotherapy but comes with long-term risks of troublesome bowel, sexual and urinary dysfunction. It is also considered too aggressive for low-risk cancers. For higher-grade cancers, local recurrence after radiotherapy carries substantial morbidity and low rates of long-term cancer control.

The choice of treatment is best done on a patient-to-patient basis depending on size and grade of the gland and tumour. There is evidence that brachytherapy has greater ablative potential on the prostate epithelium with greater long-term biochemical tumour control, but only in low-risk patients (26; 27). Most notably, Zelefsky et al. (28) recommend brachytherapy be considered the premier option for such patients.

Advantages	Disadvantages
Excellent cancer control rates	Need for anaesthesia
Good correlation between focal planning target volume and dose distribution	Patients with larger prostate volume require Androgen Deprivation Therapy (ADT)
Option for real-time dosimetry	Technically challenging procedure with high operator-dependence
Can focally treat anterior prostate	PSA level unlikely to decrease to 0 ng/mL, even after successful therapy
Low risk of urinary incontinence and long-term incontinence and rectal morbidity	Risk of irritative urinary symptoms or retention
Other urinary and sexual morbidities are treatable	Risk of prostatis and proctitis
Convenient and logistically simple	After treatment failure, additional local therapy associated with increased risk of morbidity
	Quality-of-life impairment (sexual, urinary and rectal function)

Table 2.3 Clinical advantages and disadvantages of prostate brachytherapy (20)

Brachytherapy is a convenient, effective form of radiotherapy for clinically confined cancer. However, favourable outcomes require meticulous technique. Acute urinary symptoms are frequent and long-term risks of proctitis and erectile dysfunction are comparable to the risks associated with EBRT.

Some of the advantages and disadvantages of brachytherapy according to Zerbib et al. (20) are shown in Table 2.3.

Brachytherapy is a rapidly evolving treatment option and advances in imaging devices are continuously being exploited. New technology to assist in implantation and to improve dose distribution and accuracy are being developed and should help to enhance the quality and consistency of implants.

Prostate cancer treatment by brachytherapy implants has had a controversial historical development in the radiation oncology community. The favoured technique as developed by Whitmore in 1972 was the retropubic approach. Prior to this, local ap-

plication of radium sources had been used since the early 20th century. These early techniques generally involved insertion of needles transperineally under digital guidance (physical palpatation). Other applications including urethral or rectal sources were also introduced. However, with the advent of the modern linear accelerator, external beam therapy became the primary modality of prostate irradiation (29).

A review paper of 18,000 studies by Grimm et al. (3) between 2000-2010 also indicated that brachytherapy has the highest rates of biochemical survival, although they do concede that this is partly due to patient selection criteria. The results for intermediate-risk patients, highlighting brachytherapy's success, is shown in Figure 2.9.

2.2.1 History: The Retropubic approach

In the early days of brachytherapy, a retropubic approach was used. This is where an abdominal incision is made and the prostate exposed for manual implantation of the I-125 seeds. From an appropriate volume study the total radiation dose and hence the number of seeds required is calculated and implanted through needles. The seed spacing in the needles is determined by dosimetry calculations. This technique was developed and popularised at Memorial Sloan-Kettering Cancer Center (MSKCC, New York) (30).

However, follow-up of patients treated by this method showed a biochemical disease-free rate of only 13% at 5 years. This failure of this technique was concluded to arise from imprecise placement of the seeds within the prostate due to the 'free-hand' manual approach.

There were several procedural and dosimetric limitations to consider:

1. Overly simplified and idealised nature of the volume nomogram;
2. The actual shape of an individual's prostate does not conform to the idealised ellipsoid;

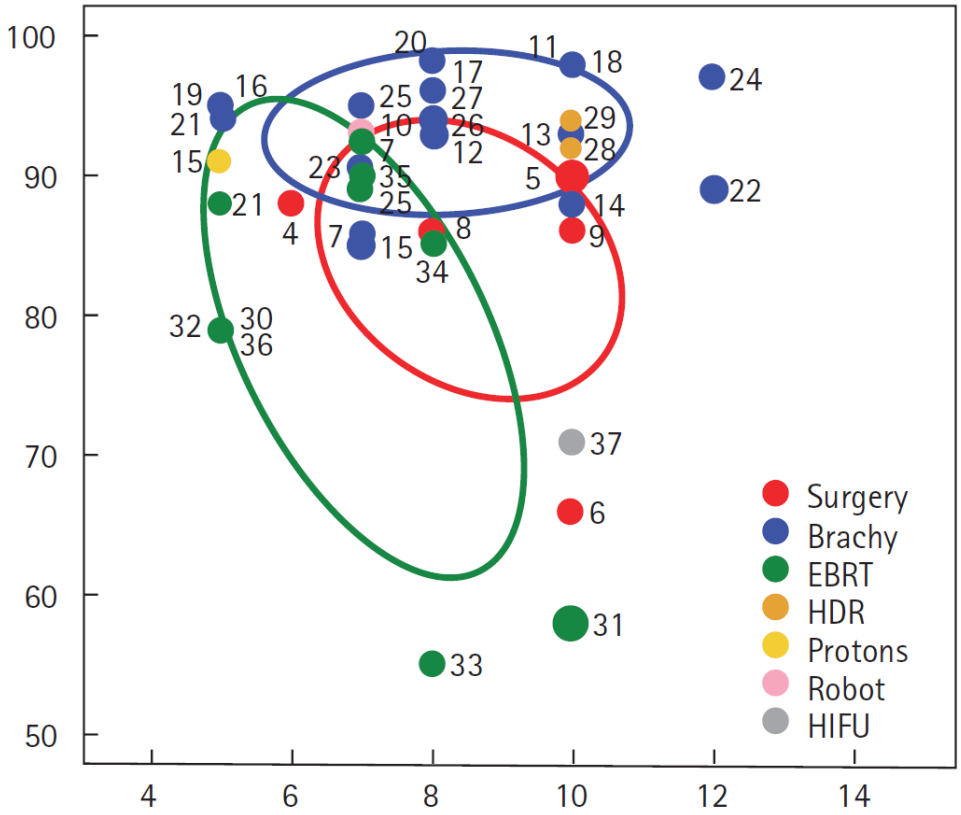

Figure 2.9 The results from the study by Grimm et al. (3) showing prostate-specific antigen (PSA)-free progression for different treatment options. Each standard deviational ellipse (SDE) represents 1 SD about the weighted mean where data points were weighted by the natural logarithm of the number of patients in the study. A minimum of four data points was required in order to calculate an SDE. Each number corresponds to the specific study and its cohort of patients studied [table not shown]. Key: Brachy, brachytherapy; HDR, high dose radiotherapy; ADT, androgen deprivation therapy; Cryo, cryotherapy; HIFU, high intensity focused ultrasound.

3. Value of calculated dose did not depend upon actual radiation source distribution. (30)

As a result of the inhomogeneity of the implanted seeds, both well and poorly distributed seeds could actually yield the same value for tumour dose. This is a less-than-ideal clinical situation as it inevitably resulted in areas of underdosage or cold spots within the gland predisposing to local failure.

Zelefsky and Whitmore (31) performed an historical review of 1,078 patients between March 1970 and December 1987 treated with permanent implantation of iodine-125 via Whitmore's retropubic approach. Of these patients, 639 (59%) experienced local relapse within a median of 47 months. A total of 598 patients (56%) had distant metastases within a median of 45 months. The overall disease-free survival rates at 5, 10 and 15 years were 81, 41 and 12% respectively. Ultimately, the long-term results demonstrated that the retropubic approach for I-125 implantation was not effective as a therapeutic option when compared to other modalities.

Significantly better results were observed in patients who received doses of 140 Gy or more and it was concluded that "achieving the optimal dose distribution and tumour dose is necessary for a high likelihood of tumour eradication". A major contributing factor to this is the source distribution and the adequacy of implant dosimetry. The high incidence of local failure highlighted the limitations of this technique, resulting in suboptimal distribution of the isotope within the prostate.

The advent of transperineal CT and ultrasound guided permanent prostatic implantation has led to dramatic improvements in the accuracy of isotope placement and thus better control of early stage localised disease. These long-term results closed the chapter on I-125 implantation via the retropubic approach, but opened up new treatment directions.

Conceptually, the open implant had great appeal by delivering a highly confined dose within the prostate and the application of this concept still remains relevant today.

According to Korb and Brawer (32), such hand-based techniques resulted in ”erratic dose distributions”, resulting in hot and cold spots in the prostate. This led to an ”unacceptable rate of local failure”. Consequently, brachytherapy declined in popularity from the 1960s onwards.

2.2.2 Holm's Transrectal Ultrasound-guided Technique

Following the failure of the retropubic approach, a new system was developed. This was via transperineal implantation of the radiation needles, first introduced by Barringer in 1917. This approach depended on digital (i.e. palpation by finger) guidance through the rectum. It was self-evident that this technique did not provide adequate information for an effective dose delivery. Holm et al. (5) proposed a technique in 1990 utilising ultrasound-guided percutaneous implantation. Many of the errors associated with early brachytherapy techniques, most notably the risks of open surgery and lack of dose distribution information, were overcome with this novel ultrasound-guided technique (4).

Planning is performed by transrectal ultrasound scanning in the dorsal lithotomy position. The scanner is mounted in a fixture apparatus and transverse scans obtained at 5 mm intervals. The series of scans is used by the physicist and physician to contour the relevant tumour and gland volumes, and thus to calculate the number and distribution of seeds required to deliver a minimum peripheral tumour dose of 160 Gy (modern techniques typically aim for a tumour dose of approximately 145 Gy).

When the implant procedure is carried out, care is taken to place the scanner at exactly the same position as during the planning procedure, especially with respect to the distance between the rotational point of the scanner and the prostate's posterior aspect. The seed implantation technique is shown in Figure 2.10.

Needle tip position is verified by a strong echo reflection on the ultrasound image. The central needles are inserted first, emptied and removed individually. The scanner is withdrawn to the next image plane (usually 5 mm) and the procedure repeated until

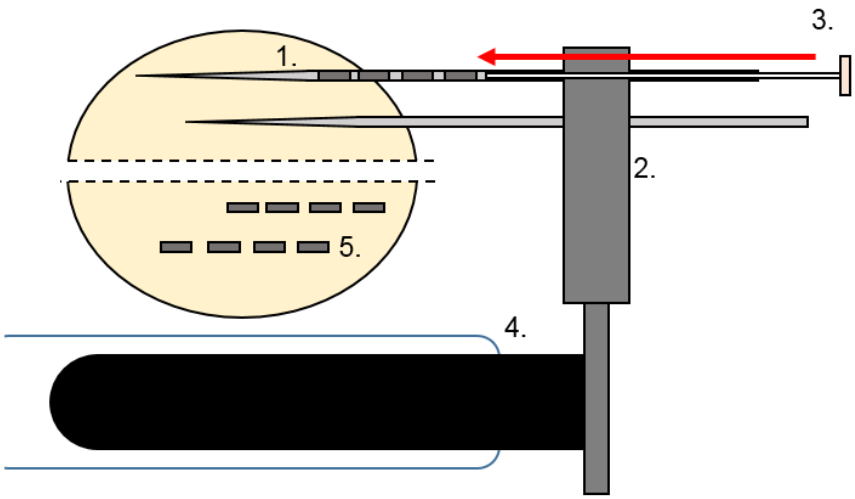

Figure 2.10 Technique of seed application: Needle loaded with seeds (1) and spacers is inserted through template attachment (2) to the correct depth. The needle is then withdrawn leaving seeds in place (3). The TRUS probe (4) verifies the location of implanted seeds (5) in the prostate in real time.

the prostate is filled with seeds according to the radiotherapy planning program. Seed position is verified by anterio-posterior and lateral X-rays, which yield the relevant geometrical data for calculation of resulting dose distribution.

Holm's study is not to evaluate the efficiency of brachytherapy in patients with prostatic cancer but to introduce and describe a new technique for interstitial seed placement. The improvements on the existing technique cover fundamental concepts in prostate brachytherapy. The advantages are listed as follows:

1. The patient is spared the inconvenience and risk of open surgery (major operative complications may be in the order of 15 per cent);

2. The precise series of prostate ultrasound sectional images allows for a much more detailed method for dose planning;

3. The simple needle-stylet system for insertion of seeds is efficient. (The modern equivalent is by template guidance);

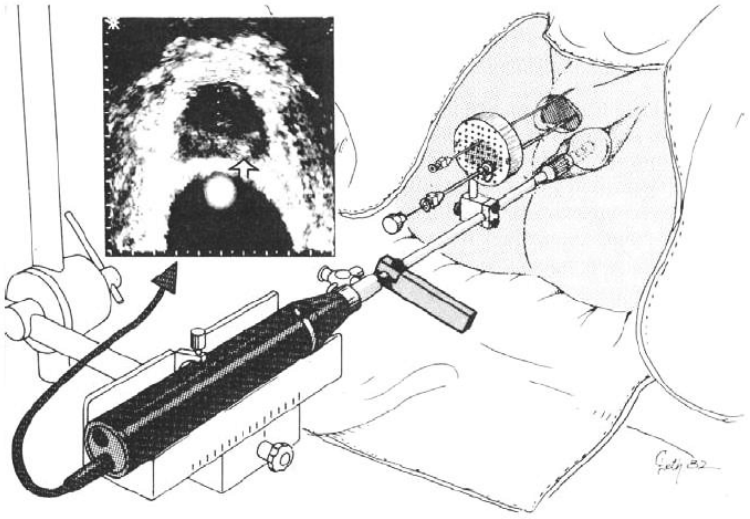

Figure 2.11 Image showing TRUS being inserted into rectal cavity for brachytherapy needle guidance. (4)

4. Because of the fixed ultrasonic guiding system, the seeds are inserted much more precisely and distributed much better than by free-hand technique.

Since 1983, technological advances in computing and imaging technology have furthered the physician's ability to produce excellent results. However, the aim has been the same through the years. That is, to continually improve the accuracy of seed placement and imaging and planning techniques for improvements in dose planning and dose homogeneity.

For example, one of the earlier steps in ultrasound-guided implantation was the development of biplanar imaging as described by (5). Exclusive transverse imaging (perpendicular to the long axis of the probe) does not allow for corrections for any superior displacement of the prostate during implantation.

An example of an ultrasound system is shown in Figure 2.12. A Bruel & Kjaer ultrasound system 1846 is employed, with a multiplanar 7 MHz ultrasound probe type 8551. The single crystal produces a 112^o sector image, and the scanning plane can be rotated 180^o to view all image planes. The ultrasound probe is described as

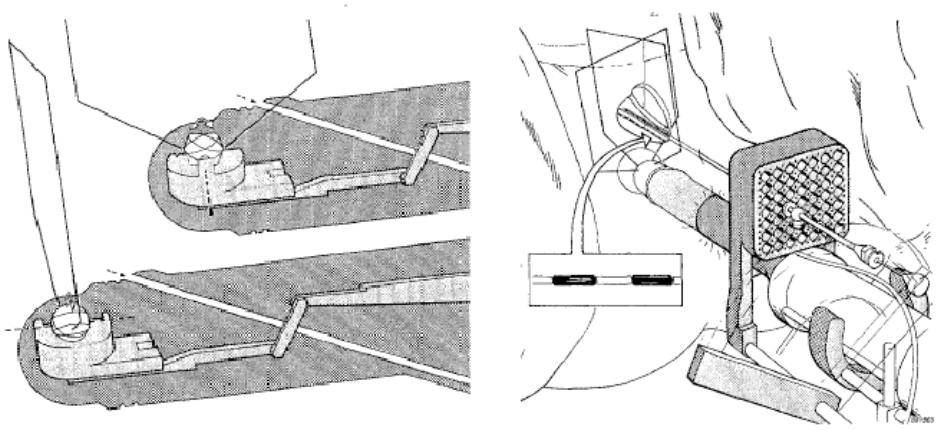

Figure 2.12 (Left) Principle of multiplanar scanning. Top: crystal sweeps back and forth in longitudinal mode. Bottom: crystal sweeps from side to side in transverse mode; (Right) Principle of multiplanar imaging during transperineal needle insertion. The needle is inserted into the prostate. Any needle can be visualised in all planes between and including transverse and longitudinal. (5)

follows:

Over the past two decades, advances in imaging and computing technology have led to sophisticated, ubiquitous, and three-dimensional sectional image-based treatment planning. Included in this process are aspects such as 3D assessment of anatomy, planning target volume and critical organ contouring, 3D dose calculations with dose volume histograms and different forms of 3D display capabilities.

2.2.3 Modern Techniques for Prostate Seed Brachytherapy

In its most basic form, prostate brachytherapy involves four key steps:

1. Pretreatment patient evaluation, which includes PSA screening, assessment of cancer stage and grade and extent of life risk;
2. Prostate volume determination (ultrasound volume study) and implant planning;
3. Seed insertion;

4. Post-procedural evaluation of implant quality.

Sectional imaging (part of steps 2 and 3) has been the main driving force behind prostate brachytherapy's push to the forefront of prostate radiation therapy, "in particular because the appropriate positioning of the seeds or needles could be improved by avoiding too large distances between the sources on the one hand, and by selectively sparing the urethra and the anterior rectal wall on the other hand" (6). Images are not only used for treatment planning, but also for direct guidance of the application- image-assisted quality control of dose delivery.

The modern technique is based on stepping the probe along the longitudinal direction from the gland base to apex (in 5 mm steps). The grid serves as a needle guidance template, giving precise coordinates for the required positions of the needles and their sides; "by this procedure, each needle and seed can be accurately positioned in a 3D coordinate system- exactly at the place determined in advance during the relevant planning procedure" (6). An example of transverse images obtained via ultrasound are shown in Figure 2.13.

Following the development of transrectal ultrasound (TRUS) and then computed tomography (CT) imaging, the precision of radioactive source placement and subsequent outcomes greatly improved. Throughout the 1990s, several institutions began implant programs that used transperineal guidance as the preferred approach. Some centres of note are the Memorial Sloan Kettering Cancer Centre, New York and the Seattle Prostate Institute, Washington.

As time progressed, brachytherapy became the preferred choice of therapy for prostate cancer over other choices such as EBRT and radical prostatectomy and has many well-understood advantages. These are described by DiBiase et al. (24) as follows:

1. Low-energy radioactive sources (I-125, which is low dose rate or Pd-103, which has a higher dose rate) have limited tissue penetration, which allows for a steep dose gradient thereby limiting the dose received to normal tissues

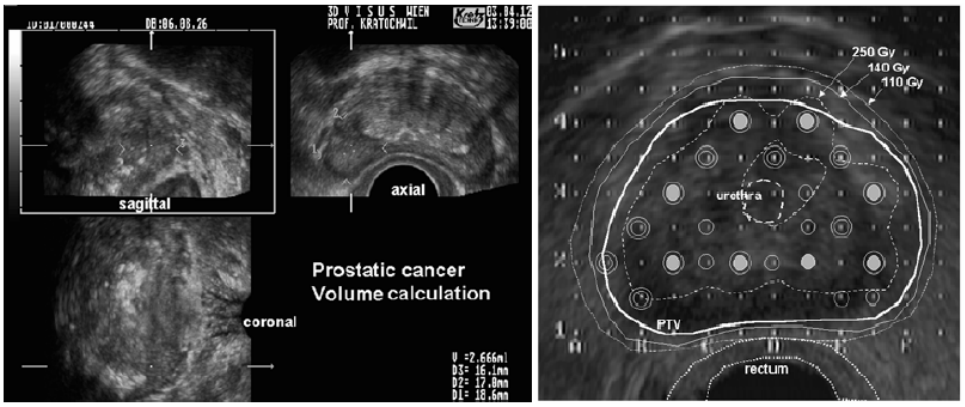

Figure 2.13 (Left) Transverse endorectal ultrasound image displaying the dimensions of the prostate (width and thickness) as well as the urethra and the rectum. In addition, there is evidence of gross tumour in the right posterior-lateral part of the prostate. (Right) The distribution of I-125 in the ultrasound prostate volume study. The prostate, the PTV, the urethra, and the rectum are delineated. The number of seeds in the volume and their topographic position within the 3D coordinate system can be precisely calculated, determined and displayed in different orientations. Isodose lines are shown in relation to the PTV (V100). Certain dose constraints for the urethra and rectum must be taken into account (6).

and minimising potential treatment-related complications;

2. Gland movement, which can significantly affect the accuracy of EBRT, is less of a problem during implantation using real-time ultrasound imaging. It is a well-known clinical problem that the prostate is a very mobile and malleable organ, and real-time monitoring of the needle and seed insertion is of utmost importance;

3. A single outpatient treatment is convenient and less time-consuming than EBRT, which is typically administered over 7 weeks;

4. The precision and conformation of brachytherapy permits the administration of high radiation doses with a low risk of rectal morbidity.

There is no debate that permanent prostate brachytherapy techniques are associated with excellent biochemical outcomes. However, prostate edema and poor imaging techniques are recognised limiting factors and new treatment planning techniques may assist in improving the implant procedure and associated dosimetry (33).

Over the past 20 years, physicians at the Seattle Prostate Institute have performed more than 10,000 LDR I-125 implants with or without supplemental EBRT (7). During this time, the Seattle technique has undergone continuous evolution, but the technical improvements had not been published until 2009. Sylvester et al describe their preplan technique and associated dosimetric outcomes. An example of error in implant is shown in Figure 2.14.

"The literature has consistently shown that excellent biochemical relapse-free survival (BRFS) outcomes occur whenever postoperative CT dosimetry reveals a high dose to 90% of the prostate and/or high volume of prostate receiving 100% of prescription dose, with either preplanned or intraoperative planned techniques". Dosimetry techniques involve creating a preplan that is simple and easy to reproduce in the operating room (OR) based on TRUS preplanning volume studies.

At the end of the procedure (post-operative), a fluoroscopic image for seed verification purposes is taken, as is an ultrasound scan to identify potential cold areas. "Some centres will excel at the preplan technique [like at Seattle] and others with the real-time technique. Fortunately, with the aid of postoperative dosimetry feedback, all brachytherapists should be able to maximise the quality of their implants" (7).

Lawton et al. (34) provide an historical perspective of prostate brachytherapy procedures and evaluate the effectiveness of Holm's TRUS-guided technique as compared with historical data for both radical prostatectomy and EBRT. Overall in Lawton's study, it was found that multiple large series from single institutions have reported favourable results from TRUS-guided implantation techniques and similarly so did their multi-institutional series.

While the failure of the retropubic approach may have discouraged the use of prostate brachytherapy, the development of transrectal ultrasound (with the ability to map the prostate in several planes) technology as well as the associated development of the perineal implantation technique of prostate seed implants revived clinical interest in the concept of implantation of radioactive sources.

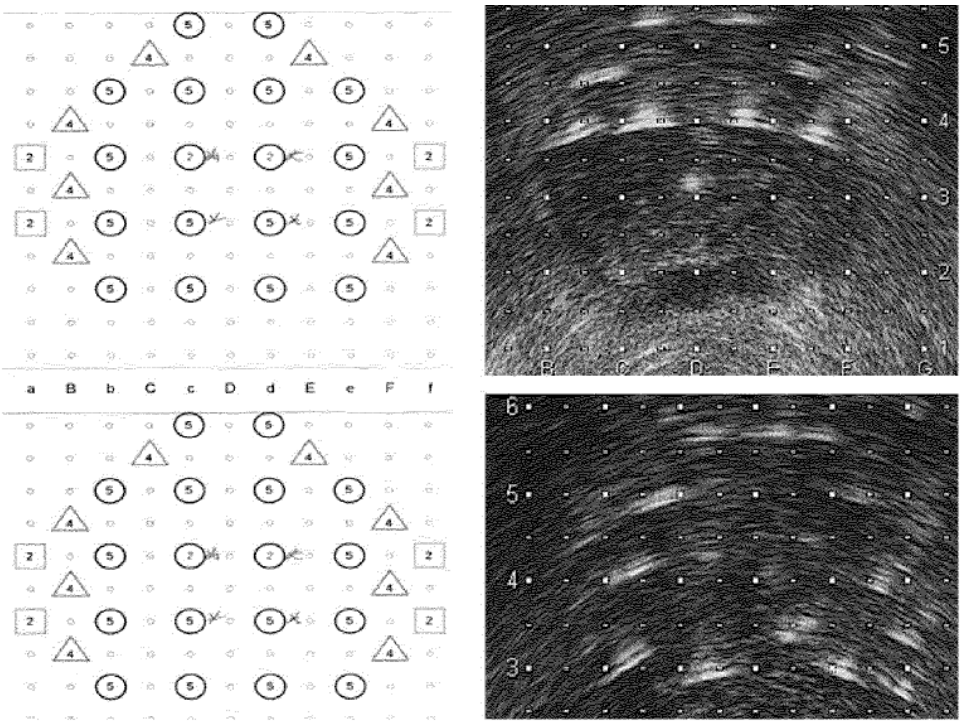

Figure 2.14 A comparison of pre-planned TRUS images to the final seed position as the implant procedure progresses (7).

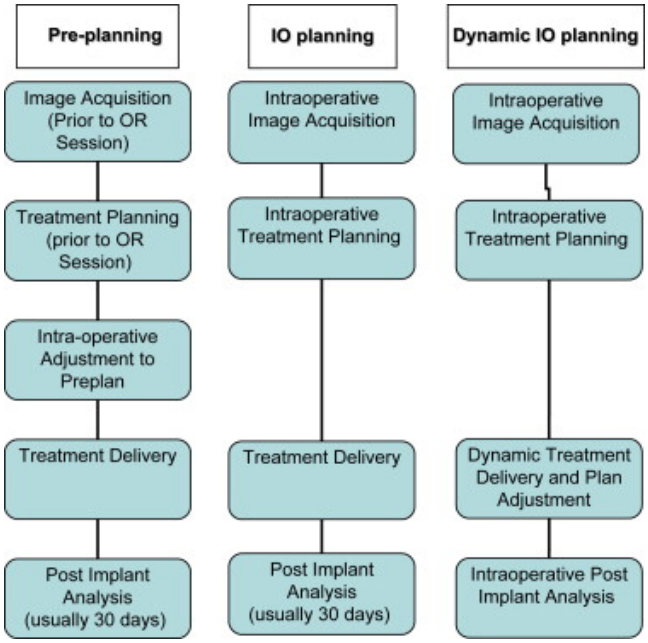

Figure 2.15 Flow diagram of basic steps involved in preplanning, interactive planning and dynamic intraoperative planning (Zaider et al)

2.3 Treatment Planning

Precise seed ordering is traditionally facilitated by preplanning. The aim of such planning is to ensure maximal target coverage while minimising dose to organs at risk and taking into account internal dose inhomogeneities. However, there are a number of fundamental issues to overcome, which are rigorously addressed in the literature.

To address these issues, first a breakdown of the treatment procedure must be outlined. Zaider et al. (35) provide a flow diagram as shown in Figure 2.15.

The implantation step is performed to adhere to the treatment plan as close as possible. However, this is technically complex to attain to 100% accuracy, and therefore adaptive replanning, such as through dynamic dose calculations, may be a preferred method. Furthermore, it is also difficult to exactly replicate the patient's position in the operating room based on treatment simulation and preplanning. Prostate edema

is another concern that may be addressed by intraoperative planning.

The primary reason it is important to obtain real-time dosimetric information during the implantation procedure is to reduce the potential for toxicity without compromising target coverage. Any need for intraoperative adjustments is eliminated by adjusting the plan in real-time as in interactive and dynamic planning.

> ”Preimplant quality assurance covers seed and needle calibrations, review of the dose calculation, plan verification...Broadly, intra-implant quality control is concerned with monitoring and correcting any disagreements between the wanted and achieved dosimetry.” (35)

While intraoperative dose planning is highly recommended, seed localisation remains a key unsolved problem as dosimetry issues, both over- and under-dosing, require careful tracking of seed positions ”as the implant progresses” (35).

2.3.1 Preplanning

The preferred method for brachytherapy implants is preplanning. In this method, an ultrasound volumetric study is performed on the patient prior to the operation; usually 6-8 weeks before. Fundamental dosimetry information such as the number of seeds required and the position of the seeds are planned according to the patient’s specific prostate volume and tumour size. A computerised three-dimensional model of the gland is generated and virtual placement of seeds performed with superimposed planar isodose curves.

In addition to ultrasound imaging, preplan CT techniques are also employed at some centres such as Memorial Sloan- Kettering Cancer Center (MSKCC) in New York. The CT scan is made several days to weeks before the procedure. Prostate, urethra and rectum contours are outlined on 5 mm slices and digitised into the treatment planning computer. Using these transverse images, seed patterns and isodose distributions can be calculated for each cross-sectional image. Following evaluation of the

isodose patterns, alterations in seed locations can be made to adjust dose distribution of the target, urethra and rectum (8).

When seed implantation occurs in the operating theatre, the patient is positioned in the same position in an attempt to exactly replicate the conditions in which the preplan was designed. Studies have shown however, that it is an extreme technical challenge to match the prostate to such preplans (36).

Following the implant, a quality check is performed by three-dimensional CT-based analysis in all planning methods. Five-millimetre thick slices are acquired with both soft tissue and bone windows, thus allowing for prostate and seed delineation. The evaluation consists of dose computation and analysis for the target structure and surrounding organs. Computer analysis is performed based on the CT scans to produce accurate isodose level displays (32).

The preplanning method was popularised by the Seattle Northwest cancer group pioneered by Holm et al. (5) at the Seattle Prostate Institute, and discussed in detail by Ragde (37). It is sometimes referred to as the Seattle method. However, despite success in past decades, there are several limitations associated with the preplanning technique as outlined in the following.

Variability in prostate shape and position is unavoidable in the time period between preplanning and implant. (38; 39). Changes are due to differences in patient positioning and relaxation of the pelvic musculature as a result of either regional or general anaesthesia. Differences in the ultrasound probe position as well as distortion of the prostate associated with needle placement and subsequent edema can also result in profound changes in the shape of the gland compared to the preplanned prostatic contour (40). These deviations result in a postplan CT dosimetry that does not always correspond to the idealised preplan.

Furthermore, an underdosage may occur reflected in a lower V100 value and potentially increased risk for local recurrence (8). Intraoperative planning as a conformal

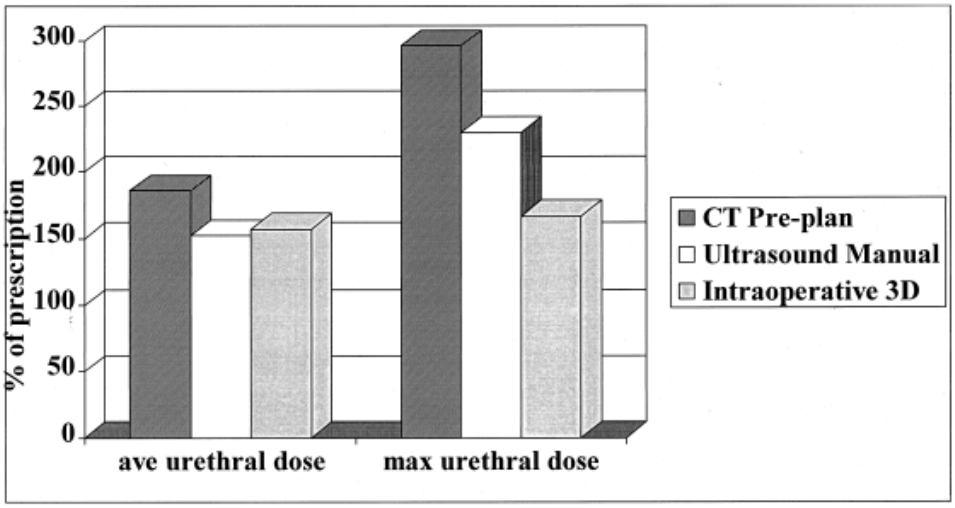

Figure 2.16 Target coverage for patients with prostates larger than 60 g according to the treatment planning technique based on the postimplantation dosimetric analysis. It is evident that significant improvement was observed for the IO-3D technique (8).

method takes the first step in addressing some of these issues.

Gewanter et al. (41) summarise the three main technical problems of the preplanned approach as follows:

1. The need for matching of the images obtained in the preplanning study with the actual implant images allows room for error in matching the images;

2. The prostate volume or shape may change as a result of any of the following-hormone treatment, positioning factors, the ultrasound probe itself or relaxation of the pelvis due to anaesthesia;

3. This approach requires the scheduling of two separate ultrasound procedures, which can be difficult as it depends on the availability of physicians, patients, and ultrasound equipment.

Recent studies have shown that preplanned techniques continue to yield favourable biochemical outcomes, yet there is also a growing movement towards intraoperative

Planning modality	Description
Intraoperative planning	Creation of a plan in the operating room immediately prior to the implant. Emphasis on single-room execution of plan
Interactive planning	Step-wise modification of the treatment plan based on real-time dosimetric feedback derived from image-based actual needle position
Dynamic dose calculation	Continuous feedback of seed positions to perform updating of calculations of dose distributions as they are being implanted

Table 2.4
Some terminology used to describe different approaches for intraoperative treatment planning for PPB.

adjustments as a way to develop a single-step procedure whereby the entire planning and implantation process can occur in the same room (7; 40).

2.3.2 Intraoperative Planning

There are several different approaches to intraoperative planning, as outlined by Polo et al. (42) and shown in Table 2.4.

The prostate is a highly mobile and malleable organ. Real-time monitoring of needle and seed insertion is of utmost importance. Vital advances in computer treatment planning and image guided treatment have made recent real-time dosimetry and implantation possible.

There are two clinical interpretations of the term 'intraoperative (IO) planning'. Both aim to minimise error introduced in preplanned treatments whereby the planned prostate volume does not necessarily match the implanted volume. The aim is to maintain the benefits of preplanning while eliminating the disadvantages of planning errors by streamlining the two procedures into a single operative session.

The first step in IO planning is to bring all planning equipment and computerised analysis directly into the operating room. In doing this, the prostate can be visualised and all dosimetry calculation performed immediately prior to the implant process. At

present, approximately 5-15% of seed implantations will not achieve optimal target coverage, which is usually defined as V100 >90% and urethral dose <150% simultaneously. However, it is undeniably advantageous to identify inadequate implants in the patient while he is still in the OR and in the treatment position (38).

The time elapsed between planning and implantation is minimised and therefore any differences between the planning and implant stages can also be minimised since the patient is stationary and the same position is maintained between planning and treatment. This form of IO planning is essentially the same as preplanned treatment apart from the time and place of planning. Once the plan is finalised, the needles are inserted accordingly with little attention paid to any probable required adjustments.

The method of dynamic IO planning accounts for this; a method also known as interactive planning. The ability to treat prostate cancer is limited by the ability to visualise the organ and brachytherapy seeds as they are being inserted. Therefore, the ideal situation would be an imaging system that provided not only anatomical information during the implant, but also provided real-time dosimetric feedback as per seed location and associated radiation levels.

Surgeons mainly rely on the TRUS probe to image the prostate in real-time as the needles are inserted and the seeds deployed. The needle tips register as bright echo spots on the ultrasound display, but due to resolution limits inherent in ultrasound technology individual seeds are easily missed in the same image. Therefore, X-ray fluoroscopy is also used to assist the surgeon in determining seed position. It is widely acknowledged that seed localisation is the most significant issue in achieving optimal dose distribution across the tumour. Currently this issue is being resolved by ever-improving ultrasound techniques and sophisticated treatment planning software for dosimetric calculations, capable of quickly determining seed number, activities and seed locations for optimal coverage of the target volume (36).

Well-documented inaccuracies in seed placement means that carrying out a plan results in a large degree of variability relative to the intended dose distribution (43).

Suboptimal seed implant leads to poor patient outcome, in the form of either local recurrence or radiation toxicity of critical structures. Unforeseen difficulties can be overcome in real-time with intraoperative adjustments. These modifications can potentially correct any areas of tumour underdosage prior to completion of the procedure, and thus have become known as interactive dose planning.

> ”The interactive implant technique allows real-time prostate measurements, and bases its dosimetry calculations on the actual gland volume and configuration at the time of implant, thus intrinsically correcting for gland movement and dynamic size changes occurring during the operation. The technique does not require extensive, expensive time-consuming preplanning.” (36)

Currently however, the majority of centres and techniques do not incorporate computational tools that allow for real-time adjustment of overall dosimetry as a result of seed movement, needle distortion and edema during the implantation process as there is still much to be done in developing real-time dosimetry and its ability to predict for good quality implants.

In the study performed by Matzkin et al. (36), it was found that short-term morbidity was minimal in both groups and did not in fact correlate with technique employed. However, when further dosimetric parameters (such as V100, V150, D90 of prostate and urethra) were considered it was found that the real-time intraoperative method achieved superior dose distribution and homogeneity. Note that V100, V150 is the percentage of volume receiving 100% and 150% of the prescribed dose respectively. D90 is the dose that covers 90% of the prostate volume. It is usually reported in grays [Gy], but can also be reported as a percentage of the prescription dose. They are common parameters used to evaluate the quality of the brachytherapy implant and are further explained in Section 2.4.

> ”The interactive implant technique allows real-time prostate measure-

> ments, and bases its dosimetry calculations on the actual gland volume and configuration at the time of implant, thus intrinsically correcting for gland movement and dynamic size changes occurring during the operation".

Current advances in imaging and computing technology have allowed for the development of real-time intraoperative dosimetry. The recommendations made by Nag below have been taken on board and practically applied in many clinical contexts worldwide as evidenced in the literature.

> "The high degree of accuracy achievable in prostate implants nowadays is partly due to technological improvements, but quality implants still require skill, adequate training and attention to detail. The ABS suggests development of real-time, online dosimetry to allow immediate feedback that could result in better implant dosimetry". (23)

Real-time intraoperative planning also has its limitations according to Shanahan et al. (44). The main issue to address is the limitation in ultrasound technology, which has intrinsically low seed visibility. For this reason, the needle tip at the time of deployment tends to be imaged rather than the final resting position of the seed itself within the gland.

Seed migration is a typical problem and is not easily detected without conventional fluoroscopy. However, it is concluded that the interactive planning consistently reduced preplanning time, procedure time, and number of needles used, thus reducing treatment time and costs while maintaining excellent dosimetric coverage (day 0 dosimetry reported D90$>$140 Gy, V100$>$90%, and V150$<$40%).

Whether a preoperative plan or an intraoperative treatment plan is used, ultrasound guidance is vital for a successful implant. Visualisation of the prostate and other critical structures is needed for the setup. Ability to localise the inserted seed, sometimes assisted by additional imaging techniques such as fluoroscopy, is necessary for

modification of the preplan and for real-time planning. Such approaches will further improve the quality of the dose distributions and the therapeutic ratio for permanent prostate implants (45).

Planning and assessment methods vary from centre to centre, but generally current techniques do not incorporate or allow for intraoperative reassessment (43).

To illustrate the need for a real-time dosimetric feedback system, several studies have been performed across the world using novel imaging techniques. One example is by French et al. (9), who developed a system able to accurately locate seeds with minimal impact on the then current protocol for prostate brachytherapy. In their study, fluoroscopic C-arm images are used in conjunction with conventional ultrasound. Conventional X-ray based methods, such as those used by Gong et al. (46) and Todor et al. (47), depend on the rotation of the C-arm fluoroscope to compute the seed distribution, which is a time-consuming and impractical method.

It is acknowledged in such studies that is it is "not possible for a radiation oncologist to accurately locate the implanted seeds using [either] only TRUS or fluoroscopy [alone]". Several existing commercial systems have already been developed that rely primarily on ultrasound imaging to compute dosimetry based on such information as needle location. However, there are incorrect assumptions inherently made in these calculations and seeds simply cannot be located using only US images. Such systems include:

1. VariSeed by Varian Medical Systems, Palo Alto, CA
2. Prostate Implant Planning Engine for RT systems by RTek, Pittsford, NY
3. Interplant Suse by Rosses Medical Systems, Columbia, MD
4. SPOT system by Nucletron Corporation, Neenandaal, Netherlands

The aim of the French study was to obtain X-ray images of the TRUS probe in-body Alternatively, French et al designed a procedure based on needle path interpolation,

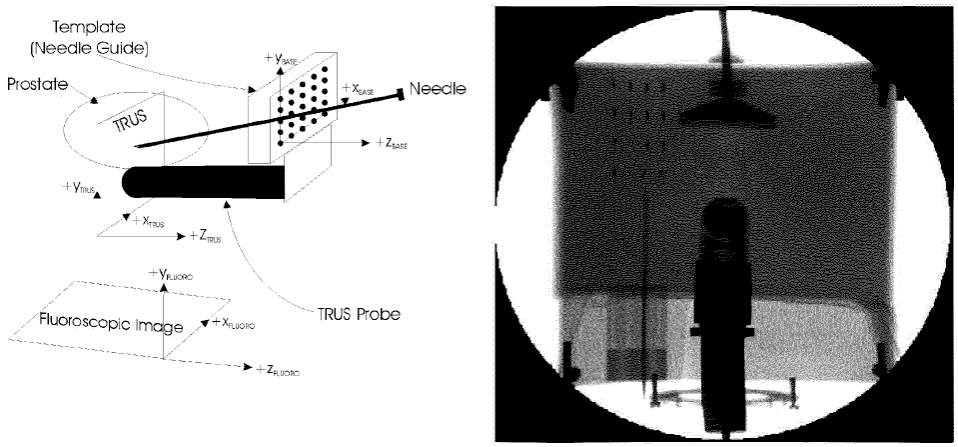

Figure 2.17 (a) Illustration of the standard TRUS probe with needles being inserted into the prostate and the coordinate system used in this study; (b) Fluoroscopic image of the phantom with TRUS probe and needle inserted (9).

which importantly required no additional equipment and had minimal change to the existing brachytherapy procedure. The transformation from the fluoroscopic image to the TRUS image is defined using a single fluoroscopic image of the TRUS probe such that the seed coordinates can be projected from the fluoroscopic images to the TRUS images (X,Z coordinates) (an example image is shown in Figure 2.17).

This demonstrates an early example of an attempt at real-time dosimetric feedback. However, to date, there is no robust system in widespread use for intraoperative treatment planning. Further examples are highlighted in Section 2.5.

2.4 Dosimetry

In order to evaluate the effectiveness of a given implantation procedure, a freedom from biochemical failure is determined. Failure is defined as a rise in PSA of 2 ng/mL and it is well known that treatment success is closely associated with the dosimetric quality of the implant (48). The American College of Radiology (ACR) and the American Society of Therapeutic Radiology and Oncology (ASTRO) published an educational tool written to assist brachytherapy practitioners (49). It is

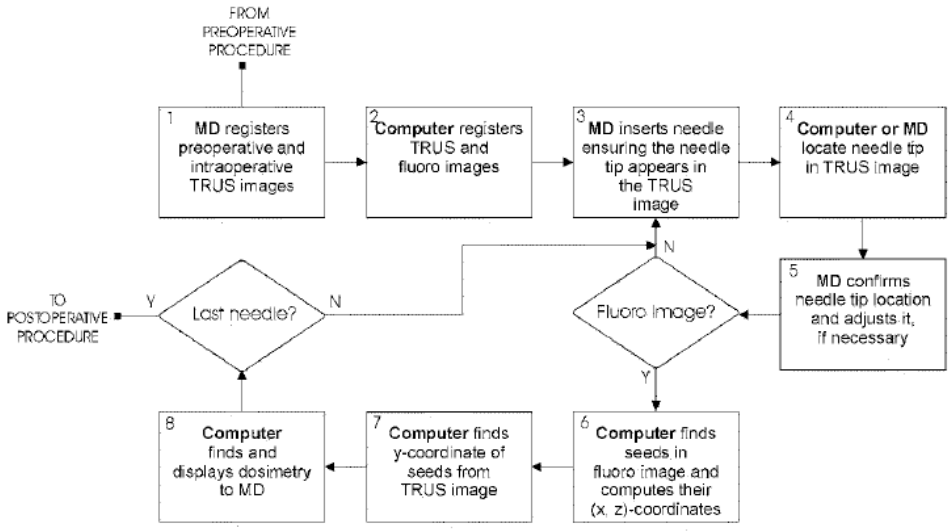

Figure 2.18 (a) Flowchart outlining French et als approach for real-time dosimetry feedback (9).

noted that dosimetric planning should be performed on all patients prior to or during the umplantation with methods listed such as TRUS, CT scanning or MRI. For dose calculations, the AAPM Task Group No.42 and its successors should be adopted.

Typical post-implant dosimetry sometimes reveals that a portion of the prostate has been underdosed. There is no method for successfully integrating intraoperative imaging into the dosimetric assessment process. According to Doyle et al. (48), intraoperative planning allows more flexibility in all key areas affecting brachytherapy efficacy. i.e. patient position, seed localisation and of course real-time dosimetry and supplemental seed implantsation. Such freedom for the brachytherapy practitioner allows the minimisation of deviations from ”intended seed location and dosimetry”.

2.4.1 Quality Assurance

The goal for any prostate brachytherapist ”is to consistently achieve high-quality implantation results, as determined by postimplant dosimetry.” (50). In order to ensure that source placement is optimised to maximise target coverage while minimising dose to the organs at risk (in this case, primarily the urethra and the rectal wall),

the standard post-implant dosimetry check must be performed. For the past decade, post-implant CT-based dosimetry has become the foremost and most reliable method for assessing dose delivered to the prostate and normal surrounding structures (51).

This method involves taking CT scans of the brachytherapy implant, with the prostate contoured on every 3-5 mm slice. Seed locations are identified on every CT slice, and all relevant structures reconstructed in three dimensions with dose distributions calculated. The timing of the post-implant dosimetry is recommended at one month after implant, since "the dose calculated at one month has been shown to most accurately represent the delivered dose over the life of the implant" (51). This is due to swelling and edema of the prostate gland associated with the physical trauma of the implant.

However, it is common for significant differences to exist between the optimised US-based treament plan and the actual post-implant dosimetry check performed. In a study by Ishiyama et al. (39), the results between intraoperative ultrasound-based dosimetry and CT-based post-implant dosimetry scans performed one day and thirty days after implant, showed significant differences in dosimetric parameters. Some centres such as the University of Texas M.D. Anderson Cancer Center (Houston, Texas) have employed a hybrid system, combining the basis of preoperative imaging with modern treatment planning software for use as intraoperative optimisation (50).

> "Postimplant dosimetry is mandatory for each patient. This information expresses the actual dose delivered and identifies variance from the original treatment plan. Although useful for seed counting, plain radiographs alone are not adequate for dosimetric analysis. We recommend the use of image-based planning such as CT or MRI to evaluate the relationship of the seeds and the prostate, bladder and rectum". (49)

There is some debate surrounding the optimal timing for post-implant CT and/or MRI. Recent studies have suggested somewhere between 2-6 weeks post-implant,

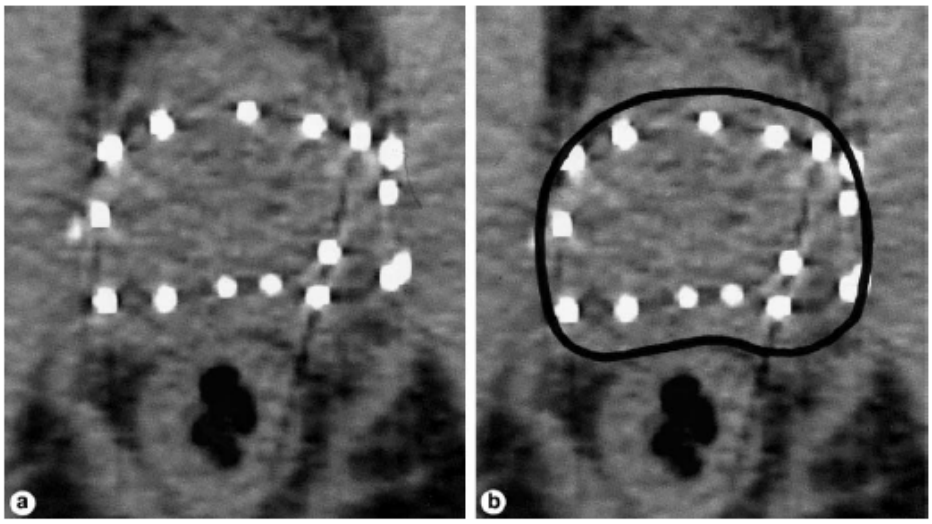

Figure 2.19 Transverse CT image of implanted prostate: (a) without contoured prostate; (b) with prostate contoured (Stock et al, 2002)

allowing any edema to subside, whilst in other situations, post-implant scans are performed at day 0 or day 1 after implantation.

The typical values reported in a useful dosimetric analysis are outlined by the American Brachytherapy Society (23):

1. The prescribed (intended) dose;
2. The D_{100} value - i.e. the dose that cover 100% of the prostate volume. However, there is some uncertainty associated with delineation of the prostate boundaries in CT scans;
3. The D_{90} value - i.e. the dose that covers 90% of the prostate volume. A D_{90} value greater than or equal to the prescribed dose is a measure of a implant quality;
4. The V_{100} - i.e. the percentage of prostate volume that received the prescribed dose. If the dosimetry indicates significant underdosage, a reimplantation or additional EBRT may be considered.

2.5 Current Methods for Real-Time Seed Imaging

Several attempts have been made at accommodating this need for a real-time imaging system in permanent prostate brachytherapy. Approaches vary from modifying existing technology to innovations in imaging and treatment planning applications.

2.5.1 Ultrasound Technology

Ultrasound imaging plays an integral part in the brachytherapy procedure. The TRUS probe (discussed in Section 2.2.2) is a standard in clinical practice and is able to visualise the implant as it occurs. By attaching the probe to a stepper apparatus, in turn attached rigidly to the patient bench, a stable and well-defined coordinate reference system can be established. However, due to the intrinsic resolution limits of ultrasound technology, it is not uncommon for seeds to be misaligned or only approximated regarding their expected positions.

Ultrasound's main advantage is in imaging soft tissue anatomy. However, it is well known to have disadvantages for localising the exact location of the small brachytherapy seeds. Several studies have been made into changing the design of the seeds themselves so as to better reflect the ultrasound waves and thus have increased visibility in ultrasound scans (52; 53; 54).

While there are some disadvantages in using ultrasound imaging for real-time seed imaging, it remains the standard for real-time imaging for its ease of use and its established history as a useful and reliable anatomical imaging device.

2.5.2 Fluoroscopy

During the implant procedure an X-ray radiograph of fluoroscopy image is taken to further verify the positions of the implanted brachytherapy sources. As discussed above, ultrasound imaging alone is not capable of localising implanted brachytherapy sources.

A common approach to this problem is to take several radiograph images and to co-register the multiple views onto a common frame of reference and thus obtain a three-dimensional map of the seeds in their implanted positions. There is a common problem however of missed seeds.

An example of this is the REDMAPS algorithm, which stands for the reduced dimensionatliy matching for prostate brachytherapy seed reconstruction (55).

In this method, The seed localisation problem from multiple fluoroscopy images is modelled as an assignment problem. This approach resolves segmented seeds in each projection image, assigning them to the same physical seed. The 3D locations of the seeds are determined by computing the intersection of the lines connecting the segmented seeds to the x-ray source positions based on the revealed seed correspondence. This is a seed assignment and geometric solution.

2.5.3 CT Imaging

CT scans are a crucial part of the brachytherapy procedure as a post-implant dosimetry check, as discussed in Section 2.4.1. Ultrasound imaging is poor at seed localisation. CT scans are perfectly suited to imaging of the high contrast material implanted into the prostate. Some studies have been conducted in placing the patient in the lithotomy position within a conventional CT scanner for the utilisation of real-time CT imaging of the implant as it occurs.

Whilst this may be a viable option for accuracy of seed localisation, it is not a cost-effective nor is it an easily accessible solution to the question of real-time seed imaging.

> Because the quality of the procedure is only evaluated using postimplantation computed tomography (CT), less than optimal dosimetric outcomes only become apparent to a physician when reviewing the postimplantation CT scans; thus, making amends for a flawed implant requires an additional surgical procedure

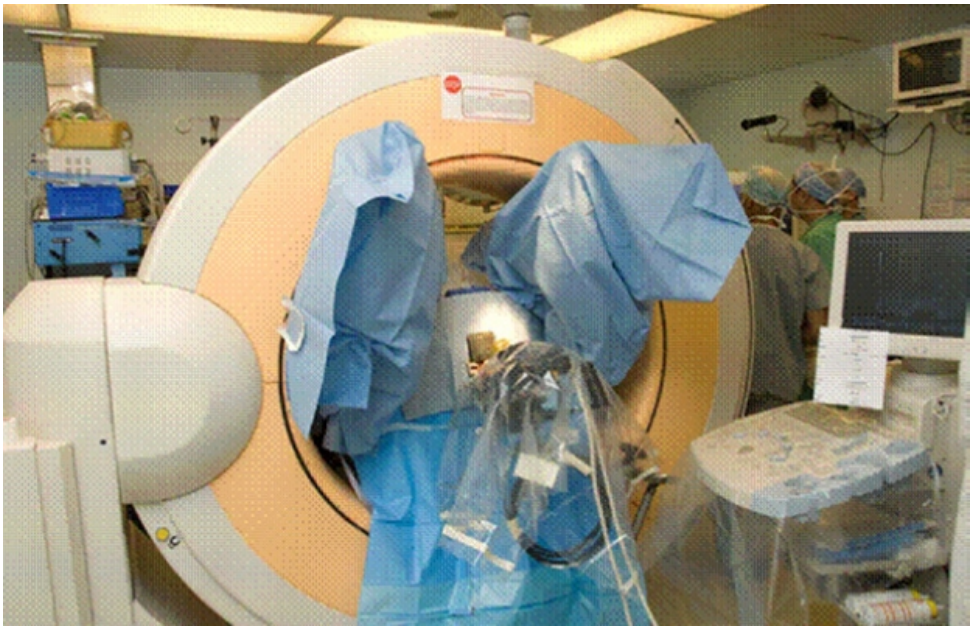

Figure 2.20 Patient shown with implanted needles in extended lithotomy position with CBCT imager in place as presented by Zelefsky et al (2010)

In a study by Zelefsky et al. (56), a technique using a mobile fluoroscopy-CBCT (cone beam CT) unit (O-arm, Medtronic Navigation), which uses an X-ray source and a Varian flat panel detector for both stationary fluoroscopy/radiography and CBCT imaging was evaluated. The central aim of this study was to establish the feasibility of fusing seed coordinates from the intraoperative CBCT images with that of the intraoperative ultrasound images. The technique was confirmed successful for use in fusing the seed coordinate positions obtained from the CBCT scans with the ultrasound frame of reference ”to allow for potential corrections of suboptimal dosimetry while the patient remains anesthetized”. A photo of the set-up is shown in Figure 2.20.

Other studies involving intraoperative CT imaging looked at the end of the implant procedure to compare its accuracy with that of standard postimplant CT scans, or to use it as a tool to correct subopimtal areas of dpse. For example, a study by Westendorp et al. (57) demonstrated the feasibility of a C-arm CT method. However, due to the nature of the C-arm configuration, the patients couldnot be imaged in the

extended lithotomy position, and scans were performed without the TRUS probe in place, which neglects the deformations introduced in the prostate.

Furthermore, in another study by Steggerda and van der Poel (58), 3D TRUS scans were successfully fused with standard CT scans. Again, most patients cannot be scanned in the standard lithotomy position in conventional CT scanners. Furthermore, Zelefsky states:

> ”One of the prominent limitations of current brachytherapy techniques precluding intraoperative quality assurance assessment is related to the relatively poor ultrasound resolution of the individual implanted seed coordinates. This primarily results from intraoperative prostatic edema, hemorrhage secondary to needle placement, and the relatively poor resolution of ultrasound images...The advantages of accurate intraoperative assessment of implant adequacy compared with the standard approaches that rely on postoperative measurements are obvious. Not only would such approaches obviate the need for post-implantation CT scan assessments, but more importantly, they would provide an opportunity for corrections or refinements of the implant before the procedure has been completed” (56).

2.6 Timepix Detectors

Although originally developed for the detection of high-energy ionising particles and radiation, semiconductor pixel detectors have found many applications in a wide number of areas, as diverse as radiation protection and in the photographic cameras of every day life.

The Timepix detector is the latest generation of the Medipix detector, which was developed by the Medipix collaboration at CERN (59; 60). The Medipix was originally proposed as a noise-free imaging solution for particle tracking in 1995. The

earliest version of the Medipix consisted of 64×64 pixels. Three subsequent generations later, and the ability for spectroscopic imaging and particle track identification, has propelled the Medipix collaboration to the forefront of pixellated semiconductor imaging devices.

The Medipix is a pixellated, hybrid semiconductor detector, consisting of 256x256 pixels, of 55μm pitch. The sensor layer is typically made of silicon, as shown in Figure 2.22. Each pixel is bonded to a supporting chip with separate read-outs. It has applications in high energy physics particle tracking as well as some imaging purposes, mostly in entomological and botanical (plant seed) studies (10).

The Medipix2 was developed towards the end of the 1990s. It consists of a high spatial, high contrast resolving CMOS pixel read-out chip working in single photon counting mode. It can be combined with different semiconductor sensors which convert the X-rays into electric signals. The incoming ionising radiation generates charge within the sensor layer, which is collected at the readout chip. The voltage is compared to a set threshold in the readout electronics. This threshold can be calibrated to a known isotope energy. Every photon that passes the sensor material within a defined energy range can therefore be measured as single events. This presents a new solution for various X-ray and gamma-ray imaging applications. The principle of operation is shown in Figure 2.21.

2.6.1 Properties of Timepix

The Timepix chip evolved from the development of the Medipix2 detector. The pixels have identical size to those of Medipix2 but with increased functionality. Every Timepix pixel can be programmed to count single events like Medipix2. However, the Timepix has the added functionality of comparing the voltage pulse generated to an internal clock, providing spectroscopic information of the incoming radiation. The voltage height is directly proportional to photon energy. As it peaks over the threshold setting and decays away, the time over the threshold can be directly calibrated to energy in keV. This is known as ToT or Time-Over-Threshold measurements.

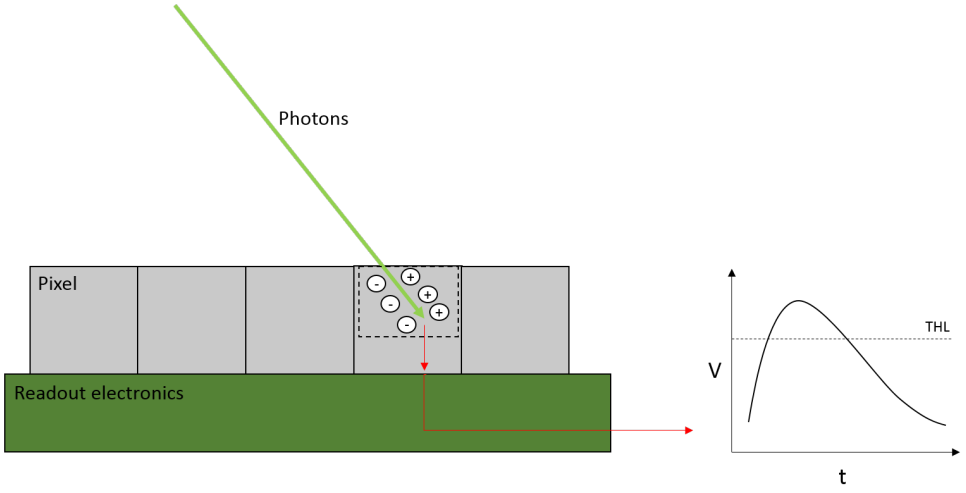

Figure 2.21 Schematic showing principle of Medipix detector operation. Ionising radiation impinges on the sensor layer and generates charge. This charge is collected in the readout electronics which is converted to an analog signal. This signal is compared to a threshold level (THL). Events above the threshold are registered as counts.

One of the advantages of the Timepix is that an appropriate sensor can be chosen such that the device can be used for registration of virtually any type of ionising radiation. The most common design makes use of 300 μm Si, but other materials such as GaAs or CdTe are also available. Each pixel in the matrix is connected to its respective preamplifier, double discriminator, and digital counter integrated on the readout chip. The Timepix detector is the focus of the majority of this thesis. The Timepix was designed as a successor to the Medipix2, the main difference being in the read-out chip (60).

Each pixel can be configured to work in one of three modes:

1. Medipix mode: integrated counter works as an event-by-event counter;
2. Timepix mode: counter works as a timer and measures when the particle is detected;
3. Time Over Threshold mode: or ToT mode. The time that the input voltage remains above the set threshold corresponds proportionally to the energy of

Figure 2.22 Photo of a single Timepix connected to FITPix USB interface.

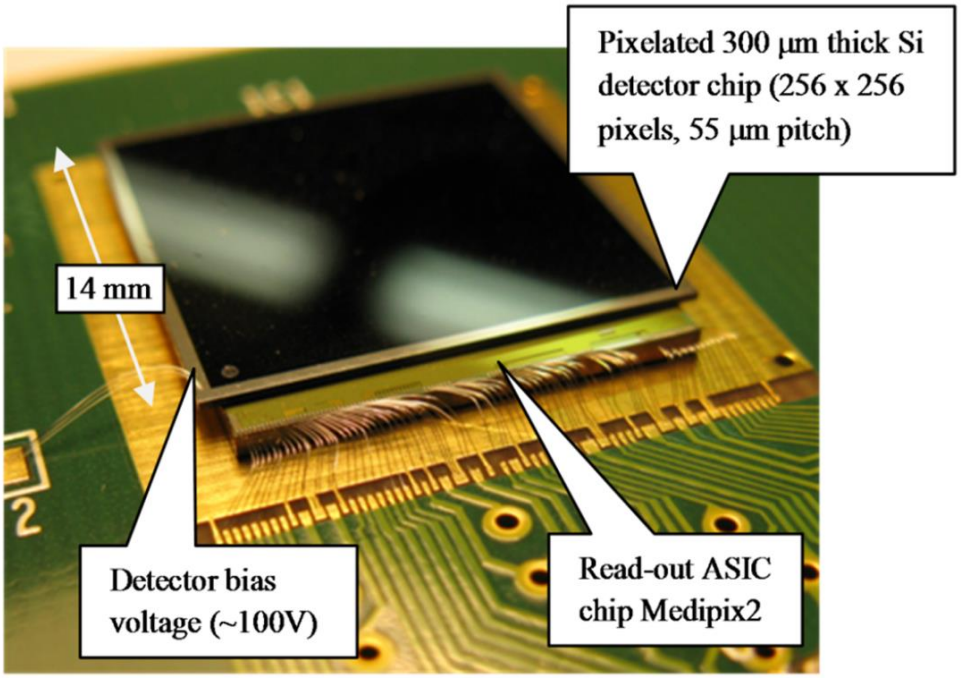

Figure 2.23 The hybrid semiconductor device Timepix consists of two chips: The pixellated sensor chip (usually 300 μm thick silicon, but also other materials are available e.g. GaAs and CdTe) and the read-out chip (10).

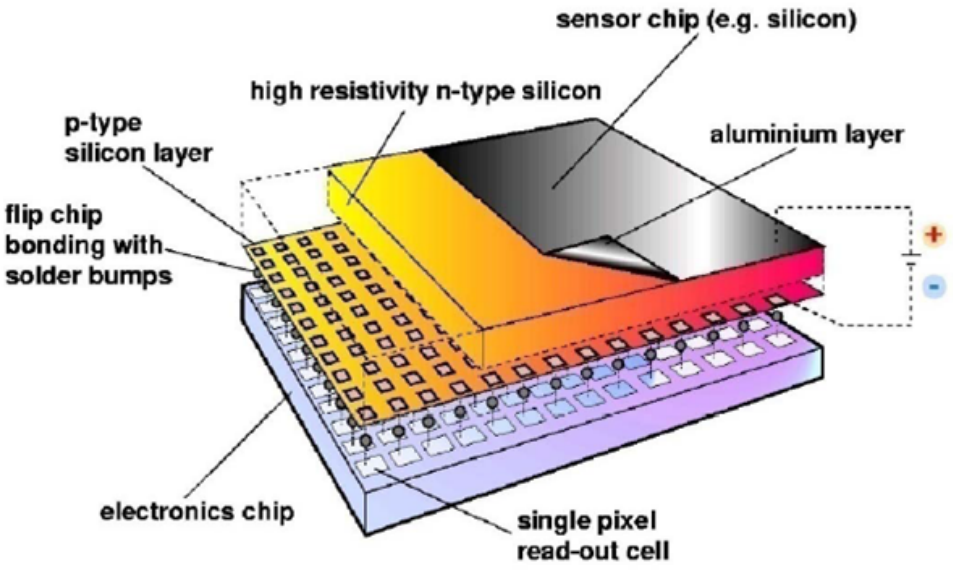

Figure 2.24 Schematic of a Medipix. Image courtesy of CERN.

the detected particle, thus allowing a direct measurement of particle energy. This is known as a Wilkinson-type analog-to-digital converter (ADC).

2.6.2 Comparison with Other Detectors

The typical procedure in radiation imaging involves a beam of radiation traversing the object you wish to image and obtaining a transmission image as the beam is modified through the object, i.e. attenuated to have its intensity, beam composition, energy spectrum modified. The recorded images correspond to the internal structure of the investigated specimen. The quality of the irradiating beam combined with the performance of the chosen detector determines the quality of the resulting radiograph.

Currently, the three main techniques for radiation imaging are:

1. Film chemical emulsions - largely unsuitable for modern diagnostic systems due to their limited dynamic range, non-linear response and absence of real-time digital output. Considered largely obsolete;

2. Charge integrating devices such as flat panels, CCD or CMOS sensors provide good spatial resolution for a low cost, but also have limitations in limited dynamic range, limited linearity, integration of noise and 'dark current' issues;

3. Single-particle counting pixel detectors contain separate electronics and digital counter for each pixel, such that every particle is processed independently (signal amplification, discrimination and counting). The digital counter increments without any dark current and full suppression of electronic noise such that the result is absolutely linear and dynamic range virtually unlimited.

One such semiconductor hybrid device in the category of single-particle counting pixel device is the Medipix (and therefore the Timepix). The typical hybrid detector

is composed of two chips. The sensor chip is a semiconductor diode with one back-side and pixellated contact. The second chip contains the read-out electronics for all pixels. The chips are connected by bump-bonding technique.

Lastly, due to its high resolution, lack of noise and practically unlimited dynamic range, the Medipix detector has many applications in high-contrast X-ray transmission radiography of soft tissue and other industrial and ecological materials. It is also highly sensitive to low energy X-rays, and therefore perfectly suited for high contrast X-ray attenuation/transmission imaging in biological samples. Besides some preliminary application in ocular brachytherapy QA (61), there have been no real medical applications of the Medipix. Some applications have been found in mixed radiation field dosimetric work (62).

2.6.2.1 Use of Timepix in Dosimetry

These properties of Timepix make it perfectly suited for use in particle tracking, and in personal dosimetry applications. However, to date, there has been no specific medical application of the device.

For example, the Timepix has been successfully used in radiography, neutronography and micro-CT. In a study performed for ocular radiotherapy QA by Weaver et al. (61), it is established that the Medipix operating in a spectroscopic mode is able to generate high-resolution dosimetric maps when placed below the treatment plaque within an eye phantom. Other applications include detection of neutrons at the ATLAS detector (CERN), and space dosimetry on the International Space System (62).

The following reasons justified our use of Timepix for application in BrachyView:

- Small physical size
- Real-time read-out
- High spatial resolution

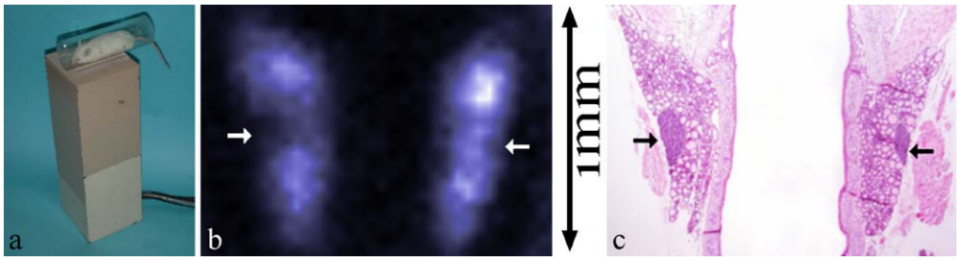

Figure 2.25 An example of a table-top mouse pinhole imaging system using an I-125 scan of a mouse thyroid (11).

2.7 Pinholes in Brachytherapy

The use of pinholes in radiation therapy is typically limited to applications in radionuclide imaging, SPECT imaging or as coded apertures. Pinhole gamma camera imaging offers the ability to obtain high-resolution images of gamma-emitting tracers in small objects such as that discussed in a study on I-125 imaging in mice by Beekman et al. (11). The excellent imaging characteristics of the pinhole lends its use to imaging the human thyroid and small animals.

In clinical radionuclide imaging, the pinhole serves as a collimator for gamma rays and has been used mainly for the imaging of small volumes such as the thyroid. Multi-pinhole imaging has also been used to image relatively small organs such as the thyroid, shoulder, hip, neck ad heart, but to date, it has not yet achieved broad clinical application (14). An example of a small mouse organ imaging application is shown in Figure 2.25.

2.7.1 Gamma Camera Mode

In brachytherapy, some studies have pursued the application of pinhole imaging for the localisation of implanted sources. However, none, to the author's knowledge, have proposed an application as an in-body imaging device and therefore as an intra-operative real-time imaging system and dynamic dose optimisation planning system.

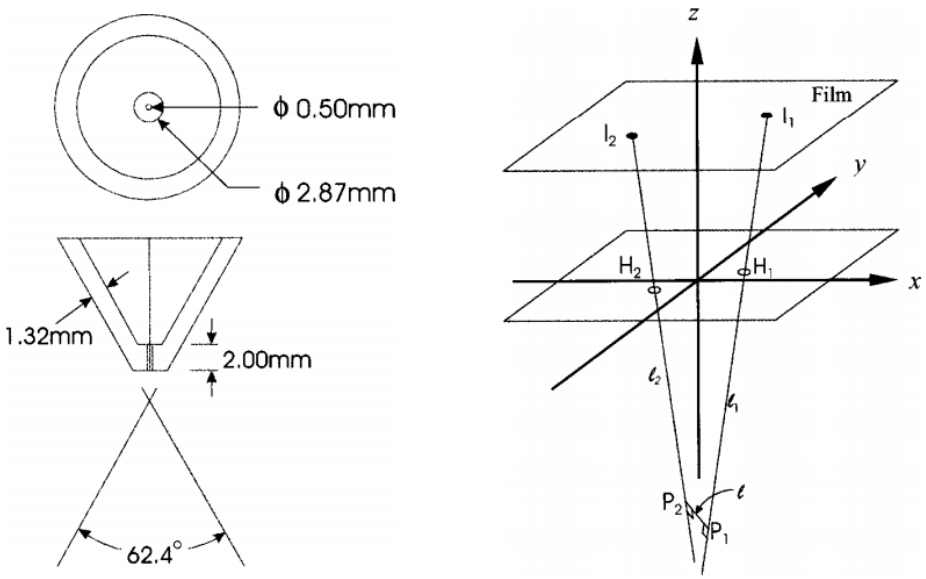

Figure 2.26 (Left) Schematic of pinhole design in tungsten collimator. (Right) Diagram illustrating two straight lines l_1 and l_2 connecting the images of the HDR source $I1$ and $I2$ to their respective pinholes $H1$ and $H2$ that produced the image, and their common perpendicular line l (12).

By using the implanted seeds themselves as the source of imaging radiation, the camera obscura concept lends itself perfectly to the application of real-time seed localisation in prostate brachytherapy. As the seeds emit their therapeutic dose, some percentage of the radiation can be transmitted to the BrachyView probe through the pinholes.

Duan et al. (12) used a tungsten collimator combined with a film screen for HDR seed localisation. This study proved that ”the pinhole imaging method is capable of providing independent and reliable real-time monitoring and verification of HDR brachytherapy”.

2.7.2 Pinhole Design

Pinhole imaging with gamma rays is based on the same geometric principle as the optical pinhole camera, where the lenses in an optical system have been replaced by the pinhole. Several fundamental factors must be considered when employing

pinhole systems. Such factors include the system sensitivity, spatial resolution and the field of view.

As discussed by Beekman et al. (11), the decrease in quality of pinhole images is a result of the decrease in count sensitivity S with increasing distance z between the emitting source and pinhole. For a point source located in the centre of the field of view, $S \approx D^2/16z^2$ where D is the hole diameter.

Now consider the resolution of the pinhole system. This is dependent on geometric factors and the intrinsic resolution of the detector as well. The geometric resolution is:

$$R_g \approx D(l+z)/l$$

where D is the diameter of the pinhole, l is the distance between the pinhole and the detector, and z is the distance between the source and the pinhole.

However, taking into consideration the intrinsic resolution R_i of the detector system and assuming a Gaussian-shaped kernel for pinhole blurring, the total resolution is given by:

$$R_t \approx \sqrt{[(\tfrac{z}{l}R_i)^2 + R_g^2]}$$

This has the effect of reducing the overall resolution.

All these factors were taken into account in the preliminary design of BrachyView. The pinhole design must be such as to cover the entire region of interest, i.e. the entirety of the prostate gland. When considering the high resolution of the Medipix device, the application in gamma camera imaging for brachytherapy procedures is suitable.

2.8 Summary & Conclusion

The traditional approach of ultrasound-based preplanning in PPB has recently been challenged by a rising group of intraoperative planning-based systems. The primary goal of such an approach is to reduce the time gap between planning and implantation, and also to introduce the ability for adaptive replanning as the implant occurs in order to account for any discrepancy between the planned prostate volume and implanted volume.

Some centres have evaluated the use of CBCT and fluoroscopy imaging to achieve this goal. However, to date no system is robust or economic enough for widespread application. BrachyView has been proposed as such a system, utilising pinholes and novel pixellated detectors in the form of the Timepix device for the development of a novel in-body imaging system capable of preplanning volumetry, intraoperative planning, and post-implant dosimetry in a single procedure in permanent implant brachytherapy for prostate cancer treatment. The development of BrachyView addresses all the issues presented in the literature review, and presents a novel solution to maximising patient outcome in the treatment of low to intermediate-risk prostate cancer.

Chapter 3

Design

3.1 BrachyView Probe

The BrachyView rectal probe design is based on a multi-pinhole lead collimator and tiled Medipix2/Timepix detectors with a geometry configured to fit inside the TRUS probe (note that the average rectal cavity diameter is approximately 25 mm). Preliminary experiments were based on a triple detector design, with later generations focusing on a gapless quad chip design (63). The first prototype of such a design is shown in Figure 3.3.

For the triple chip design, a total imaging area of 14×42 mm^2 was available as an array of 256×768 pixels, each with a pitch of 55×55 μm^2. For our purposes of experimental verification of the proposed brachytherapy seed position reconstruction method, three pinholes were used to cover the entire field of view of the prostate gland; i.e. each individual pinhole corresponding to one single detector. Future work will also investigate the use of several pinholes in a modified form of a coded aperture for example.

The first version of the quad detector design as shown in Figure 3.3 aims to overcome the mechanical shortcomings of the triple design. i.e. by removing the gaps between each detector. In detail, each Timepix detector requires wire bonds for data read-out to the FITPix and to the Pixelman software. These run along the bottom edge

of each detector in the triple configuration. By rotating each detector 90°, the wire bonds run parallel to the longitudinal axis of the supporting PCB and substrate. By using edgeless Si sensor chips, a total area of 256×1024 pixels (corresponding to $14\times56\text{mm}^2$) is achieved.

This work was made possible by the novel detector designs made in-house (at IEAP), and later made available through an external spin-off detector company Advacam. As of mid-2015, products such as the Widepix 1×5 detector array (14×70mm) were made commercially available. Images of this device are shown in Figure 3.4.

When combined with the pinhole collimator, the brachytherapy sources themselves act as the source of imaging radiation passing through the pinhole, casting their projections onto the detector plane. However, in contrast to traditional pinhole gamma camera systems, BrachyView is based on a demagnification factor since the imaging plane is smaller than the object being imaged.

This is made possible because of the unique spatial resolution capabilities of the Timepix detector. As discussed in the previous chapter, each pixel has its own independent pre-amplification channel and two signal discriminator levels. Each incident photon deposits energy in its corresponding pixel, and the energy deposition is compared to the threshold and the corresponding counter increases by one. This signal is then read out digitally by a USB interface with a refresh rate of a few hundred Hz.

The resulting matrix of counts is a projection image of the seed on the imaging plane. With a number of distinct projections of the same seed through a number of pinholes, a three-dimensional coordinate relative to the probe/pinhole system can be obtained using a back-projection triangulation method. As mentioned above, the number of pinholes chosen was kept to the minimum required, such that one detector corresponds to one detector. This was to simplify the feasibility study. The shape of the pinhole and other geometric parameters were optimised to maximise the field of view for the prostate size (typically with diameter around 40 mm). This method is explained in full detail in Chapter 5.

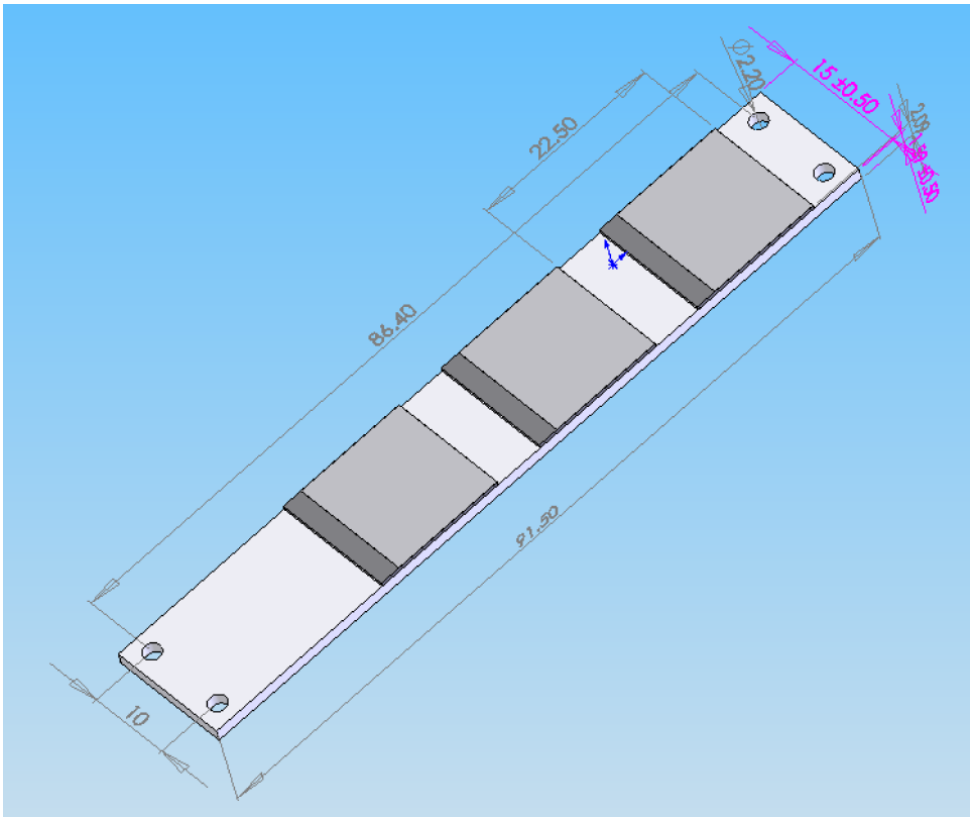

Figure 3.1 Triple chip design and the final product assembled with a 7 mm gap between each active sensor chip.

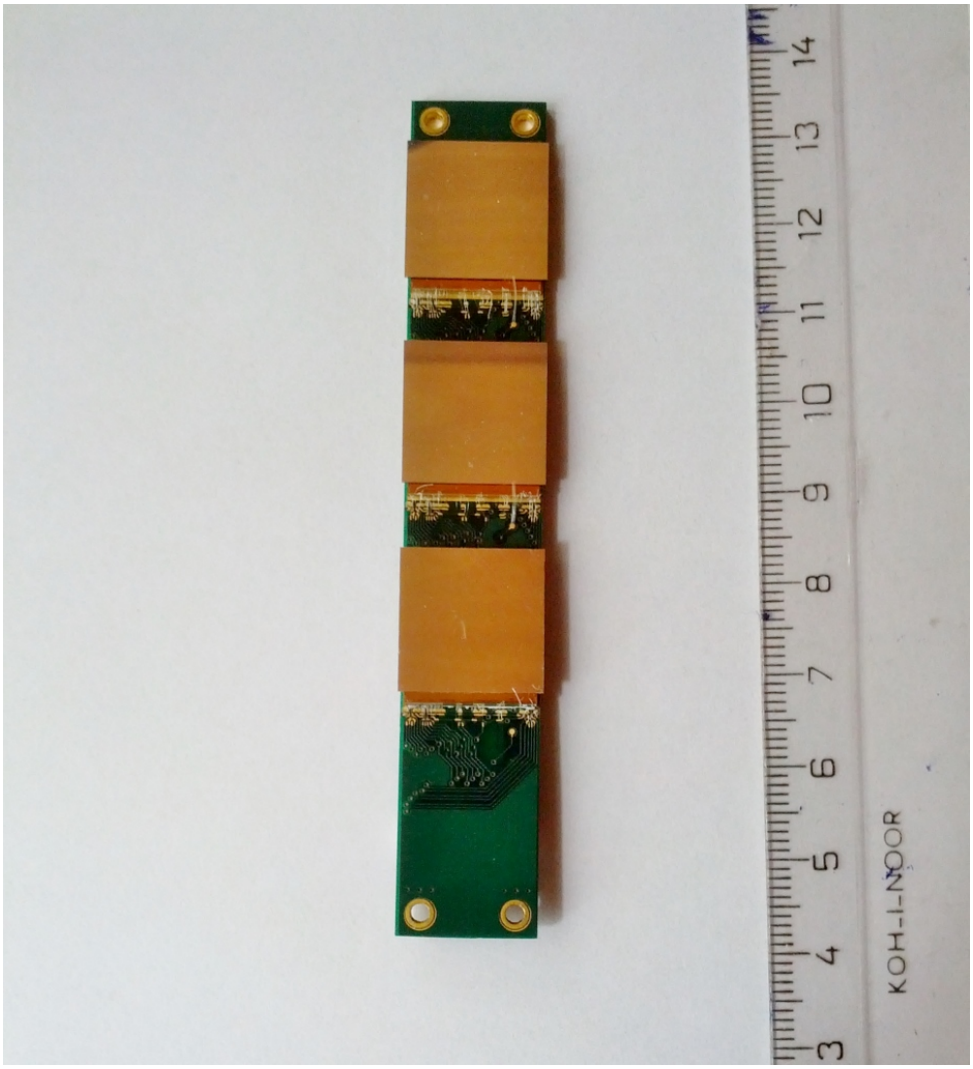

Figure 3.2 Prototype for triple chip design assembled with a 7 mm gap between each active sensor chip.

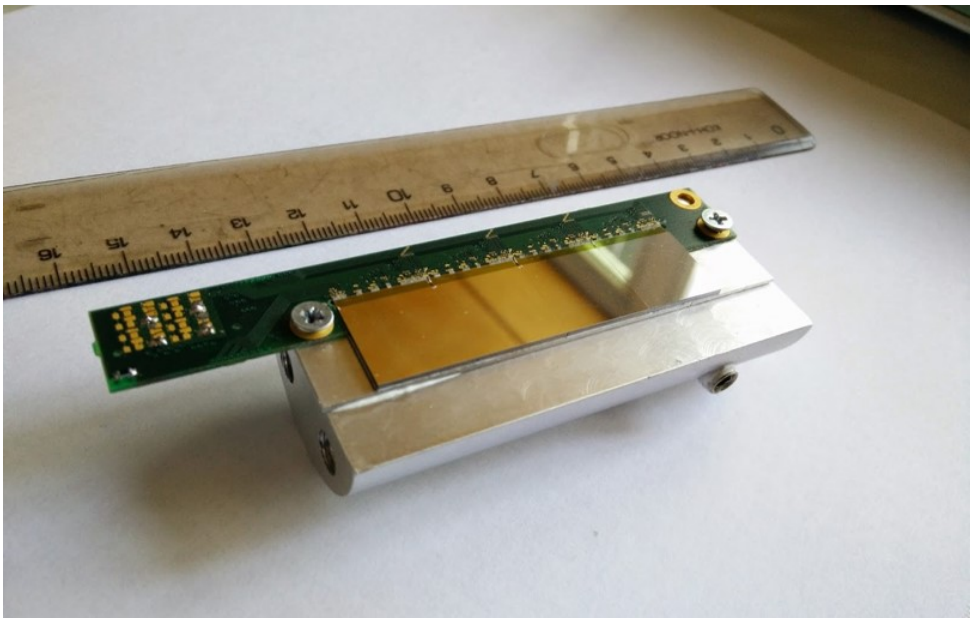

Figure 3.3 Quad chip showing gapless design mounted on an Al base (for cooling).

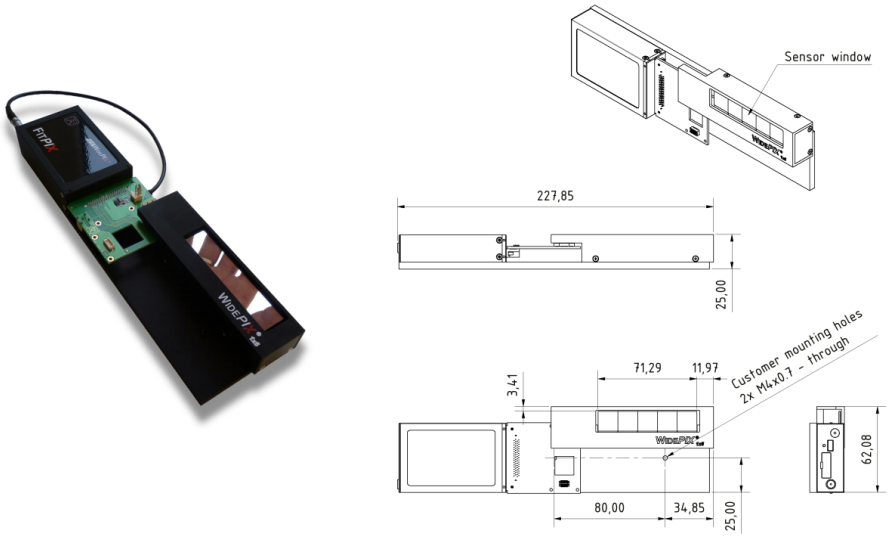

Figure 3.4 Example of Widepix 1×5 showing a 1×5 detector array. (13)

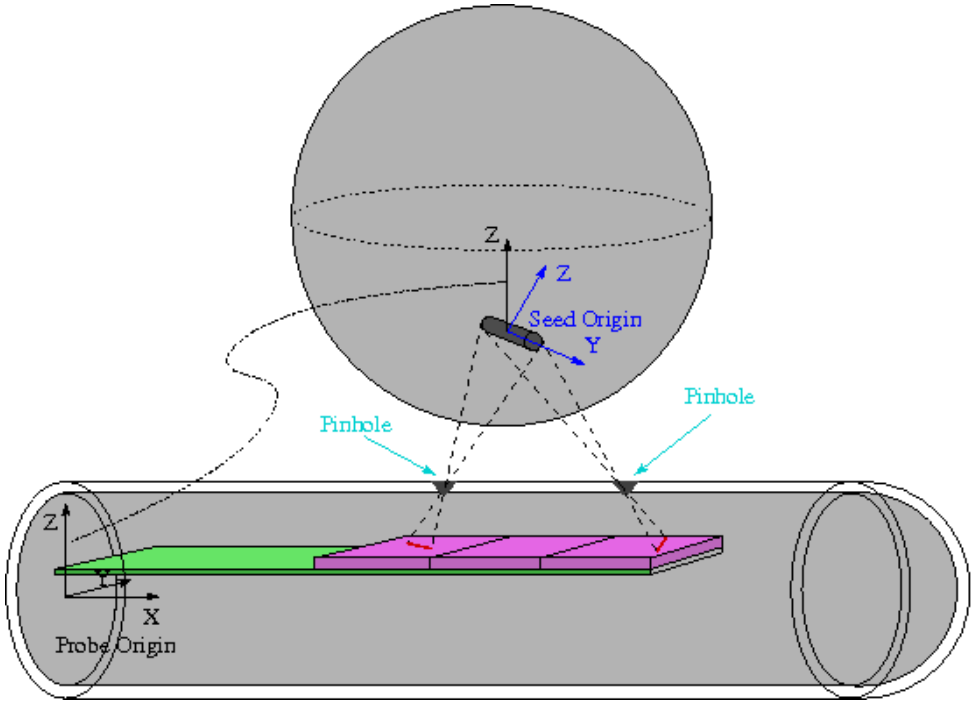

Figure 3.5 Conceptual schematic of BrachyView concept showing prostate as a grey sphere and triple detector with pinhole concept.

The concept schematic for the BrachyView probe is shown in Figure 3.5.

In this BrachyView design the diameter of the probe has to be suitable for use in-vivo in the patient's rectum, and has an outer limit of approximately 25 mm. The ultrasound hardware has not been included in Figure 3.5. The final BrachyView probe design is proposed to consist of two components:

1. The ultrasound hardware;
2. Timepix hardware and associated electronics, as well as a necessary cooling system, since each chip consumes approximately 1 W of power. A multiple chip assembly would have non-negligible heating effects.

Therefore, a rotational hardware system must be considered where an image acquisition can be completed using ultrasound and then the alternate modality (i.e. the Timepix) rotated around to the top, thus allowing several imaging modalities to be

performed with the one device. To date, some twister-ultrasound apparatus designs have already been designed, which incorporate such rotational motion. The rotational system will consist of an interior shell system, so as not to introduce any motion against the patient's rectal wall. This is a reverse-engineering problem, and beyond the scope of the purposes of this dissertation.

Chapter 4

Simulation Studies

In this chapter, two main simulation studies are presented. This simulation work was used to justify the choice of pinhole design for imaging the prostate volume. Firstly, analytic methods in MATLAB were used to quantify imaging capabilities as a function of pinhole collimator parameters. Following this, a study into the pinhole geometry using Monte Carlo method was performed. This involved the simulation of a single LDR seed, as well as multiple seeds implanted into a volume of water designed to simulate the prostate. From these results, a choice of lead pinhole collimator was made for experimental, in-phantom studies.

4.1 Study of Background Noise of BrachyView

A radioactive point source was modelled in a three-dimensional coordinate system in MATLAB (V2013b, license: Czech Technical University in Prague). The point source was positioned in a cube of water modelling the prostate volume. As the incident photons travel through the water volume, they are attenuated according to their primary energy. Assuming an apparent activity of 0.4 mCi (equivalent to 1.48 x 10^{10} decays per second), the expected number of counts per second at the detector plane can be calculated based on the amount of attenuation through water and absorption at the collimator.

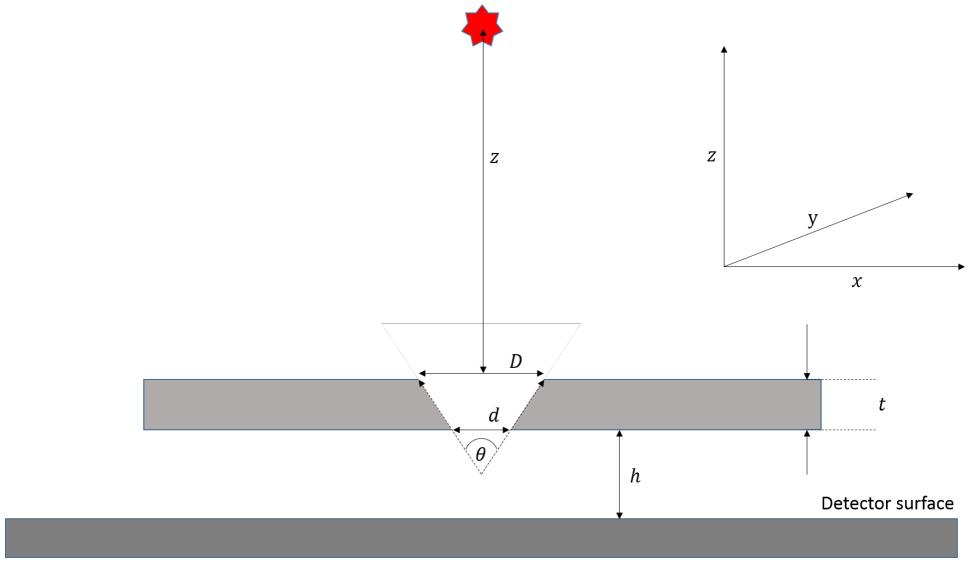

Figure 4.1 Schematic showing geometrical parameters used to evaluate background from attenuation through collimator. Image not to scale.

The probability of photon absorption in the collimator is high because of the high atomic number of lead and the low energy of the photons. However, depending on geometric factors, a proportion may also penetrate through, generating some amount of background events on the detector surface. An analytic model of the detector-collimator-source system was developed in MATLAB. An evaluation of the signal to noise ratio (background noise) was investigated in MATLAB as a function of collimator thickness to model distance from the pinhole and pinhole parameters.

The geometric factors affecting the background noise include distance of the point source from the collimator, collimator thickness, and pinhole size. These are shown in the schematic in Figure 4.1 and summarised by:

$$Background \longrightarrow f(x, y, t, h, \theta, d, z) \tag{4.1}$$

where x and y represent the position of the source in one plane, t is the thickness of the collimator, h is the vertical distance from the detector surface to the collimator, θ is the aperture opening, d is the diameter of the pinhole, and z is the vertical distance

Material	$\mu\ (mm^{-1})$	$\rho\ (g/cm^3)$
Lead	49.152	11.3
Water	0.11723	1
Air (35C)	0.000627	1.15E-3

Table 4.1
Linear attenuation coefficient values used to calculate penetration and background noise through varying thickness of collimator. Values are shown for photon energy 27 keV

.

of the source from the collimator surface.

The values used to calculate attenuation are given by NIST standards (NIST). For a Nucletron Model 6711 I-125 source, the linear attenuation coefficients corresponding to the average energy of 27 keV was used, as shown in Table 4.1. Note that the linear attenuation factor for air is taken at a temperature hotter than room temperature, accounting for the in-body nature of the BrachyView system.

The signal to noise ratio can be calculated as the ratio between the photons passing through the pinhole and those passing through the lead. This can be studied as a function of the geometric factors (see Equation 4.1).

The coordinate system modelled in MATLAB is shown in the sketch in Figure 4.2. Considering rays drawn from the point source, denoted by S, and each individual pixel coordinate as denoted by point P, the angle between the vectors PS and OP (the perpendicular joining S and the pixel directly below P) can be calculated. Assuming that point source S is isotropic, this angle is key in calculating the expected length of travel for each ray through each respective medium.

The photons travel through three regions before being detected. These are:

- Water volume;
- Collimator volume;
- Air volume.

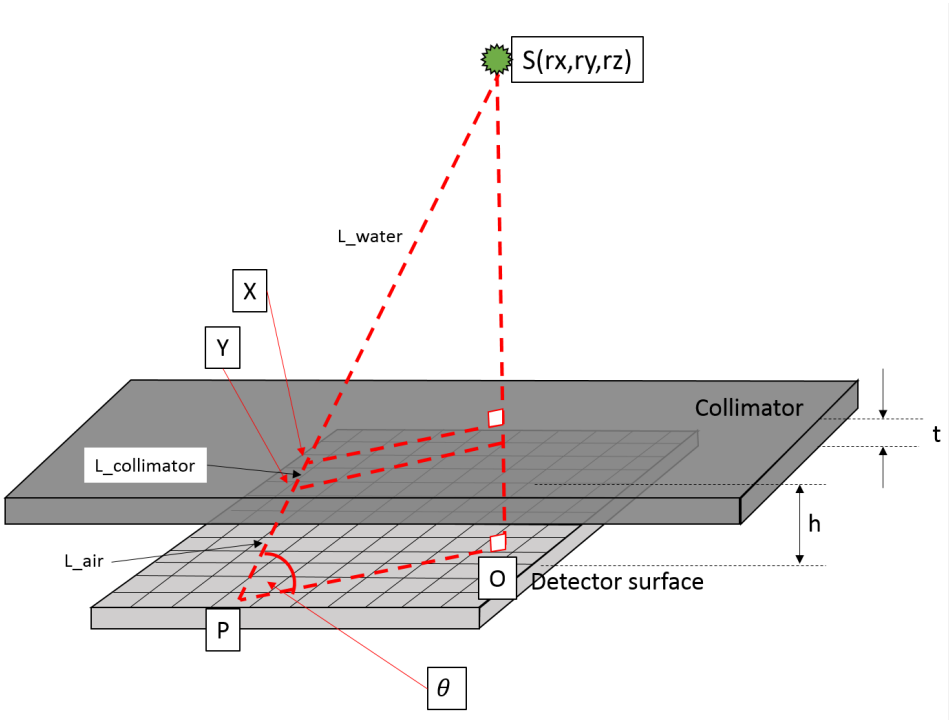

Figure 4.2 3D schematic showing geometrical parameters used to evaluate background from attenuation through collimator. r_x,r_y,r_z are the coordinates of the source in 3D. Image not to scale.

By defining the materials in the set-up as water (to approximate soft tissue), lead, and finally air, the following values can be calculated for the length of material traversed:

$$L_{water} = \frac{r_z}{sin(\theta)} \tag{4.2}$$

$$L_{collimator} = \frac{t}{sin(\theta)} \tag{4.3}$$

$$L_{air} = \frac{h}{sin(\theta)} \tag{4.4}$$

where r_z is the perpendicular distance of S from the collimator, t is the thickness of the collimator, θ is the angle between the vectors PS and OP (as shown in Figure 4.2, and h is the distance from the collimator to the detector (also see Figure 4.1). Several physical limits must be considered: the diameter of the TRUS probe 23 mm, and the size of the Timepix detectors 14 x 14 mm^2 (see Figure 3.5 for a conceptual image). Therefore, h is defined as 6 mm, allowing a maximal field of view for a typical prostate volume. This is discussed in more detail with respect to pinhole geometry in Chapter 5.

These lengths are then used in combination with the linear attenuation coefficient for each respective material. The final intensity at the detector is then calculated based on an initial activity of 0.4 mCi (typical of a fresh LDR seed). Attenuation through the material can be calculated:

$$I = I_o e^{(-\mu \cdot r)} \tag{4.5}$$

where I_o is the initial source intensity at point S, I is the new intensity after traversing through a medium of length L, μ is the linear attenuation factor evaluated at the average energy of I-125, taken at 27 keV.

Lastly, following the calculation of intensity at detector surface based on length of ray traveled, a final factor has to be taken into account. This is the detection efficiency of silicon for photon energy range coming from a typical I-125 source. Assuming an average photon energy of 27 keV, silicon has a detection efficiency of 60% (NIST value).

This model allows the calculation of expected count rates per second at the detector surface. By varying geometric parameters such as collimator thickness and pinhole diameter, a design for an experimental lead collimator can therefore be optimised.

4.2 Pinhole Geometry Optimisation

Using the method explained in Section 4.1, a distribution of counts can be obtained through the single pinhole, and an evaluation of possible transmission events through the collimator can be performed.

The point source S is placed 10 mm above the pinhole location, and the thickness of the lead collimator varied between 100 μm and 300 μm. The pinhole is treated as a point as the main aim of this investigation is to obtain an analytic model of counts at detector surface, without taking into consideration the projection image shape (this is later studied in Section 4.3).

The resulting images are shown in Figure 4.3.

In each plot shown in Figure 4.3, a map of the background counts (photons penetrating through the collimator) detected in the silicon sensor is shown on the left. The background counts superimposed with the number of signal counts as a function of increasing collimator thickness is shown on the right. Since the number of counts through the pinhole is higher than the background by several orders of magnitude, the superimposed image appears as a single bright spot. The actual number of counts can be seen in the scale on the right of each image.

By considering the central row of the modelled Timepix detector, a profile plot can be obtained for each case calculated as shown in Figure 4.4. This allows an evaluation of the photons passing directly through the collimator relative to the background noise.

It is clear from these considerations that a lead sheet of thickness 100 μm does not provide adequate shielding from an active source at a distance of z=20 mm directly above the pinhole. However, with a lead thickness larger than 200 μm, in an ideal environment ignoring scattering and blurring effects from the pinhole, this model allows an estimation of the number of counts expected per second depending on source position in the prostate volume.

It is then possible to create a table with the expected counts per second associated with position.

The plots shown in Figures 4.5 and 4.6 show the results for a point source moving in a single Z plane. As the point source is moved in a lateral distance from the pinhole, the counts at the detector plane can be modelled for different Z distances as well. As the source is moved further from the collimator, the count rate drops off exponentially as expected.

The results for locations at Z=10, 15, 20, and 30 mm are shown in Figure 4.7. With increasing Z distance, the expected count rates drop off, but as shown by the results in Figures 4.5 and 4.6, the point source signal is distinguishable from the background noise. Due to the radial symmetry of the system, a calculation in one radial direction is sufficient to obtain an overview of the overall system. Note that at Z=10 mm, and X greater than 11 mm the point source is outside the field of view for the single detector system.

These results show that a collimator thickness of at least 200 μm is sufficient to absorb the majority of photons from an I-125 LDR seed, except for those directly through the pinhole aperture.

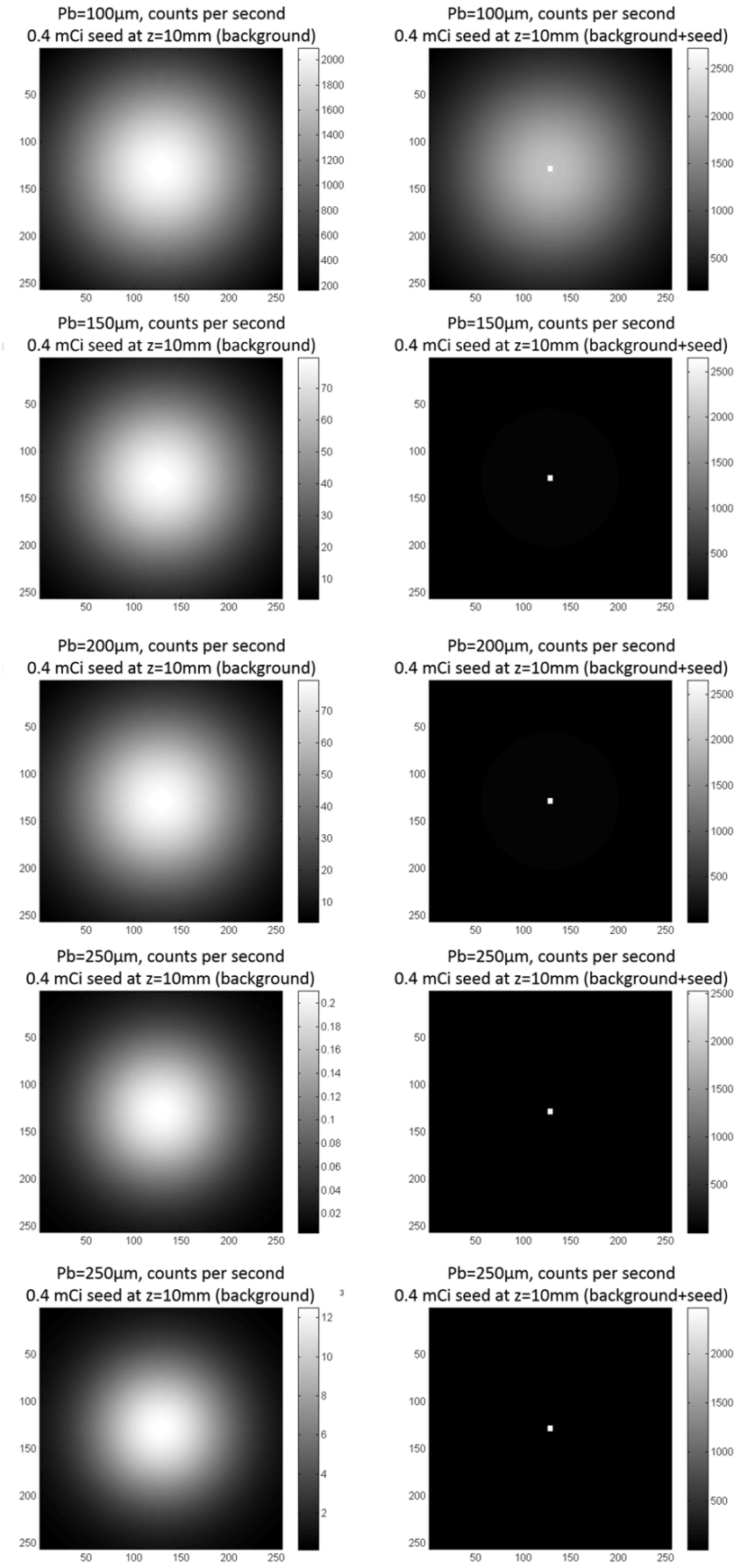

Figure 4.3 Images generated from placing a point source of 0.4 mCi at z=10 mm above the pinhole. Results show counts per second.

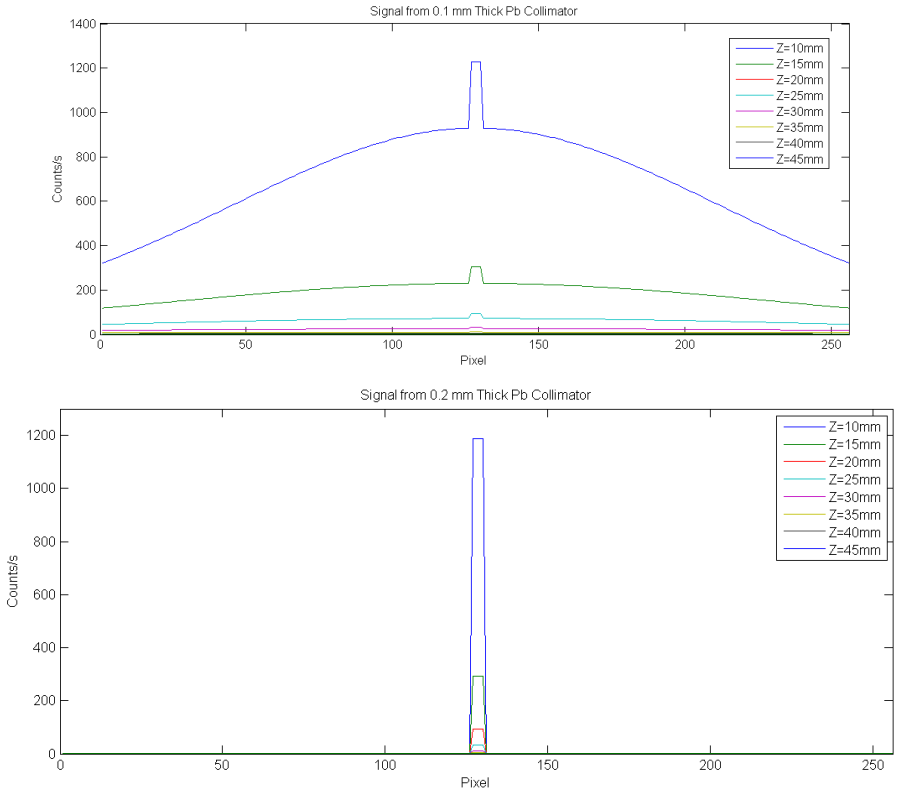

Figure 4.4 A comparison showing two different thicknesses of Pb simulated in MATLAB to create plots of a point source through a single pinhole.

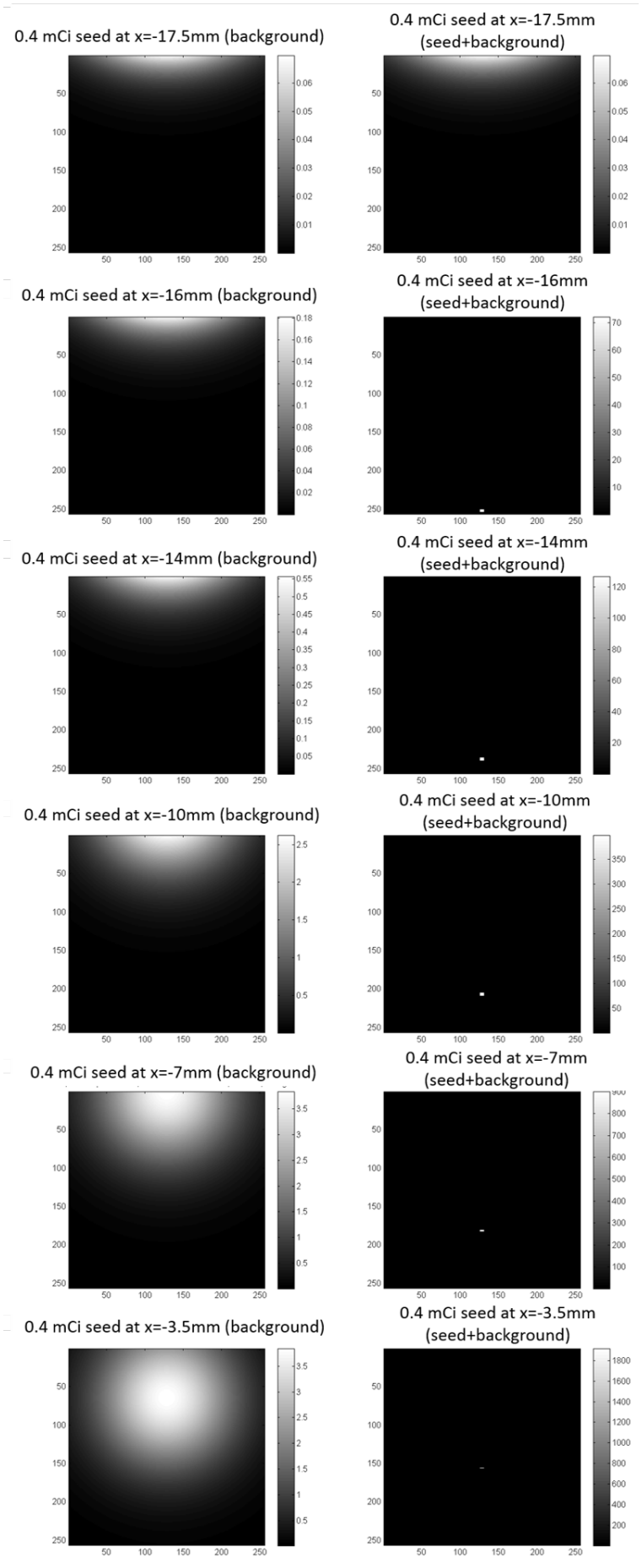

Figure 4.5 Counts per second for a moving point source in the X direction. Collimator simulated is 200 μm thick, and seed kept at z=10mm

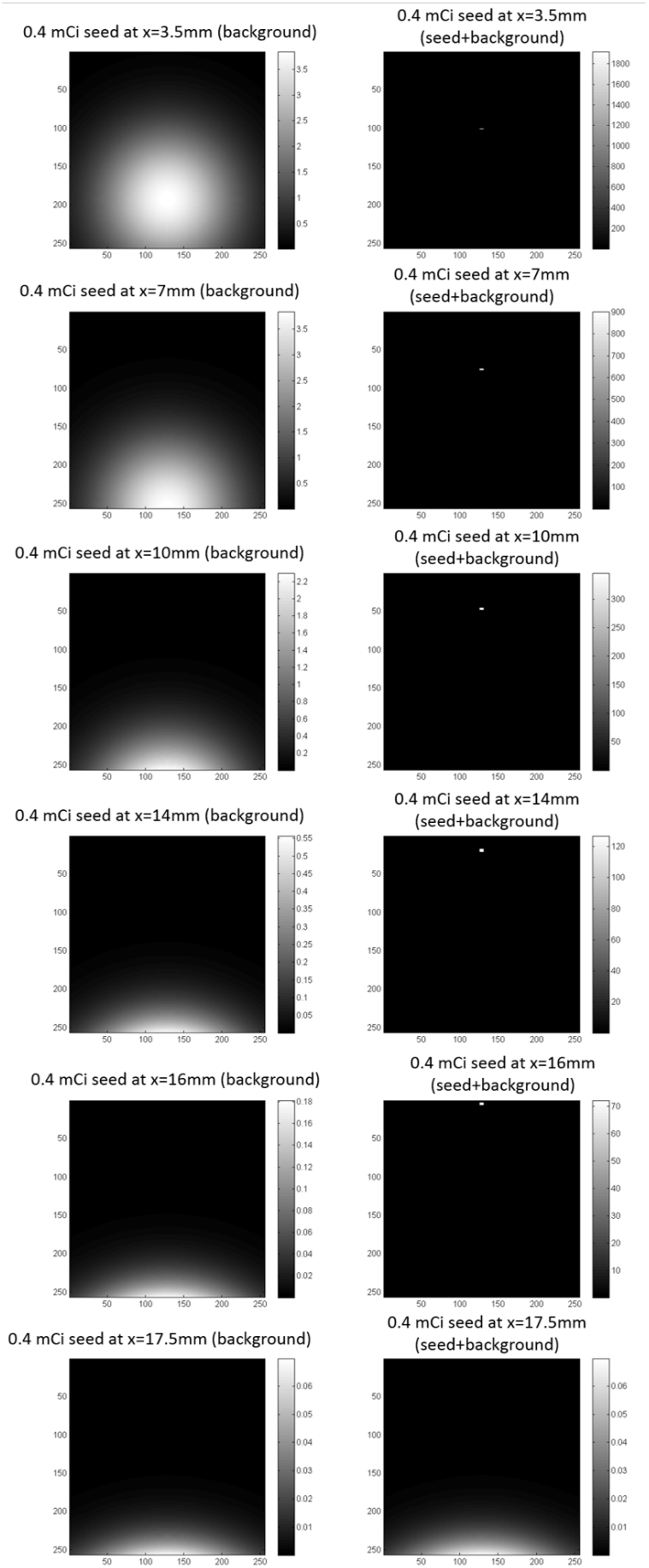

Figure 4.6 Counts per second for a moving point source in the X direction continued. Parameters as above in Figure 4.5.

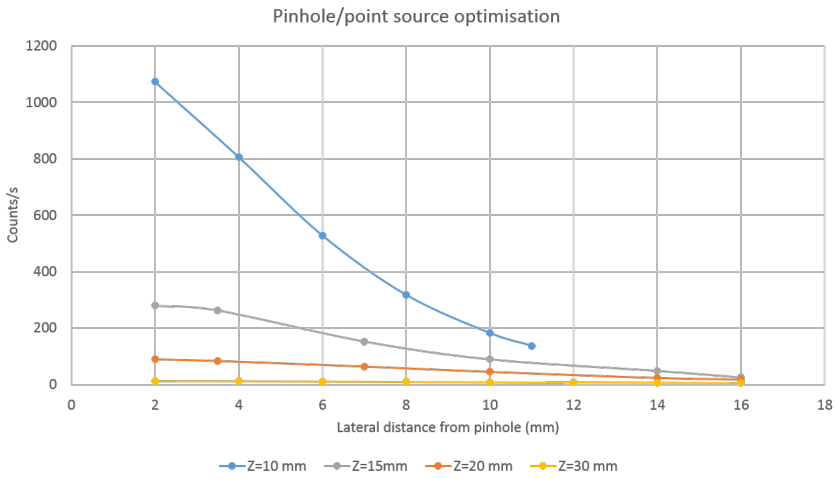

Figure 4.7 Count rate calculated from the placement of a point source at varying X distances and different Z distances from the collimator.

4.3 Monte Carlo for Pinhole Measurements

This Section outlines the further modelling of the BrachyView system using Monte Carlo methods. Following the justification of a pinhole collimator thickness as shown in Section 4.1, an evaluation of pinhole shape must be performed based on analytic approach. This was done by varying the size of the major and minor diameters of the cone pinhole and evaluating the resulting projection images obtained on the detector surfaces.

4.3.1 The Geant4 Monte Carlo Toolkit

The Geant4 (Geometry And Tracking) toolkit (64; 65) is a Monte Carlo code using object-oriented technology and C++ programming. It describes particle interactions with matter, developed originally for high energy physics experiments and then extended to space science and medical physics. Applications in low energy physics are described by Chauvie et al. (66) and Baro et al. (67) (PENELOPE group- penetration and energy loss for electrons in positrons in matter).

Geant4 is an open-source, freely downloadable software developed and maintained

by a large international collaboration based at CERN. It describes electromagnetic and hadronic interactions with complementary and alternative physics models covering an energy range from 100 eV up to the TeV scale. The Geant4-DNA package describes particle interactions down to the eV scale. The extensive physics capability is coupled with a powerful geometry component that allows the modeling of experiments as large as ATLAS and CMS detectors at CERN, or as small as the DNA helix.

Geant4 is a toolkit, which means that the user defines the tools for his/her own Geant4 application. The user has to develop a Geant4-based application describing the radiation field, the geometrical configuration and the physics processes of the experimental set-up. The user can then retrieve the required information from the simulation, i.e. the energy deposition and the particle fluence in a detector. Geant4 was adopted in this project to model the response of BrachyView in an I-125 LDR brachytherapy treatment.

There are seven physics process categories in GEANT4: electromagnetic, hadronic, decay, photolepton-hadron, optical, parameterisation and transportation. The electromagnetic processes of photons and charged particles are included in the EM Package. In particular, Rayleigh scattering, photoelectric effect, Compton scattering, pair production, ionisation, bremsstrahlung and multiple scattering are modeled in the energy range from 100 eV up to the TeV scale. Optical photon interactions can also be described.

The Geant4 Standard EM Package valid down to 1 keV is more commonly used for High Energy Physics experiments. The alternative Geant4 EM Low Energy Package is specifically addressed to low energy studies, i.e. medical physics. The G4 Low Energy Package includes two alternative approaches; one is based on the Livermore Evaluated Data Libraries (valid to down to 250 eV) and the second one is based on the physics models of the Penelope Monte Carlo code (valid down 100 eV). The electromagnetic physics models have been validated with respect to NIST reference data (68).

Fluorescence and Auger electrons can also be modelled in the simulation.

In the case of electromagnetic physics, a threshold of production of secondary particles (cut) has to be defined. The cut is expressed in range; this means that secondary particles are originated only if their range in a given material is bigger than the cut, otherwise their energy is considered locally deposited. In the simulation project of this thesis, the cut was defined to achieve higher simulation execution speed without sacrificing the accuracy of the simulation results.

Two versions of Geant4 were used in this thesis, Geant4 9.6 and Geant4 10.0.

4.4 The BrachyView Geant4 Simulation

Monte Carlo simulations were performed using Geant4 to model an LDR brachytherapy treatment in a water volume representing the prostate.

The simulation was used to determine the resolution of the BrachyView system with respect to the pinhole geometry. A Geant4 application was developed to model accurately the experimental objects as shown in Section 4.1 (i.e. I-125 seed with lead collimator and detector system).

The Geant4-based study followed the same approach of the experimental study (as discussed in Chapter 5). The Timepix and lead collimator system was studied in the case of a single LDR seed and then extended to a realistic patient LDR treatment plan.

The Nucletron 6711 brachytherapy seed, described in Section 2.1.2.1, was modelled accurately in terms of geometry and materials. Photons with an energy spectrum as illustrated in Table 2.2 were originated in a random position on the seed core, with randomised direction. Figure 4.8 shows a detailed view of the Geant4 model of the LDR seed implemented in the simulation. The experimental set-up of the simulation consisted of a single seed placed in a water volume representing the prostate. When

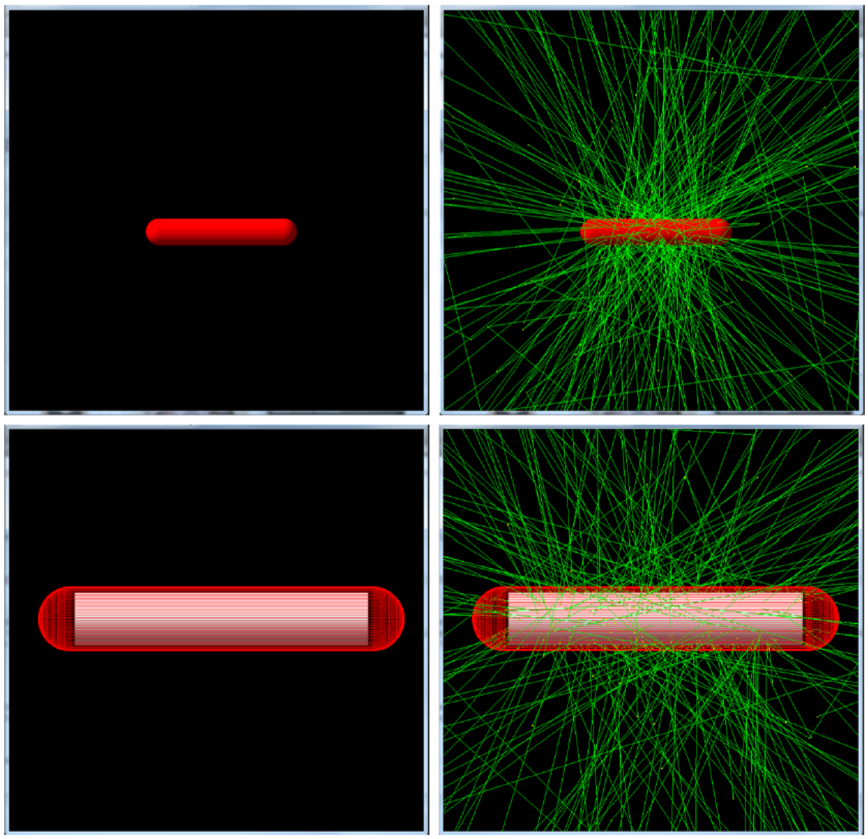

Figure 4.8 Single Model 6711 I-125 seed modeled in Geant4. The titanium shell is shown in red, and the wireframe model shows the inner silver core with the photons generated on this cylindrical surface, (shown on right).

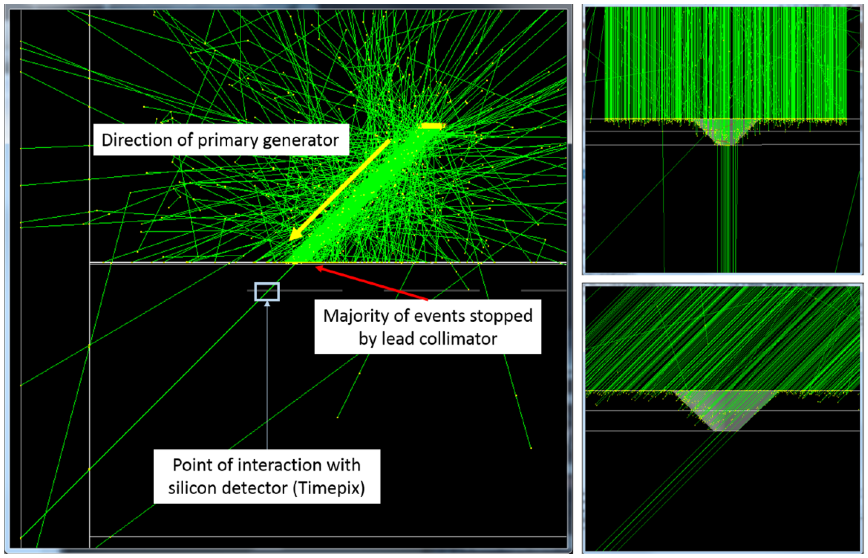

Figure 4.9 (Left) Non-isotropic source showing the simulation set-up and concept of lead collimator absorbing the majority of the primary photons. A small number of photons pass through the pinhole towards the interaction point in the silicon detector plane. (Right) Zoomed view of the pinhole showing the cone shape as discussed in Section 4.2.

modelling a realistic LDR treatment, seventy seeds were modelled in the positions as indicated by the treatment plan.

Timepix was described in detail in terms of geometry and materials. The simulation model consisted of silicon voxels repeated across a 256×256 array (14×14 mm^2) to model the pixellated detector face of the Timepix detector. The lead collimator was set below as illustrated in Figure 4.9s, with a thickness of 280 μm equal to the real experimental collimator. The pinhole was set with a major diameter D of size 800 μm and a minor diameter d equal to 180 μm (see Figure 4.9). The values D and d characterised the real collimator.

4.4.1 Pinhole Optimisation with one LDR Seed

A lead collimator was defined with three cone pinholes set at 15 mm intervals, corresponding to the BrachyView design as explained in Chapter 3. Three individual modelled Timepix devices were placed 6 mm beneath each pinhole, also in accordance with geometrical considerations of the BrachyView design. A single LDR seed

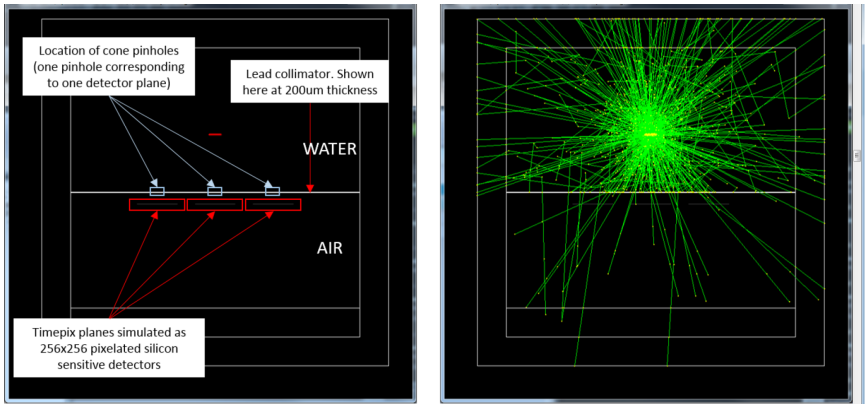

Figure 4.10 (Left) Simulation experimental set-up showing a single I-125 seed implanted in a volume of water. The pinhole collimator corresponds to a single sheet of lead with three pinholes for three detector planes. The image on the right shows the single seed as an isotropic source with 2000 primary photons.

was positioned 20 mm directly above the central pinhole, such that three projection images were obtained on three detector planes corresponding to the three separate Timepix devices as presented in Figure 3.5. These imaging planes are simulated as pixellated silicon planes with thickness 300 μm like the real detector, counting events that reach the detector pixels as shown in Figure 4.10.

4.4.2 Simulation with a clinical LDR brachytherapy treatment

A full clinical LDR brachytherapy treatment was simulated by utilising a real patient plan with 70 implanted brachytherapy seeds. The simulation experimental set-up containing the I-125 sources and single pixellated Timepix are shown in Figure 4.13.

The location of these seeds is shown in Figure 4.14, and is based on a real patient plan provided by St George Cancer Care Centre, Sydney, Australia.

The simulation experimental set-up is shown in Figure 4.15.

By varying the pinhole characteristics (diameter and thickness) a quantification of the image quality can be obtained. This is done by comparing SNR and image resolution based on geometric parameters.

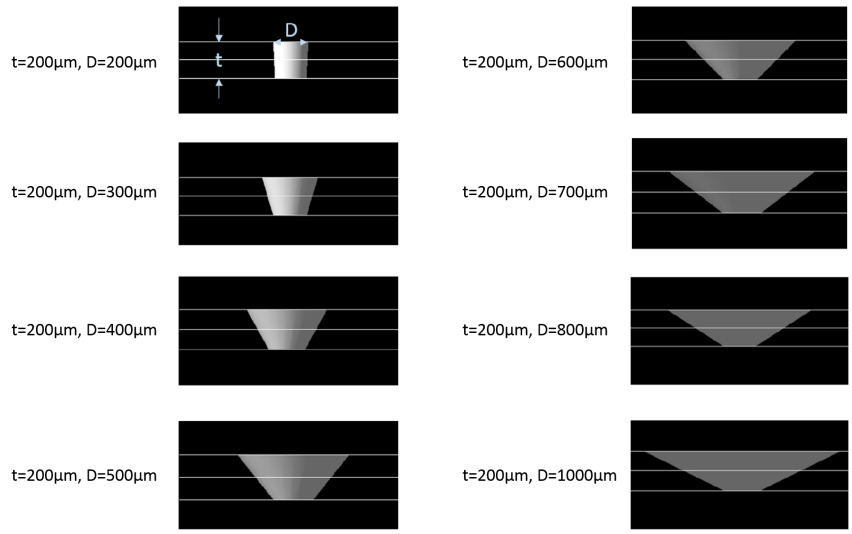

Figure 4.11 Zoomed view of the pinhole geometry modelled in the Geant4 simulation. Varying the size of the pinhole major diameter (and hence pinhole shape) allows an evaluation of image blurring effects.

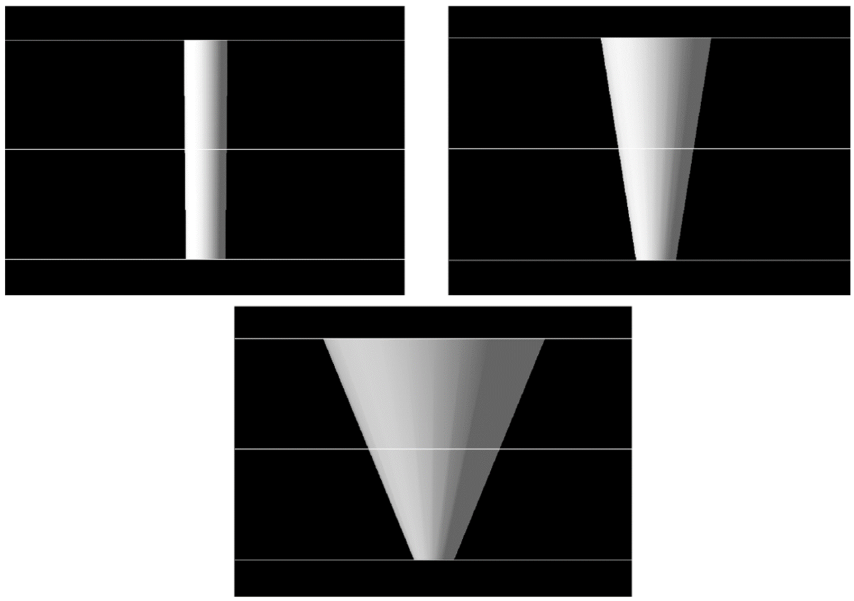

Figure 4.12 Sketch of the lead collimator with a thickness of 1000 μm. Varying collimator thickness allows an evaluation of absorbed and scattered radiation and its effect on the projection image of the individual I-125 seed and the determination of the centre of mass.

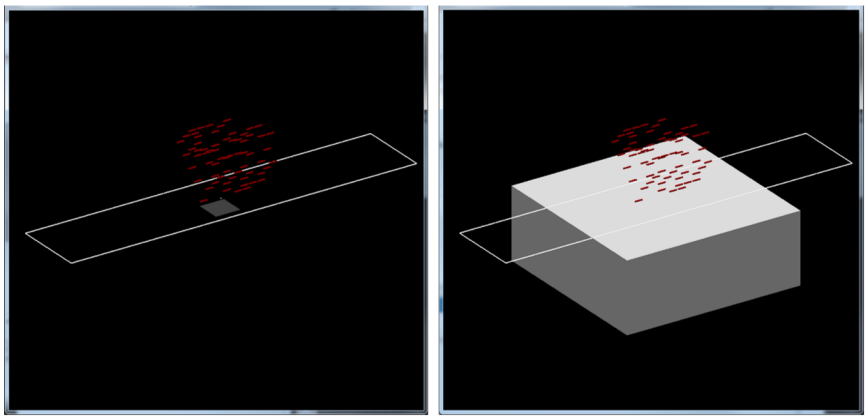

Figure 4.13 Overview of the Geant4 simulation set-up for 70 seeds in a volume of water. The I-125 seeds are shown in red, lead collimator shown as a white wireframe, and the single pixellated Timepix detector shown in dark grey. The image on the right shows the volume of air between the lead collimator and the detector as a solid grey block immediately inferior to the collimator.

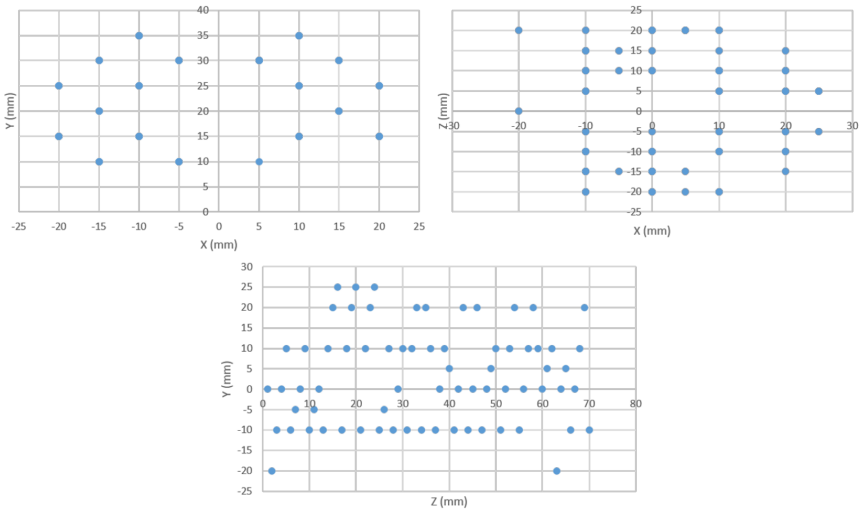

Figure 4.14 Coordinates of the 70 seeds implanted into an infinite volume of water used to simulate a realistic LDR procedure.

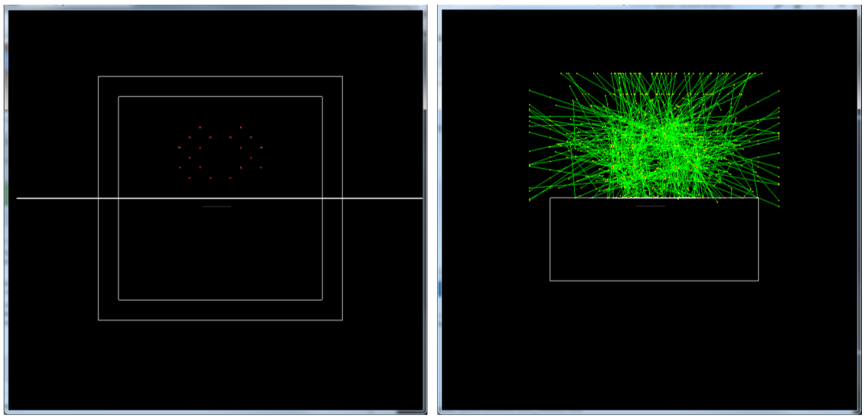

Figure 4.15 Coordinates of the 70 seeds implanted into an infinite volume of water used to simulate a realistic LDR procedure.

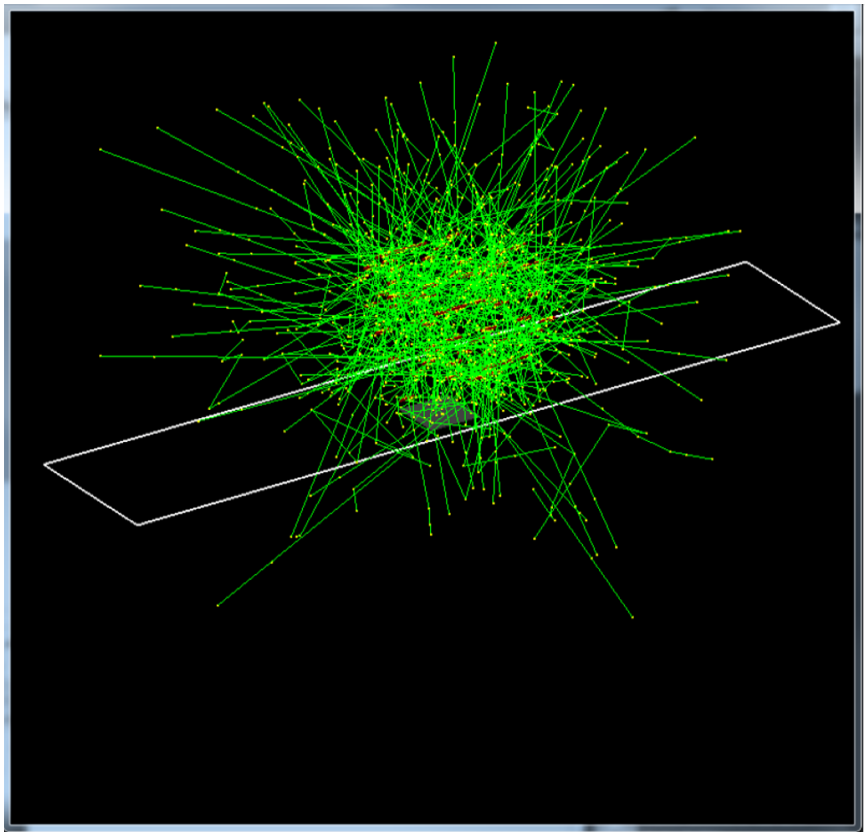

Figure 4.16 An example of an overall view showing 2000 primary photons generated from 70 implanted I-125 seeds in a volume of water. Note that 2000 photons were not used for measurements, but for purposes of figure to show isotropic sources in the volume.

4.4.3 Optimisation of Collimator by Geant4

By varying the size of the major diameter of the pinhole, count distribution maps corresponding to the triple detector imaging plane of the experimental Timepix configuration are obtained. Simulations were run for 1 billion primary photons. These were used to evaluate the size of the pinhole used in experiment and to assess the amount of noise from collimator scattering and penetration that can result from varying the geometry of the pinhole.

The results for a lead collimator of thickness 200 μm shows a large amount of scattered radiation (see Figure 4.17) as compared to the signal obtained, and with respect to the other sizes of collimator evaluated. However, it is noted that the signal to noise ratio is still favourable for us to distinguish the centre of mass of the seed projections and therefore perform the necessary calculations for source localisation.

The results from the simulations show that for lead thicknesses more than 200 μm, the majority of the scattered radiation and background noise is eliminated from the projection image, as is expected from Section 4.2. The signal-to-noise ratio can be calculated by number of counts as photons travelling directly through the pinholes as a ratio against number of counts through lead outside of the pinholes.

The signals shown in Figures 4.18, 4.19, 4.20, and 4.21 have been integrated along the Y direction through the centre of the pinholes to improve statistics. This was done in order to assess the signal to noise ratio corresponding to the changing pinhole diameter size. In a collimator with three pinholes, three resultant signal peaks are expected across the entire detector plane. By fitting Gaussian curves to each source signal peak, the centre of mass of each projection image can be determined by observing the pixel location at which the peak occurs. However, as shown in the results the optimal pinhole diameter should be at least 400 μm, which corresponds with the experimental choice of pinhole used in experimental active seed studies as described in Chapter 5.

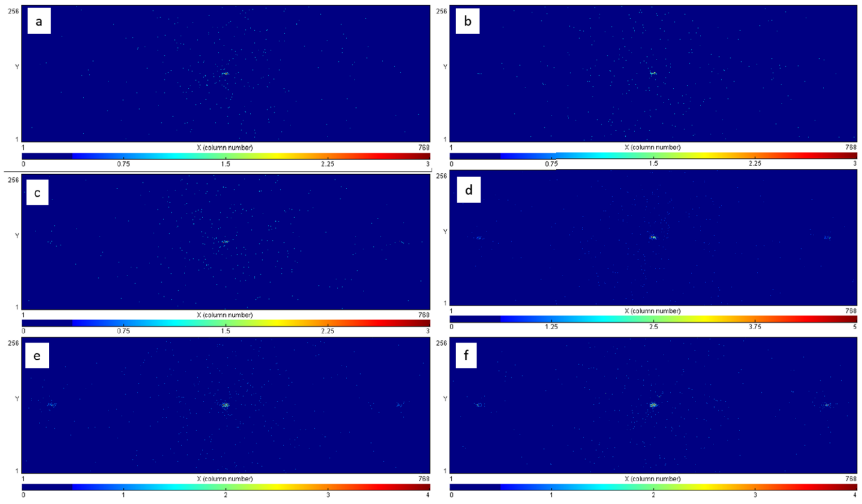

Figure 4.17 Projection images showing results from a 200μm thick lead collimator. Each of the images from (a)-(f) show the response from a triple detector configuration with changing pinhole diameter. The diameters shown are for 200, 400, 500, 700, 800, and 1000 μm. Detailed profile plots are shown in Figure 4.18.

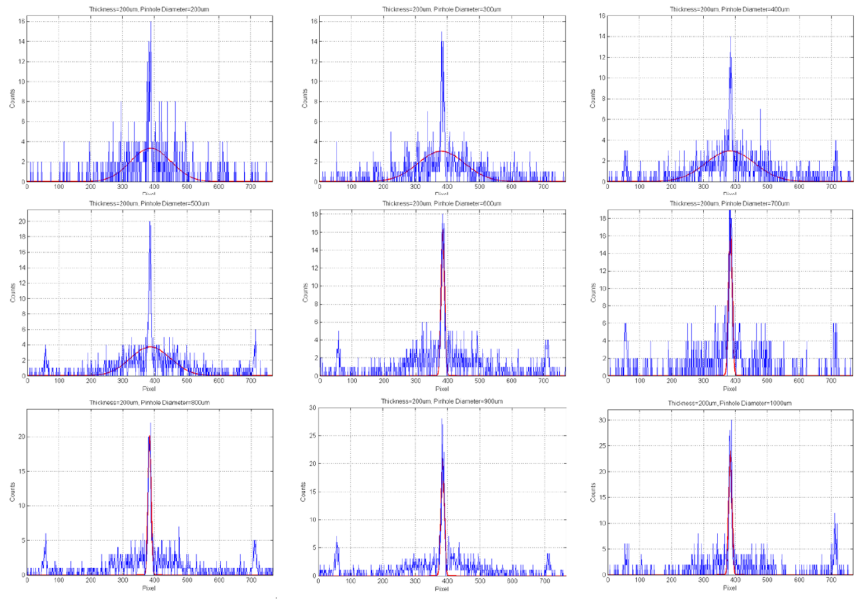

Figure 4.18 Profiles of the count distribution map as obtained for a collimator made of lead 200μm thickness with varying pinhole diameter. From top left to right, row by row, the peaks shown indicate a single seed as viewed by three detectors through three pinholes. The pinhole diameters are from 200-1000 μm in 100 μm increments. Note the low SNR for this thickness due to penetration through the thin lead collimator. Blue represents integral counts as a function of pixel distance, and red represents the automatic identification of peak values by MATLAB.

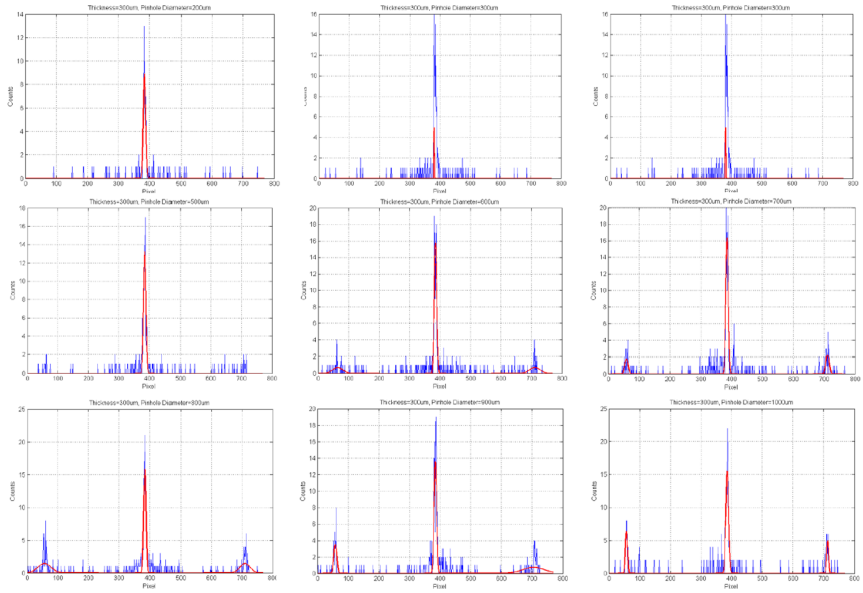

Figure 4.19 Profiles of the count distribution map as obtained for a collimator made of lead 300μm thickness with varying pinhole diameter. Compared to 200 μm as shown in Figure 4.18, there is a much higher SNR, allowing the identification of the peaks corresponding to the centre of mass of the I-125 seed.

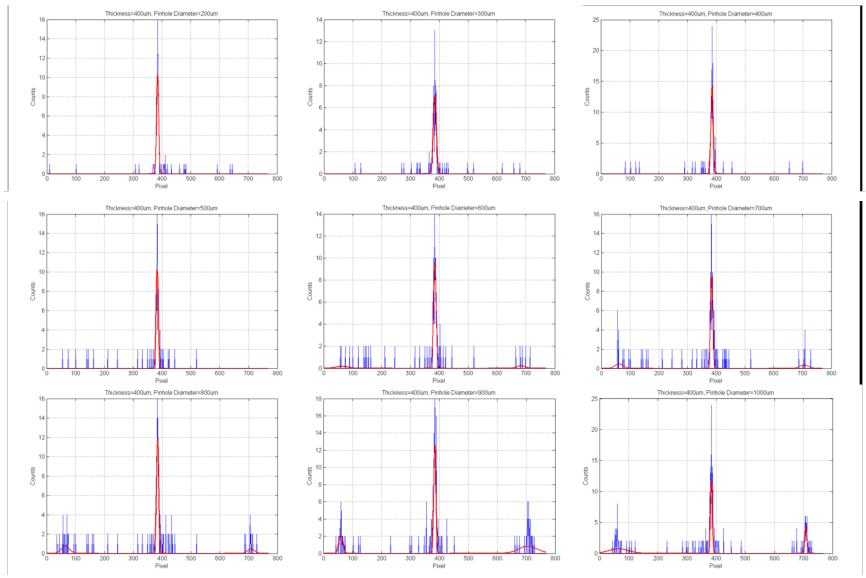

Figure 4.20 Profiles of the count distribution map as obtained for a collimator made of lead 400μm thickness with varying pinhole diameter. Similar as shown in Figure 4.19, a high SNR is achieved, however, a larger pinhole diameter is required to overcome the geometric thickness of the collimator. The outermost peaks are not visible until a pinhole diameter of 700 μm.

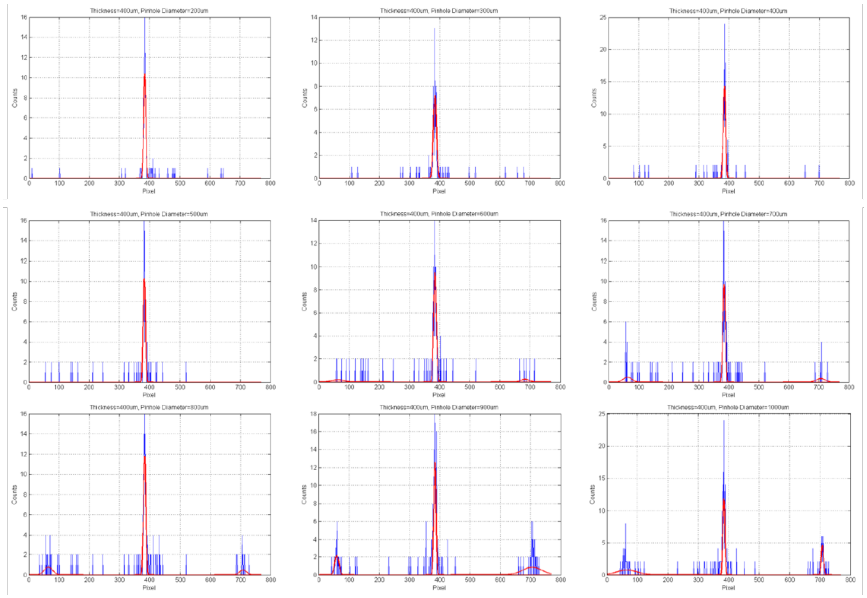

Figure 4.21 Profiles of the count distribution map as obtained for a collimator made of lead 500μm thickness with varying pinhole diameter. As shown in Figure 4.20, a larger thickness requires a larger diameter for suitable SNR and seed centre of mass identification.

4.5 Summary & Conclusion

An analytic method was employed. A point source corresponding to a 0.4 mCi I-125 source was successfully modelled in MATLAB based on geometric parameters of the BrachyView system consisting of user-defined pinhole collimator and detector parameters. Specifics of the detector system which can be modified include:

1. Collimator thickness;
2. Pinhole diameter;
3. Collimator-detector distance;
4. Number of pixels in detector;
5. Source position;
6. Source activity.

Geant4 simulations were performed to obtain a characteristaion of image quality on the Timepix detectors as a function of pinhole parameters. Energy parameters used were the same as to be expected from a typical LDR I-125 brachytherapy source, including primary photons ranging from 25-32 keV and fluorescent X-rays at 27 keV (as explained in Section 2.1.2.1). By varying the thickness of the collimator as well as pinhole diameter, an optimal thickness between 200-400 μm was found, allowing a large SNR for determination of the centre of mass of each seed projection image.

For our purposes, this allows us to use a theoretical model indicating the optimal thickness of collimator and pinhole size to obtain an optimal signal for source localisation based on the projection images obtained. While this initial model utilises a simple circular (i.e. cylindrical) pinhole, and ignores blurring and penetration issues at the pinhole edge, it is a useful preliminary indicator. Furthermore, the possibility of determination of centre of mass of each implanted seed is confirmed with the implantation of each nth seed preceded by the subtraction of background of (n-1) seeds. The centre of mass of each projection image was determined manually by operator selection.

Furthermore, it can also be used to create a reference system for calculating the expected count rate at the detector surface based on source position. When compared to the results obtained in the pinhole study in Chapter 5, there is a qualitative agreement between what is modelled and what is experimentally measured.

Future work involves undertaking further simulation to introduce higher statistics into the results. Due to the small physical size of the pinhole, and the low energy of incident photons, simulations take a large amount of time to compute before satisfactory results are obtained (a simulation consisting of 1 billion primary events yielded statistics less than 50 counts at detector surface, as shown in Figures 4.17-4.21). However, from these calculations, it is evident that the optimal thickness for the pinhole collimator is between 200-400 μm with major diameter equal to less than 1 mm, and minor diameter greater than 100 μm. Variance reduction techniques should also be employed in future work to increase precision and speed up the simu-

lation process. One example could be to pursue stratified sampling and implementing anisotropic sources to direct all primary photons to travel directly to the pinhole. However, this would not account for intra-organ scattering, which is not dosimetrically negligible.

The analytic and simulation work can be used as a reference system to calculate expected approximate experimental values and projection images on Timepix detectors. The simulation results were ultimately used as a guide for experimental manufacturing of collimator and geometrical set-up.

Chapter 5

Experimental BrachyView Feasibility Study

This chapter presents the experimental work performed using a lead collimator and single Timepix detector. Utilising real active LDR sources in plastic and gel phantoms, a proof-of-concept study was conducted, proving the feasibility of the proposed approach in BrachyView for localising implanted sources in 3D. Therefore, the localisation algorithm used in BrachyView can be tested and evaluated; initially with a small number seeds, but increasing to a more clinically realistic scenario involving a larger number of seeds.

5.1 Phantom Design

The phantom is a $60\times60\times40$ mm^3 polymethyl methacrylate (PMMA) cube. PMMA is a transparent acrylic glass compound that is often used as an approximation for human tissue, with a density of 1.18 g/cm^3. The phantom design is a simplified representation of the brachytherapy implant that utilises one main feature: the implant template coordinate system.

Figure 5.1 shows a typical brachytherapy template in which a grid system of coordinates is used to distribute the brachytherapy sources in their designated areas in the prostate according to the treatment plan. Each adjacent letter and number represents

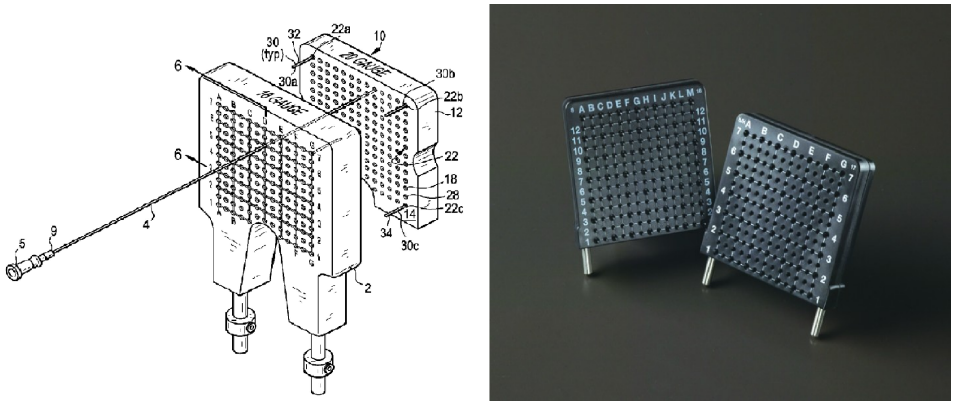

Figure 5.1 Left: Sketch of a typical brachytherapy template with needle inserted through position d6.5 (from US Patent). Right: Photograph of a disposable model as manufactured by Civco Medical Solutions (Image courtesy of Civco).

a spacing of 10 mm, with an intermediate hole located midway between at 5 mm represented by lower case letters and decimal place of 0.5.

Following the ultrasound-guided volumetric study and assessment of the required distribution of brachytherapy seeds, the implant needles are planned and ordered ahead of time. Every implant needle is pre-loaded with the number of seeds required in the specific location according to the patient-specific treatment plan and is inserted through the corresponding coordinate to be implanted through the patient's perineum (see Figure 2.11. The needle tip is guided by ultrasound imaging and the seeds deployed by the brachytherapy practitioner needle by needle. The positions in the central region around location D4 are usually left empty to avoid delivering dose to the intraprostatic urethra. The labelling of intermediate points are notated as lower case letters and decimal points, e.g. E3.5, c1, a2.5, and F5.

An alternate phantom was also designed containing a larger number of implant holes, and this was used in experiments involving a larger number of seeds, discussed in Section 5.6.

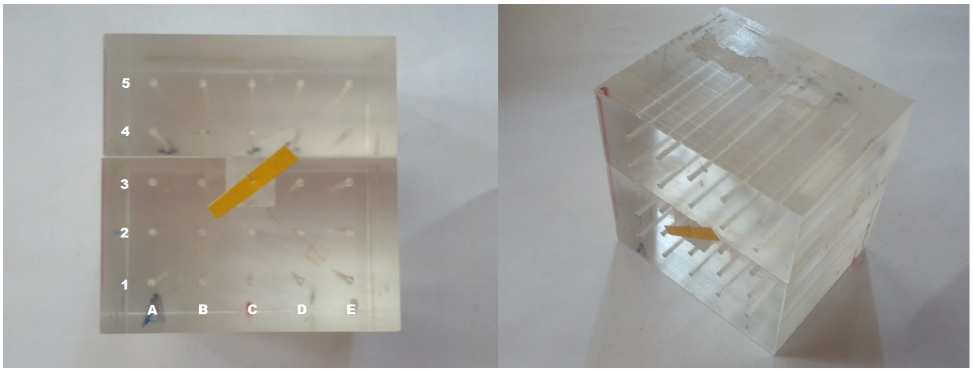

Figure 5.2 The PMMA phantom showing holes drilled for housing brachytherapy sources in experiment and the simulated grid template with pitch 10mm.

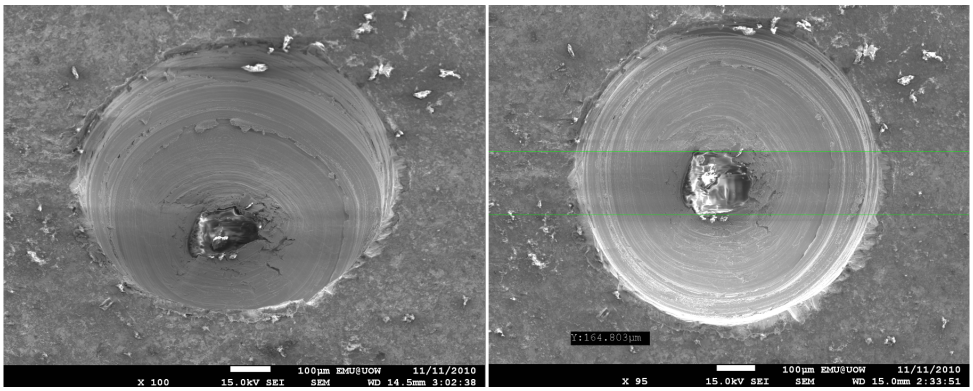

Figure 5.3 Scanning electron microscope image of lead pinhole used in experiment. The image on the right shows the inner diameter measures to approximately 180 μm. The outer diameter of the pinhole is approximately 800μm

5.2 Pinhole Collimator Design

The pinhole collimator used was developed at the Centre for Medical Radiation Physics (CMRP) and consists of a cone-shaped lead structure. It was created by inserting a stainless steel needle tip into a sheet of lead. A scanning electron microscope image of the pinhole aperture used in experiments is shown in Figure 5.3 and Figure 5.4 shows a photo of the experimental triple pinhole lead sheet collimator.

The combination of a single Timepix detector and pinhole collimator was designed to have a minimum field of view of approximately 50 mm at a distance of 10 mm

Figure 5.4 Photo of the experimental pinhole sheet used. Three pinholes spaced 14 mm apart correspond to the triple detector design of BrachyView as shown in Figure 3.5

.

given by the relation as described by Beekman et al. (11):

$$FOV \approx 2 \cdot l \cdot tan(\theta) \tag{5.1}$$

where l is the source-to-collimator distance) and θ is the angle formed by the aperture.

In this experimental study, the pinhole aperture was measured at $\pm 50.5°$, with the aperture forming the shape of a truncated cone with large face (major) diameter D, small face (minor) diameter d, and thickness T as shown in Figure 5.5). This condition was established based on the minimum distance between the inner rectal wall and the prostate, which is typically in the range between 4-10 mm. The thickness T of the lead plate is approximately 400 μm based on the parameters established in Chapter 4 which leads to the most effective attenuation of the photons emitted by the I-125 LDR sources.

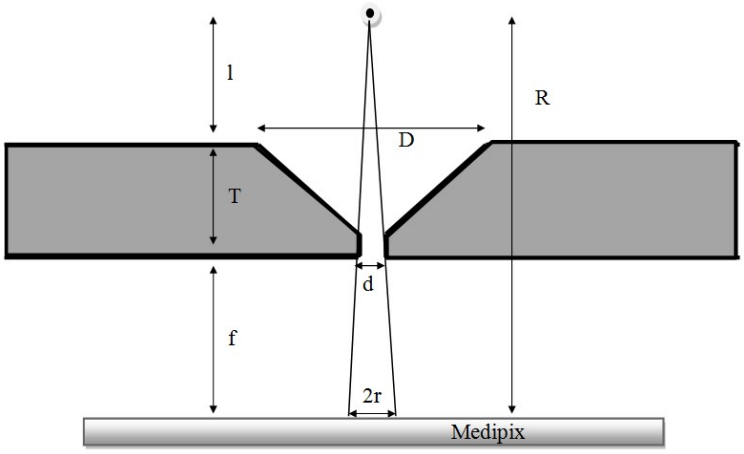

Figure 5.5 Model of the pinhole used for the design of the collimator system in BrachyView

Using the model of Figure 5.5, the count rate N can be estimated by considering the product of the portion of solid angle of a point source with activity A (decays/s) at distance R from the detector surface. The seed has been represented by a point source, identified in the centre-of-mass of the seed, since the aim of this study is the evaluation of the performance of BrachyView for the reconstruction of the seed position regardless of its orientation.

$$N = A \bullet \Omega \bullet \sigma_{Si} \tag{5.2}$$

where $\Omega = \frac{\pi r^2}{R^2}$, r is the radius of the projected area through the pinhole and σ_{Si} is the total efficiency due to Compton and the photoelectric effects in silicon detector for 27 keV gamma photons and Si detector thickness 400 μm (approximately 60% [NIST (National Institute of Standards and Technology) value]).

Considering a typical brachytherapy source with air KERMA strength 0.5 U, which corresponds to an intrinsic activity of 0.4 mCi, it is found that for an aperture of d=180 μm the expected count rate of the gamma camera exposed to a seed located at source-to-collimator distance of 50 mm would be approximately N=2700 counts/s. This calculation shows that the geometry and dimensions of the system make possi-

ble the use of the gamma camera for fast seed positioning determination, especially when only a few hundred counts are sufficient to discriminate the seed projection from the background noise (this is experimentally verified as shown in Section 5.4 as well as in simulations as shown in Chapter 4).

5.3 3D Localisation Method

The three-dimensional position of each seed is reconstructed by using a stereoscopic back-projection technique based on tracing lines between the pinholes and the centre of mass of the digitised 2D images of each seed on the detector plane. Note however, that the position of the detector inside the rectum has two major consequences in terms of image reconstruction:

1. The detector cannot be rotated around the target region and so a standard image reconstruction technique such as the multiple back-projection used in SPECT scanners cannot be adopted;

2. Due to space restrictions, the pinhole camera has a magnification factor less than 1 and therefore an imaging sensor with a high spatial resolution is necessary.

The back-projection reconstruction used for BrachyView is based on the use of 2D images generated by the incident gamma rays from the seed projected onto the sensor plane through the pinhole collimator. The pinhole is identified as the origin of the camera frame (X_{c0}, Y_{c0}, Z_{c0}).

The resulting image is the projection of a 3D object onto the detector plane assuming that each point of the object emits a gamma photon. To a first approximation, the image of the object can be represented by its centre of mass ignoring, at this stage, any information about its orientation. All images are obtained by working with the Pixelman software. Pixelman is a software package developed by the Institute of

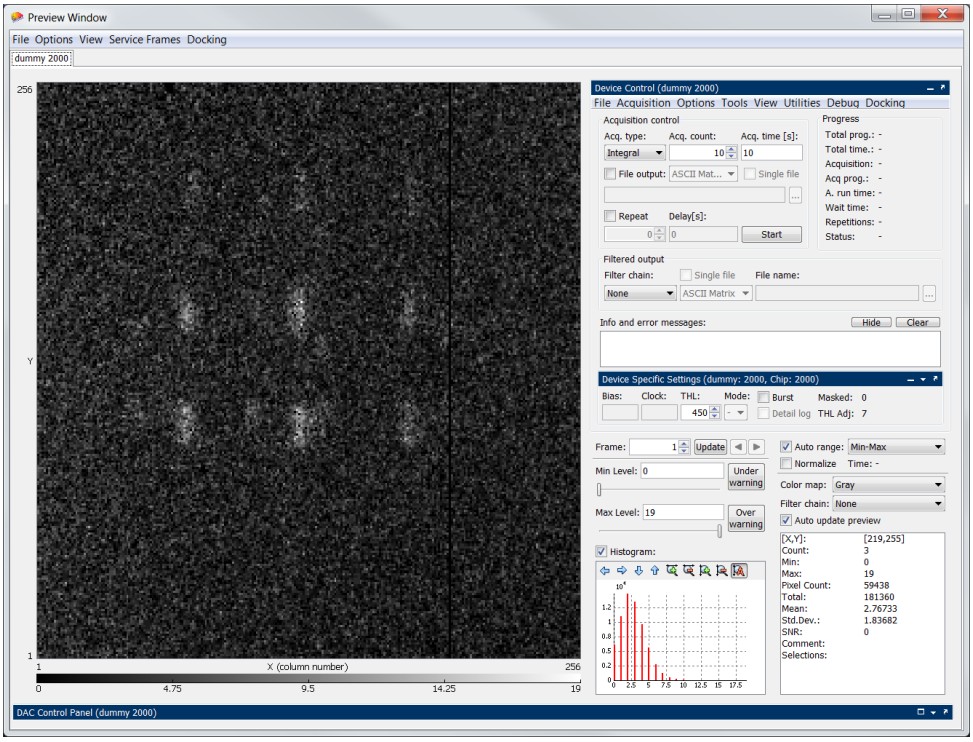

Figure 5.6 Pixelman software showing a projection image of a single Timepix detector (256×256 matrix). Data can be saved as image files (.jpg, .png etc), or as ASCII matrices. The image shown is of 20 seeds discussed in a later section.

Experimental and Applied Physics, Czech Technical University in Prague (IEAP). It supports all available Medipix2 and Timepix-based hardware. By interfacing with a USB readout (via a FITPix connector as shown in Figure 2.23, all data is displayed on-screen in real-time as shown in Figure 5.6. All the electronic settings of the attached detector chip, such as THL levels and frame length and frequency, are set using Pixelman. Data can be saved as image files or as raw ASCII matrices, with each number corresponding to one pixel of data.

By acquiring at least two images of the object from two different positions of the pinhole collimator (i.e. two different pinholes), it is possible to reconstruct the object position in real space by determining the point of intersection of the lines calculated by back-projecting from the 2D image through its corresponding pinhole. By considering the coordinates of the centre of mass of the images and the pinholes, object

localisation can be performed. Furthermore, the accuracy of reconstruction can be increased with a larger number of pinholes and projection images. For the purposes of this study, three pinholes were used in experimental measurements.

The system 'object-pinhole-2D projection' can be represented by a simple model that describes the mathematical relationship between the coordinates of the 3D point P_c in the pinhole camera frame (X_c, Y_c, Z_c) and its projection P_1 onto the image plane (x, y) as shown in Figure 5.7. This model is based on the use of an ideal camera without lenses and thus without spherical distortion.

In Figure 5.7, the image on the left represents the first projection of the seeds. Note that in this position, the seed located in position D3 is immediately blocked by the seed in position B3. Therefore, in the resulting image on the detector plane, only three of the four implanted seeds are visible. In the image on the right, the grayed image plane represents the first projection. Now all four seeds are visible on the image plane following a translation step in the Y direction (longitudinal direction) of the probe - i.e. with multiple views, all the seeds can be resolved successfully. In the case where multiple detectors are not possible, the translation can be achieved with a single detector-pinhole system, as is explained in Section 5.4.

Introducing the value f for the focal length of the set-up (i.e. the collimator-detector distance) allows us to express the geometric relationship between (X_c, Y_c, Z_c) and (x, y) by the focal length $f_x = f_y = f$, assuming no astigmatic aberration in the system (square pixel size, square pixel array, cylindrical symmetry of the pinhole) (14):

$$x = f\frac{X_c}{Z_c}, y = f\frac{Y_c}{Z_c} \tag{5.3}$$

If the origin of the image coordinate system is not in the centre of the image plane, the displacement (s_1, s_2) from the origin to the centre of the image plane is included in the projection equations, obtaining the perspective projection equation below. The

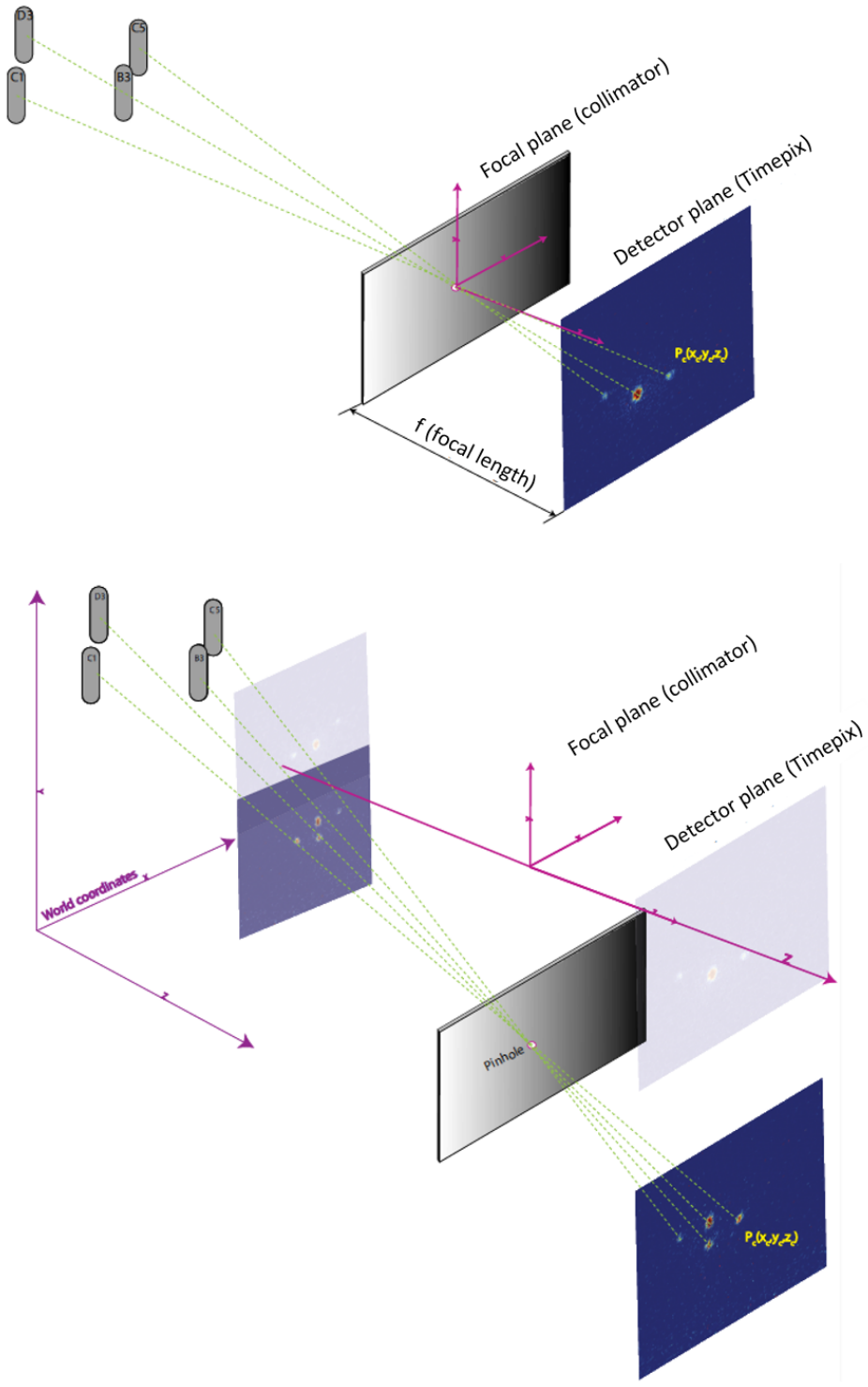

Figure 5.7 Schematic representation of the homogeneous coordinate model and reconstruction method by triangulation.

Parameter	Symbol	Value
Focal length	$f = f_x = f_y$	5.5 $\pm$ 0.1mm
Relative X translation P-to-pinhole	s_1	0
Relative Y translation P-to-pinhole	s_2	Steps of $\pm$5 $\pm$0.01 mm
2D projection image centre of mass	(x,y)	Calculated by a Gaussian fit of the pixel map

Table 5.1
Intrinsic parameters of the homogeneous coordinate model as implemented in MATLAB.

parameter s_i could represent any movement of the point P_c relative to the pinhole.

$$x = f\frac{X_c}{Z_c} + s_1, y = f\frac{Y_c}{Z_c} + s_2, z = Z_c \tag{5.4}$$

The previous relation can be reformulated using the projective geometry framework:

$$(\alpha x, \alpha y, \alpha)^T = (fX_c + s_1, fY_c + s_2, Z_c)^T \rightarrow \overline{P_1} = H\overline{P_c}, \tag{5.5}$$

where $\alpha = Z_c$ is a homogeneous scaling factor, and H is the intrinsic conversion matrix composed of the parameters which characterise the pinhole-imaging plane apparatus in the camera frame.

The above model was implemented in MATLAB and intrinsic parameters were set with the values used for the experimental set-up as shown in Table 5.1.

Rays are drawn from the projected seed image on the image plane (centre-of-mass projection) through the centre of the corresponding pinhole. This process is repeated for each time the pinhole/detector is moved relative to the source. Since skew lines in 3D do not necessarily intersect, the seed coordinate P_c is taken to be the midpoint of the shortest chord joining the two projected rays.

This method creates a dataset of 3D coordinates of seed positions within the prostate gland. The next crucial step is to make this data clinically relevant. Although the integration of the two devices in a single instrument is challenging from an engineering

standpoint, the co-registration of the datasets is a relatively straightforward task. By relating ultrasound data and Timepix-pinhole data via a common spatial coordinate frame, a co-registration can be performed. This method (albeit with CT data, but the concept remains the same) is discussed in Section 5.6. Note also that TRUS and BrachyView can be used separately; TRUS for volumetric studies and planning, and BrachyView for seed localisation (such as a dual-probe approach as described by Ali et al. (69).

5.4 Pinhole Experiment Set-up

Seed position reconstruction techniques have been tested with the use of a $60\times60\times40$ mm^3 PMMA prostate phantom. Parallel channels for housing of the I-125 seeds were drilled into the phantom following the grid template used in LDR TRUS-guided brachytherapy procedures (as shown in Figure 5.1).

For this proof-of-concept study, a single Medipix2 with imaging area 14x14 mm^2 and a single pinhole lead collimator was used. The phantom was attached to a motorised stepper, and translated relative to the pinhole/detector system in order to achieve multiple images of the same seed distribution. In this experiment, five pinhole locations above the imaging plane were modelled by using five separate projections. The schematic and a photo of the experimental set-up are shown in Figures 5.8 and 5.9.

A configuration of four seeds (Model 6711 I-125 Oncura/GE Healthcare, Princeton, USA) with strength 0.05 U was placed in positions B1, C2, B3, and A4 of the phantom (see Section 5.2). Images were acquired for 3 seconds at 50 frames/s. This was used to evaluate the spatial resolution of BrachyView and estimate the effective diameter of the pinhole collimator. The seeds were positioned in three different rows for three main reasons:

1. Evaluate the effect of the source to collimator distance (SCD);

2. Evaluate the projected image quality of two seeds positioned simultaneously:

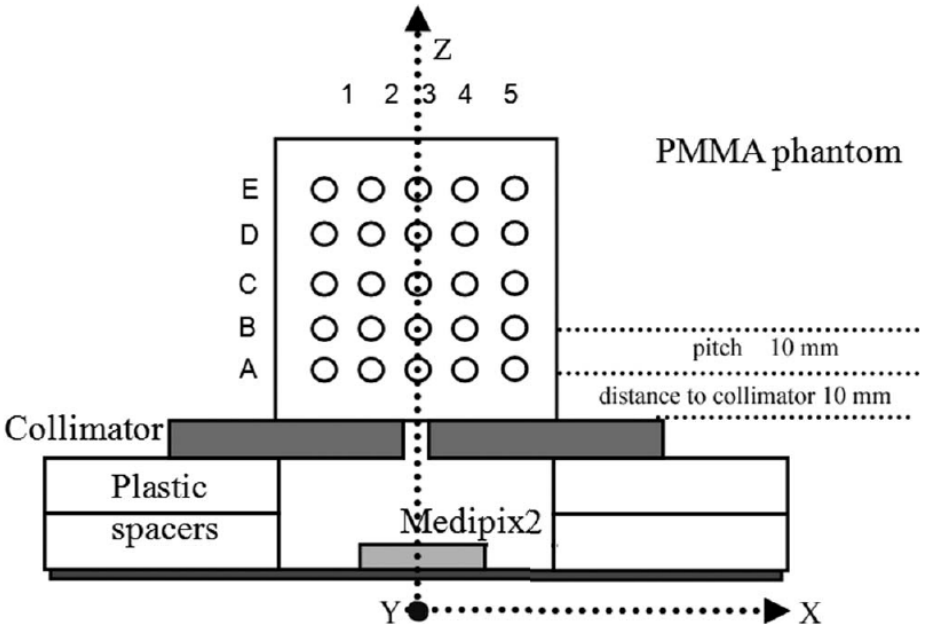

Figure 5.8 Model of the pinhole used for the design of the collimator system in BrachyView.

one in B3 (close to the detector, and hence bright), and one in C2 (far from the detector and hence weaker);

3. Verify the extension of the field of view when a seed is placed in the periphery position (for example, A4).

The spatial resolution and effective diameter of the pinhole (d_{eff}) were evaluated assuming a Gaussian fit of the projections of the seeds onto the Medipix2 detector imaging plane. Due to the alignment of the detector relative to the phantom, the numbers in the Y-direction correspond to the column numbers of the Medipix2, which are perpendicular to the long axis of the seeds. In this case, the seeds appear horizontal on the projected image generated by the detector.

Note that the activity of seeds used in experiment are 10 times less than normal in clinical practice. Therefore the time required to obtain necessary imaging statistics would be much faster in a real patient implant.

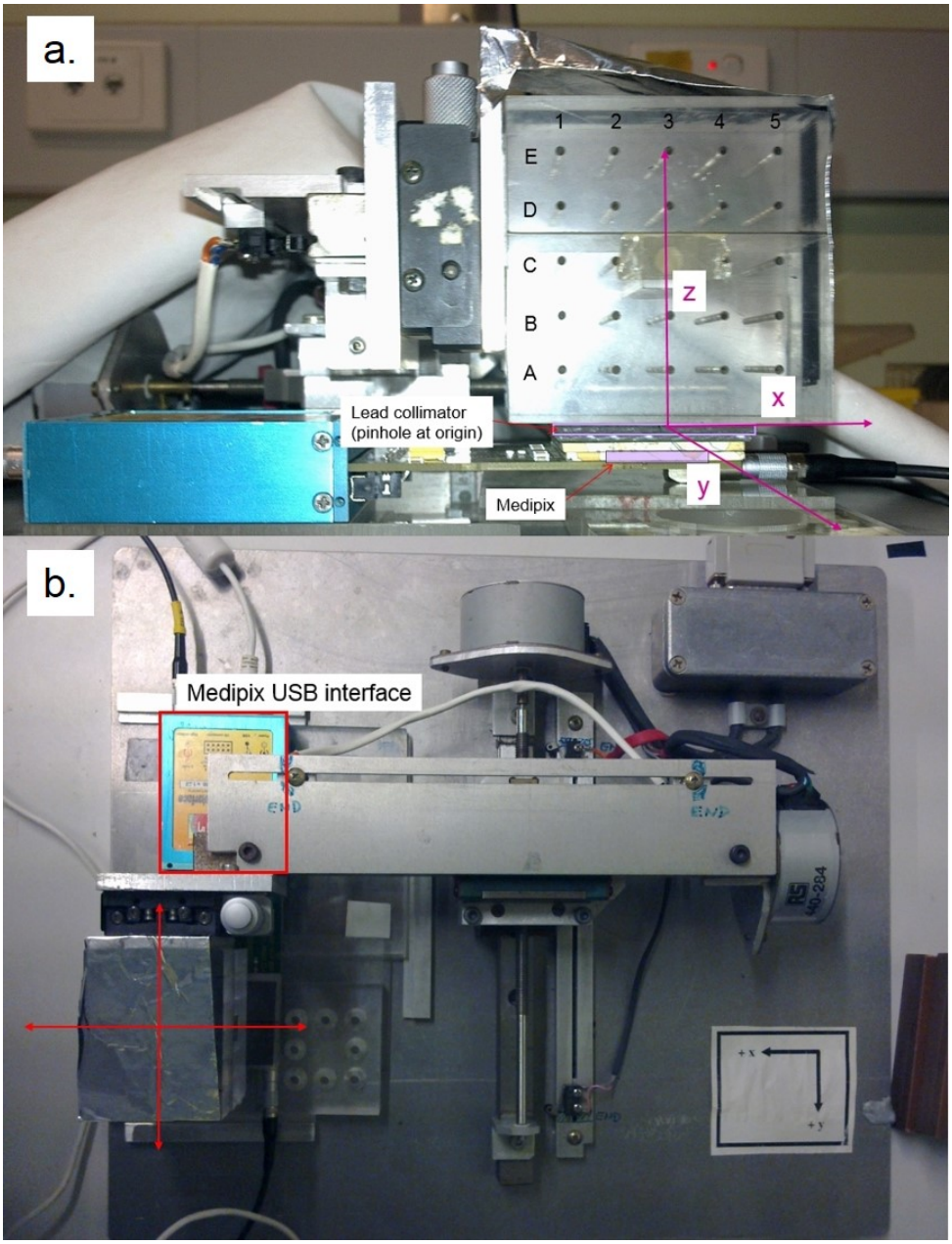

Figure 5.9 Photo of the experimental set-up showing PMMA phantom attached to motorised stepper. (a) shows the anterior view including the grid template designed to mimic a simplified prostate brachytherapy implant grid template. (b) shows the superior view including the motor stepper system movement directions used to simulate the presence of multiple detectors.

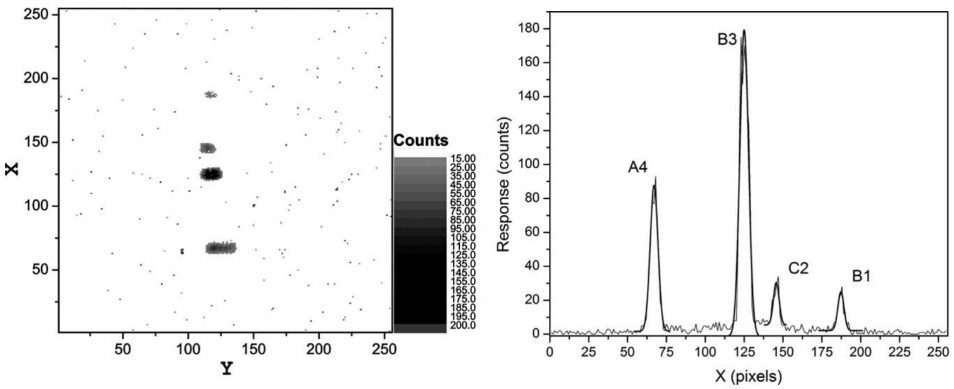

Figure 5.10 (a) Response map of BrachyView to four seeds placed into positions B1, C2, B3, and A4 of the phantom, and (b) the response profile at column Y=120 and fit by Gaussian distribution for calculation of the spatial resolution FWHM.

5.4.1 Resolution Evaluation

Before considering the 3D localisation of the active sources in the phantom, the resolution capabilities of the pinhole were investigated. Figure 5.10 shows the response map (image plane) of the system with four seeds in position. The response function can be represented by a plot by selecting one of the pixel columns (perpendicular to the X direction). For example, in Figure 5.10(b), the position Y=120 was selected to create the intensity profile. The intensity distribution of the counts in the pixels along the X direction can then be used to calculate the spatial resolution. Taking the pixel size and the focal length into account, the effective diameter of the pinhole can therefore be determined.

The precision of 3D position reconstruction can be defined by the combination of the transverse and the longitudinal accuracy. Transverse accuracy ϵ_{xy} is the degree of closeness of the reconstructed position of the seed to the expected value in the XY plane (parallel to the collimator plane). This can be obtained by the back-projection of the centre of mass of the projection image through the pinhole. This quantity is related to the spatial resolution achievable in the plane of the detector, (R_p), and it depends on the dimensions of the pinhole, (d_{eff}), in the pinhole camera resolution R_t.

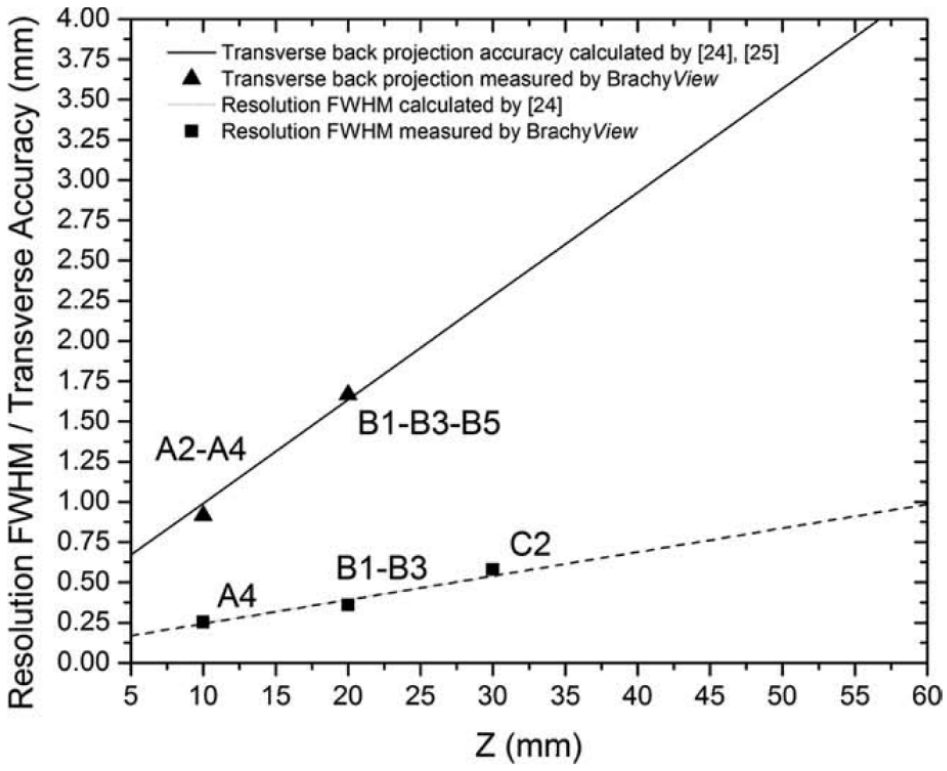

Figure 5.11 Comparison of the FWHM values obtained from the experimental response map of the BrachyView (solid squares) and transverse accuracy in the XY plane (solid triangles) for different Z positions of seeds and predicted by the model from Beekman and van der Have (14) and Marks and Brady (15).

The spatial resolution R_p as a function of the SCD and the overall transverse accuracy ϵ_{xy} are plotted in 5.11 (c) (dashed and solid line, respectively). ϵ_{xy} matches the experimental data for a value of the effective diameter of the pinhole (d_{eff}) equal to 350 μm.

$$\epsilon_{xy} = \sqrt{R_p^2 + R_t^2} = \sqrt{\left[\left(\frac{l}{f}p\right)\right]^2 + \left(\frac{d_{eff}(l+f)}{f}\right)^2} \tag{5.6}$$

Equation 5.6 is derived from geometric considerations and is entirely defined by the camera parameters: p is the detector pixel size, l is the SCD, d_{eff} is the effective pinhole diameter and f the focal length. The result obtained by Beekman and van der Have (14) is confirmed also by the work of Marks and Brady (15) based on the 3D Fourier transformation of intensity maps of the source projected by a pinhole collimator. The comparison of the transverse accuracy calculated by Equation 5.6 and measured by BrachyView is plotted in Figure 5.11.

Experimentally, Marks and Brady (15) constructed a pinhole camera with a 300 μm diameter pinhole. The 3D data sampled was obtained by capturing the intensity of the source volume behind the pinhole as a function of transverse camera position. The model developed by Marks and Brady (15) also allows the calculation of the accuracy along the Z direction based only on the fundamental camera parameters:

$$\epsilon_z \approx \frac{l^3 \cdot d}{f^2 \cdot s_2} \tag{5.7}$$

where s_2 is the increment used for translation of the camera relative to the source. The longitudinal accuracy of BrachyView calculated by this model ranges from $\pm$0.2 mm at 10 mm SCD, and up to $\pm$6 mm at 60 mm SCD (corresponding to the superior and anterior sides of prostate gland). These values indicate an accuracy range well within acceptable clinical expectations for an effective brachytherapy implant for all sizes of the prostate gland.

Some further examples of images obtained of fully loaded rows are shown in Figure 5.12.

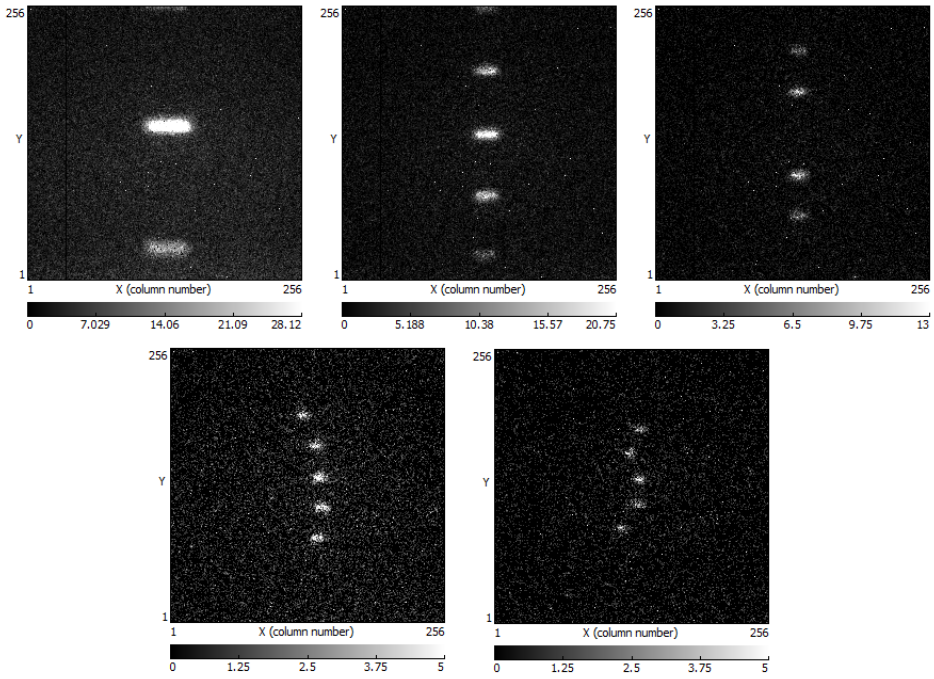

Figure 5.12 Rows A-E contain 5 positions each according to the phantom design as shown in Figure 5.2

5.5 Feasibility Study of 5 Active Sources

Using the set-up as shown in Figures 5.8 and 5.9, the reconstruction algorithm was employed to reconstruct the 3D position of the five seeds. Five active sources of intrinsic activity 0.4 mCi were placed in the phantom at positions A2, A4, B1, B3 and B5, within the field of view of the detector plane. The phantom was then translated at 5 mm increments in order to obtain the separate projection images necessary for 3D position reconstruction. The projection images were analysed to obtain 2D coordinates of the centre of mass, and each end of the seed, to create a 3D reconstruction of each seed and its corresponding active source length. These results were then compared to expected positions as considered from their positions in the PMMA phantom.

The seeds were placed in different positions in the XZ plane within the phantom, with the same Y value. The position of the seeds was chosen to test two parameters that

were identified as having potential negative effects on the reconstruction technique:

1. Blurring of the image and increasing of the background counts generated by scattered and penetrating photons through the lead collimator. This is particularly significant when the seeds are in close proximity to the collimator (seeds located in rows A and B);

2. Evaluate the image generated by seeds blocked by other seeds, i.e. the configuration with one seed in B1 and one is A2 is of interest because B1 is masked by A2 in some of the projections. This is the so-called screening effect.

Reconstruction was carried out through the use of five projections corresponding to a translational shift of the phantom at distances of -10, -5, 0, 5, and 10 mm from the origin in the Y direction. The first image was taken with the centre of the detector aligned with the phantom in the position Y= -10 mm. Each successive image was taken at a 5 mm incremental shift of the detector-pinhole set-up towards positive Y. This technique mimics the use of a multiple pinhole collimator and a detector surface equivalent to a multiple Medipix2 configuration. The projection images obtained are shown in Figure 5.13.

The technique of translating the single detector/pinhole system is illustrated in 5.14.

By determining the centre of mass of each seed projection image, as well as the corresponding edges of each seed, the position of the implanted active I-125 source is calculated in the 3D coordinate system and compared to the expected positions in the PMMA phantom. The calculated results are shown in Figures 5.15, 5.16, and 5.17.

The accuracy of 3D coordinate reconstruction decreases with the distance of the source from the collimator (SCD), however the centre of the seeds placed at row E corresponding to 60 mm SCD can still be fully resolved and localised with an accuracy of approximately 3 mm (see Figure 5.18).

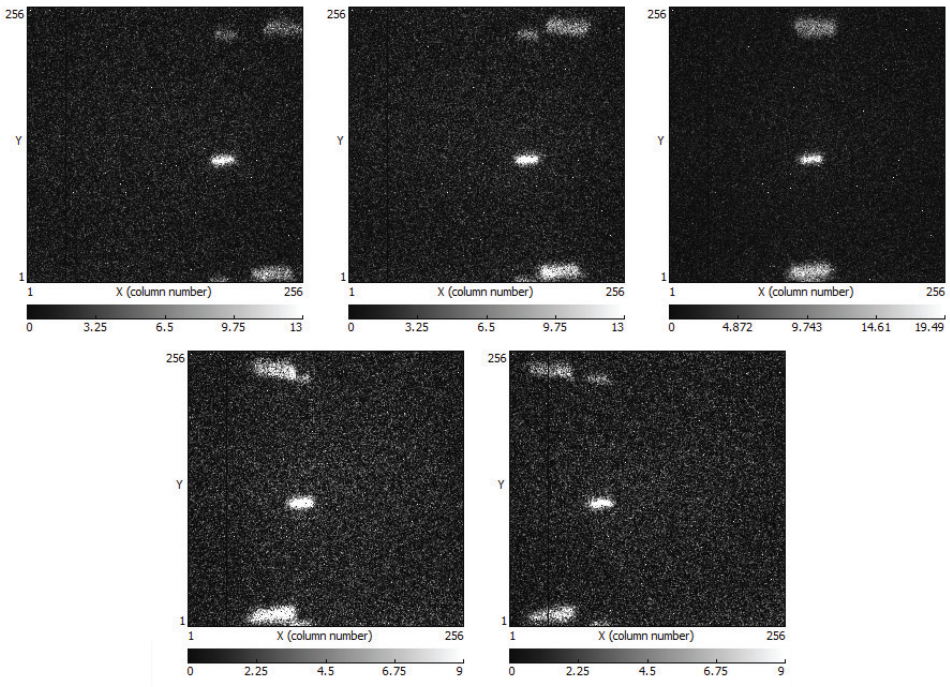

Figure 5.13 Projection images showing 5 implanted seeds at positions A2, A4, B1, B3, B5. The shape of each seed is clearly visible. Note that in the third image at the top, the seeds in positions B1 and B5 are blocked from view by seeds in row A. Each view is taken at 5mm increments along the Y-axis.

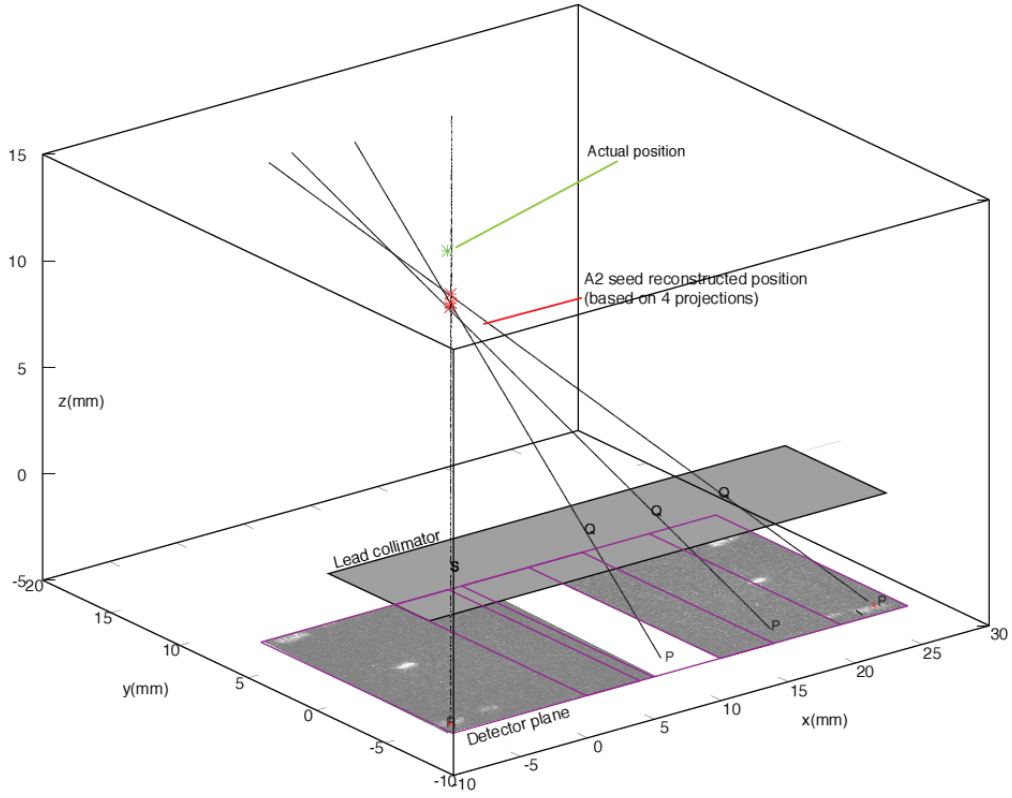

Figure 5.14 Reconstructed seed positions for seed A2 shown in three dimensions. The green star represents the expected position and the red stars represent the reconstructed position based on different views through pinhole positions Q and S at 0, 10, 15, and 20 mm as translated here in the X direction.

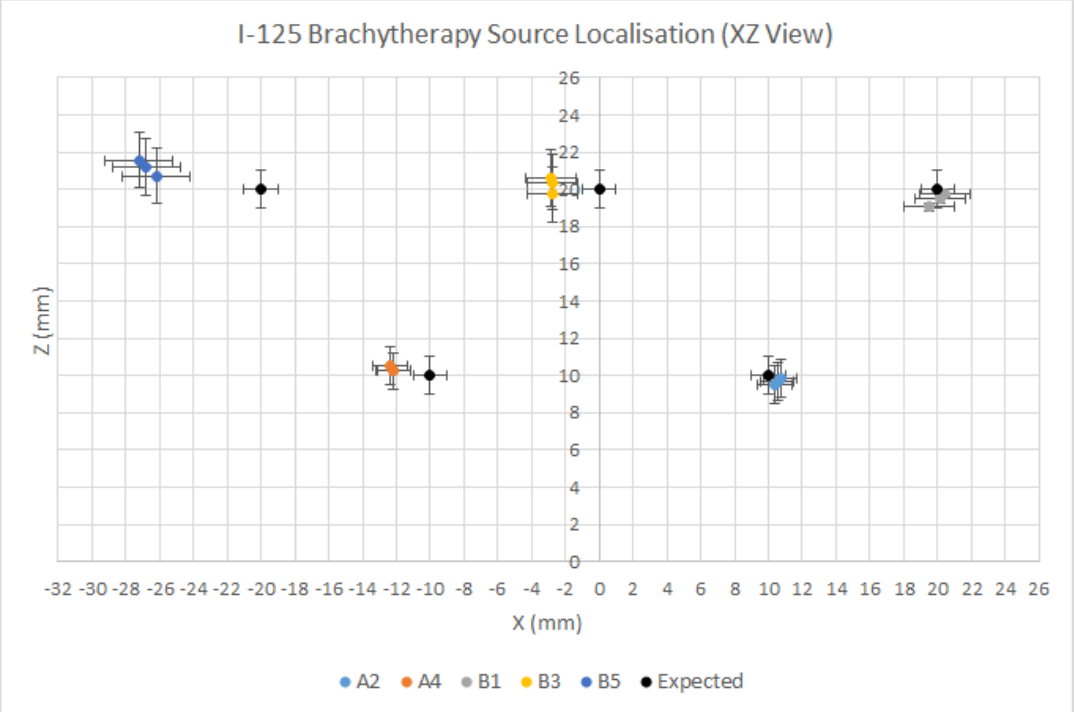

Figure 5.15 Reconstruction of the five seeds in PMMA phantom showing one particular perspective. The XZ view corresponds to the anterior surface of the phantom.

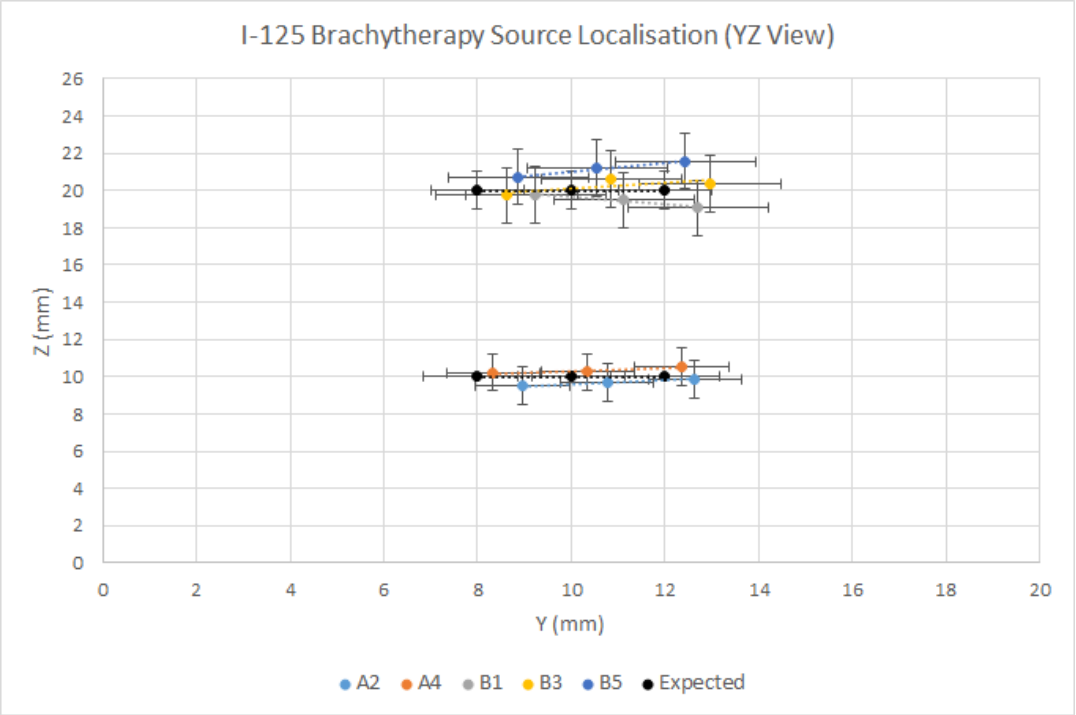

Figure 5.16 The YZ view corresponds to the longitudinal view of the phantom (i.e., side-on).

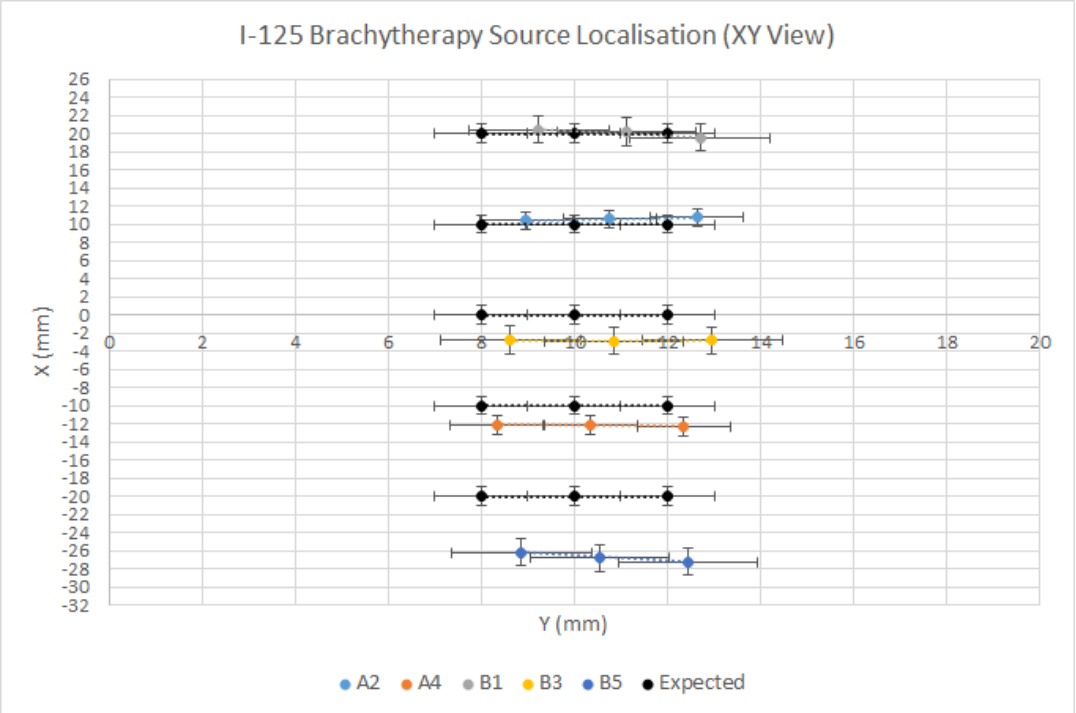

Figure 5.17 The XY view corresponds to the superior view of the phantom (i.e., top-down).

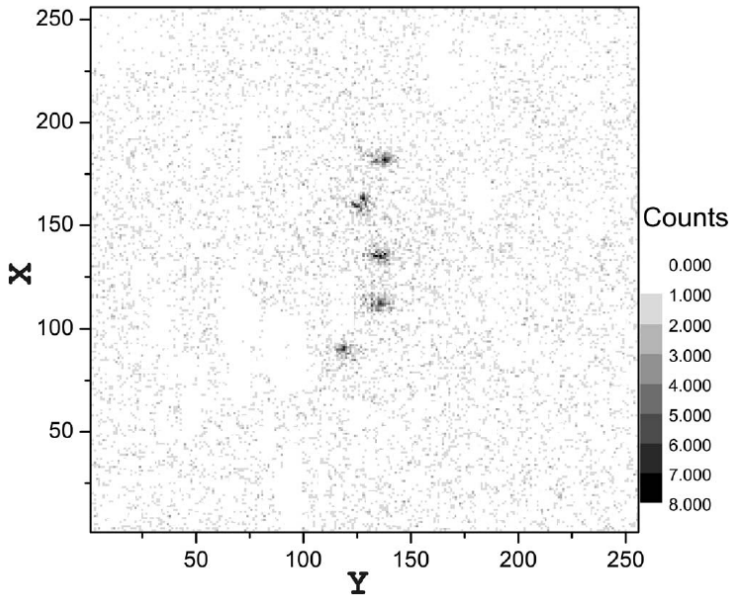

Figure 5.18 Medipix response map of five seeds implanted at positions E1, E2, E3, E4 and E5. Note that the shape of each seed is no longer visible, but the centre of mass can still be resolved, allowing for use in 3D reconstruction of seed position.

These results show that 3D reconstruction of I-125 seeds using a pinhole camera inserted into the rectum is feasible with some limitations dictated by the specific set-up used in these experiments. The main parameters characterized in this work are the transverse and longitudinal resolution of the camera.

The transverse spatial resolution measured at low SCD is in the sub-millimetre range and matches the requirements for accurate localisation of the source. On the other hand, for a 60 mm SCD the resolution is approximately 3 mm which seems to be inadequate for accurate position reconstruction of the seeds. This limitation can be addressed by the employment of a tungsten pinhole collimator manufactured by laser etching techniques which will reduce the effective pinhole diameter down to 150 μm (real pinhole diameter size down to 100 μm). The estimation of the count rate N will still be acceptable with 2700 counts/s but the transverse resolution will be substantially improved (2 mm transverse resolution at SCD of 60 mm, accordingly with the Marks and Brady (15) model described in Equation 5.6).

The longitudinal resolution is, by comparison, very robust. It is affected only by the focal length (α_1/f^2) which therefore must be determined very accurately. Data in Figure 5.17 show that the effect of an uncertainty of 100 μm on the focal length generates a variation (vertical error bars) of the seed reconstructed position in Z of less than 1 mm. The horizontal error bars are calculated by the model for the transverse accuracy of Equation 5.6). The model predicts the uncertainty obtained in the experimental data and confirms the importance of accurate manufacturing of the pinhole collimator to optimize the 3D reconstruction accuracy.

All the parameters have been investigated assuming a linear source embedded in the titanium shell and its projection is simplified by the identification of the center of mass of the seed image. This approach should still be valid for other designs of brachytherapy seeds, such as those with their radioactive material embedded in small beads encapsulated within the titanium shell. Photon scattering in the Ti shell of the seed will smooth the effect of the discrete distribution of the radioactive material inside the seed especially at high SCD and the approximation of the seed projection profile by a Gaussian fit should still be possible.

5.5.1 Summary & Conclusion

Studies using a high spatial resolution silicon detector for miniature in-body pinhole gamma camera have identified an opportunity for dynamic IO treatment planning in permanent prostate brachytherapy. A preliminary characterisation of the BrachyView concept and reconstruction technique has been carried out by the use of a single Medipix2 and a Timepix sensor coupled with a single pinhole collimator. The seed position reconstruction method is based on triangulation of the image map of the seeds projected onto the imaging surface through several pinholes.

Proof of the feasibility of this approach was carried out using Model 6711 I-125 seeds placed at different locations in a PMMA phantom. The method demonstrates the feasibility of the 3D reconstruction of the seed centre of mass position with an accuracy higher than 1 mm for seeds located within 20 mm of the collimator. A model

for estimating the 3D reconstruction accuracy based on the fundamental parameters of the camera has been implemented and validated by measurements.

The main advantage of this technique we would like to highlight in this work is the possibility to co-register the 3D dataset obtained by the pinhole camera with the images of the prostate obtained by the TRUS probe. The overall dimensions of the pinhole gamma camera are small enough to be integrated within a 25-30 mm diameter cylindrical probe which still represents an acceptable size for use with patients.

Further developments of the BrachyView project will attempt to improve the quality of the pinhole collimator using tungsten laser etching technology, manufacturing of the multiple-chip Medipix detector on a single substrate and to integrate the high spatial resolution gamma camera with a TRUS probe. Future work will also include the development of a reconstruction method based on the use of seed pattern recognition to identify the orientation of the seeds and software development for the imaging of multiple seeds in a realistic clinical scenario.

The use of imaging techniques from the nuclear imaging field such as a coded aperture pinhole collimator combined with the well-known geometry of the distributed activity in a seed would simplify the reconstruction of around 100 seeds typically implanted into a prostate for a realistic treatment plan. This new device could condense prostate permanent implant brachytherapy into a single procedure whereby volumetric study, intraoperative dynamic treatment planning, and post-implant dosimetry are all performed by a single device.

5.6 Using 20 Active Sources and Comparison with CT

An additional study was completed to test BrachyView's compatibility with a larger number of seeds implanted into a prostate phantom. Using a stepper motor system mounted on a portable optical table, the phantom was incrementally loaded with active seeds up to 20 individual sources. These sources were located at positions B3,

C2, c3.5, D2, E2, and F3 as shown in Figure 5.19, using a similar PMMA phantom as described in Section 5.1. The implant template used in this experiment was the CIVCO LDR sterile 17GA Grid for 1.3 mm diameter open-ended needles and consisted of a grid of 11x11 holes with 5 mm spacing in between each as shown in Figure 5.1. The detector used for this study was a Timepix.

The seeds (Model 6711 from Oncura) had an air KERMA strength of 0.5 U corresponding to an intrinsic activity of 0.4 mCi, as is typical for a standard LDR prostate brachytherapy procedure. The distribution of the seeds was designed to mimic a typical treatment plan, leaving a gap around the theoretical position of the intraprostatic urethra. Due to the large number of active sources being used, this work was done in a shielded CT room with under the guidance and advice of the brachytherapy practitioners at St George Cancer Care Centre.

The needles were implanted following the clinical procedure of implantation starting from the top left corner and progressing from left to right: c3.5, d3.5, B3, F3, C2, D2, E2. Thus the images acquired by the single Timepix detector showed the progression of the implant as it occurred. This allowed us to test the system's capability to resolve multiple seeds as the number of total implants gradually increased.

The time interval between implantation of two needles is approximately one minute (for an experienced oncologist) which represents the time frame available for the acquisition by the gamma camera of the photons emitted by the set of seeds in one needle. This time frame, with full active seeds can produce clear projections of each seed as shown in the results.

A single Timepix device was used in this study with a single pinhole in a sheet of lead 0.5 mm thick. Using a high accuracy motor stepper (a similar set-up as described in Section 5.4), the Timepix-pinhole system was translated at 15 mm increments in order to mimic the presence of a true multi-chip assembly, as discussed in a previous section. The pinhole used in this study was a lead cone pinhole with major diameter of 800 μm and minor diameter of 400 μm.

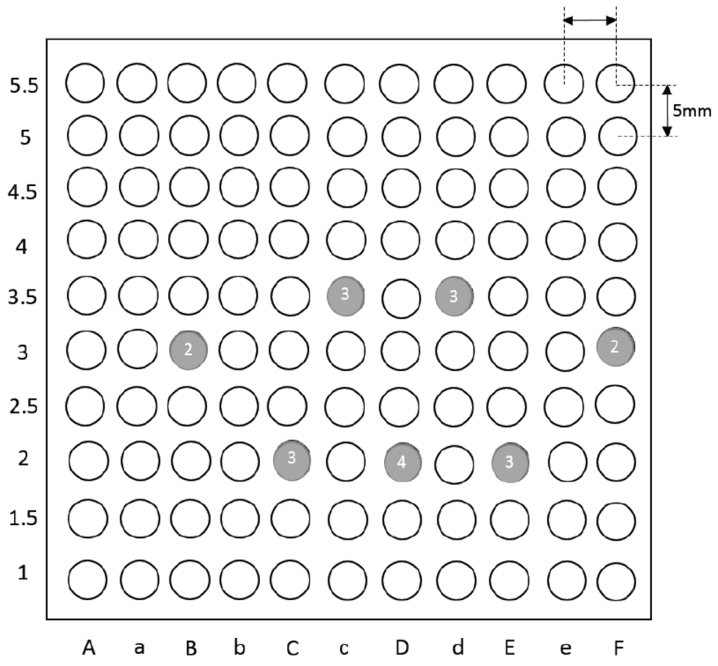

Figure 5.19 Schematic showing $60\times60\times60\text{mm}^3$ PMMA phantom and the distribution of 20 active seeds, indicated by the grey circle. The number of seeds implanted in each position are indicated by the white numbers.

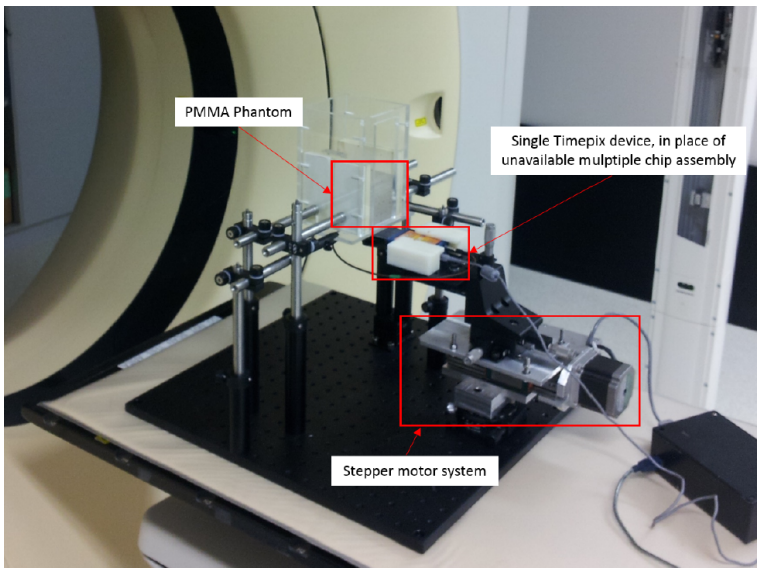

Figure 5.20 Photo of the experimental for multiple seed set-up showing single Timepix device attached to motorised stepper

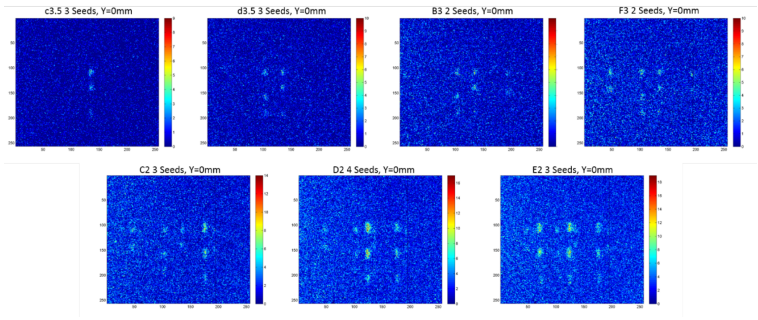

Figure 5.21 Projection images showing the progression of the implant as each needle is loaded into the platform. Images are shown in a colour scale corresponding to counts obtained.

The single Timepix was aligned with the phantom by positioning a single active seed in the D2 position at the centre of the phantom and aligning the projection of the seed with the central pixel of the detector corresponding to position (128,128). The coordinate sysem of the gamma camera has its origin defined as the position of the central pinhole, which is aligned with the central pixel of the imaging plane.

Using the reconstruction method as discussed in Section 5.3, the positions of the 20 seeds implanted in the PMMA phantom were found within 1-2 mm accuracy. The projection images obtained at the first position corresponding to Y=0 mm are shown in Figure 5.21, with each progressive needle implant showing a gradual increase in counts and a corresponding increase in background noise from scattered events. Note however, that the seed projection image and shape can be easily resolved against the background even up to the last implant of the 20th seed. The order of the needle implants correspond to the locations: c3.5, d3.5, B3, F3, C2, D2, and finally E2 containing 3,3,2,2,3,4, and 3 seeds in each needle location respectively.

The images in Figure 5.21 show a single Timepix and pinhole. By tiling each single image together, a 'single acquisition' image can be considered, showing what a true multiple detector assembly would be able to visualise. Considering there is space between each detector, corresponding to the translation required to cover the field of view, this can be represented as shown in Figure 5.22. The centre of mass of each

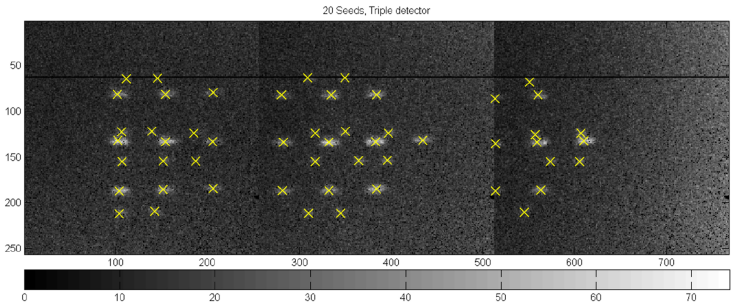

Figure 5.22 Triple detector image obtained by positioning each single projection image. By knowing the lateral shift of each detector, the multiple chip assembly can be accurately modelled and the localisation of the centre of mass of each seeds projection image can be used to calculate the 3D localisation of each seed within the phantom.

seed is indicated by the yellow crosses.

Once the pinhole measurements were completed, a full CT scan using a medical CT scanner was performed to obtain a benchmark reference for seed position reconstruction. The scanner used was a Siemens CT SOMATOM Emotion 120kV with 0.8 mm resolution (brain mode). For the purposes of this study, the CT scan was performed with a slice width of 0.8 mm, which is much smaller than used in typical medical scans, allowing us to obtain 3D reconstruction results with a higher accuracy.

The CT results were visualised to emphasise bone density; i.e. reduced contrast with no saturation for high electron density materials such as iron, steel and titanium in comparison to PMMA. This set-up reduces the saturation of the grey scale and the effect of the artefacts generated by the interaction of the X-rays from the CT-scan with high density materials in the experimental set-up, such as the pillars of the optical bench.

For co-registration with the CT scanned images, a different coordinate system was proposed. By taking the two outermost seeds (positions B2 and F2) and obtaining an average (i.e. the middle distance) between these two positions, a new origin is defined as lying on the line between. This was proposed as an alternative to using a single seed as a reference marker, which could lead to unknown degrees of uncertainty

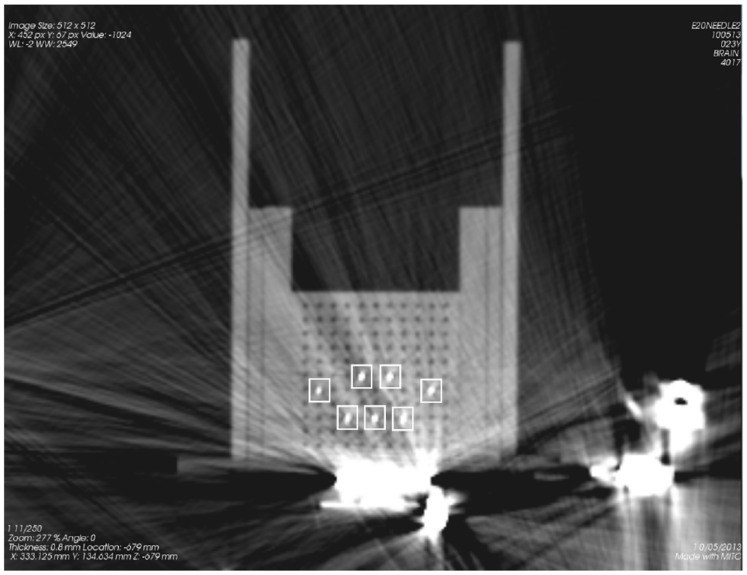

Figure 5.23 CT scan showing the distribution of the 20 seeds at the baseline slice (seeds deposited at greatest Y depth in the phantom). Each CT slice corresponds to 0.8 mm thickness.

around that origin. This method of co-registration of images is similar to that of the point-to-point registration as described in previous studies, for example by Polo et al. (42) and Gong et al. (46).

In this way, the Timepix-pinhole results are able to be checked against and co-registered with the CT reconstructed seed positions, and the approach for BrachyView in use of a multiple seed scenario verified.

A slice of the CT scan is shown in Figure 5.23.

The results of the source localisation are shown in Figures 5.24,5.26, and 5.25 as orthogonal projection views. The results are shown as a comparison between the Timepix-pinhole system and the CT reconstructed data.

The co-registration is performed as follows. By defining the midpoint between the two outermost seed positions (B3 and F3) as the origin of the coordinate system, the dataset containing information for the reconstructed seed positions can be compared between those obtained by the gamma camera BrachyView and those from the

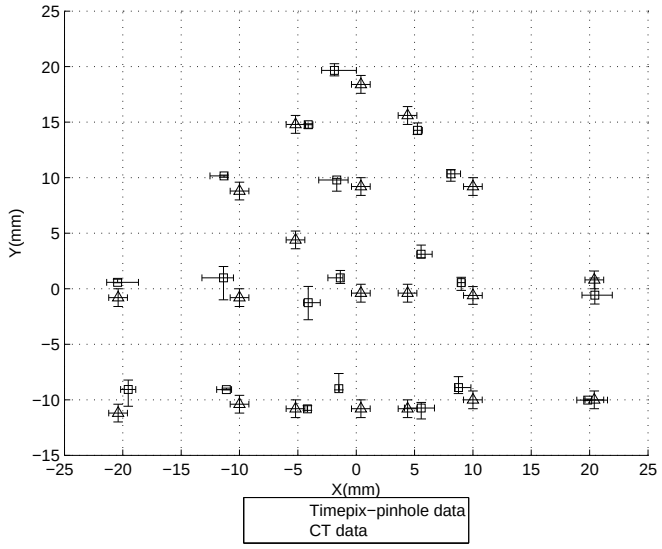

Figure 5.24 Reconstructed 3D coordinates for implanted seeds shown in orthogonal projections, comparing values obtained from the Timepix-pinhole system, and the clinical CT scan, in superior view (corresponding to XY).

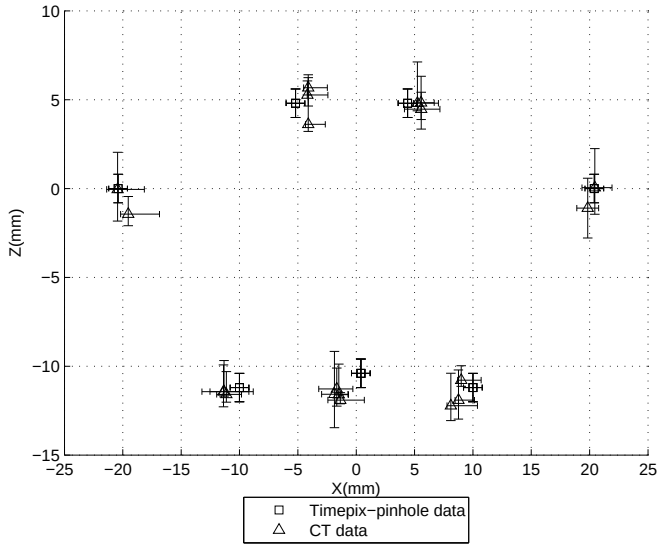

Figure 5.25 Reconstructed 3D coordinates for implanted seeds shown in orthogonal projections, comparing values obtained from the Timepix-pinhole system, and the clinical CT scan, in superior view (corresponding to XZ).

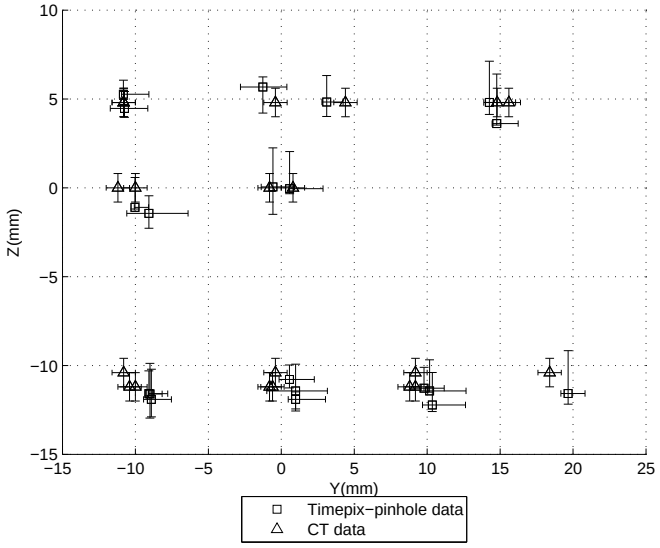

Figure 5.26 Reconstructed 3D coordinates for implanted seeds shown in orthogonal projections, comparing values obtained from the Timepix-pinhole system, and the clinical CT scan, in superior view (corresponding to YZ).

clinical CT scan.

An additional visualisation method has been developed to allow a better perception of the accuracy of the implantation by the physician who may be unfamiliar with the use of the Timepix detector. The method consists of the use of the seed centre of mass reconstructed by BrachyView to generate a 3D model of the seed population (indicated by the red seeds in Figure 5.27). The model is based on known dimensions and shape of the implanted seeds. Figure 5.27 shows the model calculated with the centre of mass of the seed population co-registered with the 3D CT of the phantom reconstructed from the DICOM slices. A selective high CT number filtering has been applied to isolate the titanium shells of the seeds from the surrounding water-equivalent materials. This fiducial-based rigid registration method which will be effective in this application not only for the CT post-implant verification but also for the TRUS dataset. The co-registration is discussed above.

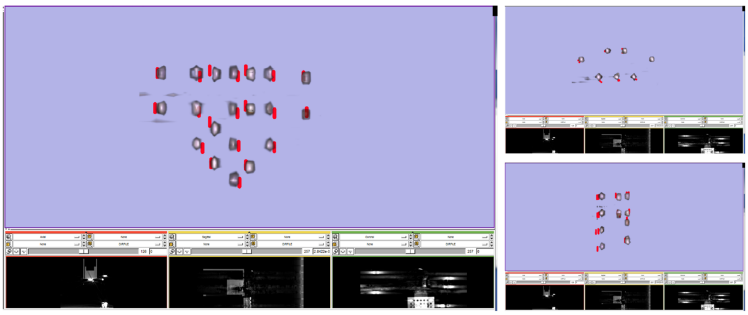

Figure 5.27 3D reconstruction and co-registration of the BrachyView analytical model of the seeds and the seeds as reconstructed using the CT scans.

5.6.1 Background Noise Consideration

Increase of the background radiation with the number of seeds implanted can be taken into account using a subtraction methodology: after each needle implantation, the frame (N) is recorded and acquisition of the new map restarted (frame N+1). Counts of the frame N are then subtracted to the frame N+1. The net count map is then used to identify the seeds implanted during the frame N+1. The subtraction procedure follows the implantation routine and maintains the background counts at an almost constant level despite the increase of the number of seeds implanted. The results of this analysis are shown in Figure 5.28.

5.7 Gel Phantom Study

Finally, measurements using a number of active seeds implanted into a gel phantom allowed us to evaluate the efficacy in another step towards a realistic clinical scenario. The PMMA phantom studies as described in previous sections prove the feasibility of the application of BrachyView for use in brachytherapy source localisation, but these phantoms are rigid and do not represent a malleable organ accurately.

By extending these feasibility studies to the use of a soft tissue-equivalent gel phantom, and by using a TRUS probe as used in actual PPB procedures, we are able to

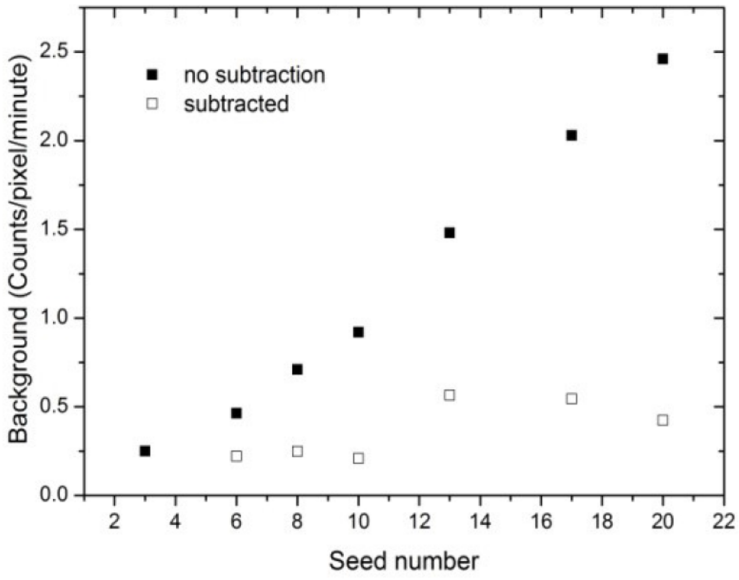

Figure 5.28 Background measurement with and without previous frame subtraction. Frame subtraction guarantees a better signal to noise ratio in a multiple seed scenario.

evaluate the system's capability to localise sources displaced due to deformations in the soft tissue arising from the presence of the TRUS probe. The gel phantom used is a tissue-equivalent medical ultrasound phantom developed by Computer Imaging Reference Systems (CIRS). It is also used in the experimental study described in Chapter 7.

The aim of this study as shown in Figure 5.30 is to reconstruct the position of active seeds implanted into the gel phantom by two methods: conventional CT scanner and Timepix single sensor. The conceptual approach is similar to that as described in Section 5.6, but in a medical tissue-equivalent phantom featuring anatomically accurate features. Lastly, the DICOM dataset acquired by the CT and the TRUS will be co-registered with the 3D dataset acquired from the Timepix.

The set-up is composed of two systems:

1. TRUS stepper stager (supplied by SGCC) mounted on the plastic stager designed at CMRP to accommodate the gel phantom. The TRUS is inserted into

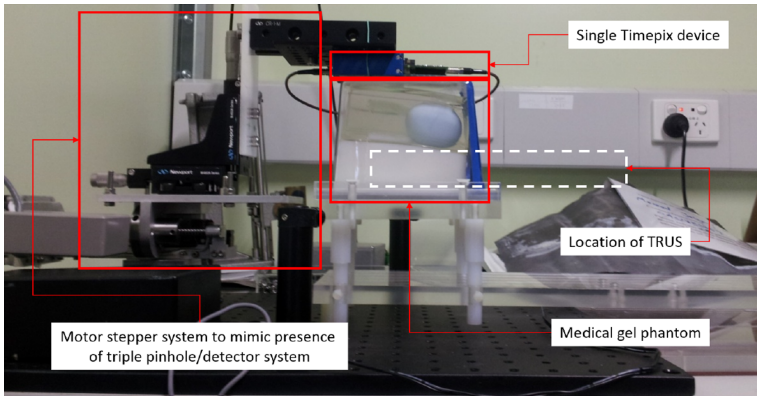

Figure 5.29 Photo of the experimental set-up for measurements in gel phantom.

the rectal cavity, allowing space for placement of the brachytherapy needle grid template;

2. On the backside of the phantom is located a motorised stepper motor with the Timepix/FITPix/pinhole system mounted upside down to sit flush with the superior surface of the phantom. The position of the Timepix is recorded with respect to the TRUS probe for post-processing and geometrical reconstruction.

The entire system as shown in Figure 5.30 is placed on the CT patient couch and scanned after seed implantation for direct comparison. A full three-dimensional co-registration with the ultrasound dataset will further allow for full volumetric and dosimetric analysis using BrachyView. These measurements were performed with the assistance of the Prostate Cancer Institute at St George Cancer Care Centre.

5.8 Software Development

A GUI was developed in MATLAB to assist in the calculation of the seed coordinates in 3D from projection images in three-dimensions. This was developed in MATLAB's built-in GUIDE (GUI Development Environment) framework. The end-goal of this part of the project is to develop a Java-based plugin for incorporation into the Pixelman software.

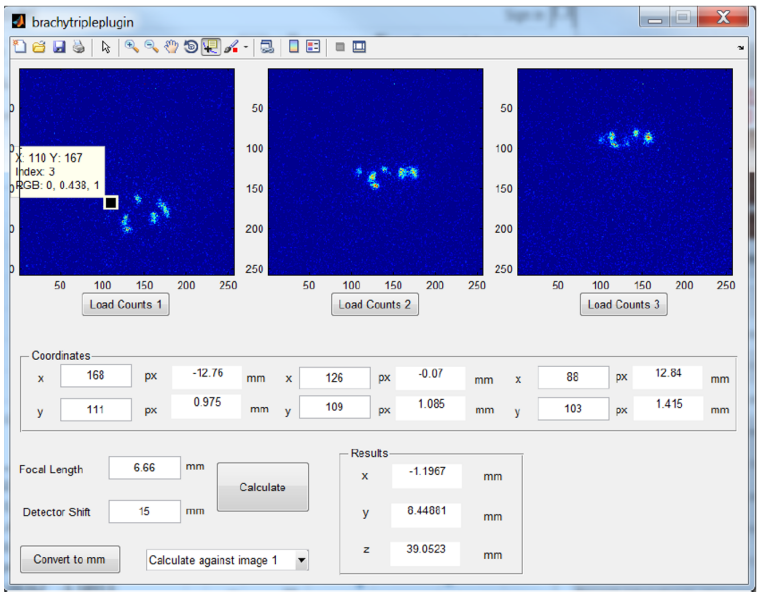

Figure 5.30 Screenshot showing the BrachyView software developed to handle Timepix data and calculate coordinates in 3D.

Currently, the GUI exists as a post-processing procedure for analysis of data acquired prior to loading the program. Once the data is loaded as a matrix of counts, the user examines the data and manually selects the seed projections and inputs their corresponding X and Y coordinates. The GUI converts these values to mm to obtain the position of each individual seed in three dimensions. This procedure is repeated seed by seed for the user to analyse externally.

5.9 Summary & Conclusion

In-phantom measurements have been performed to show the capabilities of BrachyView to resolve the implant positions within 1-2 mm of expected positions in a multi-seed scenario. Seed localisation can be performed in real-time allowing for doctors to adjust accordingly with sub-mm accuracy. While 20 active seeds are still short of the full clinical implant (between 60-120 active sources), the high resolution capabilities of the in-body gamma camera across multiple projections shows that it is able to resolve sources even at the maximal distance of 50-60 mm away from the pinhole

collimator.

The use of a single pinhole-detector set-up requires a motor stepper system which introduces systematic errors in positioning of the detector and accurate localisation of the pinhole coordinates. The actual position of the pinhole may differ from the assumed position, which manifests an error in the reconstructed positions. With the next stage of development towards a fully functional multiple chip assembly, the need for an alignment and moving apparatus would be obviated, therefore introducing a well-defined, shared rigid coordinate system as well as removing the uncertainty in pinhole location relative to this system.

The introduction of the BrachyView imaging system into the prostate LDR PPB procedure will provide a valuable tool for ITDP, as this study has shown its capability to resolve and localise seed positions within 1-2mm of expected positions in real-time. By informing physicians of this data, adjustments and improvements can be made on the PPB implant as it occurs, therefore improving patient outcomes. Furthermore, its use as a post-implant dosimetric tool has been verified by comparison with CT scans, showing a high accuracy without the need for external imaging equipment.

Chapter 6

Computed Tomography in Prostate Brachytherapy

CT imaging of the prostate brachytherapy implant is an essential part of the PPB procedure and is used as a means of post-implant dosimetry quality assurance. It is proposed that by using the Timepix detector, BrachyView can be used as a novel in-body imaging plane for use in CT reconstruction of the prostate implant. This chapter describes the feasibility test of a phantom study using tomographic methods for 3D reconstruction of LDR seed position.

6.1 Timepix in Tomography

The Medipix family of detectors has had extensive application in the use of many tomographic studies, in particular for entomological and botanical studies. It is particularly suited for measuring attenuation profiles, and so when combined with the rotational projection images in tomographic set-ups, an accurate 3D reconstruction can be obtained. The usefulness of Timepix in measuring an attenuation profile is highlighted by the work of Jakubek (10).

Medipix detectors equipped with an appropriate sensor chip (Si for small or light objects, e.g. soft tissue, GaAs or CdTe for larger or heavier objects) are well-suited for CT measurements. The extremely high resolution pixel-by-pixel measurements

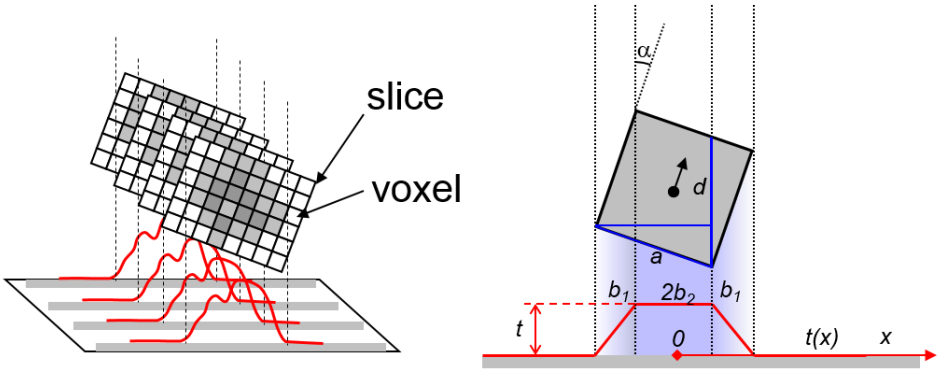

Figure 6.1 Concept of pixel-by-pixel attenuation measurements in Medipix necessary for tomographic reconstruction of sample being imaged. The attenuation profile (indicated by the red line and $t(x)$) for each slice can be calibrated to a corresponding thickness of the sample.

can be used for the measurement of intensity profiles corresponding to attenuation through the sample. The measured projections are linearised as a per pixel signal-to-equivalent-thickness calibration. The number of counts per pixel can be calibrated directly to a thickness measurement of the physical sample by appropriate methods (this is often done by a beam-hardening correction, or 'linearized signal to equivalent thickness' as outlined by Vavrik and Jakubek (70)). The concept of a pixel-by-pixel measurement of a sample is shown in Figure 6.1.

6.2 CT Measurements in PPB

Once the brachytherapy implant has been completed, the patient is taken to the CT room located elsewhere in the hospital. This multi-step procedure allows for a post-implant dosimetric assessment, but does not allow for intraoperative adjustments of the implant.

However, it is proposed that by using BrachyView, already in place in the rectum, a simple external X-ray source such as a C-arm X-ray unit or similar, can be used to provide the incident X-rays. By rotating the X-ray source around the patient's prostate, a set of projection images corresponding to attenuation profiles can be ob-

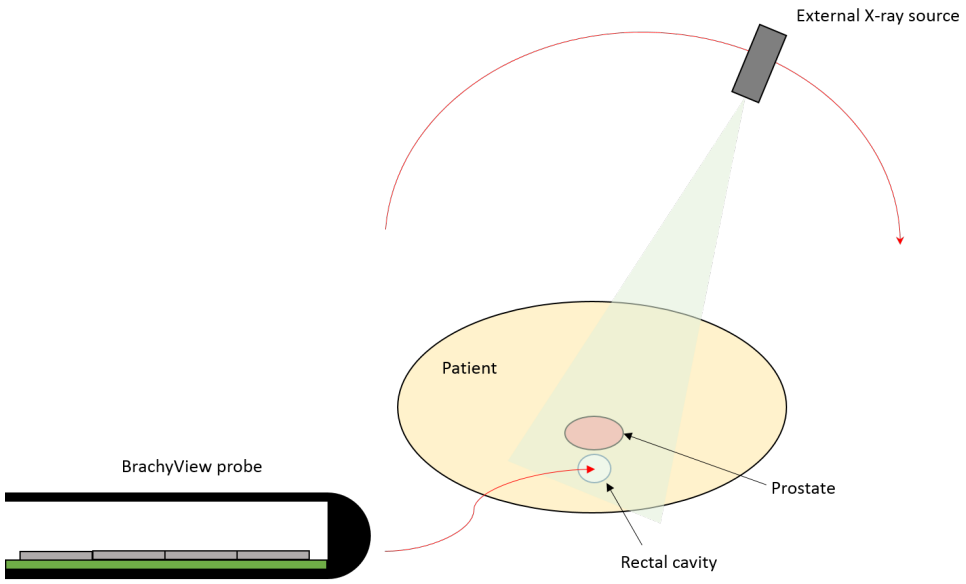

Figure 6.2 Concept for using BrachyView as an in-body imaging plane for tomography measurements. Image not to scale.

tained and used for tomographic reconstruction.

Standard CT reconstruction is done by means of a mathematical function known as the Radon transform (71). A Radon transform in two dimensions is the transform consisting of the integral of a function over a series of straight lines. In terms of a tomographic measurement, this consists of attenuation data across a range of angles θ. This information is necessary for any tomographic reconstruction.

Mathematically, the Radon theory states that any unknown function can be reconstructed from an infinite set of its projections. Therefore, if a function f represents some unknown density of a material, then the Radon transform represents the scattering data obtained as the output of a tomographic scan. An inverse Radon transform can then be performed to obtain an image reconstruction. This is the underlying principle allowing tomographic reconstruction to occur.

The visual representation of a Radon transform is commonly known as a sinogram due to its graphical appearance resembling a series of blurred, superimposed sine waves of varying amplitude and phase. The columns of R contain the attenuation

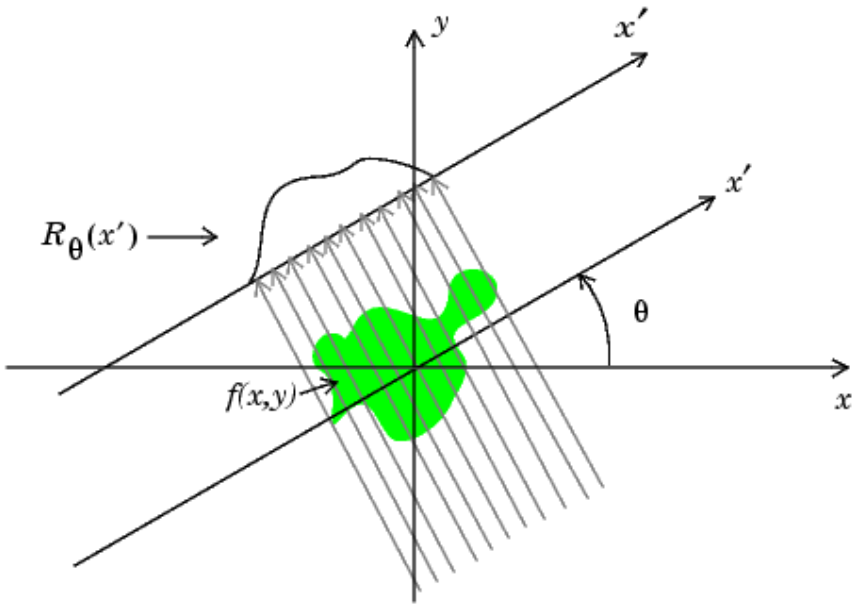

Figure 6.3 Concept of the Radon transform. Image courtesy of Hayden (16).

data for each angle in the entire dataset of projections used.

A typical tomographic reconstruction consists of the following steps:

1. Measure attenuation profile using an external X-ray source and imaging plane;
2. Repeat measurement of attenuation profiles around patient with projection data taken at every angle iteration;
3. Perform a radon transform of the data to obtain sinograms;
4. Backprojection techniques of density reconstruction (i.e. attain tomographic slices).

Consider for example the mathematical body the Shepp-Logan phantom. As illustrated in Figure 6.4 (72), an accurate representation of the original phantom can be reconstructed from the Radon transform. This is known as a filtered back-projection (FBP) technique (71), whereby every point in the projection image is back-projected

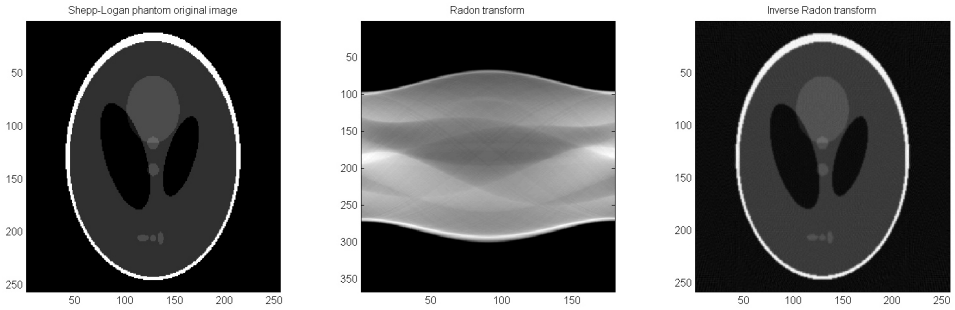

Figure 6.4 Left: Mathematical phantom used to illustrate principle of Radon transformation. Centre: Radon transform of the Shepp-Logan phantom over 180° of projections. Right: The inverse Radon transform of the sinogram in centre.

along a line for all θ. When enough back-projection angles are performed, a reconstruction of the density within the sample can be accurately determined.

In order to obtain the images necessary for tomographic reconstruction, the set-up at the Institute of Experimental and Applied Physics (Czech Technical University in Prague) is shown in Figure 6.5.

For this study, a collection of dummy seeds were used. As in the pinhole study, these are Model 6711 I-125 seeds (supplied by IsoAid, LLC), but inactive. Therefore, no dose considerations are made when taking these tomographic measurements. However, due to the pixel-to-pixel thresholding capabilities of the Timepix, it is proposed that additional dose from the active sources can be filtered out through post-processing, or even during measurements, as a way of subtracting background as described in the pinhole study. Furthermore, subtraction of background can be done spectroscopically by selection of the 22-35 keV energy window in order to block counts from the seeds themselves.

Rather than rotating the external X-ray source around the sample as is typical in a CT scan, the sample (in this case the PMMA phantom with implanted dummy seeds) is attached to a rotation table and rotated relative to the stationary imaging plane. This provides us with the rotation projection images required. Note that this does not

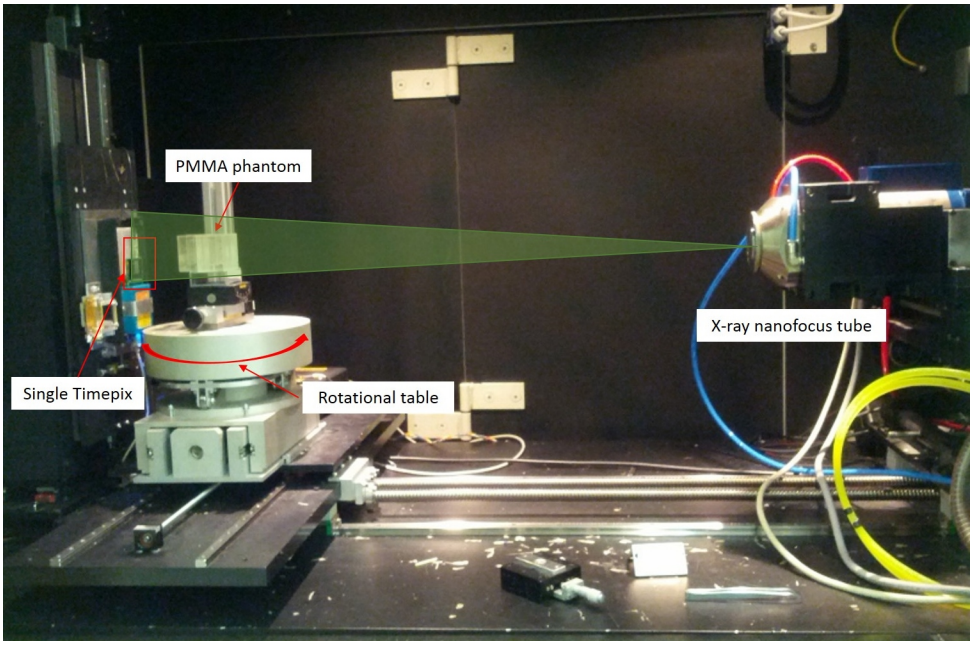

Figure 6.5 Experimental set-up of tomographic measurements using single Timepix device available at the time.

Figure 6.6 Photo of dummy brachytherapy sources used in tomographic measurements.

truly correspond to the patient/external X-ray source set-up, which would involve a stationary detector plane relative to rotational motion of the X-ray source. However, for the purposes of this thesis, a preliminary evaluation of the tomographic application of BrachyView is all that is required. Future work will investigate this process further, through the use of tomographic laminography techniques for example.

The process for obtaining a tomographic reconstruction is as follows:

1. Align the sample with the detector plane, ensuring it is horizontally parallel relative to the pixel plane;
2. Minimise magnification factor by minimising source-object and object-detector distances;
3. Obtain a minimum of 181 projection images. The extra angle is to serve as a back-up in case artifacts appear in the first image, which are not uncommon;
4. Perform a beam hardening correction for the raw data;
5. Check that the axis of rotation is in the centre of the Timepix image; for a frame of 256×256 pixels, this corresponds to column 128 of the detector. If not, some padding of the images can be used to correct this (typically as a shift of a few pixels). Padding refers to an artificial correction whereby a small number of pixel columns is interpolated into the frame to shift the experimental image to the required axis of rotation (i.e. around column 128).
6. Create sinograms;
7. Perform tomographic reconstruction.

The tomographic reconstruction can be performed by filtered back projection as discussed above. To evaluate this technique, the MATLAB function iradon (inverse radon) is used.

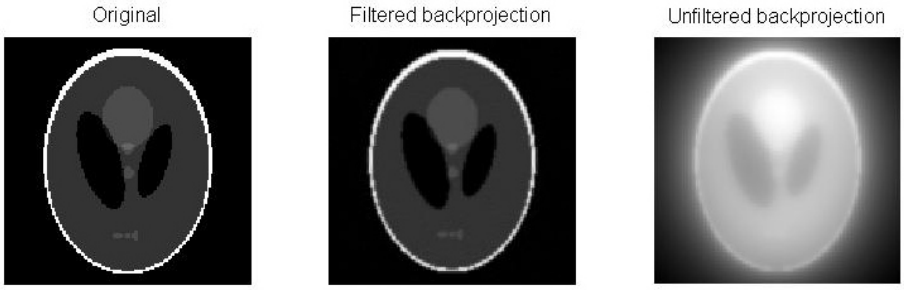

Figure 6.7 Comparing filtered and unfiltered backprojection images on the standard Shepp-Logan phantom in MATLAB.

6.2.1 Inverse Radon Transform

Given a set of projection data presented as two-dimensional sinograms, the inverse radon function is able to reconstruct the image. It utilises the filtered back-projection algorithm, where the filter is designed to work directly in the frequency domain and then multiplied by the fast Fourier transform (FFT) of the projections. The projections are zero-padded to a power of 2 before filtering to prevent spatial domain aliasing and to speed up the FFT.

The reconstructed image in tomography measurements is not a standard image as shown in Figure 6.7, since the projection images are based on the attenuation of X-ray radiation incident on the physical sample. In this case, the image being reconstructed is actually a cross-sectional slice through the physical sample (i.e. the slices necessary for 3D reconstruction). The thickness of this slice corresponds to the voxel space as defined by the physical parameters of the detector and the reconstruction algorithm itself.

An important fact of the inverse radon reconstruction is that it reconstructs an image based on parallel beam projections through the sample. In parallel beam geometry, each projection image is formed by combining a set of line integrals through an image at a specific angle.

Figure 6.3 illustrates how parallel beam geometry is applied in tomographic measurements. Note that there is an equal number of n emitters and n detectors. While this is the ideal case, it can be successfully approximated by using a point source at a large enough distance. Each detector measures the radiation emitted from its corresponding emitter. The attenuation gives a measure of the integrated density or mass of the object. This corresponds to the line integral that is calculated in the Radon transform.

The filtered backprojection algorithm forms an approximation to the image I based on the projection in the columns of R (the Radon transform). By increasing the number of projections used (θ), a more accurate reconstruction can be obtained.

In some cases, noise can be present in the projections. Many windowed filters are available in inverse radon. However, another common method of working with noisy data is by using iterative reconstructive algorithms.

6.2.2 Iterative Reconstruction

Filtered back projection is known as an analytic form of tomographic reconstruction. It yields fast computation thanks to the fast fourier transformation techniques employed, yet it is valid for an infinite number of projections and noiseless data. Furthermore, it is known that analytic models cannot involve more complex physical models.

A viable alternative to an analytic method is an iterative method, which is based on repetitive improvements of the reconstructed image to achieve maximum correspondence to its computed projections obtained from measurement.

Iterative algorithms have several advantages over analytic methods such as FBP:

1. The computation time at each iteration cost is approximately the same time as two FBPs;

2. Convergence is fast and stable even in the domain of a small number of pro-

jections (limited data) and noisy data (bad data);

3. Can handle general geometries such as varying pixel and voxel size, non-uniform voxel shapes, non-uniform pixel shapes, missing projection angles, missing angles etc;

4. Can incorporate increasingly complex physics models such as beam hardening effects, scattering and phase shift effects.

In general, iterative algorithms repeat these steps:

1. Compute numeric projections of current reconstructed image (first iteration);

2. Compare these projections with measured data;

3. Modify current reconstruction to obtain the next iteration;

4. Repeat from step 1.

An example of a common iterative algorithm is shown in Figure 6.8. From left to right on the top, a sinogram is shown and its (unfiltered) backprojection. This backprojection undergoes its own projection transformation and is then compared with the original data. Going from left to right on the bottom shows the iteration I_{n+1} and how much clearer the image is compared to I_n. Each iteration is an improvement on the previous reconstructed image. The process is explained in detail in Table 6.2.2. The iterative process converges to a solution when the change between successive iterations is negligible.

A more specific form of expectation maximisation is known as ordered subsets (OSEM). The most CPU intensive task when calculating tomographic reconstruction is the computation of the projection (P) and the back projection (BP). P and BP complexity is linearly dependent on the number of projections used, and not all the projections have to be used in every step. The iteration is hence divided into subiterations,

1. Measure projections and obtain sinogram	D
2. Compute back projection of data to obtain the first iteration	$I_1 = BP(D)$
3. Make projections of current iteration	$P(I_n)$
4. Compare with measured data to create a 'ratio'	$C = D/P(I_n)$
5. Compute back projection of the correction coefficients	$BP(C)$
6. Apply correction to current iteration and obtain new iteration	$I_{n+1} = I_n \cdot BP(C)$
7. Repeat from 3.	

Table 6.1
The process of iterative image reconstruction detailing the contents of Figure 6.8. (17)

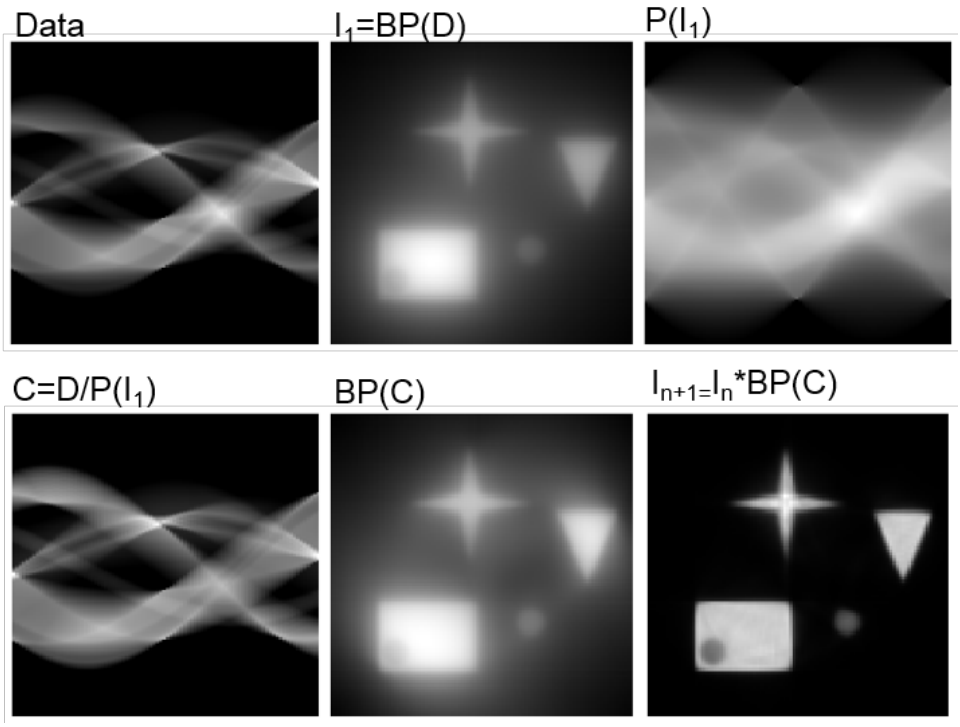

Figure 6.8 Example of iterative reconstruction. Process goes from left to right on top and then on bottom. (17; 18)

whereby each subiteration uses just a subset of all the projections. Using OSEM, the comparison between P and BP, and subsequent update is based on a smaller number of the projections (i.e. a subset) for each iteration. Therefore, the algorithm progressively uses other projections in each further iteration (or sub-iteration) leading to a much faster computation time. (73).

6.3 Phantom Measurements

A phantom study was designed to perform tomographic reconstruction of a prostate phantom with implanted dummy Model 6711 I-125 seeds, using an external X-ray source and a $60\times60\times40$ mm^3 PMMA cube containing drilled channels to mimic the brachytherapy implant template. To simulate the rotation of an external C-arm X-ray source, the sample is rotated relative to the X-ray source. Data is taken at one projection per angle covering 0-180.

Using iterative methods such as OSEM (ordered subset expectation maximisation), the phantom with implanted seeds is reconstructed from limited views and the reconstructed images are evaluated based on number of subsets used per projection set (minimum of three ordered subsets). A complete dataset of 180 projection images is used as a way of evaluating the reconstruction algorithm before testing limited angles and incomplete field of view reconstructions.

By using an external X-ray source such as a C-arm, the projection images necessary for tomographic reconstruction can be obtained using the Timepix as the imaging plane. However, as an in-body imaging device, the system has to overcome problems associated with having an imaging plane smaller than the object being reconstructed.

The experimental set-up is as shown in 6.5, with the PMMA phantom consisting of a matrix of 5×5 holes with 10 mm between each. For an evaluation of tomographic reconstruction capabilities of the BrachyView system, two areas of reconstruction are considered.

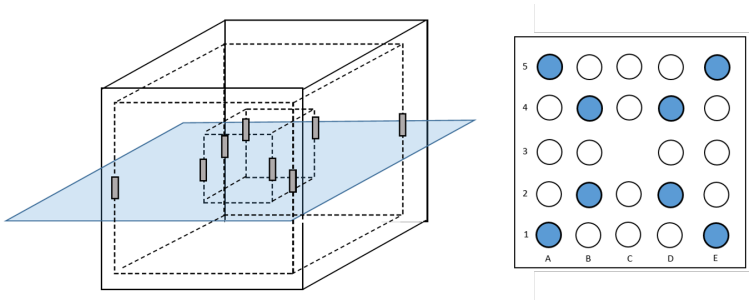

Figure 6.9 Eight seeds placed in a single plane so as to be viewed by single Medipix in rotational motion for tomographic reconstruction

Eight seeds are arranged in a two-square formation in the same plane so as to cover the entire volume of the phantom. The placement of the seeds in locations A1, A5, B2, B4, D2, D4, E1, and E5 were specifically chosen for this purpose. This can be considered as defining two 'squares':

1. Inner square consisting of seeds in locations B3, B4, D2 and D4 in locations closest to the patient's intraprostatic urethra;

2. Outer square consisting of seeds in locations A1, A5, E1 and E5 in locations at the outer edge of the patient's prostate, since a typical gland is no larger than 50 mm^3.

Their locations are shown in Figure 6.9.

By taking projection images of these seeds in the phantom, the inner and outer squares mean that we have covered all possible cases of seed position in the tomographic reconstruction. Since the reconstruction function can be repeated as a simple superposition of the sinograms, the simplest case can simply be extrapolated out to draw a conclusion for more complicated cases involving multiple seed scenarios.

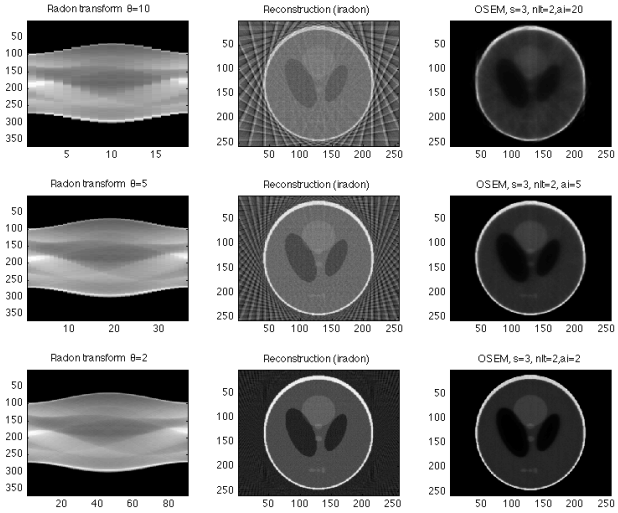

Figure 6.10 Comparison between standard filtered back projection (inverse radon) and OSEM iterative reconstruction using 3 subsets. nIt is the number of iterations and ai is the angle iteration, i.e. 10°, 5°, and 2°.

6.3.1 Matlab Simulations

As introduced in Section 6.2, the Shepp-Logan phantom is a mathematical body built into MATLAB that is commonly used for testing reconstruction algorithms (see Figure 6.7). It was developed as a purely theoretical tool to evaluate reconstructions without a need for experimental considerations. It was designed by Shepp and Logan (72) as a simulated head phantom. To demonstrate the principle of an iterative reconstruction using an OSEM approach, the algorithm is tested on a Shepp-Logan phantom, as well as other simplified mathematical bodies. The results for the Shepp-Logan phantom for different angular iterations (ai) are shown in Figure 6.10.

A mathematical evaluation of the reconstruction algorithm is performed to evaluate the presence of offset or distortion due to the incomplete sinogram datasets. For example, using a matrix corresponding to 1000×1000 elements, used to approximate the volume of the PMMA phantom (where one element corresponds to one voxel size in the reconstruction; corresponding to approximately 1000×55 μm pixels in a

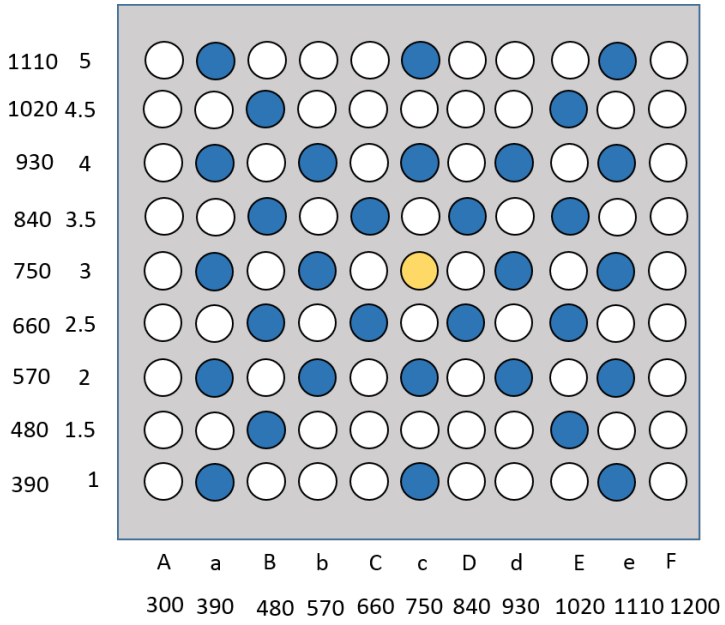

Figure 6.11 Blue circles indicate the location of simulated 'seeds' in Matlab.

60 mm^3 phantom).

By drawing a circle in the matrix equal to value 1, a high contrast density material is simulated corresponding to the presence of the high density Ti seed in the PMMA phantom. Figure 6.11 shows the location of simulated seeds.

Two-dimensional intensity profiles can be obtained by performing a Radon transform of this matrix. Therefore, a mathematical evaluation of the reconstruction algorithm can be performed.

6.4 Tomography Study

Before performing the tomographic reconstruction using data from the BrachyView system, a preliminary full CT-scan of a gel phantom was performed.

Using a mixture of commercially available tissue-equivalent gelatin, a number of dummy seeds were implanted into the gel volume through the brachytherapy tem-

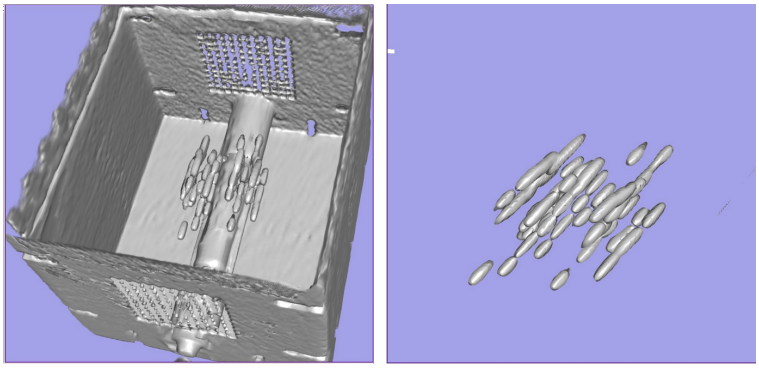

Figure 6.12 Preliminary experience with CT reconstruction of a dummy seed implant in gel phantom.

plate with the assistance of the St George Cancer Care Centre, who provided advice on the procedure and the handling techniques for LDR procedures. This allowed us to gain a deeper insight into the requirements of BrachyView for final application in a clinical context.

The following results shown in Figure 6.12 were obtained, allowing for a qualitative analysis showing that the seeds had a tendency to blur into one another, due to overlap in the tomographic reconstruction from their relatively small size compared to the CT slice. The width of the CT slice and therefore accuracy in source localisation is constrained by patient dose, therefore providing the motivation behind evaluating BrachyView's application as a high-resolution, in-body, intraoperative CT system.

Following this preliminary study, the application of Timepix detectors used in BrachyView for tomographic reconstruction was tested. While Medipix and Timepix have been successfully used in CT studies for plant and insect studies, in BrachyView, the object being imaged is much larger than the imaging plane available, presenting the novel problem of reconstructing from limited angles and limited field of view, as discussed in Section 6.2.2.

Preliminary results showing successful tomographic reconstruction have been obtained. The algorithm used was OSEM, using 3 subsets and 1 iteration for each slice.

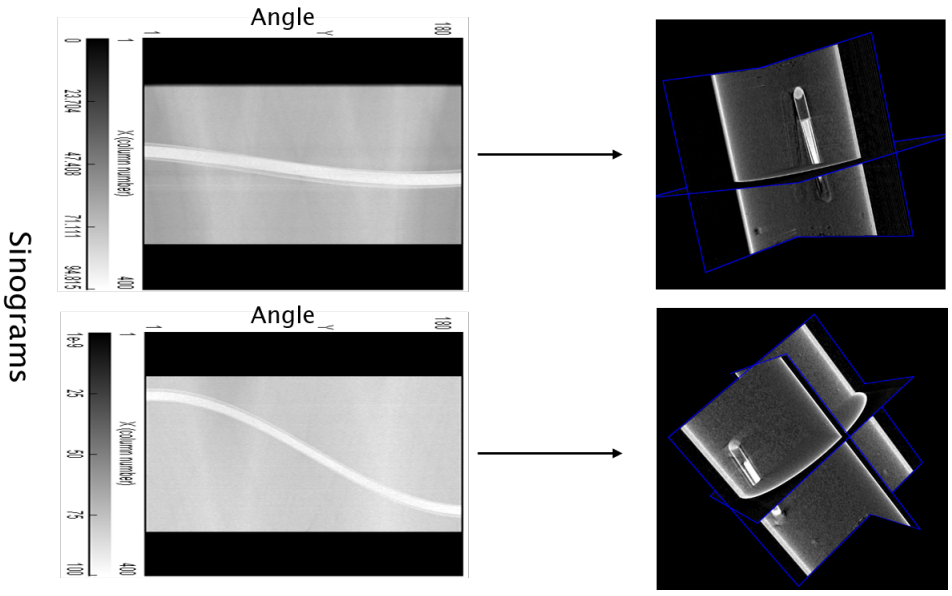

Figure 6.13 Projection images keeping a single dummy seed within the field of view of the phantom and the resulting 3D reconstruction.

Due to the imaging capabilities of the high-resolution Timepix detector, accurate 3D reconstructions of seed implant structure can be seen as in the following figures.

These results were obtained by keeping the dummy seed and the central axis of rotation completely within the field of view of the single Timepix. By shifting the single dummy seed away from the central axis of rotation, such that rotation occurs outside the field of view, a so-called 'off-axis' reconstruction can be obtained as shown in Figure 6.14.

Once this 3D reconstruction was confirmed, a multiple seed phantom study was performed for seeds located outside the central field of view of the single Timepix detector as shown in Figure 6.14. A full 3D CT reconstruction was obtained as shown in Figure 6.15.

Preliminary quantitative analysis shows the seeds within 2-5 mm of expected positions. Note the presence of a single thin sinusoidal shape in the sinogram. This corresponds to the inclusion of a thin copper wire in the centre of the phantom as a

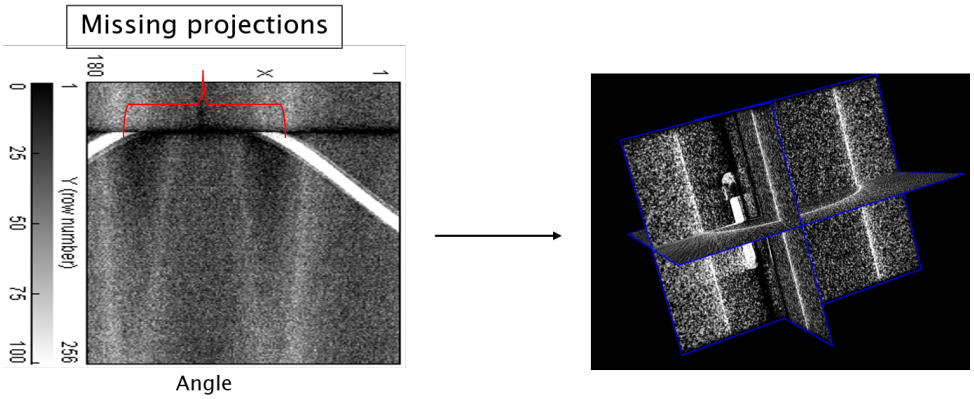

Figure 6.14 The same process is repeated for a single seed, but this time deliberately putting the seed off-axis such that the sinogram obtained is incomplete.

reference marker for calculating of expected positions.

The full 3D reconstruction is shown in Figure 6.16.

By comparing with the expected positions of the seeds based on their known positions in the phantom, a comparison can be obtained as shown in Figure 6.17. The numerical results are shown in Table 6.2. For this method, a minimum discrepancy of 0.6 mm was found with a maximum of 5 mm. For seeds more than 3 mm from expected positions, these present a dosimetric issue for the patient. Therefore, some offset correction or systematic errors must be addressed as discussed in Section 6.5. However, it is evident that some agreement between expected and calculated positions is obtained.

The results show that for seeds near the central axis of rotation, there is close agreement with that of the expected positions. However, as the reconstruction moves farther from the centre, a larger discrepancy occurs as is expected. This is due to the low amount of density information obtained as a consequence of the partial field of view problem. As the seeds on the outer perimeter move rapidly in and out of the field of view, as demonstrated by the sinograms in Figure 6.15. We only see a fairly narrow range of projections due to the small size of the imaging plane relative to the phantom, hence the partial sinogram. This results in the inner seeds getting more

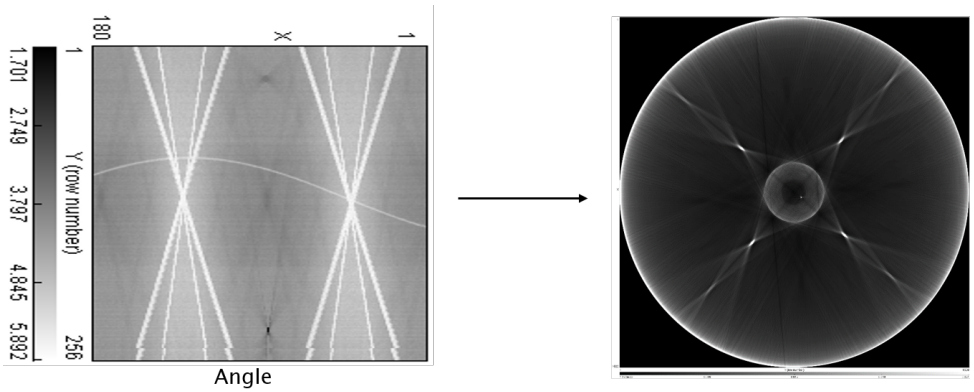

Figure 6.15 For eight seeds implanted, the Radon transform resembles a sinusoidal shape less and less as the seeds farthest from the axis of rotation move rapidly out of the field of view.

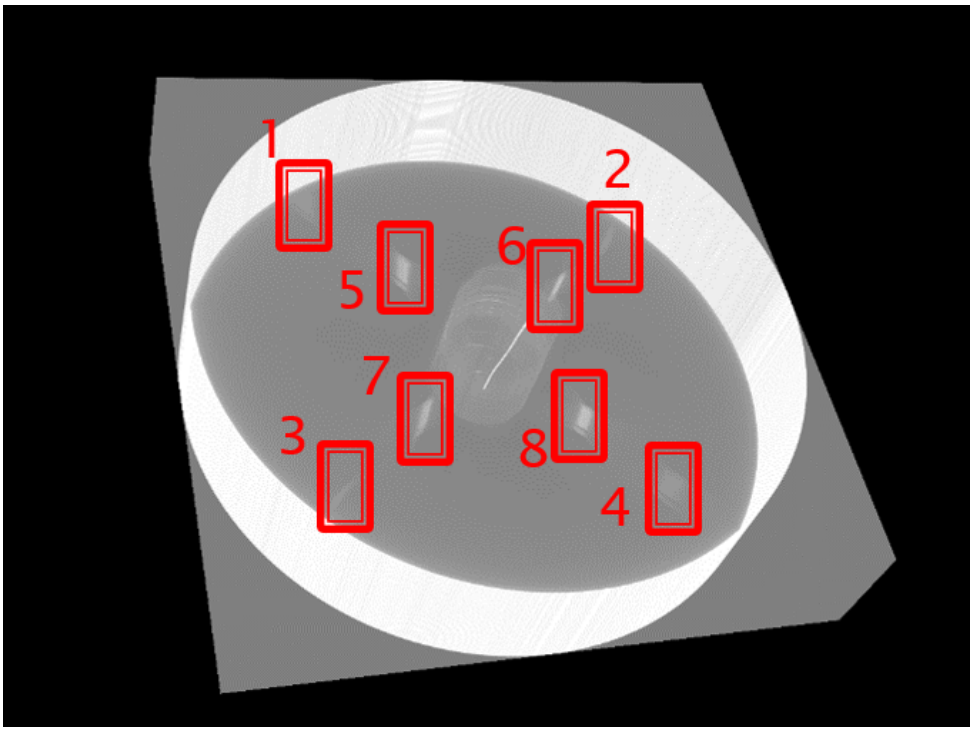

Figure 6.16 Three dimensional reconstruction of the eight dummy seeds in the phantom.

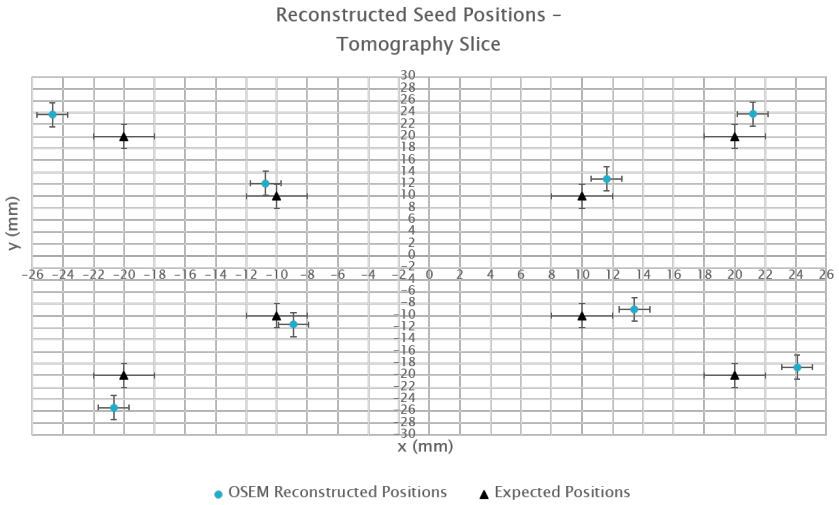

Figure 6.17 Experimental results from OSEM reconstructed data, compared to expected positions in the phantom.

projections than the outer seeds hence appearing brighter in the reconstruction.

Furthermore, an effect as described by Brunetti and Golosio (74), known as the screening or shadowing effect is evident in the tomographic slices containing the eight seeds (see the internal structure of the seeds as shown in Figure 6.15). The screening effect is overcome by a morphological technique based on computer graphics. However, this work is beyond the scope of this thesis. The resulting elongated effect is modelled in MATLAB by obtaining 2D intensity distributions, performing

Seed Position	X coordinate(mm)	Y coordinate (mm)
B2	-8.905 [1.095]	-11.49 [1.49]
D2	13.425 [3.425]	-8.96 [1.04]
D4	11.61 [1.61]	12.93 [2.93]
B4	-10.72 [0.72]	12.16 [2.16]
E5	21.18 [1.18]	23.765 [3.765]
A5	-24.69 [4.69]	23.655 [3.655]
A1	-20.675 [0.675]	-25.405 [5.405]
E1	24.095 [4.095]	-18.64 [1.36]

Table 6.2
Experimental results showing reconstructed coordinates and the difference with the expected values. Differences are shown in square brackets.

Radon transforms and testing the OSEM algorithm for an analytic model to correct for this offset.

Lastly, by increasing the step size between angles used in CT reconstruction, CT slice image quality can be assessed for the feasibility of using a limited angle approach. The angle iteration is increased as shown in Figure 6.18. However, it appears that the resulting reconstruction is degraded in quality and in fact it becomes almost impossible to localise the sources as the angle iteration (ai) increases past 5^o. The quantitative analysis is shown in Figure 6.19.

As the angle iteration increases, the accuracy in determining the exact centre of mass in each seed in the tomographic slice degrades correspondingly. This effect worsens significantly at the outer edges of the reconstruction, i.e. for seeds further from the centre of rotation. This issue should be addressed in future work, by further refinement of the reconstruction algorithm to also incorporate a priori knowledge of seed structure. However, to better investigate any distortion introduced by the OSEM algorithm, simulated work in MATLAB is performed as described in the following section.

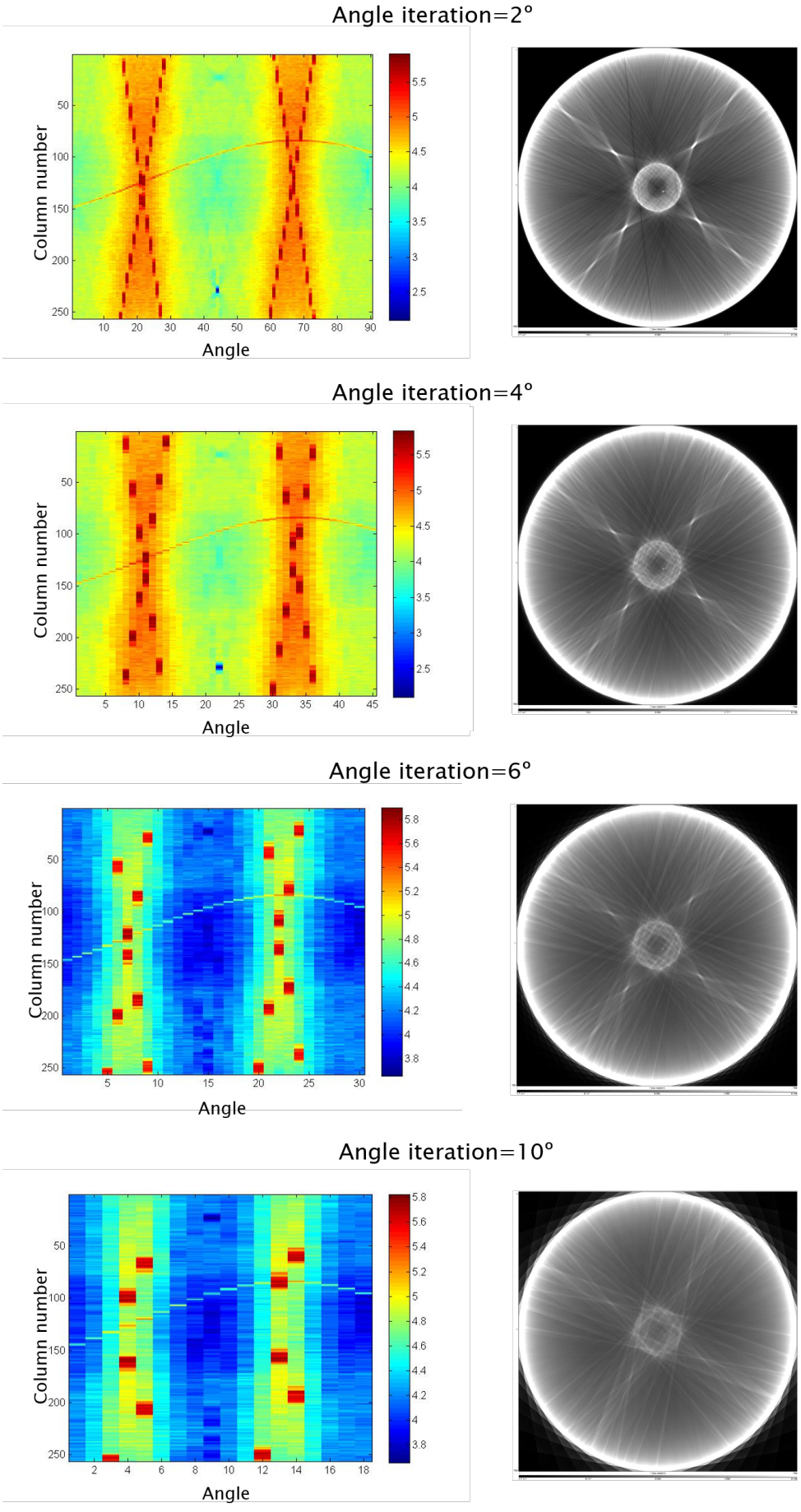

Figure 6.18 Reconstructions showing Radon transformations of varying angular iterations to evaluate the use of partial view tomographic reconstruction.

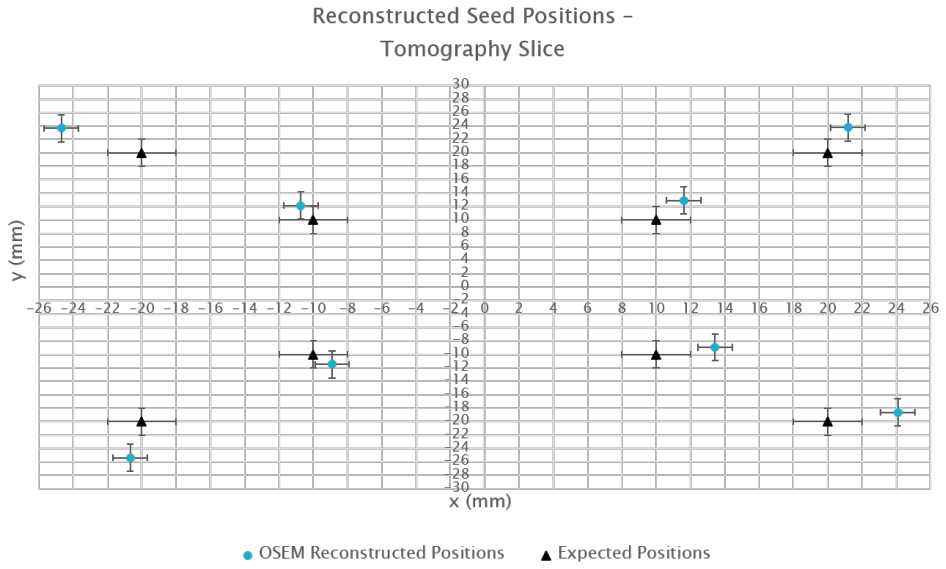

Figure 6.19 Reconstructed positions in tomographic slice of dummy seeds.

6.4.1 Matlab Simulations

In order to correct for the possibility of offset and elongated distortion error, the mathematical simulation yields results as shown in Figure 6.20.

By examining the data from this mathematical simulation, an offset relation can be obtained as a function of radial distance from the centre. For a simpler case, consider the case of 16 circular elements with a diameter of 8 elements (i.e. 0.4 mm, assuming each single element corresponds to a single voxel of 0.055 mm as in the detector plane). In Figure 6.21, the 16 seeds are located at positions corresponding to those shown in Table 6.3.

From this data, the following sinogram is obtained by the Radon transform.

The reconstructed slice is obtained through OSEM using s=6, and nIt=1.

It is noted that some distortion is evident in the reconstructed shape such that the original circular elements resemble elliptical shapes. The extent of the centre of mass offset is calculated as a function of radial distance from the centre as shown in

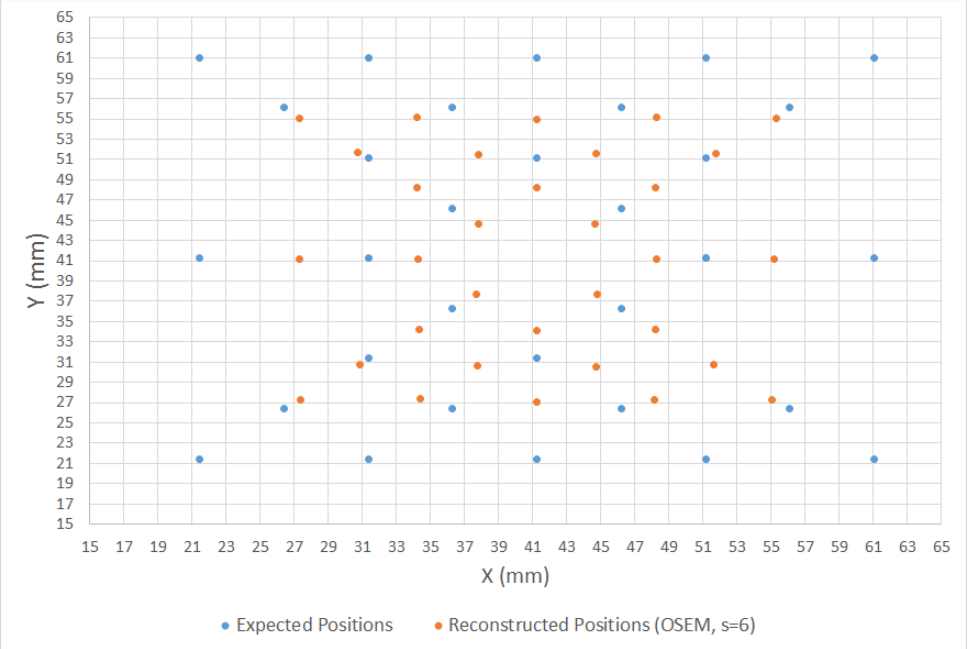

Figure 6.20 These are the results compared to expected positions for a simulated mathematical body.

Number	Position in phantom
1	A1
2	A5
3	A3
4	B2
5	B4
6	b2.5
7	b3.5
8	C1.5
9	C4.5
10	c2.5
11	c3.5
12	D2
13	D4
14	d3
15	E1
16	E5

Table 6.3 Numbers and their corresponding position 'in phantom'.

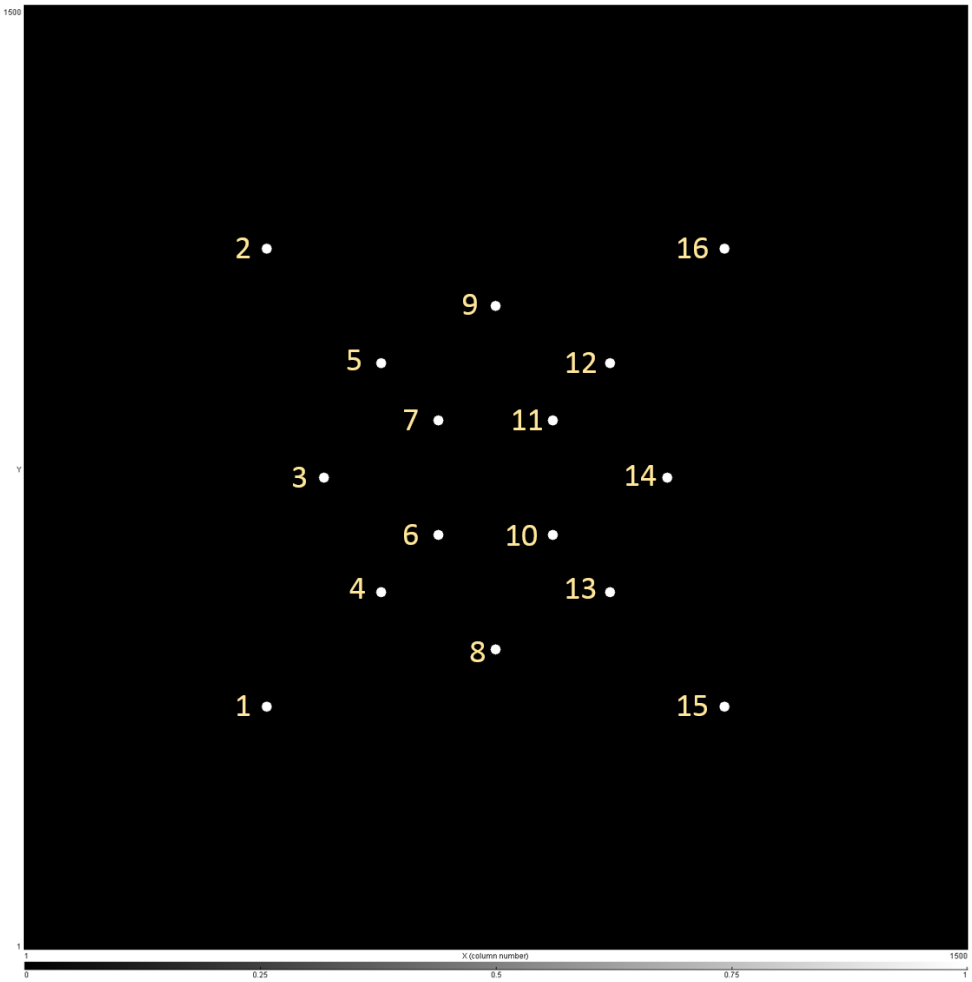

Figure 6.21 Matrix showing 16 seeds simulated as circular point sources.

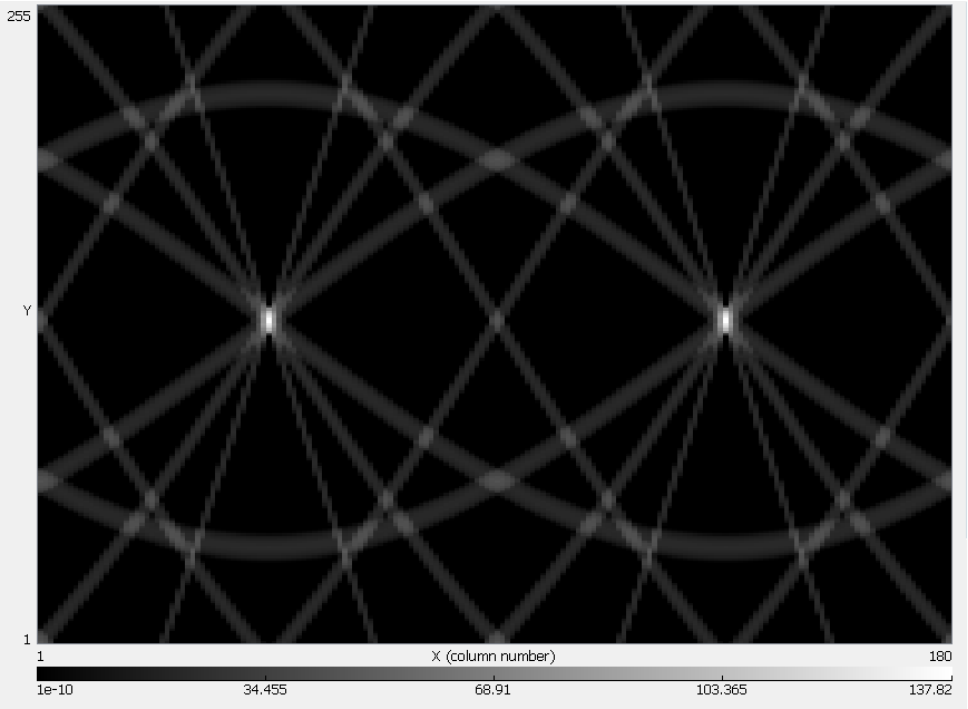

Figure 6.22 Sinogram of the 16 seeds as shown in Figure 6.21

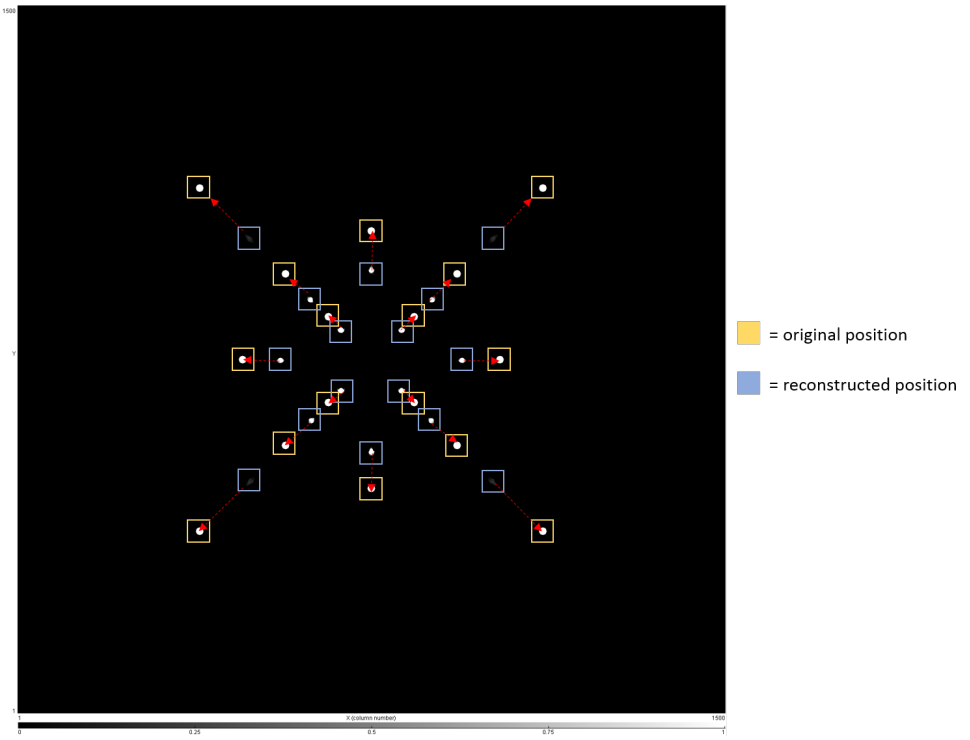

Figure 6.23 Results from OSEM reconstruction compared to original positions

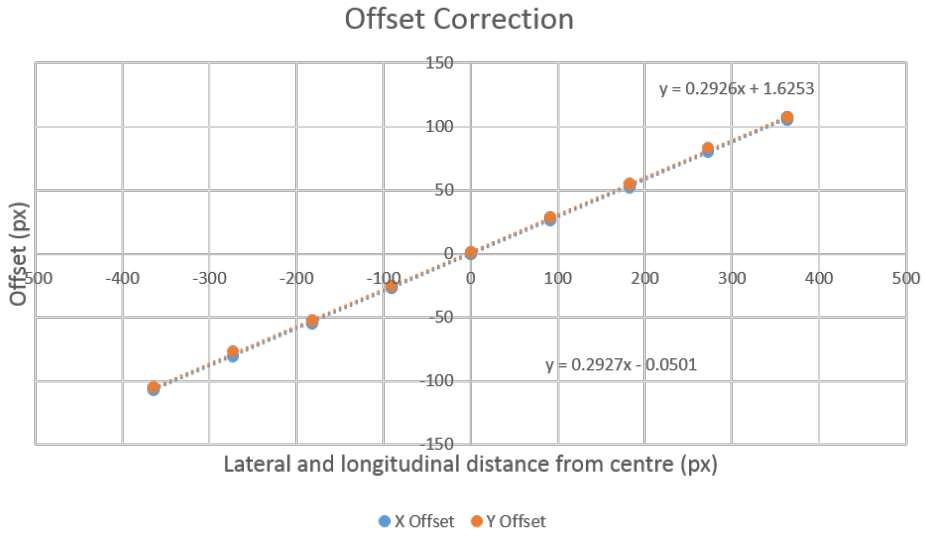

Figure 6.24 Offset factor calculation as a function of distance from centre of reconstruction.

Figure 6.24.

However, when this correction factor was applied to the experimental data, the resulting positions were not improved when compared to the expected positions.

6.5 Summary & Conclusion

The BrachyView system is a transrectal, ultra-functional imaging probe developed for use in treatment planning for permanent prostate brachytherapy. It is capable of performing pre-planning, intra-operative dynamic dosimetry and post-implant dosimetry. This proof of concept study indicates that BrachyView is capable of resolving LDR I-125 seeds accurately for post-implant.

This proof of concept study shows the viability of applying a novel design of the Timepix detector as an in-body imaging plane for tomographic reconstruction of I-125 PPB implants.

Preliminary quantitative analysis has been performed to localise sources within 2-5

mm of expected positions. However, due to systematic errors within the reconstruction algorithm, this discrepancy is yet to be addressed in future work. Systematic errors as a result of experimental set-up (e.g. axis of rotation) and assumptions made regarding other geometrical factors were not accounted for.

Furthermore, the so-called screening effect of seeds at a larger radial distance from the centre results in the reconstruction algorithm misplacing density at some offset. A continual refinement of the OSEM reconstruction algorithm is proposed with incorporation of a priori knowledge of the implanted I-125 seeds.

With BrachyView being used in the operating theatre, the system will ultimately be an ultra-functional imaging probe, able to perform pre-planning, intraoperative treatment planning, as well as a post-implant dosimetry check all within one device. By streamlining the entire brachytherapy implant procedure into a single room procedure, BrachyView will enable the physicians to perform more realistic and accurate checks in real-time, and also provide a more cost-effective solution to treatment planning for permanent prostate brachytherapy.

Chapter 7

Tissue Diagnostic X-Ray Imaging

This chapter presents the experimental work performed on a tissue-equivalent medical gel phantom, for testing the application of the Timepix detector in X-ray transmission imaging of soft tissue; namely the prostate gland and surrounding anatomical structures. The Timepix detector has unlimited dynamic contrast and has potential for use in soft tissue diagnostic imaging. By using materials of similar electron density, this feasibility study highlights BrachyView's capability for high-contrast imaging. The system is evaluated for organ delineation and even tumour diagnosis.

By showing that BrachyView can be used for various imaging applications, it will allow for a multi-modality treatment planning system that provides more accurate and real-time dosimetry and therefore better patient outcomes in sparing critical structures from incorrectly placed dose.

7.1 Use of Timepix in X-Ray Diagnostic Imaging and Phantom Measurements

For accurate dosimetry in prostate brachytherapy implant procedures, accurate volumetry of the prostate combined with seed positioning in real-time is ideal. Currently, the preference of TRUS imaging over CT for volumetric studies has been dictated by the poor resolution of soft tissue typical of conventional CT imaging.

The Timepix has unique imaging properties and fast readout time, allowing it to be used for the identification of materials of varying density and elemental composition. The high resolution and high contrast imaging properties of the Timepix suggest that it is an appropriate detector for use in soft tissue imaging applications.

It has been proven that for thin samples (0.3-0.5 cm) of plexiglass coupled with water, x-ray transmission imaging is effective for distinguishing materials of similar density as shown by Jakubek (75). Based on X-ray transmission information obtained by the Timepix detectors, the internal structure of the prostate gland and its surrounding structures can therefore be delineated and incorporated into patient treatment plans.

Furthermore, the Timepix detector has no noise and an unlimited dynamic range, making it perfectly suited for applications in biological X-ray imaging.

The aim of this study was to investigate whether Timepix detectors can be used to identify thicknesses of material relevant to a medical and clinical context. By applying Timepix in such X-ray transmission imaging, the applicability of BrachyView for soft tissue diagnostic imaging can be assessed, therefore adding another imaging modality to the in-body imaging probe.

For this study, a tissue-equivalent medical phantom was used. The phantom is pictured in Figure 7.1 and was developed by CIRS (Computer Imaging Reference Systems) as a disposable phantom specifically designed for training procedures which involve scanning the prostate by TRUS. It consists of clear acrylic, urethane and Zerdine, which is described as a ”durable and accurate tissue-mimicking material...[that] accurately simulates the ultrasound characteristics of human liver tissue” (76).

Two main scenarios were investigated using this tissue-equivalent phantom.

Firstly, using the BrachyView triple detector prototype as shown in Figure 3.2, an assessment of the Timepix’s ability to distinguish soft tissue structures is performed. In the experimental set-up, the triple Timepix detector is wall-mounted adjacent to the phantom such that the prostate is aligned within the field of view. The sensor on

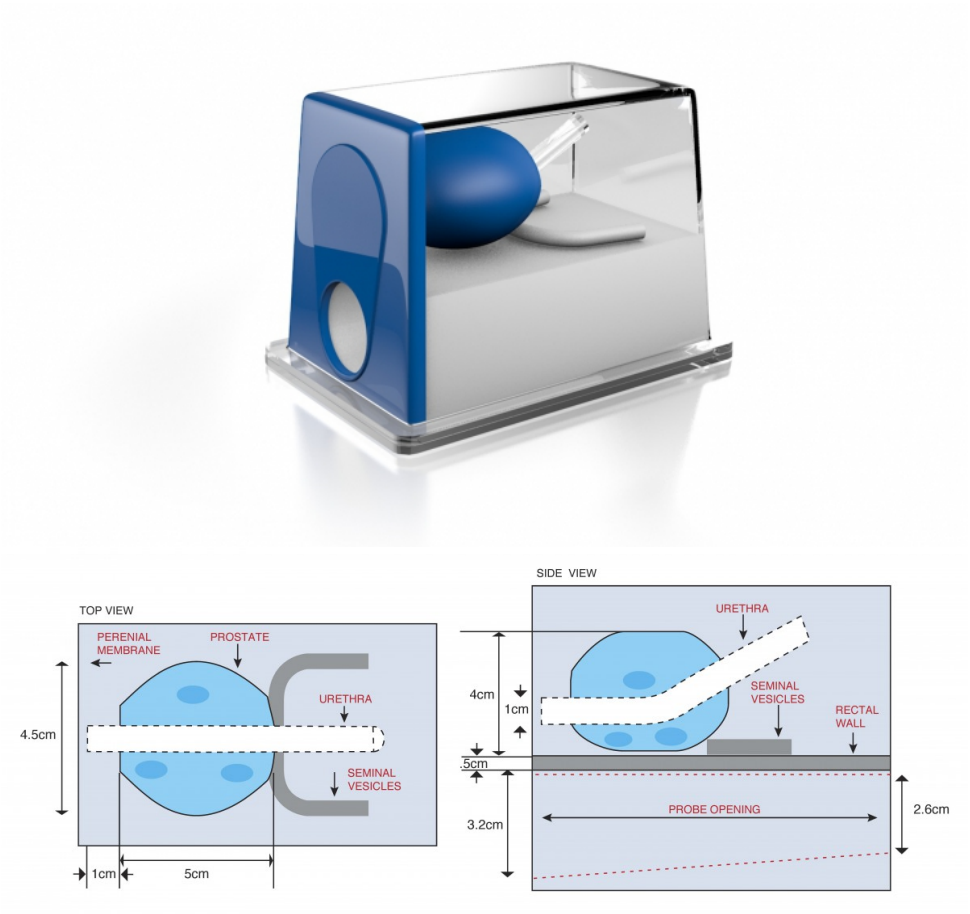

Figure 7.1 Schematic showing prostate phantom used for ultrasound imaging training purposes. Image courtesy of Computerised Imaging Reference Systems (CIRS).

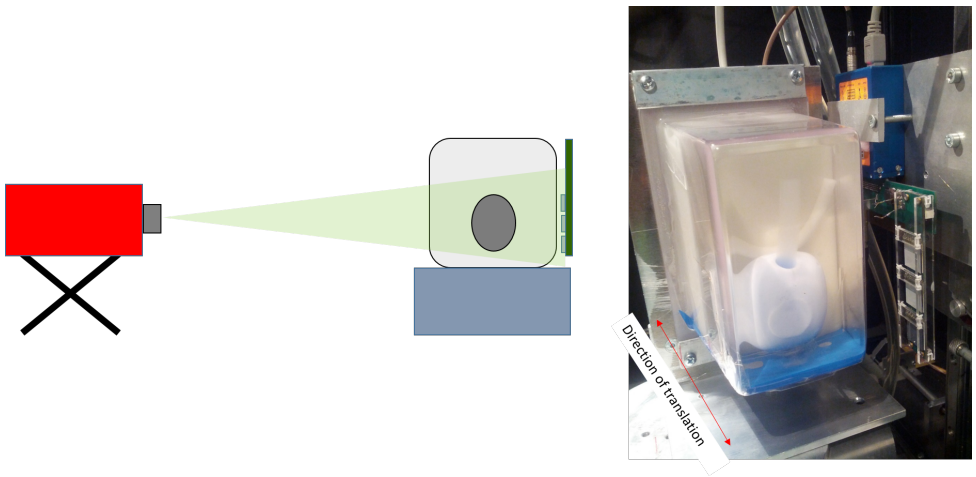

Figure 7.2 Experimental set-up to evaluate use of TimePix in soft tissue diagnostic imaging.

this triple detector was the standard 300 μm thick Si.

Note that while the proposed set-up for the actual prostate implant procedure calls for the use of a transrectal probe, this study was performed out of the rectal cavity due to the physical limitations of the X-ray cabinet set-up. However, accounting for the spherical nature of the prostate and average rectal wall-prostate distance of approximately 5-10 mm, the measurements can be considered equivalent to a true transrectal set-up, as far as our purposes go.

Based on previous studies for optimisation of X-ray voltage (77), images were acquired at 50 kV at a power of 7.5 W. The phantom is mounted as shown in Figure 7.2 and scanned laterally with images obtained at 1 mm increments to determine the location of the prostate boundary and any other features present, such as the intraprostatic urethra, or the seminal vesicles as indicated by Figure 7.1.

Once the prostate boundary was identified, additional thicknesses of tissue-equivalent plastic were introduced into the field of view of the triple detector, allowing an evaluation of the Timepix's ability to distinguish varying thicknesses of material of similar elemental composition.

For this experiment, 2 mm thick slabs of PET plastic (polyethylene terephthalate with

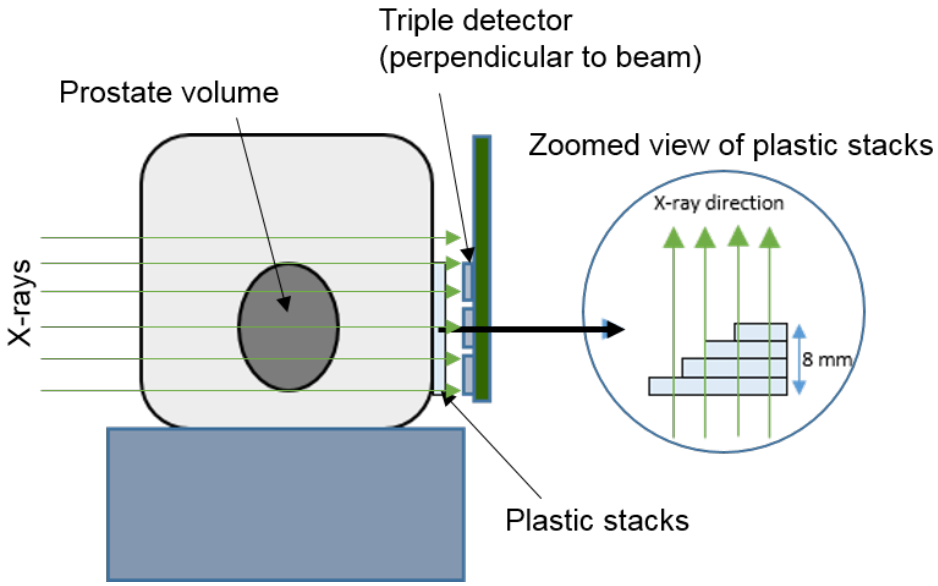

Figure 7.3 Schematic showing the tissue-equivalent prostate phantom with stacked plastic layers (configuration shown on right) stuck on the side. These are placed in direct field of view of the Timepix detectors. For the 300 μm thick sensor, each plastic layer used was 2 mm thick. For the 1 mm sensor, each plastic layer was 0.2 mm.

a density of 1.38 g/cm^3) were stacked atop one another to create a step sequence of thicknesses corresponding to 2, 4, 6 and 8 mm total thickness. These plastic slabs were introduced into the field of view such regions of interest within both the prostate region and the surrounding 'tissue' (or gel) were located behind each thickness step accordingly.

Standard transmission X-ray images are acquired for a total of 20 minutes. This time was selected to provide a satisfactory number of events per pixel for us to establish a suitable signal-to-noise ratio. The quantification of the Timepix's resolving and contrast power is performed by a standard SNR equation shown below:

$$SNR = \frac{|\mu_1 - \mu_2|}{\sqrt{\sigma_1^2 + \sigma_2^2}} \tag{7.1}$$

where μ is the mean value, and σ is the standard deviation in each respective region of interest.

After this measurement was completed, an additional study was performed utilising a thicker sensor to maximise our detection efficiency and thereby reducing the acquisition time and increasing our imaging contrast capabilities. The triple detector was replaced with a single Si sensor of 1 mm thickness and the X-ray tube brought as close as possible to the phantom surface to maximise beam intensity. Furthermore, instead of using 2 mm thick slabs of tissue-equivalent plastic, much thinner slices of 0.2 mm were used to push the limits of the detector evaluation.

The SNR of the system was evaluated as a function of exposure time, normalised as number of photons/pixel in order for us to establish a feasible operating time for brachytherapy practitioners interested in obtaining soft tissue diagnostic images of a patient's prostate using the BrachyView system.

For the time being, no incorporation of actual tissue samples has been considered nor the amount of body fat and other surrounding tissue such as bone and other internal organs. However, considering that our system only had a maximum output of approximately 9W and when compared with kW clinical systems, this feasibility study serves as a primarily qualitative evaluation of the applicability of Timepix for soft tissue diagnostic imaging.

7.2 X-ray Transmission Imaging with Gel Phantom

Once a suitable signal to thickness calibration was performed (also referred to as beam hardening calibration), the images obtained are evaluated for mean values and standard deviation in each respective region of interest; i.e. for regions in the images corresponding to the prostate tissue and the surrounding soft tissue. Each region is evaluated behind the PET layers and without any additional plastic thickness. The SNR can therefore be evaluated as a function of thickness, based on the thicknesses of tissue-equivalent plastic introduced.

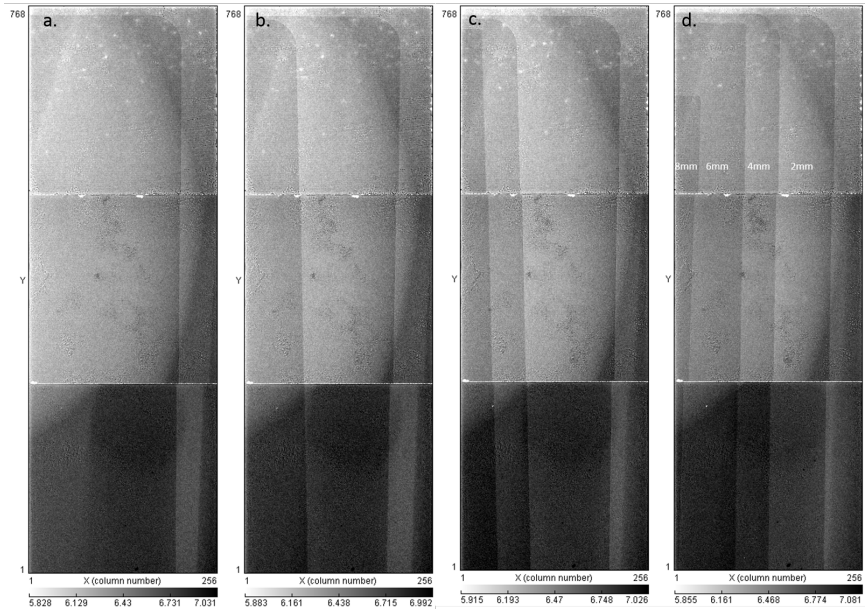

Figure 7.4 Example of images obtained on triple Timepix detector. The prostate region can be delineated as the bright circular shape across all three detectors, with the lowermost detector only seeing the distal edge of the prostate boundary. From left to right, the boundary of each plastic stack layer can be seen as they are added incrementally. i.e. one plastic region on the (a) up to four plastic stacks as shown in (d). Each step thickness of additional PE plastic represents a change of 2 mm additional plastic as shown in white (d).

7.2.1 300 μm Si Sensor

Figures 7.4 and 7.5 show the results obtained for the 300 μm silicon sensor chip, arranged in a linear 3×1 triple detector configuration. The X-ray energy used was 50 kV, with an exposure time of 1200 s, equivalent to approximately 15,000 incident photons per pixel. Successive layers of PET plastic were stacked on top of each other within the field of view and the SNR in each region evaluated with respect to the transmission image obtained with no plastic material present. Each additional layer of plastic was 2 mm thick as described in Section 7.1.

Initial inspection shows a clear delineation of the prostate boundary with respect to the soft gel surroundings, as indicated by the white circular mass in Figure 7.4, allowing the SNR to be calculated for two regions of interest: one region inside the prostate, and the other in the surrounding tissue, as shown in Figure 7.5.

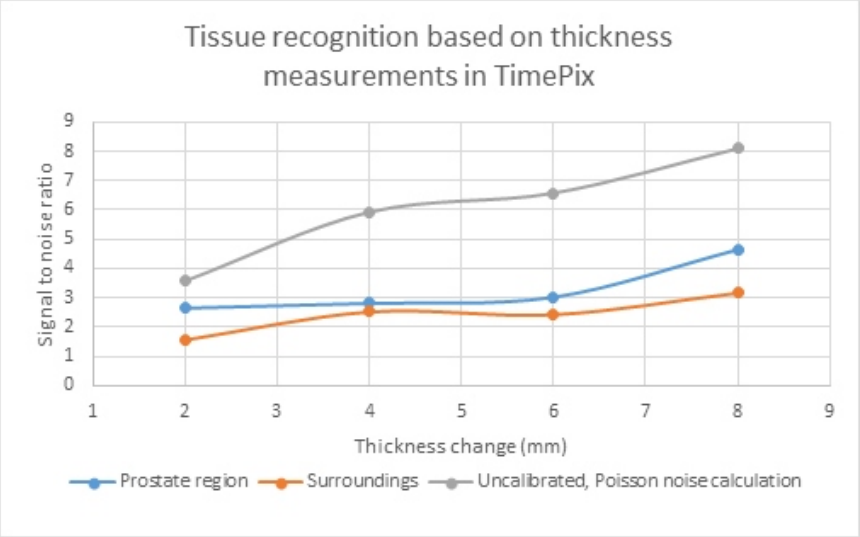

Figure 7.5 SNR as calculated for the region in the prostate and also in the area surrounding the prostate showing the expected SNR as a function of thickness change.

Furthermore, a theoretical SNR calculation is performed based on an assumed Poisson noise distribution as shown in grey. This was done by comparing the experimentally obtained standard deviation of each region of interest with the expected square root value typically associated with a general Poisson noise distribution, as shown in Equation 7.1.

The experimentally-measured SNR was approximately equal to 1.5-3 for non-prostate tissue and 2.5-4.5 for prostate tissue, which are lower than the range of values predicted by the Poissonian distribution of approximately 3.5-8; this can be attributed to fluctuations in the output power of the X-ray source, and possible temperature dependence of the detectors leading to statistical fluctuations in the acquired signal. Despite this, the Timepix detector is able to satisfactorily differentiate between prostate and non-prostate tissue for most ranges of thickness change.

7.2.2 1mm Si Sensor

The results shown in Figure 7.4 show the applicability of a standard 300 μm thick Si sensor in identifying anatomical features within a tissue-equivalent prostate phan-

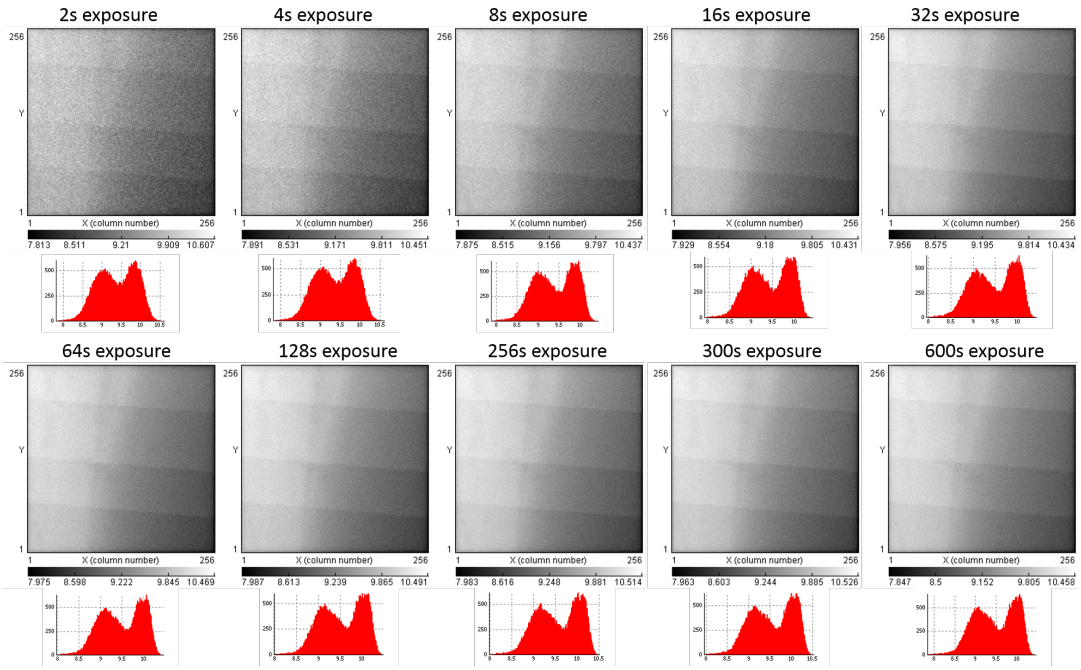

Figure 7.6 Images of the prostate boundary obtained by single 1 mm Si sensor. The prostate region appears darker in the beam hardening corrected data as it is of lower density than the surrounding tissue, and therefore appears as a lower equivalent thickness from high signal (i.e. raw counts). The red spectra are count bins as calibrated for thickness and beam hardening correction. The two peaks show a clear delineation between prostate tissue and surrounding tissue allowing a diagnostic analysis of tissue thickness and boundaries.

tom. The further possibilities of BrachyView are evaluated by performing imaging characterisation of a 1 mm thick Si sensor on the same phantom configuration. A thicker sensor chip means higher efficiency, and therefore higher statistics within a shorter time, allowing for more accurate imaging performance.

By using a single detector and even thinner samples of plastic (0.2 mm) the contrast of such a detector evaluated as a signal to noise ratio as a function of exposure time can be evaluated as discussed previously. By decreasing the X-ray source-phantom distance to 10 mm, and increasing tube output to its maximum capacity (at 90 kV and 110 μA), maximum beam intensity can be achieved.

The images obtained once corrected for beam hardening are shown in Figure 7.6.

The exposure time is normalised to average number of photons per pixel as detected

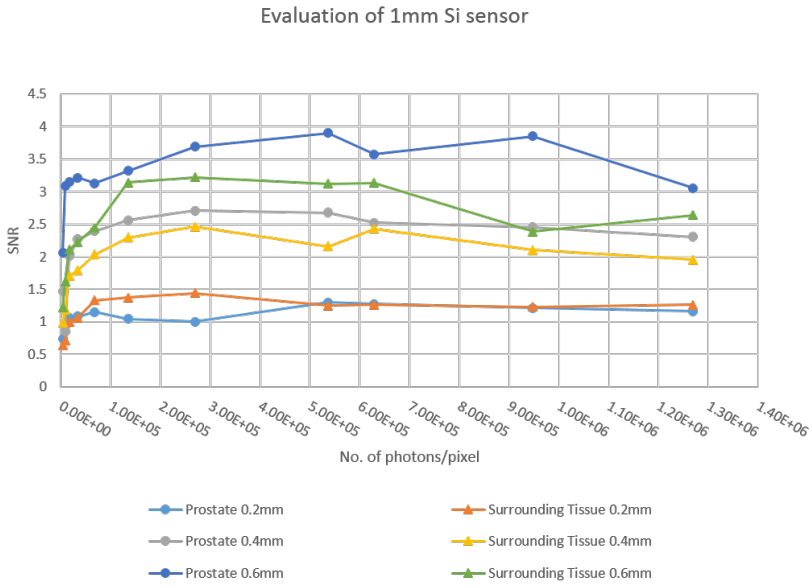

Figure 7.7 SNR for thickness change of 0.2mm within two different regions of interest in the imaging field of view. Exposure time is shown as a function of photons/pixel. By identifying where the plateau in SNR occurs, the time for this particular system can achieve optimal imaging characteristics is shown.

by the Timepix sensor, allowing an estimation of the imaging time required to achieve optimal SNR for thin samples within a change of 0.2 mm as long as the contrast achieved remains above a certain noise threshold.

Figure 7.7 shows that a certain optimal value of SNR can be achieved within the first 100,000 photons/pixel whereby increasing exposure time does not lead to any discernible benefit in imaging power. By comparing this with the typical clinical kW X-ray source, which is able to achieve much higher intensity and power than our experimental system, it is clear that a suitable image allowing us to assess soft tissue anatomical features can be obtained within clinically realistic times. Additional dose to the patient can therefore be limited accordingly, yet still yielding high contrast for soft tissue.

7.3 Summary & Conclusion

For accurate dosimetry in prostate brachytherapy implant procedures, accurate volumetry of the prostate combined with seed positioning in real-time is required. Currently, the preference of TRUS imaging over CT for volumetric studies has been dictated by the poor resolution of soft tissue typical of conventional CT imaging.

The Timepix's unique imaging properties and fast readout time allows it to be used for the identification of materials of varying density and similar elemental composition, based on the high resolution and high contrast X-ray transmission imaging ability of the Timepix detector.

While initial tests with the standard 300 μm thick sensor show positive imaging properties, the extension of the BrachyView design to utilise a 1 mm thick Si sensor will provide much greater efficiency, allowing for quicker acquisition times and thereby reducing the dose to the patient and overall operation time if applied in a clinical context. The evaluation of SNR shows that a plateau in SNR occurs as soon as approximately 100,000 photons/pixel are observed, which for this particular experimental system was approximately equal to 30 seconds of exposure time. Any additional exposure time does not result in an improvement in SNR, showing that fluctuations in the system begin to contribute to the noise more than standard Poisson distribution.

BrachyView is being developed as a method for intra-operative dynamic dose planning as well as a post-implant verification system utilising high-resolution Timepix detectors. Additionally, the area of diagnostic imaging has also been raised as a possible application of the Timepix detector. This study shows that we are able to resolve the anatomical structures within a medical tissue-equivalent prostate phantom with an acceptable level of SNR as a function of tissue thickness corresponding to changes in patient anatomy.

This soft tissue imaging combined with seed position determination indicates that BrachyView has strong potential as a dynamic dose planning device for use in low

dose rate prostate brachytherapy procedures. By showing that the same device can be used for various imaging applications, BrachyView allows for better implant dosimetry and therefore better patient outcomes in sparing critical structures from excessive radiation from incorrectly placed seeds.

With the combined ability for diagnostic imaging, monitoring the insertion of seeds to their initial positions, and post-implant dosimetry checks, BrachyView is an ultra-functional system allowing for many different imaging modalities within a single cost-effective and convenient solution.

Future work will involve a repetition of such measurements involving real tissue samples and consultation with pathological laboratories including prostate lesions, calcifications and other biological material of note for brachytherapy practitioners.

Chapter 8

Summary of Contributions & Future Research

A prototype novel in-body imaging device based on pixellated semiconductor detectors has been developed for application in prostate brachytherapy treatments. The technology used involves a novel application of the Timepix device, as developed by the Medipix Collaboration at CERN, as well as a lead pinhole collimator system. The ability of the system to localise radioactive sources in 3D has been demonstrated through simulation and experimental evaluation. The application of BrachyView in other imaging modalities has also been proposed, with preliminary feasibility studies showing possible use in CT imaging, as well as soft tissue diagnostic imaging.

This research leads to the application of a multifunctional rectal probe allowing volumetric studies using both ultrasound and/or X-ray CT imaging. Furthermore, intra-operative dynamic dose planning based on real-time seed position determination in the prostate, and post-implant dosimetry based on these locations are presented as an all-inclusive 'one-stop shop' procedure.

8.1 Contributions

A review of the current state of prostate brachytherapy treatments was presented, with particular focus given to the LDR technique as summarised in Chapter 1. The

development of the Medipix family of detectors has given rise to a high-resolution, real-time semiconductor detector with application in radiation physics. Due to these favourable characteristics, the latest generation of Medipix, known as Timepix, was nominated as a candidate for use in the BrachyView system.

The proposed system involving a novel application of a pinhole collimator required an analytic evaluation as well as optimisation by simulation work. The novel design of this device was detailed in Chapter 3, with subsequent characterisation performed by Monte Carlo methods presented in Chapter 3. It was concluded that a lead collimator was suitable for the purposes of BrachyView.

Several imaging modalities are involved in the quality assurance of an LDR implant, and these were outlined in Chapters 4-7.

The primary method of source localisation in 3D was with the use of a multiple pinhole collimator. In these feasibility studies, using a ray-tracing stereoscopic technique, LDR sources were found within 1-3 mm of expected positions. This is within the accepted tolerance of implant position error according to the literature, therefore proving BrachyView's efficacy as a real-time treatment visualisation system. Furthermore, when compared with a clinical gold standard of a CT scan, it was further determined that the results obtained with BrachyView were within 1-2 mm of expected positions. This is in comparison with results typically taken from an intraoperative ultrasound scan, which is unable to determine source position with the same accuracy.

Secondly, the possibility of applying BrachyView in CT imaging was investigated. Using the in-body Timepix as the imaging plane, a full 3D reconstruction of sources implanted in the phantom was obtained. However, because the imaging plane is intrinsically smaller than the object to be imaged, the partial field of view presents an obstacle to overcome. Using an iterative reconstruction algorithm (OSEM), it was found that for a phantom study, a 3D reconstruction can yield CT results within 5 mm of expected positions.

Lastly, BrachyView was tested as a diagnostic tool, in its ability to distinguish soft tissue and therefore overcome conventional CT problems. Using standard X-ray transmission techniques and a tissue-equivalent medical gel phantom, a BrachyView prototype was tested. The Timepix detector has high resolution and high contrast imaging properties, suggesting it is an appropriate detector for use in soft tissue imaging applications.

The work done in developing the BrachyView system has been recognised in the international brachytherapy community as a promising treatment option for prostate cancer patients.

Several speaking engagements and outreach events both in Australia and abroad have been presented highlighting BrachyView as a promising direction for prostate cancer therapy. These included talks with high school, university students, and Rotary clubs. On June 27, 2012, the BrachyView project was presented in the University-wide speaking competition '3 Minute Thesis'. The premise of the competition was to present innovative research with an impact on society in three minutes or less to an intelligent yet non-specialist audience. The talk was awarded best presentation at the University of Wollongong, and was later commended at the Trans-Tasman finals held at University of Queensland. These are outlined in detail in Section 1.2.

On May 22, 2013, the publication "BrachyView: Proof-of-principle of a novel in-body gamma camera for low dose-rate prostate brachytherapy" was featured as the chosen 'Science Spark' topic of the day at Memorial Sloan Kettering Cancer Care Center in New York, USA. The image highlighted from the article was also featured at the CyberLibrary Cafe in the Zuckerman Research Center.

BrachyView was also recently highlighted at the 2014 European BrachyPhys Task Group (ESTRO) meeting "Further potentials for high quality brachytherapy in the future". The American Brachytherapy Society meeting in Houston also recognised BrachyView as one of the important highlights of the year out of all brachytherapy projects in development.

8.2 Future Work

While proof-of-concept of an in-body multifunctional probe was clearly demonstrated, there are a number of considerations to improve and further the development of BrachyView as a functional intraoperative treatment planning and imaging system. While a lead collimator with 3-5 pinholes was suitable for feasibility studies, increasing the number of pinholes and optimising the field of view may enable a higher accuracy in source localisation in 3D. Furthermore, the use of a tungsten collimator has also been proposed as a further step in collimator design. However, due to the technical requirements of machining a tungsten collimator, this has not yet been experimentally verified. Additionally, further work with Monte Carlo methods is recommended for optimising and characterising further pinhole geometries and parameters of the BrachyView set-up. This is part of ongoing work conducted at CMRP.

The identification of implanted brachytherapy sources on the imaging plane through the pinholes has been done manually in this study. An automated system involves the development of a software package that will not only identify the projection images, but also perform the calculations to give the 3D coordinates of the implant. These coordinates will then need to be compared to two things:

- Planned positions;
- Real-time patient anatomy changes.

This will need to be presented in a way that is easily comprehensible and operated by brachytherapy practitioners and attending staff in the operating theatre during an LDR procedure. As part of this software development, integration of the Pixelman software has to be considered, in communicating with the Timepix detectors.

While the CT imaging as discussed in Chapter 6 presents a method of reconstructing the LDR implant in full 3D, there are a number of technical issues that may present

obstacles in a clinical scenario. These include introducing extra dose to the patient, as well as uncertainties arising from the partial field of view problem. However, as shown from the results from the pinhole measurements, BrachyView may in fact supercede the need for CT imaging as a post-implant dosimetric tool, or at the very least may be used as an additional, intermediate step for post-implant verification.

Lastly, the physical design of the BrachyView probe has to be finalised, along with its integration with existing ultrasound hardware. However, as shown in this thesis, the co-registration of such imaging datasets is relatively straightforward and can produce results that are both accurate, and clinically reliable. While BrachyView is to be integrated into existing prostate brachytherapy hardware, the mechanical combination of the TRUS and Timepix detector apparatus is not imperative for the successful application of BrachyView.

The prototype of the BrachyView system combined with the finalisation of imaging software, will present an opportunity for brachytherapy practitioners to have a real-time, dosimetric tool, able to localise implanted sources in 3D with sub-mm accuracy. This ability to adjust implants as they occur will reduce localisation error and therefore improve patient treatment outcome, thereby allowing a greater quality of life for each patient affected by prostate cancer.

Bibliography

[1] P. Wai, N. Krstajic, J. Adamovics, and S. Doran, "Dosimetry of the Amersham 6711 Oncoseed using PRESAGE and optical CT," *Journal of Physics: Conference Series*, vol. 56, no. 1, pp. 245–238, 2006.

[2] D. Miszczak, "Modern brachytherapy techniques - real-time high dose rate brachytherapy for prostate cancer," *Acta Physica Polonica A*, vol. 115, no. 2, pp. 583–5, 2009.

[3] P. Grimm, I. Billiet, D. Bostwick, A. Dicker, S. Frank, J. Immerzeel, M. Keyes, P. Kupelian, W. Lee, S. MacHtens, J. Mayadev, B. Moran, G. Merrick, J. Millar, M. Roach, R. Stock, K. Shinohara, M. Scholz, E. Weber, A. Zietman, M. Zelefsky, J. Wong, S. Wentworth, R. Vera, and S. Langley, "Comparative analysis of prostate-specific antigen free survival outcomes for patients with low, intermediate and high risk prostate cancer treatment by radical therapy. results from the Prostate Cancer Results Study Group," *BJU International*, vol. 109, no. S1, pp. 22–29, 2012.

[4] H. H. Holm, N. Juul, J. F. Pedersen, H. Hansen, I. Stroyer, and H. W. Herr, "Transperineal iodine-125 seed implantation in prostatic cancer guided by transrectal ultrasonography," *The Journal of Urology*, vol. 167, no. 2, pp. 985–988, 2002.

[5] H. H. Holm, S. Torp-Pedersen, and P. Myschetzky, "Transperineal seed-implantation guided by biplanar transrectal ultrasound," *Urology*, vol. 36, no. 3, pp. 249–252, 1990.

[6] R. Potter, *Modern Imaging in Brachtherapy*. Brussel: European Society of Therapeutic Radiology and Oncology, 2002, pp. 123–151.

[7] J. E. Sylvester, P. D. Grimm, S. M. Eulau, R. K. Takamiya, and D. Naidoo, "Permanent prostate brachytherapy preplanned technique: The modern Seattle method step-by-step and dosimetric outcomes," *Brachytherapy*, vol. 8, no. 2, pp. 197–206, 2009.

[8] M. J. Zelefsky, Y. Yamada, G. Cohen, E. S. Venkatraman, A. Y. C. Fung, E. Furhang, D. Silvern, and M. Zaider, "Postimplantation dosimetric analysis of permanent transperineal prostate implantation: improved dose distributions with an intraoperative computer-optimized conformal planning technique," *International Journal of Radiation Oncology *Biology* Physics*, vol. 48, no. 2, pp. 601–608, 2000.

[9] D. French, J. Morris, M. Keyes, O. Goksel, and S. Salcudean, "Computing intraoperative dosimetry for prostate brachytherapy using TRUS and fluoroscopy," *Academic Radiology*, vol. 12, no. 10, pp. 1262–1272, 2005.

[10] J. Jakubek, "Semiconductor pixel detectors and their applications in life sciences," *Journal of Instrumentation*, vol. 4, no. 03, p. P03013, 2009.

[11] F. Beekman, D. McElroy, F. Berger, S. Gambhir, E. Hoffman, and S. Cherry, "Towards in vivo nuclear microscopy: iodine-125 imaging in mice using micro-pinholes," *European Journal of Nuclear Medicine and Molecular Imaging*, vol. 29, no. 7, pp. 933–938, 2002.

[12] J. Duan, D. J. Macey, P. N. Pareek, and I. A. Brezovich, "Real-time monitoring and verification of in-vivo high dose rate brachytherapy using a pinhole camera," *Medical Physics*, vol. 28, no. 2, pp. 167–173, 2001.

[13] Widepix s.r.o., "WidePIX 1x5 product datasheet version 1.0," 2015. [Online]. Available: http://www.widepix.cz/files/datasheets/WidePIX%201x5%20v1.0%20Datasheet.pdf

[14] F. Beekman and F. van der Have, "The pinhole: gateway to ultra-high-resolution three-dimensional radionuclide imaging," *European Journal of Nuclear Medicine and Molecular Imaging*, vol. 34, no. 2, pp. 151–161, 2007.

[15] D. L. Marks and D. J. Brady, "Three-dimensional source reconstruction with a scanned pinhole camera," *Optics Letters*, vol. 23, no. 11, pp. 820–822, 1998.

[16] B. F. Hayden, "Slice reconstruction: Radon transform," 2005. [Online]. Available: http://homepages.inf.ed.ac.uk/rbf/CVonline/LOCAL_COPIES/AV0405/HAYDEN/Slice_Reconstruction.html

[17] J. Jakubek, C. Granja, J. Dammer, R. Hanus, T. Holy, S. Pospisil, R. Tykva, J. Uher, and Z. Vykydal, "Phase contrast enhanced high resolution X-ray imaging and tomography of soft tissue," *Nuclear Instruments and Methods in Physics Research, Section A: Accelerators, Spectrometers, Detectors and Associated Equipment*, vol. 571, no. 1-2, pp. 69–72, 2007.

[18] J. Jakubek, "Data processing and image reconstruction methods for pixel detectors," *Nuclear Instruments and Methods in Physics Research Section A: Accelerators, Spectrometers, Detectors and Associated Equipment*, vol. 576, no. 1, pp. 223–234, 2007.

[19] AIHW, "Cancer in Australia - an overview, 2012," Australian Institute of Health and Welfare, Tech. Rep., 2012.

[20] M. Zerbib, M. J. Zelefsky, C. S. Higano, and P. R. Carroll, "Conventional treatments of localized prostate cancer," *Urology*, vol. 72, no. 6S1, pp. S25–S35, 2008.

[21] Australian Bureau of Statistics. (2010) 3303.0 - causes of death, Australia, 2008.

[22] R. Becker, J. Silvi, D. Ma Fat, A. L'Hours, and R. Laurenti, "A method for deriving leading causes of death," *WHO Bulletin*, vol. 84, no. 4, pp. 297–304, 2006.

[23] S. Nag, D. Beyer, J. Friedland, P. Grimm, and R. Nath, "American brachytherapy society (ABS) recommendations for transperineal permanent brachytherapy of prostate cancer," *International Journal of Radiation Oncology *Biology* Physics*, vol. 44, no. 4, pp. 789–799, 1999.

[24] S. J. DiBiase, S. C. Jacobs, H. M. Jack, and J. G. Ciril, *Brachytherapy for Prostate Cancer*. Oxford: Academic Press, 2003, pp. 403–408.

[25] D. C. Beyer, "The evolving role of prostate brachytherapy," *Cancer Control*, vol. 8, no. 2, pp. 163–170, 2001.

[26] M. A. Kollmeier and M. J. Zelefsky, "How to select the optimal therapy for early-stage prostate cancer," *Critical Reviews in Oncology/Hematology*, vol. 83, no. 2, pp. 225 – 234, 2012.

[27] R. Kirby and S. G. Madhavan, "Prostate cancer," *Surgery (Oxford)*, vol. 28, no. 12, pp. 594 – 598, 2010.

[28] M. J. Zelefsky, Y. Yamada, X. Pei, M. Hunt, G. Cohen, Z. Zhang, and M. Zaider, "Comparison of tumor control and toxicity outcomes of high-dose intensity-modulated radiotherapy and brachytherapy for patients with favorable risk prostate cancer," *Urology*, vol. 77, no. 4, pp. 986 – 990, 2011.

[29] W. J. Ellis, "Prostate brachytherapy," *Cancer and Metastasis Reviews*, vol. 21, no. 2, p. 125, 2002.

[30] A. Dawson, Nancy and J. Vogelzang, Nicholas, *Prostate Cancer*, ser. Current Clinical Onoclogy. New York: Wiley-Liss, Inc, 1994.

[31] M. J. Zelefsky and J. Whitmore, "Long-term results of retropubic permanent iodine-125 implantation of the prostate for clinically localized prostatic cancer," *The Journal of Urology*, vol. 158, no. 1, pp. 23–30, 1997.

[32] L. Korb and M. Brawer, "Modern brachytherapy for localized prostate cancers: The Northwest Hospital (Seattle) experience," *Reviews in Urology*, vol. 3, no. 1, pp. 51–60, 2001.

[33] L. Potters, "Permanent prostate brachytherapy in men with clinically localised prostate cancer," *Clinical Oncology*, vol. 15, no. 6, pp. 301–315, 2003.

[34] C. A. Lawton, M. DeSilvio, W. R. Lee, L. Gomella, D. Grignon, M. Gillin, G. Morton, T. Pisansky, and H. Sandler, "Results of a phase ii trial of transrectal ultrasound-guided permanent radioactive implantation of the prostate for definitive management of localized adenocarcinoma of the prostate (Radiation Therapy Oncology Group 98-05)," *International Journal of Radiation Oncology*Biology*Physics*, vol. 67, no. 1, pp. 39–47, 2007.

[35] M. Zaider, G. Cohen, J. Meli, and A. B. Rosenfeld, "Quality assurance/quality control issues for intraoperative planning and adaptive repeat planning of image-guided prostate implants," *International Journal of Radiation Oncology *Biology* Physics*, vol. 71, no. S1, pp. S152–S156, 2008.

[36] H. Matzkin, I. Kaver, L. Bramante-Schreiber, R. Agai, O. Merimsky, and M. Inbar, "Comparison between two iodine-125 brachytherapy implant techniques: pre-planning and intra-operative by various dosimetry quality indicators," *Radiotherapy and Oncology*, vol. 68, no. 3, pp. 289–94, 2003.

[37] H. Ragde, "Radiotherapy for prostate cancer: Brachytherapy alone," *Urology*, vol. 64, no. 4, pp. 631–632, 2004.

[38] L. Igidbashian, D. Donath, J. F. Carrier, S. Lassalle, Y. Hervieux, S. David, J. P. Bahary, and D. Taussky, "Poor predictive value of intraoperative real-time dosimetry for prostate seed brachytherapy," *International Journal of Radiation Oncology *Biology* Physics*, vol. 72, no. 2, 2008.

[39] H. Ishiyama, R. Nakamura, T. Satoh, S. Tanji, M. Uemae, S. Baba, and K. Hayakawa, "Differences between intraoperative ultrasound-based dosimetry and postoperative computed tomography-based dosimetry for permanent interstitial prostate brachytherapy," *Brachytherapy*, vol. 9, no. 3, pp. 219–223, 2010.

[40] K. Yoshida, T. Ohashi, A. Yorozu, K. Toya, T. Nishiyama, S. Saito, T. Hanada, Y. Shiraishi, and N. Shigematsu, "Comparison of preplanning and intraoperative planning for I-125 prostate brachytherapy," *Japanese Journal of Clinical Oncology*, vol. 43, no. 4, pp. 383–389, 2013.

[41] R. M. Gewanter, C.-S. Wuu, J. L. Laguna, A. E. Katz, and R. D. Ennis, "Intraoperative preplanning for transperineal ultrasound-guided permanent prostate brachytherapy," *International Journal of Radiation Oncology *Biology* Physics*, vol. 48, no. 2, pp. 377–380, 2000.

[42] A. Polo, C. Salembier, J. Venselaar, and P. Hoskin, "Review of intraoperative imaging and planning techniques in permanent seed prostate brachytherapy," *Radiotherapy and Oncology*, vol. 94, no. 1, pp. 12–23, 2010.

[43] D. A. Todor, M. Zaider, G. Cohen, M. Worman, and M. Zelefsky, "Intraoperative dynamic dosimetry for prostate implants," *Physics in Medicine and Biology*, vol. 48, no. 9, pp. 1153–71, 2003.

[44] T. G. Shanahan, P. J. Nanavati, P. W. Mueller, and R. B. Maxey, "A comparison of permanent prostate brachytherapy techniques: preplan vs. hybrid interactive planning with postimplant analysis," *International Journal of Radiation Oncology *Biology* Physics*, vol. 53, no. 2, pp. 490–496, 2002.

[45] D. Pfeiffer, S. Sutlief, F. Wenzheng, H. M. Pierce, and J. Kofler, "AAPM task group 128: quality assurance tests for prostate brachytherapy ultrasound systems," *Medical Physics*, vol. 35, no. 12, pp. 5471–89, 2008.

[46] L. Gong, P. S. Cho, B. H. Han, K. E. Wallner, S. G. Sutlief, S. D. Pathak, D. R. Haynor, and Y. Kim, "Ultrasonography and fluoroscopic fusion for prostate brachytherapy dosimetry," *International Journal of Radiation Oncology*Biology*Physics*, vol. 54, no. 5, pp. 1322–1330, 2002.

[47] D. Todor, G. Cohen, H. Arnols, and M. Zaider, "Operator-free, film-based 3D seed reconstruction in brachytherapy," *Physics in Medicine and Biology*, vol. 47, no. 12, pp. 2031–2048, 2002.

[48] L. Doyle, A. J. Hesney, K. L. Chapman, H. Liu, P. R. Weiner, A. P. Dicker, Y. Yu, and T. N. Showalter, "Re-implantation of suboptimal prostate seed implantation: Technique with intraoperative treatment planning," *Journal of Contemporary Brachytherapy*, vol. 4, no. 3, pp. 176–181, 2012.

[49] C. National Guideline, "ACR and ASTRO practice guideline for transperineal permanent brachytherapy of prostate cancer," 2010, (NGC) Website.

[50] R. J. Kudchadker, T. J. Pugh, D. A. Swanson, T. L. Bruno, Y. Bolukbasi, and S. J. Frank, "Preoperative treatment planning with intraoperative optimization can achieve consistent high-quality implants in prostate brachytherapy," *Medical Dosimetry*, vol. 37, no. 4, pp. 387–390, 2012.

[51] R. G. Stock and N. N. Stone, "Importance of post-implant dosimetry in permanent prostate brachytherapy," *European Urology*, vol. 41, no. 4, pp. 434–439, 2002.

[52] B. Al-Qaisieh, D. W. Smith, E. Brearley, S. St. Clair, and P. Bownes, "Comprehensive I-125 multi-seed comparison for prostate brachytherapy: Dosimetry and visibility analysis," *Radiotherapy and Oncology*, vol. 84, no. 2, pp. 140–147, 2007.

[53] F. G. Mitri, B. J. Davis, J. F. Greenleaf, and M. Fatemi, "In vitro comparative study of vibro-acoustography versus pulse-echo ultrasound in imaging permanent prostate brachytherapy seeds," *Ultrasonics*, vol. 49, no. 1, pp. 31–38, 2009.

[54] J. Mamou, S. Ramachandran, and E. J. Feleppa, "Angle-dependent ultrasonic detection and imaging of two types of brachytherapy seeds using singular spectrum analysis," *Journal of the Acoustical Society of America*, vol. 124, no. 6, pp. 347–52, 2008.

[55] L. Junghoon and et al., "Intraoperative 3d reconstruction of prostate brachytherapy implants with automatic pose correction," *Physics in Medicine and Biology*, vol. 56, no. 15, pp. 5011–27, 2011.

[56] M. J. Zelefsky, M. Worman, G. N. Cohen, X. Pei, M. Kollmeier, J. Yamada, B. Cox, Z. Zhang, E. Bieniek, L. Dauer, and M. Zaider, "Real-time intraoperative computed tomography assessment of quality of permanent interstitial seed implantation for prostate cancer," *Urology*, vol. 76, no. 5, pp. 1138–1142, 2010.

[57] H. Westendorp, C. J. Hoekstra, A. van't Riet, A. W. Minken, and J. J. Immerzeel, "Intraoperative adaptive brachytherapy of iodine-125 prostate implants guided by c-arm cone-beam computed tomography-based dosimetry," *Brachytherapy*, vol. 6, no. 4, pp. 231–237, 2007.

[58] M. Steggerda and H. van der Poel, "The applicability of simultaneous CT-US imaging for the evaluation of prostate implants," *Radiotherapy and Oncology*, vol. 71, no. S2, pp. S104–S105, 2004.

[59] M. Campbell, E. Heijne, G. Meddeler, E. Pernigotti, and W. Snoeys, "A readout chip for a 64×64 pixel matrix with 15-bit single photon counting," *IEEE Transactions on Nuclear Science*, vol. 45, no. 3, pp. 751–753, 1998.

[60] X. Llopart and M. Campbell, "First test measurements of a 64k pixel readout chip working in single photon counting mode," *Nuclear Instruments and Methods in Physics Research Section A: Accelerators, Spectrometers, Detectors and Associated Equipment*, vol. 509, no. 13, pp. 157–163, 2003.

[61] M. Weaver, J. Green, M. Petasecca, M. L. F. Lerch, D. Cutajar, D. Franklin, J. Jakubek, M. G. Carolan, M. Conway, S. Pospisil, T. Kron, P. Metcalfe, M. Zaider, and A. B. Rosenfeld, "Three-dimensional dosimetry imaging of I-125 plaque for eye cancer treatment," *Nuclear Instruments and Methods in Physics Research Section A: Accelerators, Spectrometers, Detectors and Associated Equipment*, vol. 633, no. S1, 2011.

[62] L. S. Pinsky, A. Empl, H. Son, N. Stoffle, C. Amberboy, J. Hauss, J. Jakubek, Z. Vykydal, D. Turecek, S. Pospisil, K. Lee, E. Semones, N. Zapp, H. Kitamura, O. Ploc, Y. Uchihori, Y. Nakahiro, and D. Cooke, "Preparing for the

first Medipix detectors in space," in *Aerospace Conference, 2012 IEEE*, 2012, pp. 1–6.

[63] A. Rozenfeld and J. Jakubek, "Imaging method and system," 2012. [Online]. Available: https://www.google.com/patents/US20120230574

[NIST] NIST. Tables of x-ray mass attenuation coefficients and mass energy-absorption coefficients.

[64] S. Agostinelli, J. Allison, K. Amako, J. Apostolakis, H. Araujo, P. Arce, M. Asai, D. Axen, S. Banerjee, G. Barrand, F. Behner, L. Bellagamba, J. Boudreau, L. Broglia, A. Brunengo, H. Burkhardt, S. Chauvie, J. Chuma, R. Chytracek, G. Cooperman, G. Cosmo, P. Degtyarenko, A. Dell'Acqua, G. Depaola, D. Dietrich, R. Enami, A. Feliciello, C. Ferguson, H. Fesefeldt, G. Folger, F. Foppiano, A. Forti, S. Garelli, S. Giani, R. Giannitrapani, D. Gibin, J. G. Cadenas, I. Gonzlez, G. G. Abril, G. Greeniaus, W. Greiner, V. Grichine, A. Grossheim, S. Guatelli, P. Gumplinger, R. Hamatsu, K. Hashimoto, H. Hasui, A. Heikkinen, A. Howard, V. Ivanchenko, A. Johnson, F. Jones, J. Kallenbach, N. Kanaya, M. Kawabata, Y. Kawabata, M. Kawaguti, S. Kelner, P. Kent, A. Kimura, T. Kodama, R. Kokoulin, M. Kossov, H. Kurashige, E. Lamanna, T. Lampn, V. Lara, V. Lefebure, F. Lei, M. Liendl, W. Lockman, F. Longo, S. Magni, M. Maire, E. Medernach, K. Minamimoto, P. M. de Freitas, Y. Morita, K. Murakami, M. Nagamatu, R. Nartallo, P. Nieminen, T. Nishimura, K. Ohtsubo, M. Okamura, S. O'Neale, Y. Oohata, K. Paech, J. Perl, A. Pfeiffer, M. Pia, F. Ranjard, A. Rybin, S. Sadilov, E. D. Salvo, G. Santin, T. Sasaki, N. Savvas, Y. Sawada, S. Scherer, S. Sei, V. Sirotenko, D. Smith, N. Starkov, H. Stoecker, J. Sulkimo, M. Takahata, S. Tanaka, E. Tcherniaev, E. S. Tehrani, M. Tropeano, P. Truscott, H. Uno, L. Urban, P. Urban, M. Verderi, A. Walkden, W. Wander, H. Weber, J. Wellisch, T. Wenaus, D. Williams, D. Wright, T. Yamada, H. Yoshida, and D. Zschiesche, "Geant4: a simulation toolkit," *Nuclear Instruments and*

Methods in Physics Research Section A: Accelerators, Spectrometers, Detectors and Associated Equipment, vol. 506, no. 3, pp. 250 – 303, 2003.

[65] J. Allison, K. Amako, J. Apostolakis, H. Araujo, P. Dubois, M. Asai, G. Barrand, R. Capra, S. Chauvie, R. Chytracek, G. Cirrone, G. Cooperman, G. Cosmo, G. Cuttone, G. Daquino, M. Donszelmann, M. Dressel, G. Folger, F. Foppiano, J. Generowicz, V. Grichine, S. Guatelli, P. Gumplinger, A. Heikkinen, I. Hrivnacova, A. Howard, S. Incerti, V. Ivanchenko, T. Johnson, F. Jones, T. Koi, R. Kokoulin, M. Kossov, H. Kurashige, V. Lara, S. Larsson, F. Lei, O. Link, F. Longo, M. Maire, A. Mantero, B. Mascialino, I. McLaren, P. Lorenzo, K. Minamimoto, K. Murakami, P. Nieminen, L. Pandola, S. Parlati, L. Peralta, J. Perl, A. Pfeiffer, M. Pia, A. Ribon, P. Rodrigues, G. Russo, S. Sadilov, G. Santin, T. Sasaki, D. Smith, N. Starkov, S. Tanaka, E. Tcherniaev, B. Tome, A. Trindade, P. Truscott, L. Urban, M. Verderi, A. Walkden, J. Wellisch, D. Williams, D. Wright, and H. Yoshida, "Geant4 developments and applications," *IEEE Transactions on Nuclear Science*, vol. 53, no. 1, pp. 270–278, 2006.

[66] S. Chauvie, S. Guatelli, V. Ivanchenko, F. Longo, A. Mantero, B. Mascialino, P. Nieminen, L. Pandola, S. Parlati, L. Peralta, M. Pia, M. Piergentili, P. Rodrigues, S. Saliceti, and A. Tnndade, "Geant4 low energy electromagnetic physics," in *Nuclear Science Symposium Conference Record, 2004 IEEE*, vol. 3, 2004, pp. 1881–1885.

[67] J. Baro, J. Sempau, J. Fernandez-Varea, and F. Salvat, "PENELOPE: An algorithm for Monte Carlo simulation of the penetration and energy loss of electrons and positrons in matter," *Nuclear Inst. and Methods in Physics Research, B*, vol. 100, no. 1, pp. 31–46, 1995.

[68] K. Amako, S. Guatelli, V. Ivanchenko, M. Maire, B. Mascialino, K. Murakami, P. Nieminen, L. Pandola, S. Parlati, M. Pia, M. Piergentili, T. Sasaki, and L. Urban, "Comparison of Geant4 electromagnetic physics models against

the NIST reference data," *Nuclear Science, IEEE Transactions on*, vol. 52, no. 4, pp. 910–918, 2005.

[69] I. Ali, O. Algan, S. Thompson, P. Sindhwani, T. Herman, C. Chih-Yao, and S. Ahmad, "A comparative study of seed localization and dose calculation on pre- and post-implantation ultrasound and CT images for low-dose-rate prostate brachytherapy," *Physics in Medicine and Biology*, vol. 54, no. 18, pp. 5595–611, 2009.

[70] D. Vavrik and J. Jakubek, "Radiogram enhancement and linearization using the beam hardening correction method," *Nuclear Instruments and Methods in Physics Research Section A: Accelerators, Spectrometers, Detectors and Associated Equipment*, vol. 607, no. 1, pp. 212 – 214, 2009.

[71] J. Radon, "On the determination of functions from their integral values along certain manifolds," *IEEE Transactions on Medical Imaging*, vol. 5, no. 4, pp. 170–176, 1986.

[72] L. Shepp and B. Logan, "The fourier reconstruction of a head section," *IEEE Transactions on Nuclear Science*, vol. 21, no. 3, pp. 21–43, 1974.

[73] B. F. Hutton, "An introduction to iterative reconstruction," *Alasbimn Journal*, vol. 5, no. 18, 2002.

[74] A. Brunetti and B. Golosio, "A new algorithm for computer tomographic reconstruction from partial view projections," *Medical Physics*, vol. 28, no. 4, pp. 462–468, 2001.

[75] J. Jakubek, "Energy-sensitive X-ray radiography and charge sharing effect in pixelated detector," *Nuclear Instruments and Methods in Physics Research Section A: Accelerators, Spectrometers, Detectors and Associated Equipment*, vol. 607, no. 1, pp. 192 – 195, 2009.

[76] CIRS, "CIRS tissue simulation & phantom technology," 2015. [Online]. Available: http://www.cirsinc.com/

[77] I. Jandejsek, J. Dammer, J. Jakubek, D. Vavrik, and J. Zemlicka, "Contrast optimization in x-ray radiography with single photon counting imagers of Medipix type," *Journal of Instrumentation*, vol. 7, no. 12, p. C12011, 2012.

[78] A. Al-Hebshi, G. Morton, and R. Sankraatcha, "A dosimetric comparison of high dose rate (HDR) and low dose-rate (LDR) prostate brachytherapy," *Radiotherapy and Oncology*, vol. 72, p. S36, 2004.

[79] AIHW and AACR, "Prevention of high-dose-rate brachytherapy accidents," *Annals of the ICRP*, vol. 35, no. 2, pp. iii–iii, 2005.

[80] R. Accorsi and S. D. Metzler, "Analytic determination of the resolution-equivalent effective diameter of a pinhole collimator," pp. 750–63, 2004.

[81] AIHW, "Cancer in Australia: an overview, 2008," Australian Institute of Health and Welfare, Tech. Rep., 2008.

[82] T. Akimoto, H. Katoh, Y. Kitamoto, T. Tamaki, K. Harada, K. Shirai, and T. Nakano, "Rectal bleeding after high-dose-rate brachytherapy combined with hypofractionated external-beam radiotherapy for localized prostate cancer: Impact of rectal dose in high-dose-rate brachytherapy on occurrence of grade 2 or worse rectal bleeding," *International Journal of Radiation Oncology *Biology* Physics*, vol. 65, no. 2, pp. 364–370, 2006.

[83] T. Akimoto, H. Katoh, S.-e. Noda, K. Ito, T. Yamamoto, B. Kashiwagi, and T. Nakano, "Acute genitourinary toxicity after high dose rate (HDR) brachytherapy combined with hypofractionated external-beam radiation therapy for localized prostate cancer: Second analysis to determine the correlation between the urethral dose in HDR brachytherapy and the severity of acute genitourinary toxicity," *International Journal of Radiation Oncology *Biology* Physics*, vol. 63, no. 2, pp. 472–478, 2005.

[84] Z. A. Allen, G. S. Merrick, W. M. Butler, K. E. Wallner, B. Kurko, R. L. Anderson, B. C. Murray, and R. W. Galbreath, "Detailed urethral dosimetry in

the evaluation of prostate brachytherapy-related urinary morbidity," *International Journal of Radiation Oncology *Biology* Physics*, vol. 62, no. 4, pp. 981–987, 2005.

[85] B. Al-Qaisieh, "Pre- and post-implant dosimetry: an inter-comparison between UK prostate brachytherapy centres," *Radiotherapy and Oncology*, vol. 66, no. 2, pp. 181–183, 2003.

[86] B. Al-Qaisieh, D. Ash, D. M. Bottomley, and B. M. Carey, "Impact of prostate volume evaluation by different observers on CT-based post-implant dosimetry," *Radiotherapy and Oncology*, vol. 62, no. 3, pp. 267–273, 2002.

[87] B. Al-Qaisieh, T. Witteveen, B. Carey, A. Henry, D. Bottomley, J. Smith, K. Franks, and P. Bownes, "Correlation between pre- and postimplant dosimetry for iodine-125 seed implants for localized prostate cancer," *International Journal of Radiation Oncology *Biology* Physics*, vol. 75, no. 2, pp. 626–630, 2009.

[88] M. D. Altschuler, P. A. Findlay, and R. D. Epperson, "Rapid, accurate, three-dimensional location of multiple seeds in implant radiotherapy treatment planning," *Physics in Medicine and Biology*, vol. 28, no. 11, p. 1305, 1983.

[89] M. D. Altschuler and A. Kassaee, "Automated matching of corresponding seed images of three simulator radiographs to allow 3D triangulation of implanted seeds," *Physics in Medicine and Biology*, vol. 42, no. 2, p. 293, 1997.

[90] M. Aoki, K. Miki, H. Sasaki, M. Kido, J. Shirahama, S. Takagi, M. Kobayashi, C. Honda, and C. Kanehira, "Evaluation of rectal bleeding factors associated with prostate brachytherapy," *Japanese Journal of Radiology*, vol. 27, no. 10, p. 444, 2009.

[91] D. Ash, B. Al-Qaisieh, D. Bottomley, B. Carey, and J. Joseph, "The correlation between D90 and outcome for I-125 seed implant monotherapy for localised prostate cancer," *Radiotherapy and Oncology*, vol. 79, no. 2, pp. 185–189, 2006.

[92] L. Astrom, D. Pedersen, C. Mercke, S. Holmang, and K. A. Johansson, "Long-term outcome of high dose rate brachytherapy in radiotherapy of localised prostate cancer," *Radiotherapy and Oncology*, vol. 74, no. 2, 2005.

[93] N. B.V, "Brachytherapy: high precision, targeted radiotherapy," 2010.

[94] M. Batic, J. Burger, V. Cindro, G. Kramberger, I. Mandic, M. Mikuz, A. Studen, and M. Zavrtanik, "Verification of high dose rate Ir-192 source position during brachytherapy treatment," *IEEE Transactions on Nuclear Science*, vol. 58, no. 5, pp. 2250–56, 2011.

[95] F. J. Beekman, A. P. Colijn, B. Vastenhouw, V. M. Wiegant, and M. A. F. M. Gerrits, "High-resolution emission tomography of small laboratory animals: physics and gamma-astronomy meet molecular biology," *Nuclear Instruments and Methods in Physics Research Section A: Accelerators, Spectrometers, Detectors and Associated Equipment*, vol. 509, no. 1-3, pp. 229–234, 2003.

[96] L. E. C. M. Blank, D. Gonzalez Gonzalez, T. M. de Reijke, N. F. Dabhoiwala, and K. Koedooder, "Brachytherapy with transperineal iodine-125 seeds for localized prostate cancer," *Radiotherapy and Oncology*, vol. 57, no. 3, pp. 307–313, 2000.

[97] E. J. Bloemen-van Gurp, L. H. P. Murrer, B. Haanstra, F. van Gils, A. Dekker, B. J. Mijnheer, and P. Lambin, "In-vivo dosimetry using a linear MOSFET-array dosimeter to determine the urethra dose in I-125 permanent prostate implants," *International Journal of Radiation Oncology *Biology* Physics*, vol. 73, no. 1, pp. 314–321, 2009.

[98] I. A. Brezovich, J. Duan, P. N. Pareek, J. Fiveash, and M. Ezekiel, "In vivo urethral dose measurements: A method to verify high dose rate prostate treatments," *Medical Physics*, vol. 27, no. 10, pp. 2297–2301, 2000.

[99] J. Bucci, W. J. Morris, M. Keyes, I. Spadinger, S. Sidhu, and V. Moravan, "Predictive factors of urinary retention following prostate brachytherapy," *In-*

*ternational Journal of Radiation Oncology *Biology* Physics*, vol. 53, no. 1, pp. 91–98, 2002.

[100] M. Bues, E. J. Holupka, P. Meskell, and I. D. Kaplan, "Effect of random seed placement error in permanent transperineal prostate seed implant," *Radiotherapy and Oncology*, vol. 79, no. 1, pp. 70–4, 2006.

[101] A. Bujold, D. Donath, S. Lassalle, J.-P. Bahary, and D. Taussky, "Can intraoperative inverse planning predict rectal dose in permanent seed implants of the prostate?" *Brachytherapy*, vol. 5, no. 2, p. 106, 2006.

[102] C. Buron, B. Le Vu, J.-M. Cosset, P. Pommier, D. Peiffert, M. Delannes, T. Flam, S. Guerif, N. Salem, L. Chauveinc, and A. Livartowski, "Brachytherapy versus prostatectomy in localized prostate cancer: Results of a french multicenter prospective medico-economic study," *International Journal of Radiation Oncology *Biology* Physics*, vol. 67, no. 3, pp. 812–822, 2007.

[103] J. A. Cesaretti, R. G. Stock, D. P. Atencio, S. A. Peters, C. A. Peters, R. J. Burri, N. N. Stone, and B. S. Rosenstein, "A genetically determined dose-volume histogram predicts for rectal bleeding among patients treated with prostate brachytherapy," *International Journal of Radiation Oncology *Biology* Physics*, vol. 68, no. 5, pp. 1410–1416, 2007.

[104] G. Cheng, H. Liu, L. Liao, Y. Yu, G. B. David, M.D, R. Philip, H. Hedvig, and Ph.D, *Image-Guided Brachytherapy*. Oxford: Elsevier, 2002, pp. 125–130.

[105] M.-S. Chew, J. Xue, C. Houser, V. Misic, J. Cao, T. Cornwell, J. Handler, Y. Yu, and E. Gressen, "Impact of transrectal ultrasound- and computed tomography-based seed localization on postimplant dosimetry in prostate brachytherapy," *Brachytherapy*, vol. 8, no. 2, pp. 255–264, 2009.

[106] O. Chibani and J. F. Williamson, "MCPI: a sub-minute monte carlo dose calculation engine for prostate implants," *Medical Physics, vol.32, no.12, Dec*, vol. 32, no. 12, pp. 3688–98, 2005.

[107] B. Cyganek and J. P. Siebert, *An Introduction to 3D Computer Vision Techniques and Algorithms*. John Wiley and Sons, Ltd., 2009.

[108] J. Dammer, P. M. Frallicciardi, J. Jakubek, M. Jakubek, S. Pospisil, E. Prenerova, D. Vavrik, L. Volter, F. Weyda, and R. Zemek, "Real-time in-vivo μ-imaging with Medipix2," *Nuclear Instruments and Methods in Physics Research Section A: Accelerators, Spectrometers, Detectors and Associated Equipment*, vol. 607, no. 1, pp. 205–207, 2009.

[109] R. Das, W. Toye, T. Kron, S. Williams, and G. Duchesne, "Thermoluminescence dosimetry for in-vivo verification of high dose rate brachytherapy for prostate cancer," *Australasian Physical and Engineering Sciences in Medicine*, vol. 30, no. 3, p. 178, 2007.

[110] B. Davis, "American Brachytherapy Society consensus guidelines for transrectal ultrasound-guided permanent prostate brachytherapy," *Brachytherapy*, vol. 11, pp. 6–19, 2012.

[111] M. De Brabandere, C. Kirisits, R. Peeters, K. Haustermans, and F. Van den Heuvel, "Accuracy of seed reconstruction in prostate postplanning studied with a CT- and MRI-compatible phantom," *Radiotherapy and Oncology*, vol. 79, no. 2, pp. 190–197, 2006.

[112] E. Dehghan, A. K. Jain, M. Moradi, X. Wen, W. James Morris, S. E. Salcudean, and G. Fichtinger, "Brachytherapy seed reconstruction with joint-encoded C-arm single-axis rotation and motion compensation," *Medical Image Analysis*, vol. 15, no. 5, pp. 760–771, 2011.

[113] E. Dehghan, J. Lee, M. Moradi, X. Wen, G. Fichtinger, S. Salcudean, T. Jiang, N. Navab, J. Pluim, and M. Viergever, *Prostate Brachytherapy Seed Reconstruction Using C-Arm Rotation Measurement and Motion Compensation Medical Image Computing and Computer-Assisted Intervention MICCAI 2010*, ser. Lecture Notes in Computer Science. Springer Berlin / Heidelberg, 2010, vol. 6361, pp. 283–290.

[114] E. Dehghan, M. Moradi, X. Wen, D. French, J. Lobo, W. Morris, S. E. Salcudean, and G. Fichtinger, "Prostate implant reconstruction from C-arm images with motion-compensated tomosynthesis," *Medical Physics*, vol. 38, no. 10, pp. 5290–5302, 2011.

[115] M. Ding, Z. Wei, L. Gardi, D. B. Downey, and A. Fenster, "Needle and seed segmentation in intra-operative 3D ultrasound-guided prostate brachytherapy," *Ultrasonics*, vol. 44, no. S1, pp. 331–336, 2006.

[116] J. M. Fagerstrom, J. A. Micka, and L. A. DeWerd, "Response of an implantable MOSFET dosimeter to Ir-192 HDR radiation," *Medical Physics*, vol. 35, no. 12, pp. 5729–37, 2008.

[117] G. Fichtinger, J. P. Fiene, C. W. Kennedy, G. Kronreif, I. Iordachita, D. Y. Song, E. C. Burdette, and P. Kazanzides, "Robotic assistance for ultrasound-guided prostate brachytherapy," *Medical Image Analysis*, vol. 12, no. 5, pp. 535–45, 2008.

[118] L. Fog, R. Nicholls, and T. van Doorn, "On the use of Kodak CR film for quality assurance of needle loading in I-125 seed prostate brachytherapy," *Australasian Physical and Engineering Sciences in Medicine*, vol. 30, no. 3, p. 221, 2007.

[119] S. Fogh, L. Doyle, A. Yu, J. Li, P. Weiner, D. Suh, E. Comber, A. P. Dicker, Y. Yu, Y. Xiao, and A. Harrison, "A comparison of preplan transrectal ultrasound with preplan-CT in assessing volume and number of seeds needed for real-time ultrasound-based intra-operative planning in prostate I-125 seed implantation," *Brachytherapy*, vol. 9, no. 4, pp. 335–340, 2010.

[120] F. van der Have and J. B. Freek, "Photon penetration and scatter in micro-pinhole imaging: a monte carlo investigation," *Physics in Medicine and Biology*, vol. 49, no. 8, pp. 1369–86, 2004.

[121] D. B. Fuller, H. Jin, J. A. Koziol, and A. C. Feng, "CT-ultrasound fusion prostate brachytherapy: A dynamic dosimetry feedback and improvement

method. A report of 54 consecutive cases," *Brachytherapy*, vol. 4, no. 3, pp. 207–216, 2005, 1538-4721.

[122] P. Ghadjar, O. Matzinger, B. Isaak, F. Behrensmeier, A. Stroux, C. A. Rentsch, G. N. Thalmann, and D. M. Aebersold, "Association of urethral toxicity with dose exposure in combined high-dose-rate brachytherapy and intensity-modulated radiation therapy in intermediate- and high-risk prostate cancer," *Radiotherapy and Oncology*, vol. 91, no. 2, pp. 237–242, 2009.

[123] A. H. Goldan, K. S. Karim, A. Reznik, C. B. Caldwell, and J. A. Rowlands, "Photon counting readout pixel array in 0.18-μm CMOS technology for on-line gamma-ray imaging of palladium-103 seeds for permanent breast seed implant (PBSI) brachytherapy," *SPIE - The International Society for Optical Engineering*, vol. 6913, pp. 69 130S–12, 2008.

[124] J. C. Gore and S. Leeman, "The reconstruction of objects from incomplete projections," *Physics in Medicine and Biology*, vol. 25, no. 1, p. 129, 1980.

[125] J. B. A. Habraken, K. d. Bruin, M. Shehata, J. Booij, and et al., "Evaluation of high-resolution pinhole SPECT using a small rotating animal," *The Journal of Nuclear Medicine*, vol. 42, no. 12, pp. 1863–9, 2001.

[126] B. H. Han, K. Wallner, G. Merrick, W. Butler, S. Sutlief, and J. Sylvester, "Prostate brachytherapy seed identification on post-implant TRUS images," *Medical Physics*, vol. 30, no. 5, pp. 898–900, 2003.

[127] Z. Han, "Seed localisation in LDR prostate brachytherapy using in-body high resolution detectors with pinhole collimators," Ph.D. dissertation, 2009.

[128] R. Hartley, *Multiple View Geometry in Computer Vision*. Cambridge, UK: Cambridge, 2003.

[129] R. L. Hatton, B. F. Hutton, S. Angelides, K. K. L. Choong, and G. Larcos, "Improved tolerance to missing data in myocardial perfusion SPET using OSEM

reconstruction," *European Journal of Nuclear Medicine and Molecular Imaging*, vol. 31, no. 6, pp. 857–61, 2004.

[130] B. H. Heintz, R. E. Wallace, and J. M. Hevezi, "Comparison of I-125 sources used for permanent interstitial implants," *Medical Physics*, vol. 28, no. 4, pp. 671–682, 2001.

[131] K. Helle and J. Reed, "Brachytherapy template adaptor," Patent US20 130 012 757 A1, 2011.

[132] B. Helmick, R. Tarver, R. Chan, and S. Caldwell, "Evaluation of post-plan dosimetry using TRUS and CT after transperineal prostate seed implant," *Medical Dosimetry*, vol. 27, no. 4, pp. 289–293, 2002.

[133] G. T. Herman and A. Kuba, "Discrete tomography in medical imaging," *Proceedings of the IEEE*, vol. 91, no. 10, pp. 1612–1626, 2003.

[134] R. Holly, G. C. Morton, R. Sankreacha, N. Law, T. Cisecki, D. A. Loblaw, and H. T. Chung, "Use of cone-beam imaging to correct for catheter displacement in high dose-rate prostate brachytherapy," *Brachytherapy*, vol. 10, pp. 299–305, 2011.

[135] J.-Y. Hong, J.-E. Rah, T.-S. Suh, H.-S. Jang, and S. Kim, "Overlapped seed localization in seed implant brachytherapy," *Medical Engineering and Physics*, vol. 31, no. 2, pp. 261–267, 2009.

[136] P. J. Hoskin, P. J. Bownes, P. Ostler, K. Walker, and L. Bryant, "High dose rate afterloading brachytherapy for prostate cancer: catheter and gland movement between fractions," *Radiotherapy and Oncology, vol.68, no.3, Sept*, vol. 68, no. 3, pp. 285–288, 2003.

[137] H. M. Hudson and R. S. Larkin, "Accelerated image reconstruction using ordered subsets of projection data," *IEEE Transactions on Medical Imaging*, vol. 13, no. 4, pp. 601–609, 1994.

[138] Ishiyama, Satoh, Kitano, Tsumura, Kotani, Okusa, Uemae, Baba, and Hayakawa, "Four-year experience of interstitial permanent brachytherapy for japanese men with localized prostate cancer," *Japanese Journal of Clinical Oncology*, vol. 38, no. 7, p. 469, 2008.

[139] H. Ishiyama, R. Nakamura, T. Satoh, S. Tanji, M. Uemae, S. Baba, and K. Hayakawa, "Inter-software variability in post-implanted CT analysis for interstitial permanent brachytherapy for prostate cancer: Differences in automatically detected seed location," *Radiotherapy and Oncology*, vol. 89, no. 2, pp. 214–216, 2008.

[140] T. Ivanova, L. Gilbert, and D. A. Todor, "High-dose-rate brachytherapy source tracking by MOSFET dosimetry system," *Brachytherapy*, vol. 8, no. 2, pp. 130–130, 2009.

[141] P. Iversen, L. Nielsen, M. Bak, F. Rasmussen, N. Juul, S. Torp-Pedersen, F. Laursen, H. H. Holm, and H. Von Der Maase, "Ultrasonically guided iodine-125 seed implantation with external radiation in management of localized prostatic carcinoma," *Urology*, vol. 34, no. 4, pp. 181–186, 1989.

[142] A. Jain, A. Deguet, I. Iordachita, G. Chintalapani, S. Vikal, J. Blevins, Y. Le, E. Armour, C. Burdette, D. Song, and G. Fichtinger, "Intra-operative 3D guidance and edema detection in prostate brachytherapy using a non-isocentric C-arm," *Medical Image Analysis*, vol. 3, pp. 731–743, 2010.

[143] J. Jakubek, J. Dammer, C. Granja, T. Holy, S. Pospisil, and J. Uher, "Compact system for high resolution X-ray transmission radiography, in-line phase enhanced imaging and micro CT of biological samples," in *IEEE Nuclear Science Symposium Conference Record*, vol. 2, 2011, pp. 1077–1080.

[144] I. Jandejsek, P. Soukup, and J. Jakubek, "Image processing for X-ray transmission radiography with 3D voxel detector," *Journal of Instrumentation*, vol. 6, no. 12, p. C12061, 2011.

[145] R. J. Jaszczak and et al., "Pinhole collimation for ultra-high-resolution, small-field-of-view spect," *Physics in Medicine and Biology*, vol. 39, no. 3, pp. 425–437, 1994.

[146] L. Junghoon, C. Labat, A. K. Jain, D. Y. Song, E. C. Burdette, G. Fichtinger, and J. L. Prince, *Optimal matching for prostate brachytherapy seed localization with dimension reduction*. Proceedings 12th International Conference. Springer Verlag. Part, 2009, pp. 59–66.

[147] H. Ju-Young, R. Jeong-Eun, S. Tae-Suk, J. Hong-Seok, and K. Siyong, "Overlapped seed localization in seed implant brachytherapy," *Medical Engineering and Physics*, vol. 31, no. 2, pp. 261–7, 2009.

[148] M. Keyes, S. Miller, V. Moravan, T. Pickles, M. McKenzie, H. Pai, M. Liu, W. Kwan, A. Agranovich, I. Spadinger, V. Lapointe, R. Halperin, and W. J. Morris, "Predictive factors for acute and late urinary toxicity after permanent prostate brachytherapy: Long-term outcome in 712 consecutive patients," *International Journal of Radiation Oncology*Biology*Physics*, vol. 73, no. 4, pp. 1023–1032, 2009.

[149] Kono, nbsp, Y, Kubota, K, Mitsumoto, T, Tanaka, A, Ishibashi, Kobayashi, Ito, Itami, J, Kanemura, M, Minowada, and S, "Scintigraphic detection of I-125 seeds after permanent brachytherapy for prostate cancer," *The Journal of Nuclear Medicine*, vol. 49, no. 4, pp. 541–5, 2008.

[150] F. Krejci and et al., "Single grating method for low dose 1-D and 2-D phase contrast X-ray imaging," *Journal of Instrumentation*, vol. 6, no. 1, p. C01073, 2011.

[151] S. Krimmel, J. Baumann, Z. Kiss, A. Kuba, A. Nagy, and J. Stephan, "Discrete tomography for reconstruction from limited view angles in non-destructive testing," *Electronic Notes in Discrete Mathematics*, vol. 20, no. 0, pp. 455–474, 2005.

[152] A. Kuba, L. Rusko, L. Rodek, and Z. Kiss, "Preliminary studies of discrete tomography in neutron imaging," *IEEE Transactions on Nuclear Science*, vol. 52, no. 1, pp. 380–385, 2005.

[153] I. Kwan, I. Cornelius, A. Howie, and A. Rosenfeld, "Development of MOSFET array for in vivo rectal dosimetry in HDR brachytherapy," *Australasian Physical and Engineering Sciences in Medicine*, vol. 29, no. 1, pp. 149–50, 2006.

[154] I. S. Kwan, D. Wilkinson, D. Cutajar, M. Lerch, A. Rosenfeld, A. Howie, J. Bucci, Y. Chin, and V. L. Perevertaylo, "The effect of rectal heterogeneity on wall dose in high dose rate brachytherapy," *Medical Physics*, vol. 36, no. 1, pp. 224–32, 2009.

[155] S. E. M. Langley and R. W. Laing, "4D brachytherapy, a novel real-time prostate brachytherapy technique using stranded and loose seeds," *BJU International*, vol. 109, pp. 1–6, 2012.

[156] P. Lindsay, J. Battista, and J. Van Dyk, "The impact of seed localization uncertainties on predicting I-125 prostate brachytherapy dose distributions," *Proceedings of the 22nd Annual International Conference of the IEEE Engineering in Medicine and Biology Society*, vol. 4, pp. 2675–2678, 2000.

[157] X. Llopart, R. Ballabriga, M. Campbell, L. Tlustos, and W. Wong, "Timepix, a 65k programmable pixel readout chip for arrival time, energy and/or photon counting measurements," *Nuclear Instruments and Methods in Physics Research Section A: Accelerators, Spectrometers, Detectors and Associated Equipment*, vol. 581, no. 12, pp. 485–494, 2007.

[158] W. Lu, J. M. Michalski, J. L. Garcia-Ramirez, and C. Hallemeier, "TRUS guided intraoperative prostate seed implantation based on preplanning," *International Journal of Radiation Oncology*Biology*Physics*, vol. 72, no. S1, pp. S571–S571, 2008.

[159] A. Mahmoudieh, C. Tremblay, L. Beaulieu, B. Lachance, F. Harel, E. Lessard, J. Pouliot, and E. Vigneault, "Anatomy-based inverse planning dose optimization in HDR prostate implant: A toxicity study," *Radiotherapy and Oncology*, vol. 75, no. 3, pp. 318–324, 2005.

[160] L. K. McNeely, N. N. Stone, J. Presser, J. H. Chircus, and R. G. Stock, "Influence of prostate volume on dosimetry results in real-time I-125 seed implantation," *International Journal of Radiation Oncology *Biology* Physics*, vol. 58, no. 1, pp. 292–9, 2004.

[161] G. J. Meijer, H. A. van den Berg, C. W. Hurkmans, P. E. Stijns, and J. H. Weterings, "Dosimetric comparison of interactive planned and dynamic dose calculated prostate seed brachytherapy," *Radiotherapy and Oncology*, vol. 80, no. 3, pp. 378–384, 2006.

[162] S. R. Meikle, P. Kench, A. G. Weisenberger, R. Wojcik, M. F. Smith, S. Majewski, S. Eberl, R. R. Fulton, A. B. Rosenfeld, and M. J. Fulham, "A prototype coded aperture detector for small animal SPECT," *IEEE Transactions on Nuclear Science, vol.49, no.5, pt.1, Oct*, vol. 49, no. 5, pp. 2167–71, 2002.

[163] G. S. Merrick, W. M. Butler, B. G. Tollenaar, R. W. Galbreath, and J. H. Lief, "The dosimetry of prostate brachytherapy-induced urethral strictures," *International Journal of Radiation Oncology *Biology* Physics*, vol. 52, no. 2, pp. 461–468, 2002.

[164] S. D. Metzler, J. E. Bowsher, K. L. Greer, and R. J. Jaszczak, "Analytic determination of the pinhole collimator's point-spread function and RMS resolution with penetration," *IEEE transactions on medical imaging*, vol. 21, no. 8, pp. 878–87, 2002.

[165] S. Miranda, P. Antonini, S. Roldan, A. Tormo, S. Rodriguez, M. Santos, J. Richart, F. Lliso, J. Perez-Calatayud, V. Carmona, and F. Ballester, "Dose escalation in permanent brachytherapy for prostate cancer: Preliminary results," *Brachytherapy*, vol. 9, no. S1, pp. S100–S101, 2010.

[166] P. Mobit and I. Badragan, "Dose perturbation effects in prostate seed implant brachytherapy with I-125," *Physics in Medicine and Biology*, vol. 49, no. 14, pp. 3171–8, 2004.

[167] M. A. Moerland, M. J. H. van Deursen, S. G. Elias, M. van Vulpen, I. M. Jrgenliemk-Schulz, and J. J. Battermann, "Decline of dose coverage between intraoperative planning and post implant dosimetry for I-125 permanent prostate brachytherapy: Comparison between loose and stranded seed implants," *Radiotherapy and Oncology*, vol. 91, no. 2, pp. 202–206, 2009.

[168] M. Moradi, S. Sara Mahdavi, S. Deshmukh, J. Lobo, E. Dehghan, G. Fichtinger, W. Morris, S. Salcudean, A. Martel, and T. Peters, *Towards Intra-operative Prostate Brachytherapy Dosimetry Based on Partial Seed Localization in Ultrasound and Registration to C-arm Fluoroscopy Medical Image Computing and Computer-Assisted Intervention MICCAI 2011*, ser. Lecture Notes in Computer Science. Springer Berlin / Heidelberg, 2011, vol. 6891, pp. 291–298.

[169] W. J. Morris, M. Keyes, D. Palma, M. McKenzie, I. Spadinger, A. Agranovich, T. Pickles, M. Liu, W. Kwan, J. Wu, V. Lapointe, E. Berthelet, H. Pai, R. Harrison, W. Kwa, J. Bucci, V. Racz, and R. Woods, "Evaluation of dosimetric parameters and disease response after iodine-125 transperineal brachytherapy for low- and intermediate-risk prostate cancer," *International Journal of Radiation Oncology *Biology* Physics*, vol. 73, no. 5, pp. 1432–1438, 2009.

[170] Y. Morvan, "Acquisition, compression and rendering of depth and texture for multi-view video," Ph.D. dissertation, 2009.

[171] M. Muntener, A. Patriciu, D. Petrisor, D. Mazilu, H. Bagga, L. Kavoussi, K. Cleary, and D. Stoianovici, "Magnetic resonance imaging compatible robotic system for fully automated brachytherapy seed placement," *Urology*, vol. 68, no. 6, pp. 1313–1317, 2006.

[172] N. Naderi and J. van Beek, "Transperineal permanent brachytherapy of localised prostate cancer," *European Urology Supplements*, vol. 7, no. 12, pp. 732–741, 2008.

[173] S. Nag, W. Bice, K. DeWyngaert, B. Prestidge, R. Stock, and Y. Yan, "The American Brachytherapy Society recommendations for permanent prostate brachytherapy postimplant dosimetric analysis," *International Journal of Radiation Oncology *Biology* Physics, vol.46, no.1, 1 Jan*, vol. 46, no. 1, pp. 221–30, 2000.

[174] S. Nag, J. P. Ciezki, R. Cormack, S. Doggett, K. DeWyngaert, G. K. Edmundson, R. G. Stock, N. N. Stone, Y. Yan, and M. J. Zelefsky, "Intraoperative planning and evaluation of permanent prostate brachytherapy: report of the American Brachytherapy Society," *International Journal of Radiation Oncology *Biology* Physics*, vol. 51, no. 5, pp. 1422–30, 2001.

[175] T. Nakano and et al., "High dose-rate brachytherapy source localization: positional resolution using a diamond detector," *Physics in Medicine and Biology*, vol. 48, no. 14, pp. 2133–46, 2003.

[176] T. Nakano, N. Suchowerska, D. McKenzie, and M. Bilek, "Real-time verification of HDR brachytherapy source location: implementation of detector redundancy," *Physics in Medicine and Biology*, vol. 50, no. 2, pp. 319–27, 2005.

[177] S. Narayanan, P. S. Cho, and R. J. Marks, "Fast cross-projection algorithm for reconstruction of seeds in prostate brachytherapy," *Medical Physics*, vol. 29, no. 7, pp. 1582–9, 2002.

[178] R. Nath, J. W. S. Bice, W. M. Butler, Z. Chen, A. S. Meigooni, V. Narayana, M. J. Rivard, and Y. Yu, "Response to 'Comment on 'AAPM recommendations on dose prescription and reporting methods for permanent interstitial brachytherapy for prostate cancer: Report of Task Group 137"," *Medical Physics*, vol. 37, no. 4, pp. 1933–1933, 2009.

[179] R. Nath, W. S. Bice, W. M. Butler, Z. Chen, A. S. Meigooni, V. Narayana, M. J. Rivard, and Y. Yu, "AAPM recommendations on dose prescription and reporting methods for permanent interstitial brachytherapy for prostate cancer: Report of Task Group 137," *Medical Physics*, vol. 36, no. 11, pp. 5310–5322, 2009.

[180] C. Noel, P. J. Parikh, M. Roy, P. Kupelian, A. Mahadevan, G. Weinstein, C. Enke, N. Flores, D. Beyer, and L. Levine, "Prediction of intrafraction prostate motion: Accuracy of pre- and post-treatment imaging and intermittent imaging," *International Journal of Radiation Oncology*Biology*Physics*, vol. 73, no. 3, pp. 692–698, 2009.

[181] J. R. Novak and et al., "Verification of the sensitivity and resolution dependence on the incidence angle for slit-slat collimation," *Physics in Medicine and Biology*, vol. 53, no. 4, pp. 953–66, 2008.

[182] Y. Nyui, K. Ogawa, and E. Kunieda, "Visualization of iodine-125 seed sources for prostate brachytherapy," *Medical Imaging Technology*, vol. 25, no. 3, pp. 177–84, 2007.

[183] P. F. Orio Iii, I. B. Tutar, S. Narayanan, S. Arthurs, P. S. Cho, Y. Kim, G. Merrick, and K. E. Wallner, "Intraoperative ultrasound-fluoroscopy fusion can enhance prostate brachytherapy quality," *International Journal of Radiation Oncology *Biology* Physics*, vol. 69, no. 1, pp. 302–307, 2007.

[184] R. C. Orth, M. J. Wallace, and M. D. Kuo, "C-arm Cone-beam CT: General principles and technical considerations for use in interventional radiology," *Journal of Vascular and Interventional Radiology*, vol. 20, no. 7 S1, pp. S538–S544, 2009.

[185] R. Potter, "Image-guided brachytherapy sets benchmarks in advanced radiotherapy," *Radiotherapy and Oncology*, vol. 91, no. 2, pp. 141–146, 2009.

[186] J. Palmer and P. Wollmer, "Pinhole emission computed tomography: method

and experimental evaluation," *Physics in Medicine and Biology*, vol. 35, no. 3, p. 339, 1990.

[187] H. Park, J. Y. Kim, B. M. Lee, S. K. Chang, S. Y. Ko, S. J. Kim, D. S. Park, and H. S. Shin, "A comparison of preplan MRI and preplan CT-based prostate volume with intraoperative ultrasound-based prostate volume in real-time permanent brachytherapy," *Journal of Radiation Oncology*, vol. 29, no. 3, pp. 199–205, 2012.

[188] M. Petasecca, K. J. Loo, M. Safavi-Naeini, Z. Han, P. E. Metcalfe, S. Meikle, S. Pospisil, J. Jakubek, J. A. Bucci, M. Zaider, M. L. F. Lerch, Y. Qi, and A. B. Rosenfeld, "Brachyview: Proof-of-principle of a novel in-body gamma camera for low dose-rate prostate brachytherapy," *Medical Physics*, vol. 40, no. 4, 2013.

[189] J. Phan, D. A. Swanson, L. B. Levy, R. J. Kudchadker, T. L. Bruno, and S. J. Frank, "Late rectal complications after prostate brachytherapy for localized prostate cancer," *Cancer*, vol. 115, no. 9, pp. 1827–1839, 2009.

[190] T. Pickles, M. Keyes, and W. J. Morris, "Brachytherapy or conformal external radiotherapy for prostate cancer: A single-institution matched-pair analysis," *International Journal of Radiation Oncology *Biology* Physics*, vol. 76, no. 1, pp. 43–49, 2010.

[191] M. Pinkawa, B. Asadpour, M. D. Piroth, B. Gagel, J. Klotz, K. Fischedick, H. Borchers, G. Jakse, and M. J. Eble, "Rectal dosimetry following prostate brachytherapy with stranded seeds - comparison of transrectal ultrasound intra-operative planning (day 0) and computed tomography-postplanning (day 1 vs. day 30) with special focus on sources placed close to the rectal wall," *Radiotherapy and Oncology*, vol. 91, no. 2, pp. 207–212, 2009.

[192] M. Pinkawa, B. Gagel, B. Asadpour, M. Piroth, J. Klotz, H. Borchers, G. Jakse, and M. Eble, "Seed displacements after permanent brachytherapy

for prostate cancer in dependence on the prostate level," *Strahlentherapie und Onkologie*, vol. 184, no. 10, pp. 520–5, 2008.

[193] D. Pokhrel, M. J. Murphy, D. A. Todor, E. Weiss, and J. F. Williamson, "Reconstruction of brachytherapy seed positions and orientations from cone-beam CT x-ray projections via a novel iterative forward projection matching method," *Medical Physics*, vol. 38, no. 1, pp. 474–486, 2011.

[194] A. S. Pradhan and U. Quast, "In-phantom response of LiF TLD-100 for dosimetry of Ir-192 HDR source," *Medical Physics*, vol. 27, no. 5, pp. 1025–1029, 2000.

[195] B. R. Prestidge M.D, W. S. Bice, E. J. Kiefer, and J. J. Prete, "Timing of computed tomography-based postimplant assessment following permanent transperineal prostate brachytherapy," *International Journal of Radiation Oncology *Biology* Physics*, vol. 40, no. 5, pp. 1111–1115, 1998.

[196] Z.-Y. Qi, X.-W. Deng, S.-M. Huang, J. Lu, M. Lerch, D. Cutajar, and A. Rosenfeld, "Verification of the plan dosimetry for high dose rate brachytherapy using metal–oxide–semiconductor field effect transistor detectors," *Medical Physics*, vol. 34, no. 6, pp. 2007–2013, 2007.

[197] A. Ravi, C. B. Caldwell, and J.-P. Pignol, "Experimental evaluation of an online gamma-camera imaging of permanent seed implantation (OGIPSI) prototype for partial breast irradiation," *Medical Physics*, vol. 35, no. 6, pp. 2485–2492, 2008.

[198] A. Ravi, C. Caldwell, B. Keller, A. Reznik, and J. Pignol, "Online gamma-camera imaging of 103 pd seeds (OGIPS) for permanent breast seed implantation," *Physics in Medicine and Biology*, vol. 52, no. 19, pp. 5921–32, 2007.

[199] P. Ravindran, C. Lewis, J. Van Dyk, and D. D'Souza, "Intra-operative dosimetry of trans-rectal ultrasound guided I-125 prostate implants using C-arm fluoroscopic images," *Journal of Medical Physics*, vol. 31, no. 2, pp. 61–66, 2006.

[200] D. R. Reed, K. E. Wallner, S. Narayanan, S. G. Sutlief, E. C. Ford, and P. S. Cho, "Intraoperative fluoroscopic dose assessment in prostate brachytherapy patients," *International Journal of Radiation Oncology *Biology* Physics*, vol. 63, no. 1, pp. 301–307, 2005.

[201] E. Roeloffzen, "Prediction of acute urinary retention after I-125 prostate brachytherapy," Ph.D. dissertation, 2010.

[202] E. M. A. Roeloffzen, I. M. Lips, M. P. R. van Gellekom, J. van Roermund, S. J. Frank, J. J. Battermann, and M. van Vulpen, "Health-related quality of life up to six years after I-125 brachytherapy for early-stage prostate cancer," *International Journal of Radiation Oncology *Biology* Physics*, vol. 76, no. 4, pp. 1054–1060, 2010.

[203] A. B. Rosenfeld, D. L. Cutajar, M. L. F. Lerch, G. J. Takacs, J. Brady, T. Braddock, V. L. Perevertaylo, J. Bucci, J. Kearsley, M. Zaider, and M. Zelefsky, "In vivo dosimetry and seed localization in prostate brachytherapy with permanent implants," *IEEE Transactions on Nuclear Science*, vol. 51, no. 6, pp. 3013–3018, 2004.

[204] A. Sahgal and M. Roach III, "Permanent prostate seed brachytherapy: A current perspective on the evolution of the technique and its application," *Nature Clinical Practice Urology*, vol. 4, no. 12, pp. 658–670, 2007.

[205] S. K. Saxena, S. D. Sharma, A. Dash, and M. Venkatesh, "Development of a new design I-125 brachytherapy seed for its application in the treatment of eye and prostate cancer," *Applied Radiation and Isotopes*, vol. 67, no. 7-8, pp. 1421–5, 2009.

[206] E. Schussler, J. Calligy, and R. G. Stock, "Comparison of dose and volume parameters for prostate brachytherapy in prediction of biochemical failure," *International Journal of Radiation Oncology *Biology* Physics*, vol. 75, no. 3S1, pp. S618–S618, 2009.

[207] S. Jiang, N. Hata, and R. Kikinis, "Needle insertion simulation for image-guided brachytherapy of prostate cancer," in *Bioinformatics and Biomedical Engineering, 2008. ICBBE 2008. The 2nd International Conference on*, 2008, pp. 1682–1685.

[208] J. Sharkey, S. D. Chovnick, R. J. Behar, R. Perez, J. Otheguy, Z. Solc, W. Huff, and A. Cantor, "Outpatient ultrasound-guided palladium-103 brachytherapy for localized adenocarcinoma of the prostate: A preliminary report of 434 patients," *Urology*, vol. 51, no. 5, pp. 796–803, 1998.

[209] N. S. Sheth, S. E. Sim, A. M. Grebler, J. M. Geltzeiler, I. S. Keselman, Y. S. Litvin, I. Waldman, M. F. Weiss, S. A. Murphy, and J. Yang, "I-125 seed nomogram for real-time intraoperative prostate brachytherapy," *Brachytherapy*, vol. 9, no. S1, pp. S93–S94, 2010.

[210] R. L. Siddon and L. M. Chin, "Two-film brachytherapy reconstruction algorithm," *Medical Physics*, vol. 121, no. 1, pp. 77–83, 1985.

[211] E. Y. Sidky, C. M. Kao, and X. Pan, "Accurate image reconstruction from few-views and limited-angle data in divergent-beam CT," *Journal of X-Ray Science and Technology*, vol. 14, no. 2, pp. 119–139, 2006.

[212] F. Siebert, M. Hirt, P. Niehoff, and G. Kovacs, "Imaging of implant needles for real-time hdr-brachytherapy prostate treatment using biplane ultrasound transducers," *Medical Physics*, vol. 36, no. 8, pp. 3406–12, 2009.

[213] F.-A. Siebert, M. De Brabandere, C. Kirisits, G. Kovacs, and J. Venselaar, "Phantom investigations on ct seed imaging for interstitial brachytherapy," *Radiotherapy and Oncology*, vol. 85, no. 2, pp. 316–323, 2007.

[214] R. Singh, H. Al-Hallaq, C. A. Pelizzari, G. P. Zagaja, A. Chen, and A. B. Jani, "Dosimetric quality endpoints for low-dose-rate prostate brachytherapy using biological effective dose (bed) vs. conventional dose," *Medical Dosimetry*, vol. 28, no. 4, pp. 255–9, 2003.

[215] V. Singh, L. Mukherjee, X. Jinhui, K. R. Hoffmann, P. M. Dinu, and M. Podgorsak, "Brachytherapy seed localization using geometric and linear programming techniques," *IEEE Transactions on Medical Imaging*, vol. 26, no. 9, 2007.

[216] L. J. Slate, H. R. Elson, M. A. S. Lamba, W. M. Kassing, M. Soldano, and W. L. Barrett, "A Monte Carlo brachytherapy study for dose distribution prediction in an inhomogeneous medium," *Medical Dosimetry*, vol. 29, no. 4, pp. 271–8, 2004.

[217] W. L. Smith, C. Lewis, G. Bauman, G. Rodrigues, D. D'Souza, R. Ash, D. Ho, V. Venkatesan, D. Downey, and A. Fenster, "Prostate volume contouring: A 3D analysis of segmentation using 3DTRUS, CT, and MR," *International Journal of Radiation Oncology *Biology* Physics*, vol. 67, no. 4, pp. 1238–1247, 2007.

[218] D. Snyder, J. O'Sullivan, R. Murphy, D. Politte, B. Whiting, and J. Williamson, "Image reconstruction for transmission tomography when projection data are incomplete," *Physics in Medicine and Biology*, vol. 51, no. 21, pp. 5603–19, 2006.

[219] M. C. Solhjem, B. J. Davis, T. M. Pisansky, T. M. Wilson, L. A. Mynderse, M. G. Herman, B. F. King, and S. M. Geyer, "Prostate volume measurement by transrectal ultrasound and computed tomography before and after permanent prostate brachytherapy," *International Journal of Radiation Oncology *Biology* Physics*, vol. 60, no. 3, pp. 767–776, 2004.

[220] P. Soukup, J. Jakubek, I. Jandejsek, and J. Zemlicka, "X-ray color imaging with 3D sensitive voxel detector," *Journal of Instrumentation*, vol. 6, no. 12, pp. C12 014–20, 2011.

[221] N. N. Stone and R. G. Stock, "Prostate brachytherapy in patients with prostate volumes $\geq$50 cm^3: dosimetic analysis of implant quality," *International Jour-*

*nal of Radiation Oncology *Biology* Physics*, vol. 46, no. 5, pp. 1199–1204, 2000.

[222] Y. Su, B. J. Davis, K. M. Furutani, M. G. Herman, and R. A. Robb, "Prostate brachytherapy seed reconstruction using an adaptive grouping technique," *Medical Physics*, vol. 34, no. 7, pp. 2975–2984, 2007.

[223] Y. Su, B. J. Davis, M. G. Herman, A. Manduca, and R. A. Robb, "Examination of dosimetry accuracy as a function of seed detection rate in permanent prostate brachytherapy," *Medical Physics*, vol. 32, no. 9, pp. 3049–3056, 2005.

[224] Y. Su, B. J. Davis, K. M. Furutani, M. G. Herman, and R. A. Robb, "Dosimetry accuracy as a function of seed localization uncertainty in permanent prostate brachytherapy: increased seed number correlates with less variability in prostate dosimetry," *Physics in Medicine and Biology*, vol. 52, no. 11, pp. 3105–9, 2007.

[225] A. V. Taira, G. S. Merrick, W. M. Butler, R. W. Galbreath, J. Lief, E. Adamovich, and K. E. Wallner, "Long-term outcome for clinically localized prostate cancer treated with permanent interstitial brachytherapy," *International Journal of Radiation Oncology *Biology* Physics*, vol. 79, no. 5, pp. 1336–1342, 2011.

[226] K. Tanderup, S. Beddar, C. E. Andersen, G. Kertzscher, and J. E. Cygler, "In vivo dosimetry in brachytherapy," *Medical Physics*, vol. 40, no. 7, 2013.

[227] I. B. Tutar, L. Gong, S. Narayanan, S. D. Pathak, P. S. Cho, K. Wallner, and Y. Kim, "Seed-based transrectal ultrasound-fluoroscopy registration method for intraoperative dosimetry analysis of prostate brachytherapy," *Medical Physics*, vol. 35, no. 3, pp. 840–848, 2008.

[228] A. van't Riet, H. J. te Loo, A. F. G. V. M. Ypma, A. C. A. Mak, F. H. S. Van Slooten, C. J. M. Hoekstra, and M. C. Stenfert Kroese, "Ultrasonically guided transperineal seed implantation of the prostate: Modification of the

technique and qualitative assessment of implants," *International Journal of Radiation Oncology *Biology* Physics*, vol. 24, no. 3, pp. 555–558, 1992.

[229] O. N. Vassiliev, R. J. Kudchadker, D. A. Swanson, T. L. Bruno, M. van Vulpen, and S. J. Frank, "Displacement of periurethral stranded seeds and its dosimetric consequences in prostate brachytherapy," *Brachytherapy*, vol. 10, no. 5, pp. 401–408, 2011.

[230] F. A. Vicini, V. R. Kini, G. Edmundson, G. S. Gustafson, J. Stromberg, and A. Martinez, "A comprehensive review of prostate cancer brachytherapy: defining an optimal technique," *International Journal of Radiation Oncology *Biology* Physics*, vol. 44, no. 3, pp. 483–491, 1999.

[231] S. Voulgaris, J. Nobes, R. Laing, and S. Langley, "State-of-the-art: prostate LDR brachytherapy," *Prostate Cancer and Prostatic Diseases*, vol. 11, no. 3, p. 237, 2008.

[232] Z. Vykydal and J. Jakubek, "USB lite–miniaturized readout interface for Medipix2 detector," *Nuclear Instruments and Methods in Physics Research Section A: Accelerators, Spectrometers, Detectors and Associated Equipment*, vol. 633, no. S1, pp. S48–S49, 2011.

[233] Z. Vykydal, J. Jakubek, and M. Svestkova, "Micro-probe for medical radiation imaging based on Medipix2 detector," in *Nuclear Science Symposium Conference Record (NSS/MIC), 2009 IEEE*, 2009, pp. 2795–2797.

[234] L. Meira-Belo, E. Rodrigues, and S. Grynberg, "Methodology for characterizing seeds under development for brachytherapy by means of radiochromic and photographic films," *Applied Radiation and Isotopes*, vol. 74, pp. 26–30, 2013.

[235] K. Wallner, J. Roy, and L. Harrison, "Dosimetry guidelines to minimize urethral and rectal morbidity following transperineal I-125 prostate brachytherapy," *International Journal of Radiation Oncology *Biology* Physics*, vol. 32, no. 2, pp. 465–471, 1995.

[236] K. Wallner, J. Roy, M. Zelefsky, Z. Fuks, and L. Harrison, "Fluoroscopic visualization of the prostatc urethra to guide transperineal prostate implantation," *International Journal of Radiation Oncology *Biology* Physics*, vol. 29, no. 4, pp. 863–867, 1994.

[237] J. Z. Wang, N. A. Mayr, S. Nag, J. Montebello, N. Gupta, N. Samsami, and C. Kanellitsas, "Effect of edema, relative biological effectiveness, and dose heterogeneity on prostate brachytherapy," *Medical Physics*, vol. 33, no. 4, pp. 1025–32, 2006.

[238] F. M. Waterman and A. P. Dicker, "The impact of postimplant edema on the urethral dose in prostate brachytherapy," *International Journal of Radiation Oncology *Biology* Physics*, vol. 47, no. 3, pp. 661–664, 2000.

[239] F. M. Waterman and A. P. Dicker, "Probability of late rectal morbidity in I-125 prostate brachytherapy," *International Journal of Radiation Oncology *Biology* Physics*, vol. 55, no. 2, pp. 342–353, 2003.

[240] J. Williamson, "Brachytherapy technology and physics practice since 1950: a half-century of progress," *Physics in Medicine and Biology*, vol. 51, no. 13, pp. R303–25, 2006.

[241] J. Williamson, "Current brachytherapy quality assurance guidance: Does it meet the challenges of emerging image-guided technologies?" *International Journal of Radiation Oncology *Biology* Physics*, vol. 71, no. S1, pp. S18–S22, 2008.

[242] K. S. Won, E. E. Kim, M. Mar, S. Gohar, W. Erwin, W. Wei, and I. Gayed, "Is iterative reconstruction an improvement over filtered back projection in processing gated myocardial perfusion SPECT?" *The Open Medical Imaging Journal*, vol. 2, pp. 17–23, 2008.

[243] J. M. Woolfenden, H. B. Barber, J. R. Oleson, and W. J. Wild, "Rapid in vivo localization of a lost brachytherapy seed," *Medical Physics*, vol. 11, no. 4, pp. 558–559, 1984.

[244] P. Wust, D. W. von Borczyskowski, T. Henkel, C. Rosner, R. Graf, W. Tilly, V. Budach, R. Felix, and F. Kahmann, "Clinical and physical determinants for toxicity of I-125 seed prostate brachytherapy," *Radiotherapy and Oncology*, vol. 73, no. 1, pp. 39–48, 2004.

[245] J. Xue, F. Waterman, J. Handler, and E. Gressen, "Localization of linked I-125 seeds in postimplant TRUS images for prostate brachytherapy dosimetry," *International Journal of Radiation Oncology *Biology* Physics*, vol. 63, no. S1, pp. S522–S523, 2005.

[246] Y. Yoshioka, K. Konishi, O. Ryoong-Jin, I. Sumida, H. Yamazaki, S. Nakamura, K. Nishimura, N. Nonomura, A. Okuyama, and T. Inoue, "High-dose-rate brachytherapy without external beam irradiation for locally advanced prostate cancer," *Radiotherapy and Oncology*, vol. 80, no. 1, pp. 62–8, 2006.

[247] S. R. Zakavi, A. Zonoozi, V. D. Kakhki, M. Hajizadeh, M. Momennezhad, and K. Ariana, "Image reconstruction using filtered backprojection and iterative method: Effect on motion artifacts in myocardial perfusion SPECT," *Journal of Nuclear Medicine Technology*, vol. 34, no. 4, pp. 220–223, 2006.

[248] M. J. Zelefsky, T. Hollister, A. Raben, S. Matthews, and K. E. Wallner, "Five-year biochemical outcome and toxicity with transperineal CT-planned permanent I-125 prostate implantation for patients with localized prostate cancer," *International Journal of Radiation Oncology *Biology* Physics*, vol. 47, no. 5, pp. 1261–1266, 2000.

[249] M. J. Zelefsky, Y. Yamada, G. N. Cohen, N. Sharma, A. M. Shippy, D. Fridman, and M. Zaider, "Intraoperative real-time planned conformal prostate brachytherapy: Post-implantation dosimetric outcome and clinical implications," *Radiotherapy and Oncology*, vol. 84, no. 2, pp. 185–189, 2007.

[250] M. J. Zelefsky and M. Zaider, "Low-dose-rate brachytherapy for prostate cancer: Preplanning vs. intraoperative planning–intraoperative planning is best," *Brachytherapy*, vol. 5, no. 3, pp. 143–144, 2006.

[251] M. Zhang, M. Zaider, M. Worman, and G. Cohen, "On the question of 3D seed reconstruction in prostate brachytherapy: the determination of x-ray source and film locations," *Physics in Medicine and Biology*, vol. 49, no. 19, pp. N335–45, 2004.

[252] K. Zourari, E. Pantelis, A. Moutsatsos, L. Petrokokkinos, P. Karaiskos, L. Sakelliou, E. Georgiou, and P. Papagiannis, "Dosimetric accuracy of a deterministic radiation transport based Ir-192 brachytherapy treatment planning system. part i: Single sources and bounded homogeneous geometries," *Medical Physics*, vol. 37, no. 2, pp. 649–661, 2010.